High-performance Pt-free Oxygen Reduction Reaction Electrocatalysts Derived from Carbon Supported Spinel Cobalt Ferrite and Co/Fe-Nitrogen Coordinated Active Centers for Advanced Energy Applications

Thesis Submitted to AcSIR

For the Award of the Degree of

DOCTOR OF PHILOSOPHY

In

Chemical Science

By

Mr. Varchaswal Kashyap

(Registration Number: 10CC14J26015)

Under the guidance of

Dr. Sreekumar Kurungot

CSIR-National Chemical Laboratory,
Pune-411008, India

December 2018

सीएसआईआर - राष्ट्रीय रासायनिक प्रयोगशाला
(वैज्ञानिक तथा औद्योगिक अनुसंधान परिषद)
डॉ. होमी भाभा मार्ग, पुणे - 411 008, भारत
CSIR - NATIONAL CHEMICAL LABORATORY
(Council of Scientific & Industrial Research)
Dr. Homi Bhabha Road, Pune - 411 008, India

Certificate

This is to certify that the work incorporated in this Ph.D. thesis entitled **"High-performance Pt-free Oxygen Reduction Reaction Electrocatalysts Derived from Carbon Supported Spinel Cobalt Ferrite and Co/Fe-Nitrogen Coordinated Active Centers for Advanced Energy Applications"** submitted by **Mr. Varchaswal Kashyap** to Academy of Scientific and Innovative Research (AcSIR) in fulfillment of the requirements for the award of the Degree of ***Doctor of Philosophy***, embodies original research work under my supervision at Physical and Materials Chemistry Division, CSIR-National Chemical Laboratory, Pune-411008, India. I further certify that this work has not been submitted to any other University or Institution in part or full for the award of any degree or diploma. Research material obtained from other sources has been duly acknowledged in the thesis. Any text, illustration, table etc., used in the thesis from other sources, have been duly cited and acknowledged.

Varchaswal Kashyap
(Student)

Dr. Sreekumar Kurungot
(Supervisor)

Communication Channels
NCL Level DID : 2590
NCL Board No. : +91-20-25902000
EPABX : +91-20-25893300
: +91-20-25893400
FAX
Director's Office : +91-20-25902601
COA's Office : +91-20-25902660
SPO's Office : +91-20-25902664
WEBSITE
www.ncl-india.org

DECLARATION

I, hereby declare that all the experiments in thesis entitled **"High-performance Pt-free Oxygen Reduction Reaction Electrocatalysts Derived from Carbon Supported Spinel Cobalt Ferrite and Co/Fe-Nitrogen Coordinated Active Centers for Advanced Energy Applications"** submitted for the degree of Doctor of Philosophy in Chemical Sciences to the Academy of Scientific and Innovative Research (AcSIR) have been carried out by me at the Physical and Materials Chemistry Division, CSIR-National Chemical Laboratory, Pune-411008, India, under the supervision of **Dr. Sreekumar Kurungot**. This work is original and has not been submitted to any other University or Institution in part or full for the award of any degree or diploma.

Varchaswal Kashyap

Mr. Varchaswal Kashyap
Physical and Materials Chemistry Division,
CSIR-National Chemical Laboratory,
Pune-411008, India.

Date: 1/05/2019

Acknowledgements

At this moment of my life, I wish to give my vote of thanks and gratitude to the most amazing people whom I met during my doctoral thesis work and who significantly helped me to reach this level. I am indebted to them and feel acknowledging their efforts could be a humble way to remember their efforts.

Firstly, I take it as my privilege to express my gratitude to my Research Guide, Dr. Sreekumar Kurungot, who encouraged me to solve the tuff research problems through his constant monitoring and suggestions. I have been fortunate enough to have him as the supervisor who provided all the freedom to work on my own idea with minimal restrictions and helped me to recover back when at times of uncertainty. I appreciate his constant support when there was no proper research outcome even after the two years of constant efforts in my initial phase of the research and with his encouragement and guidance I could overcome this phase. His advices and constant monitoring of the research work have helped me to solve the problems systematically, which finally led in the form of nice publications. The morning meetings, monthly plans, work presentations and weekly literature presentations have given me enormous confidence to start independent research work with sharp understanding of the scientific culture. His amazing power to manage the time for each and every part of life is quite inspiring and definitely stands out as a model to success.

I am grateful to Prof. Ashwini K. Nangia (Director CSIR-NCL) and Dr. Sourav Pal (Former Director CSIR-NCL) who gave me an opportunity to work in this prestigious national laboratory and provided all the facilities to encourage the research work. I am also grateful to Dr. P. A. Joy, Head and Chairman of Physical and Materials Chemistry Division, for allowing me to use all the available facilities in the division.

My special and sincere thanks to my DAC members Dr. Rahul Banerjee, Dr. C. P. Vinod, Dr. J. Nithyanadhan and DAC chairperson Dr. Amol A. Kulkarni for their valuable suggestions, fruitful discussion and advices during the DAC meetings. Their time to time scientific suggestions and encouragements to solve the problem have enormously helped me in shaping my thesis.

I am very much thankful to Mr. Golap, Dr. Selveraj and Mr. Dev who were helpful in the characterization of various samples at Center for Materials Characterizations (CMC).

I am highly indebted to SAO employees Ms. PrurnimaKohle, Mr. P. V. Iyer, Ms. Komal, Ms. Harshita, Ms. Vrushali, Mr. Santosh and others for processing my documents on time.

My sincere thanks to Ms. SunitaBharve and Mr. GatiNayar for providing me the library support for various scientific journals and helping me to conduct time to time plagiarism checking.

I am forever indebted to all my former teachers from my initial schooling to college life. I feel deep esteem for Prof. S.K. Sengupta, Prof. Biswajit Ray, Prof. Satyen Saha, Prof. Biswajit Matti and Prof. Pankaj Srivastava from my former Banaras Hindu University, who built the foundation of my research life.

I would like to thank my friends in B.H.U., Vikas Tripathi, Arvind Tripathi, Ratnakar Dutt Sukla, Ravindra Yadav, Rajneesh, Rahul Kumar, Akhilesh Pandey, Sanjeev Kumar Soni, Swechha Pandey, Dilip Pandey and Vipin Kumar Singh for their support and affection during my college life.

My special gratefulness to my seniors, Dr. Palaniselvem Thangavelu, Dr. Sreekuttan M. Unni, Dr. Vishal M. Dhavale, Dr. Bihag Annothumkool, Dr. Harshita B. A. and Dr. Santosh K. Singh for their mentoring and care during my initial days in CSIR-NCL. I must thank again Dr. Palaniselvem for giving initial training in my first phase at NCL.

I can never forget my ever-trustful friends in the lab, Roby Soni, Ayesha Nadeema, Rajith, Siddhu, Pranav, Meena, Vidyanand, Manna, Sachin, Dr. Gavrav, Dr. Raji, Dr. Shilpa, and Dr. Debasree for all their affection, help and support.

I would like to thank my CSIR-NCL friends, Arun Dadwal, Pratiksh Patel (pinka), Singham, Sameer Saikh, Indrapal, KorraPravin, Pravin Shinde, Anup, Vikas Chaturvedi, Sandeep, Swecha Pandey, Ashwini Wali, Sharad Gupta, Zenoy, Priti Jain, Yogesh Gwali, Mukta, Punam Yadav, Swati Parmar, Parul Trivedi, Preety Singh, Yogendra Patil, Chhaya Patil, Sarath Ramdas and Sanup Nair for providing me an excellent working ambience during my research work.

I find no words to express my feeling for my father (Mr.V.Vidhata) and mother (Smt. C. Devi) whose moral support, love, and constant support have helped me to reach at this level. Their awareness for education and firm determination for my higher education have always boosted me. I also express my heartfelt gratitude to my younger brother (Urajswal Kashyap), my sister (Varchaswini Vishakha) and my brother-in-law Mr. Avanindra for their constant support and affection. I owe deeply to my cousins and relatives, Mr. Vachaspati, Smt. Lilawati, Mr. and Mrs. Dux, Mr. Jamdagni Kashyap, Mr. Patanjali Kashyap, Mr. Pragyapati Kashyap, Susma, Kushum, Upma, Pratima, Divyansu, Mr. and Mrs. Vishwamitra, Lallan, and others who stood by my side when needed. I cannot forget my neighbors and friends, Vicky bhaiya, Munna bhaiya, Ankit Jaiswal, and Ashutosh Sukla who always supported me. I must again thank to my uncle especially, Mr. Patanjali Kashyap, who stood by my side when I intensively needed help.

Above all, I thank God for giving me strength and wisdom to achieve success and do well to society.

Though, many have not been mentioned but their support and affection is with me.

Varchaswal Kashyap

List of Abbreviations

Abbreviation	Expansions
AEMFC	Anion Exchange Membrane Fuel Cell
ADT	Accelerated Durability Test
BET	Brunauer-Emmett-Teller
CA	Chronopotentiometry
CE	Counter Electrode
CF	Cobalt Ferrite
CFZn	Zinc Substituted Cobalt Ferrite
CFZr	Zirconium Substituted Cobalt Ferrite
CF/N-rGO	Cobalt Ferrite/ Nitrogen Doped Reduced Graphene Oxide
CNF	Carbon Nanofibre
CNT	Carbon Nanotube
CP	Chronopotentiaometry
CSIR	Council of Scientific and Industrial Research
CV	Cyclic Voltamogram
CO	Carbon Monoxide
DFT	Density Functional Theory
DMFC	Direct Methanol Fuel Cell
DST	Department of Science and Technology
EDAX	Energy Dispersive X-ray Analysis
ECSA	Equivalent Series Resistance
FT-IR	Fourier Transformed Infrared

GC	Glassy Carbon
GO	Graphene Oxide
Gr	Graphene
HER	Hydrogen Evolution Reaction
HR-TEM	High Resolution Transmission Electron Microscopy
IR	Infrared
K-L	Koutecky-Levich
LSV	Linear Sweep Voltammetry
MEA	Membrane Electrolyte Assembly
MCFC	Molten Carbonate Fuel Cell
N-rGO	Nitrogen Doped Reduced Graphene Oxide
OCV	Open Circuit Voltage
OER	Oxygen Evolution Reaction
ORR	Oxygen Reduction Reaction
PAFC	Phosphoric Acid Fuel Cell
PBI	Polybenzimidazole
PEMFC	Polymer Electrolyte Membrane Fuel Cell
PGM	Platinum Group Metal
RE	Reference Electrode
rGO	Reduced Graphene Oxide
RHE	Reversible Hydrogen Electrode
RDE	Rotating Disc Electrode
RRDE	Rotating Ring Disc Electrode
SAED	Selected Area Electron Diffraction
SEM	Scanning Electron Microscopy

SOFC	Solid Oxide Fuel Cell
TEM	Transmission Electron Microscopy
TGA	Thermogravimetric Analysis
WE	Working Electrode
XRD	X-ray Diffraction
XPS	X-ray Photoelectron Spectroscopy
ZAB	Zinc-Air Battery

Table of Contents

Chapter 3

Size Optimized Cobalt Ferrite Nanoparticle Supported N-doped Reduced Graphene Oxide as an Efficient Oxygen Reduction Catalyst for Primary Zinc-air Battery

Chapter 4

Structural Modification in the Spinel Cobalt Ferrite Matrix with Zn Substitution for Enhanced Oxygen Reduction Reaction

Chapter 5

Zirconium Substitution in the Spinel Cobalt Ferrite Matrix for Bifunctional Activity: A Potential Electrode Material for Rechargeable Zinc-air Battery

Chapter 6

Electrochemical Activity of Fe/CoN_x Grafted Carbon in Acidic and Basic Media

PREFACE

The issues of increasing side effects of the conventional fossil fuel based energy systems with the continuously increasing energy demand have forced the scientific community to develop suitable clean energy generation and storage systems. In this respect, lithium-ion batteries, supercapacitors, fuel cells and metal-air batteries have come up as clean substitutes for the traditional non-renewable energy resources and created diverse scientific and technological interest. Further, in order to ensure the penetrability of such systems in the energy market, it is desirable that these devices should be efficient and cost-effective. In general, the major cost contributing factor in these devices is the electrode material. The ability of a material to serve as an electrode material is depending on how well it can help to facilitate the specific electrode processes. For example, in the case of the metal-air batteries and fuel cells, the oxygen reduction reaction (ORR) is the rate determining process and hence a catalyst which can facilitate this reaction at a reduced overpotential becomes the ideal candidate. On the other hand, in the case of a rechargeable metal-air battery, both ORR and oxygen evolution reaction (OER) become relevant, thereby, the multifunctionality of the catalyst becomes important. Since ORR and OER are the two prominent electrode processes which have a direct effect on deciding the energy efficiency of some of the electrochemical systems as mentioned above, it is important to find out cost-effective and energy efficient catalysts to facilitate these reactions.

Until now, electrocatalysts based on noble metals (Pt, Ir, Pd and its alloys) have been the most effective catalysts available for enhancing the sluggish ORR and OER, but they are scarce, have poor durability, and have a high cost. Considering these prohibitive factors of the noble-metal composites, many studies aimed to minimize these factors are being conducted. Among the viable and cost-effective alternatives to Pt for ORR, the first-row transition metals are widely explored because of their tunable properties and easy availability for the applications. Transition-metal oxides, chalcogenides, oxynitrides, and their complexes have shown good performance in catalyzing these crucial reactions. Additionally, attempts to develop hybrid catalysts such as with the graphitic carbon framework and metal oxide composites have tremendously enhanced the performance. More interestingly, when heteroatom-doped graphitic carbon such as N-doped graphene or N-doped carbon nanotubes are used as supports for nanoparticles of early transition-

metal oxides like CoO, Co_3O_4, $MnCo_2O_4$, $ZnFe_2O_4$, and $CuCo_2O_4$, the potential synergistic effect of the heteroatom-doped conducting carbon and the nanoparticles resulted in outstanding ORR activity. Similarly, for OER, nanometer-sized NiFe hydroxides, $NiCo_2O_4$, $ZnCo_2O_4$, and CoO exhibit remarkably high activity and durability.

Although these oxides are capable of displaying interesting catalytic activity characteristics, the intrinsic activities of these types of systems are found to be largely depending on other parameters such as particle size, morphology, and how well the catalyst particles are dispersed on a conducting substrate and additionally the surface intermediates involved in the process. Herein, we have explored the close relation of particle size, dispersion characteristics of the active particles on a conducting carbon, substitution effect of other metals and controlled interplay of the surface intermediates for the cobalt and iron metal atoms in facilitating the reactions like ORR and OER. Substituting some portion of Fe by Zn in the spinel lattice of cobalt ferrite nanocrystals can favorably influence the overpotential for ORR. However, the substitution of Zr in a cobalt ferrite matrix shows a significant level of improvement for the overpotentials of both ORR and OER, thereby positioning the composite as a potential bifunctional electrocatalyst. Basically, the electrochemical faradaic reactions are controlled by the transition states formed in between the reaction process and the adsorption energies of these states. In acidic and basic media, the stability of the transition states changes significantly with a direct impact on the ORR activity. To understand this and to gain insightful information on the mechanistic aspects, we have studied the variation in the ORR activity with the nature of the medium for cobalt and iron atom incorporated active centers. The functioning of the catalyst is demonstrated in the primary zinc-air battery in correlation of the transition states over the catalyst. The findings of the individual chapters are highlighted below:

Chapter 1 deals with a brief description of the global energy consumption scenario, strategic development of the energy devices and the key components involved to effectively implement the ideas. The recent reports have clearly highlighted the need of the green energy devices as the major substitutes to the petroleum-based energy sources which can notably reduce the globalwarming and ultimately the human risk factors. Among these renewable energy devices, metal-air batteries and fuel cells are of prime importance owing to their high energy density and environmental benign characteristics. The fabrication of commercially viable fuel cells and

metal-air batteries depends on developing the highly efficient and cost-effective catalysts for assisting ORR, which is the bottleneck for the devices. In the case of realizing rechargeable metal-air batteries, along with ORR, how well the catalyst can facilitate OER also becomes equally important. **Chapter 1** briefly highlights the status of the noble metal and noblemetal-free electrocatalysts, their synthesis methods and activity characteristics in the real devices. A concise state-of-the-art survey on these aspects are included in the chapter. After discussing about the requirements in a realistic perspective considering the current status of development of the energy systems, the chapter ends with a section dealing with the scope and objectives of the dissertation.

Chapter 2 provides a glimpse of the synthetic strategies adopted for the preparation of the various carbon materials such as graphene oxide (GO), chemically reduced N-doped graphene oxide (N-rGO), metal oxide nanoparticles etc. by simple and scalable chemical methods. The chapter also deals with the working principles of the various material characterization techniques and the plethora of information disclosed for the materials by the techniques. Here, details of instrumentation and sampling of the structural characterization techniques are summarized briefly. Discussions on the high-resolution transmission electron microscopy (HR-TEM) for imaging, powder X-ray diffraction (PXRD) method for structural analysis, energy dispersive X-ray diffraction (EDAX) method for elemental analysis, Raman spectroscopy for identifying defects in carbon framework, infrared(IR) spectroscopy for characterizing chemical bonds and X-ray photoelectron spectroscopy (XPS) for surface analysis and theromogravimetric analysis (TGA) for understanding compositional aspects are included for the detailed understanding of various catalysts. The chapter also briefly explains the working principles of a set of electrochemical techniques which are adopted for characterizing the materials and also for evaluating the performance aspects of the devices. These include cyclic voltammetry (CV), linear sweep voltammetry (LSV), chronopotentiometry (CP), chronoamperometry (CA), rotating disk electrode (RDE), rotating ring disk electrode (RRDE), single-cell testing of Zn-air battery etc.

Chapter 3 discloses how high-quality dispersion of fine particles of cobalt ferrite (CF) could be attained on nitrogen-doped reduced graphene oxide (CF/N-rGO) and how this material in association with a microporous carbon phase could deliver significantly enhanced activity

towards electrochemical ORR. The study indicates that the microporous carbon phase plays a critical role in spatially separating the layers of CF/N-rGO and in creating a favorable atmosphere to ensure the seamless distribution of the reactants to the active sites located on CF/N-rGO. In terms of the ORR current density, the heat-treated hybrid catalyst at 150 ^{o}C (CF/N-rGO-150) is found to be clearly outperforming (7.4 ± 0.5 mA/cm^2) the state-of-the-art 20 wt.% Pt supported carbon catalyst (PtC) (5.4 ± 0.5 mA/cm^2). The mass activity and stability of CF-N-rGO-150 is distinctly superior to Pt/C even after 5000 electrochemical cycles. Distinctly, the battery performance of this system is found to be superior to that of Pt/C in less concentrated KOH solution as the electrolyte.

Chapter 4 deals with an effective strategy wherein an efficient Pt-free electrocatalyst for ORR is prepared by stoichiometrically substituting some fraction of Fe with Zn in the cobalt ferrite and anchoring these spinel nanoparticles on nitrogen-doped reduced graphene oxide (N-rGO). Zn substitution is found to be significantly altering the ratio of Fe^{2+}/Fe^{3+} in the cobalt ferrite nanocrystal system with a concomitant promotional influence on its electrocatalytic activity towards ORR. The nanoparticle composition with a Co, Fe and Zn molar ratio of 1.0:1.7:0.3, represented by the formula $CoFe_{1.7}Zn_{0.3}O_4$(CFZn(0.3)), supported over N-rGO has shown 10 mV and 20 mV positive shifts in the onset and half-wave potentials, respectively, for ORR in 0.1 M KOH in comparison to the nanoparticles of $CoFe_2O_4$ supported over N-rGO (CF/N-rGO). The optimum Zn substitution is found to be narrowing down the difference with the state-of-the-art Pt/C for ORR by 100 and 110 mV in terms of the onset and half-wave potentials, respectively.

Chapter 5 explains how solvothermal synthesis of zirconium-substituted cobalt ferrite nanoparticles has been accomplished by the introduction of zirconium (Zr) in the spinel matrix to obtain a cost-effective and robust electrocatalyst that does not use noble metals. A variation in the cobalt ferrite structure $CoFe_{2-x}Zr_xO_4$ with Zr (0.1-0.4) substitution has significantly altered the overpotential for the electrocatalytic ORR and OER, leading to an optimum composition of CFZr(0.3). The incorporation of the foreign Zr^{4+} ion in the cobalt ferrite spinel lattices has effectively enhanced the oxygen evolution reaction (OER) activity from the parent cobalt ferrite (CF) nanocrystals. However, a nominal change in the ORR current density has been observed due to Zr-incorporation. For the OER, the Zr substituted catalyst has shown a 40 mV negative shift in the overpotential in comparison with the CF nanoparticles at 10 mA/cm^2 current density.

Interestingly, the *in-situ* grafting of Zr-substituted cobalt ferrite nanoparticles over N-doped reduced graphene oxide (CFZr(0.3)/N-rGO) has remarkably enhanced performance during ORR and moderately favored OER with an overall potential difference(ΔE) of 0.840 V.The notable performance of the catalyst as a bifunctional material is observed during the cycling of the rechargeable ZAB. The prepared catalyst showed an increase of 200 mV in the overall operating overpotential after performingfor 10 cycles at 15 mA/cm^2 as against the 350 mV increase shown by the Pt/C catalyst under the same conditions.

In **Chapter 6,** a discussion on the mechanistic aspect of the ORR process is included. The study is performed by engrafting Fe and Co active centers in the homemade conducting carbon and by studying the ORR performance under acidic and basic pH conditions to understand the influence of the medium and participating moieties towards the performance. In the half-cell reaction, the onset potential and half-wave potential for ORR are governed by the surface intermediates and concomitantly driven by the adsorption energies of the intermediates over the active centers. The iron and cobalt active center-engrafted carbon catalyst behaves differently in acidic and basic electrolytes owing to the dissociation of the surface intermediates. The iron-based catalyst shows improved onset potential as against the cobalt-based one. Similarly, the cobalt-based catalyst shows improved half-wave potential against the iron active-center-grafted catalyst. The combined synergistic effect of the two catalysts is realized in the composition represented as Fe/2Co-N-GVC, where improved onset and half-wave potentialsare noted in the basic medium.

Chapter 7 summarizes the crucial observations and findings of the thesis in order to develop the electrocatalysts for advanced energy applications. The chapter highlights the flow of work captured in each chapter in the thesis by emphasizing the scientific rationale involved in the selection of the different work components to effectively meet the final objectives of the thesis. The chapter also covers a section which highlights the future prospects of the works completed for this thesis purpose, considering the wider scope of the similar materials as developed through this study for various other related applications.

Chapter 1

An Overview of the Cathode Catalysts for the Development of Cost-effective Energy Devices: Metal-Air Batteries and Fuel Cells

The present chapter gives a brief description of the global energy consumption scenario, strategic development of energy devices and the key components and considerations involved to effectively implement the ideas. Many recent reports have clearly highlighted the requirement of deploying potential green energy devices as major substitutes to the petroleum-based energy sources in order to effectively address the issues related to global warming and environmental pollution. Of these, metal-air batteries and polymer electrolyte membrane fuel cells (PEMFCs) appear to be the two of the most promising renewable energy devices, mainly credited to their high energy density characteristics. The fabrication of commercially viable PEMFCs and metal-air batteries depends on developing the highly efficient and cost-effective catalysts for assisting ORR, which is the bottleneck for the devices. In the case of realizing rechargeable metal-air batteries, along with ORR, how well the catalyst can facilitate OER also becomes equally important. The present chapter briefly highlights the status of the noble metal and noble metal-free electrocatalysts, their synthesis methods and activity characteristics in the real devices. A concise state-of-the-art survey on these aspects is included in the chapter. After discussing about the requirements in a realistic perspective considering the current status of development of the energy systems, the chapter ends with a section dealing with the scope and objectives of the dissertation.

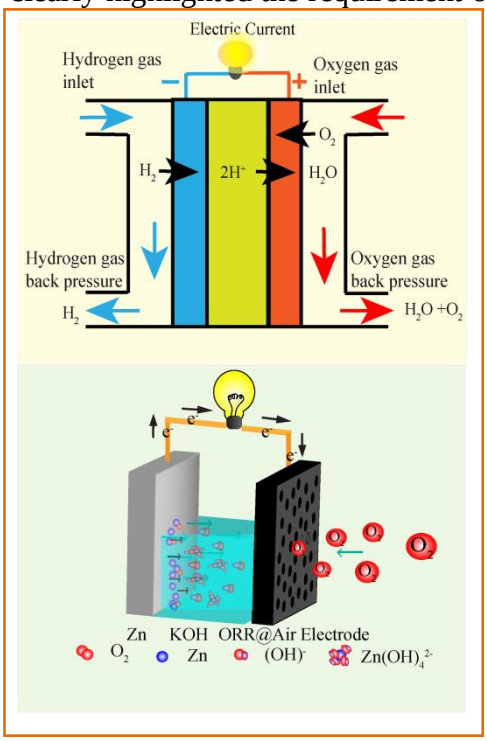

1.1. Introduction:

In the current global scenario, increased energy demand and its associated negative effects such as global warming and environmental pollution have intrinsically penetrated the human life at economic and health care level.[1-2] The conventional energy sources, for instance, coal, petroleum, wood etc. have tremendously devastated the animal kingdom and several species have already vanished due to massive deforestation and global disturbances. The intense use of conventional energy sources has given rise to the increased CO_2 level which is critical in some cases to become real threat to the living organisms. Recently, New Delhi, the Capital of India, witnessed the direct effect of carbon pollution when high-level particulate matter accumulated in the atmospheric air and upset the daily activities of the citizens for weeks. The particulate matter concentration was even higher than > 35μg/cm^3 in the city, which was above the alarming guidelines by the world health organization (WHO) in the year 2015.

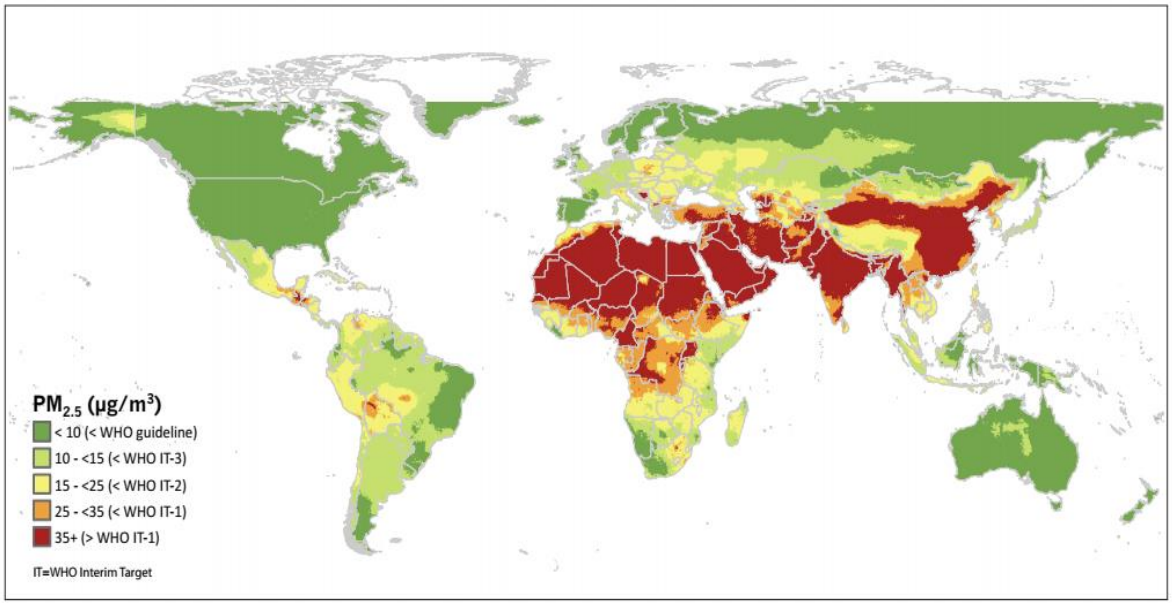

Figure 1.1.*Comparison of the annual average distribution of the particulate matter in the air with respect to the WHO guideline (the year 2015).* ***(Source: 'State of Global Air/2017****'; The State of Global Air is the collaboration between the Institute for Health Metrics and Evaluation's Global Burden of Diseases Project and the Health Effect Institute).*

According to the WHO report in the year 2015, in most of the cities of Africa, Gulf Countries, China and India, the air-breathing quality is worst and above the critical level for human habitat

(**Figure 1.1**). A major cause of the changing climate is arising from the use of the conventional energy sources and as the technologically advanced devices are coming more and more in the market, the energy requirement is supposed to increase concomitantly day-by-day. According to the International Energy Agency (IEA) in the year 2014, global primary energy consumption was 109,613 (TWh) and the supply was estimated to be 155,481 terawatt-hours (TWh). Of these, a major portion of the energy comprises of petroleum products and natural gas. The post effect of the use of these sources is developing a situation which is fatal to the living beings. The fossil fuels look promising and can instantly fulfill the energy requirement. However, the serious limitations and issues related to health and environment and limited availability of the conventional energy resources enforce to look for alternative energy sources. In this respect, renewable energy sources give a fruitful and convincing solution to tackle many of these issues. Broadly these sources include solar, wind, hydroelectric, hydrothermal and geothermal energies. A statistical data for global primary energy consumption (PEC) was provided by BP Statistical Review of World Energy 2017, which gives a clear idea of the energy consumption from the various energy sources (**Figure 1.2**). The report clearly says that the majority of the energy use is provided by coal (33%) and natural gas (24%), whereas the renewable sources comprise of only 3% of the total. Further, a projection of changes in the energy sources in the forthcoming years is estimated by the U.S. Energy Information Administration and reported in International Energy Outlook 2017 (**Figure 1.3**).

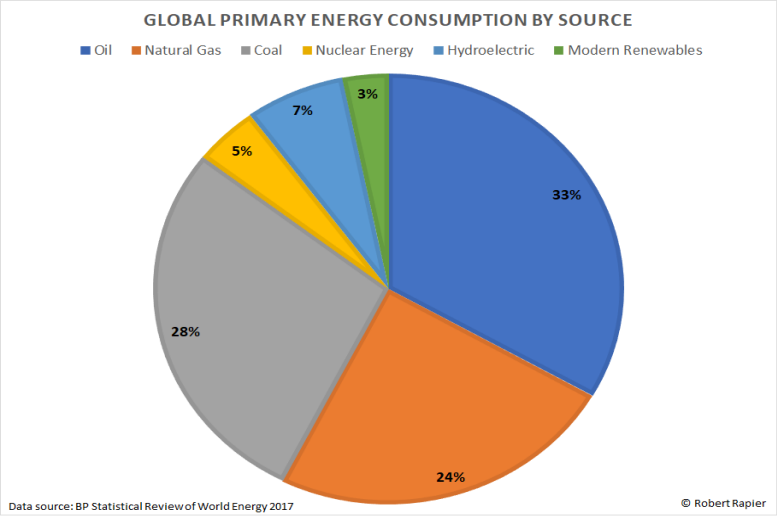

Figure 1.2.*Global primary energy consumption distribution based on the available energy sources* **(*Source:* 'BP Statistical Review of World Energy/2017'**).

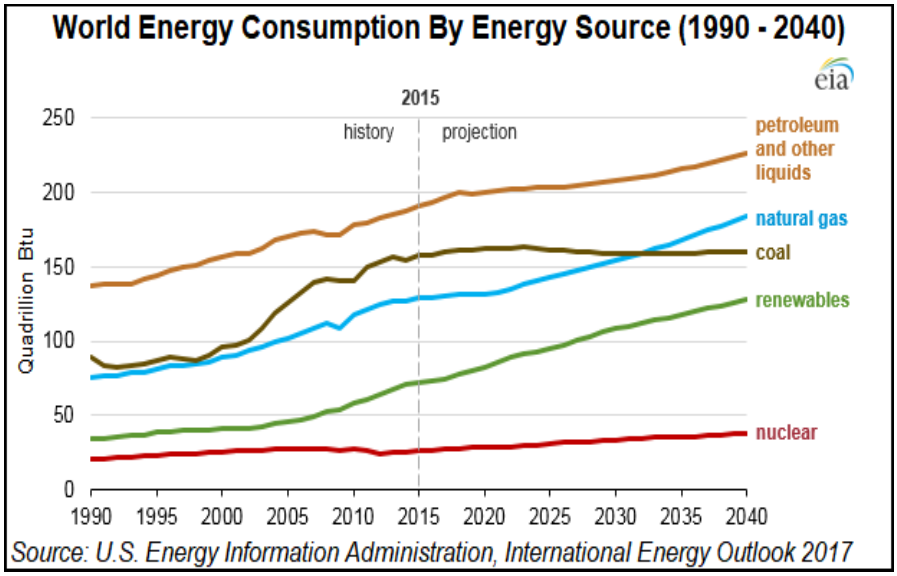

Figure 1.3.*A projected scenario of the use of the available energy sources from the year 1990-2040* **(*Source:* 'International Energy Outlook 2017').**

The impactful shift to sustainable energy harvesting from the conventional sources depends upon the capacity to efficiently convert and store the renewable energy in chemical form. In this context, batteries, sueprcapacitors and fuel cells are of particular interest from both fundamental and industrial point of view.[3-6] Despite great potential to convert chemical energy to electrical energy, some of these systems have their own limitations that prevent them from being scaled-up for commercial applications. A Ragone plot presented in **Figure 1.4** describes the physical significances of these devices. Some devices like supercapacitors have notable power density but they suffer from the issue of low energy density; whereas the batteries and fuel cells display significantly high energy density while failing to maintain high power output. Though metal-air batteries and fuel cells experience low power output, they have great prospects in powering systems for both automobile and stationary applications. The high energy density offered by these systems make them favorable choices as these systems can provide power for longer durations, which is an important requirement as in the case of PEMFC driven cars recently launched by few automobile manufacturers.

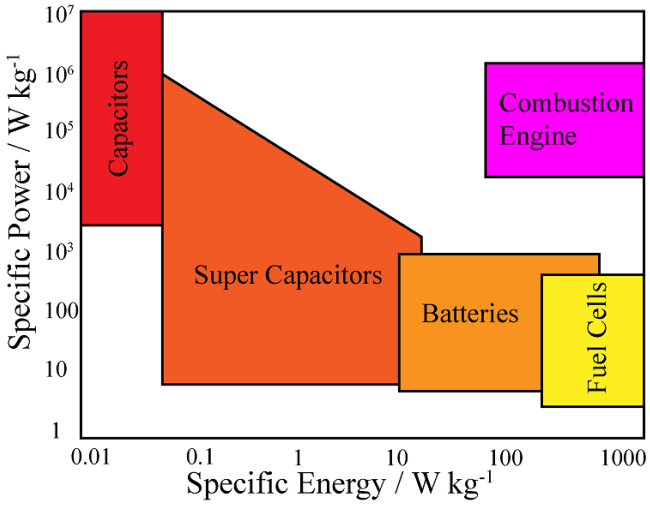

Figure 1.4.*The Ragone plot, a plot which correlates the specific energy density and specific power density for the various energy storage and conversion devices.*

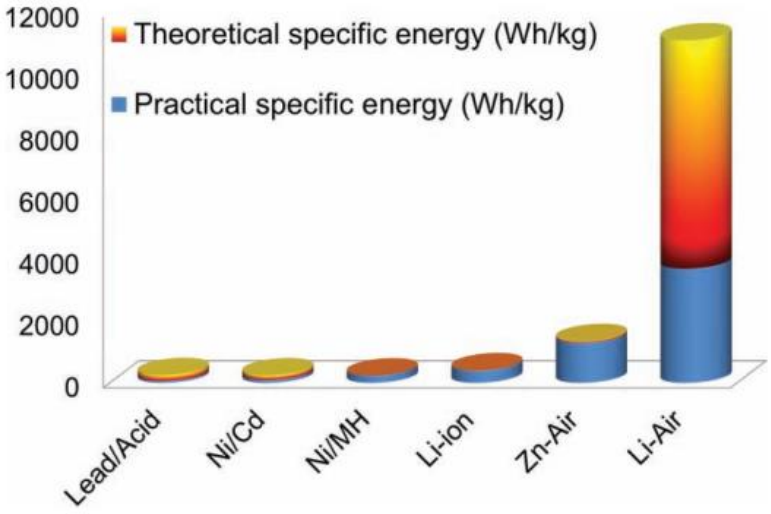

Figure 1.5.*Comparison of the theoretical and practical energy densities of various kinds of batteries. (Reprinted with the permission from* **John Wiley and Sons; License Number: 4470620258406***).*

The energy density of these devices is largely depending on the efficiency of the electrodes, which usually will be made up of an electroactive material with an ability to facilitate the concerned electrode reaction. A report from Lee *et al.* gives an idea of the energy density of the various metal-air batteries (**Figure 1.5**).[2] In the case of both PEMFC and metal-air battery,

oxygen reduction reaction (ORR) catalyst is a pivotal component due to the sluggish nature of the ORR process, where an efficient catalyst plays a vital role in reducing the overpotenial for the electrode process. Hence, this has a direct influence on deciding the energy efficiency of these systems. Currently, carbon-supported Pt and its alloys are being used as the ORR catalysts. These catalysts contribute significantly to the overall cost of the systems.[7] For example, the commercial Pt/C catalyst comprises Pt nanoparticles supported over carbon, which accounts for more than 50% of the cost of the devices.[3] Hence, there has been a tough challenge in front of the researchers to develop noble metal-free electrocatalysts as viable alternatives to the state-of-the-art Pt-based catalysts for ORR applications. A recent break through is the development of hetero-atom doped carbon materials, which gives a promising opportunity of realizing a metal-free electrocatalyst for ORR. Among them, nitrogen doping has gained substantial momentum and many promising systems have been reported in recent literature. This N-doping can activate its neighboring carbon atoms for enhanced oxygen adsorption, which is a crucial and primary requirement for oxygen reduction reaction (ORR).[8] In addition to such metal-free systems, metal oxide nanoparticle-decorated carbon systems have also shown considerable activity for ORR.[9-11]

Among the carbon supported catalysts, graphene supported transition-metal oxides appear to be a promising class of non-precious-metal catalyst. They usually display high chemical stability, electrical conductivity and surface area.[12-13] The activity imparted by these types of catalysts arises primarily from the synergistic effects of the two-dimensional honeycomb-type graphene sheets and the metal oxide nanoparticles. Several transition metal oxide-based nanoparticles supported on graphene sheets have been reported to show enhanced performance for ORR. For example, there are reports on the transition metal oxides such as CoO,[14] $MnCo_2O_4$,[15] Co_3O_4,[16] Fe_3O_4,[17] $MnFe_2O_4$,[18] and $CuCo_2O_4$[10] supported over N-doped graphene system exhibiting interestingly high ORR activity, which in many cases is close to that of the commercially available Pt/C catalyst.[19] Though these catalysts have promising activity characteristics, their demonstration in real fuel cells and metal-air batteries have several unresolved issues associated.[3, 5-6, 20] One of such issues is related to the acid stability of many ORR active metal oxides, which restricts their application in cases where alkaline electrolytes are involved. A case is the anion exchange membrane fuel cells (AEMFCs) where many metal oxide-based systems work well, whereas, in PEMFCs they often raise a challenge in terms of durability.

Like fuel cells, many reports on metal oxide-based air electrodes for metal-air batteries also highlight the prospects of these materials in redefining the overall cost aspects of these systems. Among the various forms of the metal-airbatteries,the Zn-air battery (ZAB) is a promising system owing to its high energy density, user-friendly and environmental benign features.[21-23]A direct advantage of deploying the metal oxide-based ORR catalysts in ZABs is the fact that these systems use alkaline electrolytes. Hence, the issue of catalyst stability can be accounted to greater extent in these class of systems.

1.2. Metal Air Batteries and Fuel Cells:

As mentioned previously, the metal-air batteries and fuel cells are the two potential energy technologies which are expected play vital roles in many futuristic applications. Since the materials developed as part of this thesis work have direct applications in metal-air batteries and fuel cells, a brief discussion by highlighting the specific features and classifications of these devices is included in the following sections. The discussion will be first focused onto the different types of the metal-air batteries, followed by on the different classes of the fuel cells.

1.2.1. Li-Air Battery:

In 1996, a rechargeable Li-Air battery was demonstrated by Abraham *et al*. The battery was constructed with Li^+ conducting polymer, lithium metal, and a carbon composite electrode.[24] As the lithium metal is explosive with water, the non-aqueous organic polymer electrolyte was used to maintain the conductivity between the electrodes.[25] There has been consistent efforts to develop rechargeable Li-Air batteries as evident from many recent literatures (**Figure 1.6**).[2, 26-27] Since the ORR catalyst work well in the moist conditions, the advanced Li-Air battery is usually a hybrid of non-aqueous and aqueous electrolytes.[28-29]A notable contribution in the battery advancement has come with the inclusion of the LiSICON separator.[30-31] The separator selectively allows the passage of Li^+ ion from the organic electrolyte to aqueous electrolyte without causing any explosive reaction.

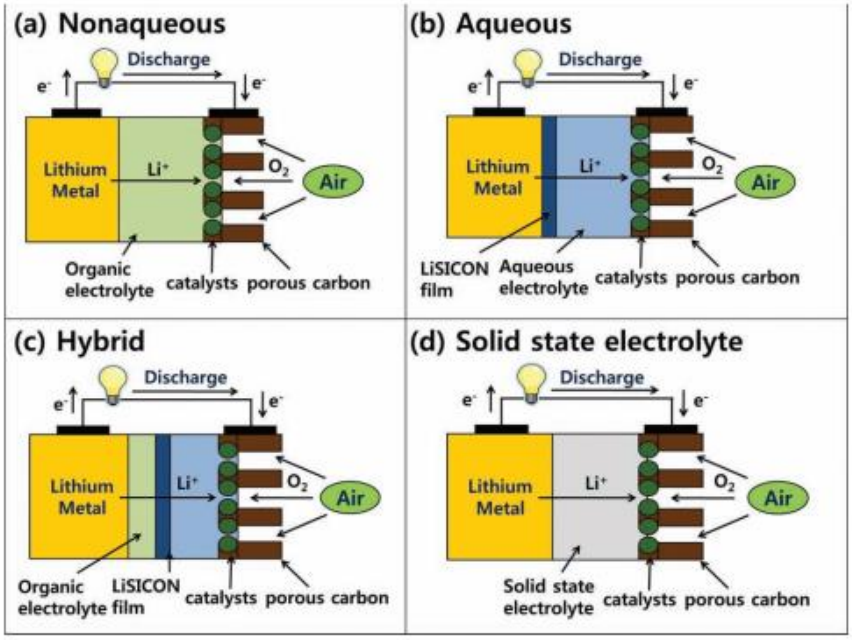

Figure 1.6. *Schematic representations of the various types of Li-Air batteries. (Reprinted with the permission from* **John Wiley and Sons; License Number: 4470620258406**).

1.2.2. Zn-Air Battery:

Similar to the Li-Air batteries, the Zn-Air batteries (ZABs) are also having a very high energy density (~ 1100 Wh/kg) compared to the commercial lead acid (~150-200 Wh/kg) and lithium-ion (250-300 Wh/kg) batteries.[32] The main advantages of these batteries over the Li-Air batteries are their less moistures sensitivity and user-friendly features. Though ZAB has less energy density compared to the Li-Air battery, they are less explosive, more cost-effective and environmentally less hazardous. These features make them as attractive candidates for various techno-commercial applications.[33-34] As in the case of the other air batteries, ZAB also involves an active anode material (*i.e.*, Zn metal) and an air-breathing cathode (*i.e.*, an ORR catalyst coated gas diffusion layer).[21-22] **Figure 1.7** represents the functioning of a typical Zn-air battery.[5] In a battery, the two electrodes are separated with a separator by maintaining the ionic contact through the KOH solution. The atmospheric oxygen diffuses inside the cathode electrode, facilitated by the pressure gradient of air inside and outside of the electrode. The oxygen molecule in air undergoes reduction to hydroxyl ions over the ORR catalyst layer. In the reduction process, the electrons generated from the oxidation of Zn metal over the anode are utilized. Thus generated hydroxyl ion move from the cathode to the anode through the KOH

electrolyte. The reaction over the cathode electrode is termed as the three-phase reaction as it involves catalyst (solid), electrolyte (liquid) and oxygen (gas).

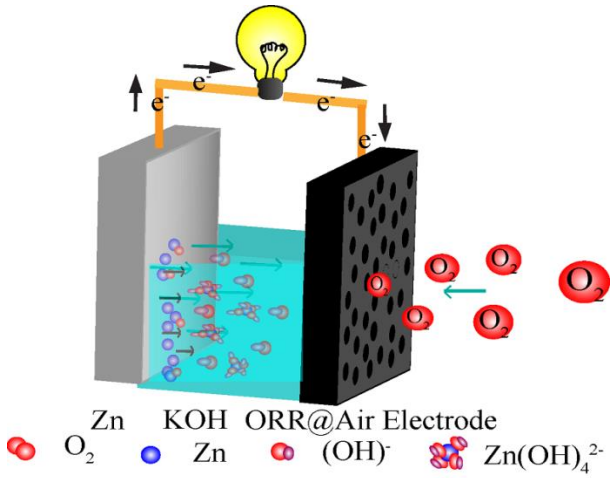

Figure 1.7.*A schematic representation of a typical primary Zn-Air battery (ZAB).*

1.2.3. Fuel Cells:

Fuel cells are also potential energy conversion devices owing to their high conversion efficiency and near zero emission of toxic gases to the environment. Depending on the working principles and the fuels used, the fuel cells can be classified into different categories.[3] A discussion on the types of fuel cells is included in the following section:

(i) Proton Exchange Membrane Fuel Cell (PEMFC): PEMFCs are being considered as the technologically most advanced version of the fuel cells. The cell comprises of anode, cathode and a polymeric separator membrane which can selectively transport protons from the anode to the cathode of the cell.[35-36]A schematic representation of the PEMFC is presented in **Figure 1.8**.As can be seen from the figure, the anode serves as the electrode where hydrogen oxidation occurs, the cathode where the oxygen reduction occurs and the electrolyte serves a critical role to selectively carry the protons generated at the anode without allowing permeation of hydrogen or oxygen molecules across the electrodes. The construction of the system allows flow of electrons through the external circuit and generation of water as the byproduct from the cathode side of the cell. The PEMFCs are further categories as the low-temperature proton exchange fuel cell (LT-PEMFC) and high-temperature proton exchange membrane fuel cell (HT-PEMFC). LT-PEMFC operates below 100^{o}C and Nafion membrane is being used as the electrolyte. HT-PEMFC

operates at temperatures in the range of 130-170 ºC and phosphoric acid doped polybenzne imidazole (PBI) membrane is generally being used as the electrolyte.[3]In both the cases, performance of the cell is highly depending on the activity of the oxygen reduction electrocatalyst (ORR).

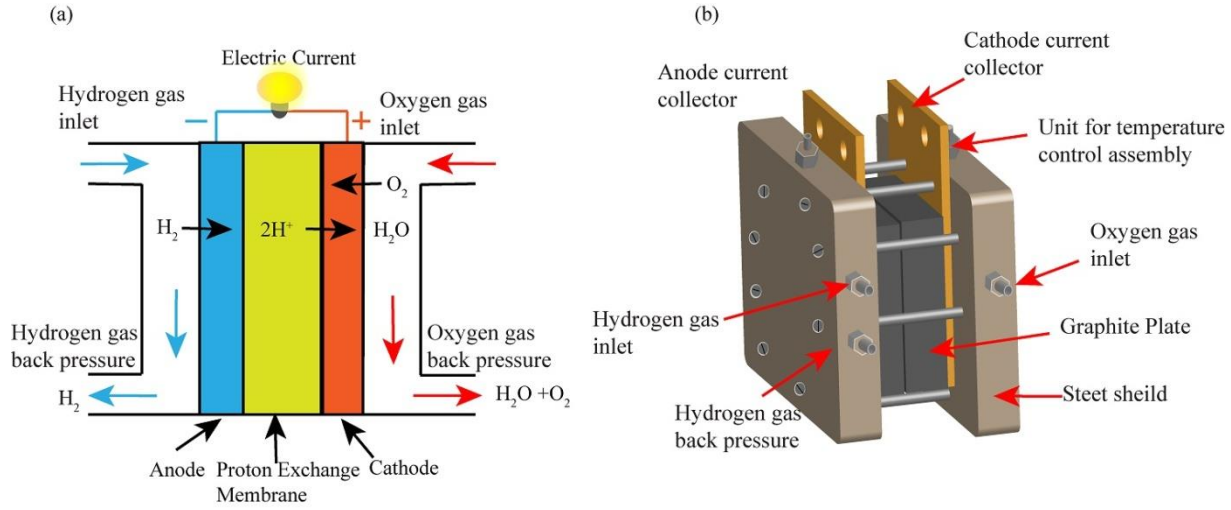

Figure 1.8. *(a) A schematic representation illustrating the working principle of proton exchange membrane fuel cell (PEMFC) and (b) a single cell test fixture of the PEMFC.*

(ii) Alkaline Fuel Cell (AFC): Structurally, an AFC is similar to a PEMFC; the cell operates at around 100 ºC but the polymer electrolyte membrane is selective for OH^- transport. The AFC has the capability to reach 60-70% conversion efficiency of the fuel to electrical energy.[37] The polymer membrane is usually doped in potassium hydroxide (KOH) for attaining a phase which can facilitate the transport of OH^- ions from the cathode to the anode of the system. The negatively charged OH^- ions are utilized at the anode leading to the formation of water.[38]

(iii) Phosphoric Acid Fuel Cell (PAFC): These fuel cells operate at 175-200 ºC. Here, liquid phosphoric acid serves as the electrode. The chemical reaction in the PAFC is similar to that in a PEMFC.[39]

(iv) Molten Carbonate Fuel Cell (MCFC): This fuel cell operates at high temperate as molten carbonate salt serves as the conducting electrolyte. Generally, the temperature of operation

ranges from 600 to 700 ^{o}C. A conducting porous material is generally used as the electrode. MCMC gives a conversion efficiency of 50-60%.

(v) Solid Oxide Fuel Cell (SOFC): The electrode material as well as the electrolyte is a ceramic material with metal oxides as a constituent. The basic advantage of this fuel cell is efficiency in the range of 50-60% and a separate reformer is not required for the cell.[40] Due to the high operating temperature (600-1000 ^{o}C) of the cell, many hydrocarbon fuels can be directly employed as the fuel gas for this system. The *in-situ* generated hydrogen will help the system to work and this advantage helped the system to achieve several high capacity installations at various places.

(vi) Direct Methanol Fuel Cell (DMFC): The working principle of a DMFC is similar to that of a PEMFC. The system uses a proton conducting polymer electrolyte, but liquid methanol will be employed as the fuel in the anode side.[41] The anode catalyst facilitates methanol oxidation with the generation of protons and electrons and cathode catalyst helps to undergo oxygen reduction.

I-V Characteristic of the Fuel Cells:

The current (I)-voltage (V) polarization plot is a very important performance data which is required to understand and evaluate the performance characteristics of fuel cells. A typical fuel cell polarization curve can be distinguished in the three active regions: 1) activation polarization region which intensively depends on the intrinsic activity of the catalyst, 2) ohmic polarization region where the resistance components contribute and 3) concentration polarization region which offers the mass transfer resistance in the overall performance (**Figure 1.9**).[42] At very low dragging current conditions, the output voltage is because of the chemical reactions and this region corresponds to the activation region. The linear region in the plot shows the ohmic polarization. The internal resistance of the various components offers moderate change in voltage with increase in the current density. However, at high current density,the voltage loss is sharp because of the limited gas exchange efficiency which is caused mainly by the flooding in the catalyst layer and insufficient gas transport by the gas diffusion layer to cater the requirements as demanded by the catalyst surface.[43] Interestingly, performance of the PEMFCs can be enhanced by the thermodynamics of faradaic reactions and the electrical efficiency of the devices. The overpotential in the charge transfer processes induces a major contributing factor to

the resistance. In PEMFCs, the cathode charge transfer resistance is a major factor in deciding the overall overpotential of the system. Any strategy which can reduce the overpotential can lead to enhanced performance of the device. The thermodynamic efficiency of the device can be enhanced by improving the fuel processing, adequate water management, and temperature control. However, to realistically achieve a significant improvement on the electrical efficiency of the system, one should address the voltage drops arising from the ohmic, activation and concentration overpotentials.

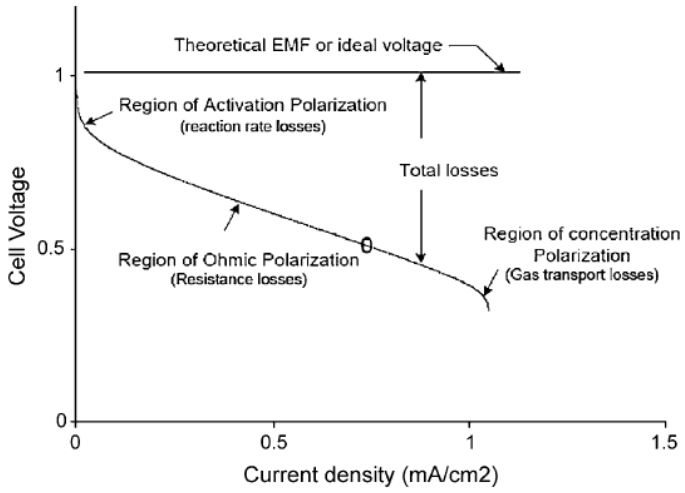

Figure 1.9. *A typical fuel cell polarization curve.*[42] (*Reprinted with the permission from* **Elsevier*; License Number: 4470611428448***).*

Further, a comparative study of the hydrogen fuel cells has been given in **Table1**. It is clear from the table that the PEMFC is more promising among the different types of the fuel cells, mainly due to the power ranges it can offer, which is in the range of 30 W to 250 kW.

Table 1. *Comparison of the different types of fuel cells.*[42](*Reprinted with the permission from* **Elsevier*; License Number: 4470611428448***).*

Parameters	**PEMFC**	**AFC**	**PAFC**	**SOFC**	**DMFC**
Electrolyte	Solid polymer membrane	Liquid solution of KOH	Phosphoric Acid (H_3PO_4)	Stabilized solid oxide (Y_2O_3, ZrO_2)	Solid polymer membrane
Operating temperature (ºC)	50-100	50-200	200	800-1000	60-200
Charge Carrier	H^+	OH^-	H^+	$O^{\cdot}$	H^+
Fuel	H_2	H_2	H_2	H_2 , CO, CH_4	CH_4OH
Oxidant	O_2	O_2	O_2	O_2	O_2
Cell Voltage (V)	1.1	1.0	1.1	0.8-1.0	0.2-0.4
Power Density(kW/m^3)	3.8-6.5	~1.0	0.8-1.9	0.1-1.5	~0.6
Efficiency	40-50%	~50%	40%	>50%	40%
Installation Cost(US $/kW)	<1500	1800	2100	3000	-

1.3. Oxygen Reduction Reaction (ORR):

ORR is one of the well-known faradaic reactions and the reaction mechanism of which is not fully disclosed due to the complexness of the process. The process changes the behavior depending upon the electrode materials, catalysts, and the electrolyte.[7, 33, 44] Researchers have put a lot of efforts to explore the reaction mechanism, pathways in acidic and alkaline media on experimental as well as theoretical level.[19] In acidic media, the proton combines with reduced oxygen. On the other hand, in basic media, the hydroxyl ion plays an important role. The reaction intermediates formed on the surface of the catalyst vary in terms of the adsorption and desorption free energies.[8] In general, the ORR reaction for the two-electron transfer pathway can be given as[45]:

Acidic Media:

$$O_2 + 2H^+ + 2e- \rightarrow H_2O_2 \qquad E_o = 0.67\,V \qquad (1)$$

$$H_2O_2 + 2H^+ + 2e- \rightarrow 2H_2O \qquad E_o = 1.76\,V \qquad (2)$$

The hydrogen peroxide formed in the first step can undergo the alternative decomposition process as given below leading to the formation of O_2 and H_2O:

$$2H_2O_2 \rightarrow 2H_2O + O_2 \qquad (3)$$

Alkaline Media[19]:

$$O_2 + H_2O + 2e- \rightarrow HO_2^- + OH^- \; E_o = -0.065\,V \quad (4)$$

$$HO_2^- + H_2O + 2e- \rightarrow 3OH^- E_o = 0.867\,V \quad (5)$$

The peroxide ions formed can also follow the alternative decomposition reaction as follows:

$$2HO_2^- \rightarrow 2OH^- + O_2 \; E_o = 0.867\,V \quad (6)$$

However, the ORR activity of the catalyst reflects in the exchange current density, on-set potential and the reduction pathway for the reaction.

1.3.1. Associative Mechanism: When oxygen molecule approaches the surface of Pt, the oxygen molecule gets first adsorbed without dissociation of the O_2 bond. Thereafter, the reduction occurs through a set of processes as indicated in the following equations: [46]

$$Pt + O_2 \rightarrow Pt - O_{2_{ads}} \quad (7)$$

$$Pt - O_{2_{ads}} + H^+ + e- \rightarrow Pt - HO_{2_{ads}} \quad (8)$$

$$Pt - HO_{2_{ads}} + H^+ + e- \rightarrow H_2O + Pt - O_{ads} \quad (9)$$

$$Pt - O_{ads} + H^+ + e- \rightarrow Pt - OH_{ads} \quad (10)$$

$$Pt - OH_{ads} + H^+ + e- \rightarrow H_2O + Pt \quad (11)$$

Here, followed by the adsorption of the O_2 molecule over the Pt surface, the formation of peroxide ion takes place over the Pt surface, which could be further reduced to water as the final product.

1.3.2. Dissociative Mechanism: The reaction mechanism involves the cleavage of the O-O bond and formation of the Pt-O bond. The corresponding reactions are presented as below:

$$Pt + \frac{1}{2}O2_{ads} \rightarrow Pt - O_{ads} \quad (12)$$

$$Pt - O_{ads} + H^+ + e- \rightarrow Pt - OH_{ads} \quad (13)$$

$$Pt - OH_{ads} + H^+ + e- \rightarrow H_2O + Pt \quad (14)$$

The above equations depict that the dissociated molecule is adsorbed over the surface of the catalyst. The oxygen gets transformed directly to water without the involvement of any hydrogen peroxide formation. Moreover, the reaction mechanism mentioned above is reported to be the

prominent one over the Pt surface. By changing the electrode material, the reaction intermediate can be changed. For example, in the case of the graphene-based electrode materials, as explored through few theoretical studies, involvement of the following steps in the oxygen reduction mechanism is reported [8, 47-49]:

$$O_2(g) + 2H_2O(l) + 4e- + * \rightarrow OOH* + OH^- + H_2O(l) + 3e- \quad (15)$$

$$OOH* + OH- + H_2O(l) + 3e- \rightarrow O* + 2OH- + H_2O + 2e- \quad (16)$$

$$O* + 2OH- + H_2O(l) + 2e- \rightarrow OH* + 3OH- + e- \quad (17)$$

$$OH* + 3OH- + e- \rightarrow 4OH- \quad (18)$$

The above-mentioned equations are derived from the theoretical studies over the heteroatom doped graphene system. The free energy of the transition states changes by altering the electrode material. This shows that the key to determining the product of the reduction is influenced by the free energy of the transition states. The theoretical free energy diagram of the heteroatom doped graphene is given below, which indicates that the N-doped graphene system has the lowest activation energy for the formation of the transition states.[8]

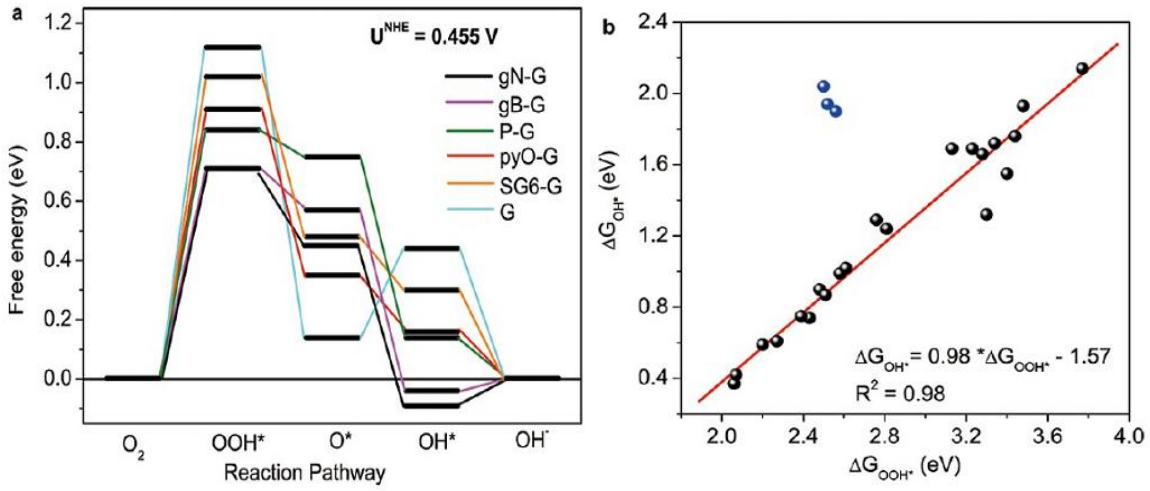

Figure 1.10.*(a) Correlation between the adsorption free energy of the various transition states formed over the heteroatom-doped graphene at equilibrium U^o and (b) the adsorption free energies of the intermediates OOH* (ΔG_{OOH*}) and OH* (ΔG_{OH*}) on the active site of ORR over the heteroatom doped graphene.*[8]*(Reprint with the permission from* **American Chemical Society***).*

1.4. Noble Metal and Noble Metal-Free Oxygen Reduction Catalysts, their Synthesis and Applications:

As mentioned before, considering the cost aspects of the PEMFCs and metal-air batteries, there has been a paradigm shift in the area of electrocatalyst development of these types of systems based on low and platinum-free materials.[50] Some of the strategies in this direction include development of systems based on alloys, core-shell structures, metal oxides, chalcogenide composites and hetero atom doping on carbon morphologies.[51-55] The Pt alloys are a superior class of catalysts for ORR and some of such systems are already part of the commercially available PEMFC systems.[56] Some of the key features of the alloy catalysts which make them beneficial to the ORR activity include high surface roughness caused by the dissolution of the transition metal counterparts, shifting of the d-band position in the structure and ability to delaying the process of oxide species formation.[56-58] Pt alloys consisting of different metals have been synthesized and their relative activity characteristics have been compared in various literatures. Among the different transition metals, Co, Fe and Ni are the widely explored base metal counterparts for Pt, and, in many cases, remarkably improved ORR activity could be obtained.[53] Alloys based on other metals also were reported in the literature. In terms of activity, the sputtered alloy polycrystalline films of first row transition metals follow the order as: Pt < Pt_3Ti < Pt_3V < Pt_3Ni < Pt_3Fe ~ Pt_3Co.[58] Interestingly, the post-treatment of these alloys were found to be further tuning their ORR performance and the order of ORR activity in such systems follows as: Pt < Pt_3Ti < Pt_3V < Pt_3Fe < Pt_3Ni < Pt_3Co.[57] Similarly, alloying Pt with rareearth metals such as Y, Sc, Hf, La, Ce, Ga and Gd were also reported to be increasing the activity and stability of Pt significantly.[59-60] **Figure 1.11** gives a comparison of the ORR activities of the alloy catalysts based on Pt and few rare earth metals.

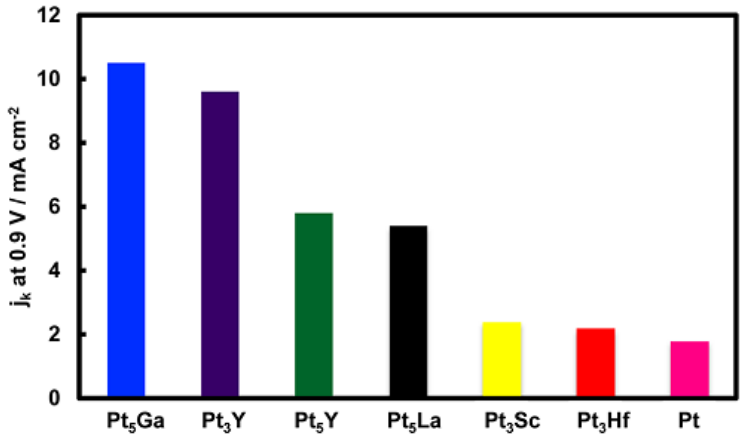

Figure 1.11.*Comparision of the specific activities of the early transition metal alloys of Pt thin films to polycrystalline Pt at 0.90 V.*[56](*Reprinted with the permission from* **RSC Publishing; License Number: 4472971505648***).*

Apart from the above-mentioned alloying process, various shape-controlled and structurally modifiedsystems such as ordered Pt alloys (intermetallic), Pt alloy with a nanostructured thin film (NSTF) and porous Pt alloys have also been employed for activity enhancement (**Figure 1.12**). One dimensional structures such as nanorods, nanowires, and nanotubes of Ptusually expose low energy facets, and they generally display modulated performance characteristics. The oxygen binding energy for these facets is relatively weaker compared to that occurs on the surface of the traditional nanoparticles, resulting in high ORR activity. Synthesis methodologies such as electrospinning, microwave irradiation and polyol method are being used to prepare both thin and ultrathin Pt alloy nanowires. Apart from these, there is a report suggesting the synthesis of Pt-Fe and Pt-Co nanowires through thermal decomposition of $Fe(CO)_5$ or $Co(CO)_8$ and reduction of $Pt(acac)_2$.[53] The diameters of the prepared nanowires are in the range of 2.5-6.3 nm. Similarly, the Pt-Ni alloys are also reported and have significant activity characteristics for ORR (**Table 1.13**).

Though the alloys help to significantly reduce the amount of the Pt in the systems, a further lowering of the Pt content is imposed using the core-shell materials. The core-shell materials alter the d-band position of Pt in the nanocrystal sowing to the strain in the lattice. One of the methods for making the core shell structured Pt system is a reported copper-mediated under potential deposition (UPD) process. In this method, a metallic Cu monolayer is first deposited over the metallic core structure of a less expensive metal system using the UPD method.[61]

Subsequently, the monolayer is displaced by noble metal atoms because of the difference in the standard reduction potential between the species ($Cu + Pt^{+2} \rightarrow Pt + Cu^{+2}$). As the reaction proceeds, a monolayer of Pt over the surface is formed.

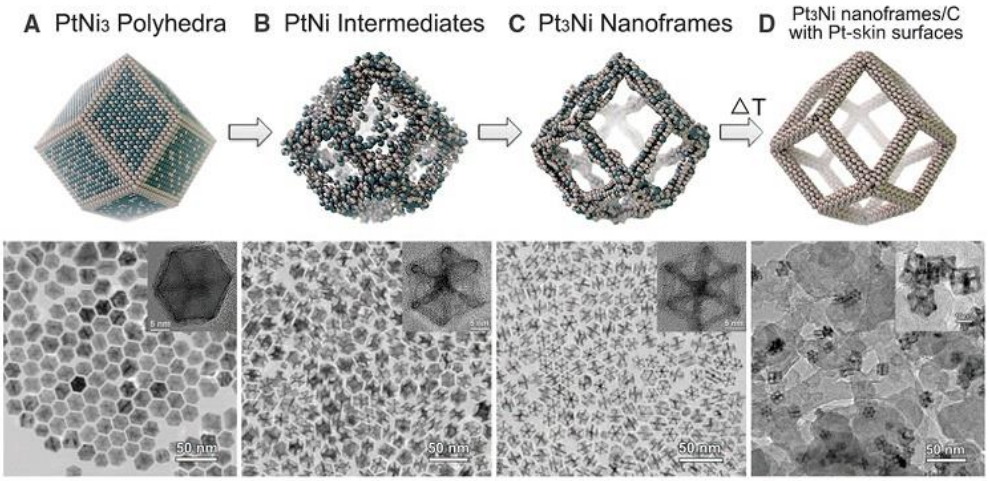

Figure 1.12. *Schematic representations and the corresponding TEM images of the different stages during the evolution process of the polyhedral to nanoframes of the various Pt based systems.*[62] (*Reprinted with the permission from* **The American Association for the Advancement of Science; License Number: 4470721162285**).

Table 1.13. *Information regarding the synthesis, structural features and activity characteristics of the Pt-Ni octahedra.*[63] (*Reprinted with the permission from* **American Chemical Society**).

methods	solvent	capping/shape directing agents	temp (°C)	shape selectivity	edge length (nm)	Pt/Ni molar ratio	specific activity (mA cm^{-2})	Pt mass activity (A mg^{-1})
without assistance of CO containing chemicals	DMF	none	200	fair	8–9	1	3[a]	0.68
	DMF	none	120	good	9	1	3.14[b]	1.45
	benzyl alcohol	PVP, benzoic acid	150	excellent	12	0.5		
	DMF	benzoic acid	160	good	4	3	2.2[b]	1.80
	none	none	200	fair	5.8	1.5	3.99[a]	1.96
with assistance of CO containing chemicals	none	OAm, OA, $W(CO)_6$	230	excellent	11	3	1.2[a]	0.3
	benzyl ether	Oam, OA, $W(CO)_6$	230	excellent	9	2.5	10.1[b]	3.3
	diphenyl ether	OAm, CO	210	fair	10	3	1.26	0.44
	DMF	benzoic acid, $Mo(CO)_6$	170	good	4	3	8.2[b]	6.98[c]

1.4.1. Activated Carbon materials: As a cost-effective alternative to the Pt-based electrocatalysts, recently, the hetero-atom doped carbon and composite structures have emerged as potential systems due to their promising ORR characteristics. Doping of carbon material with hetero atoms, such as boron (B), nitrogen (N), sulfur (S) and phosphorous (P), has been reported to have the ability to shift the electron density from the carbon framework, thereby favoring O_2 adsorption and modulating the transition states to facilitate ORR.[8] In a pure conducting carbon network (sp^2 carbon), replacement of carbon with a heteroatom creates change in the electron density of the surrounding carbon atom (**Figure 1.13**). Among the various types of the heteroatom doped carbon systems as the ORR catalysts, the nitrogendoped (N-doped) carbon systems are widely explored. Some of such systems show onset potentials and half-wave potentials very close to the state-of-the-art Pt/C catalysts.[64-65] The heteroatom doping in the graphene framework is generally introduced by annealing a carbon material such as graphene oxide (GO) with hetero atom precursors (like melamine for nitrogen, boron oxide for boron, benzyl disulphide for sulfur and, triphenylphosphine for phosphorus).[66-67]

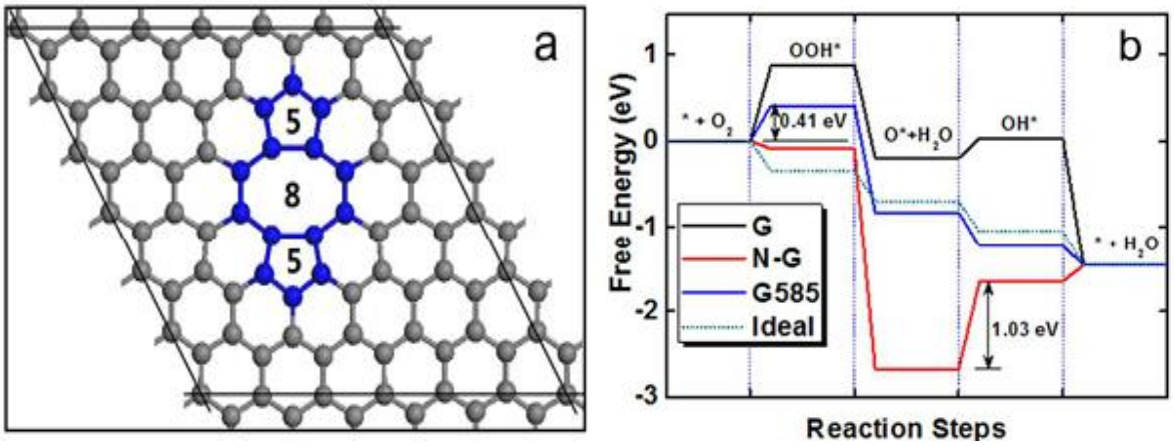

Figure 1.13. *(a) A graphical representation showing the G585 defect in a graphene sheet; (b) theoretical free energy calculation of the transition states over the perfect monolayer graphene (G), N-doped graphene (N-G), graphene with G585 defect (G585)in the sheet and over an ideal catalyst for reduction of a molecular oxygen at equilibrium potential.*[68](*Reprinted with the permission from* **Royal Society of Chemistry; License Number: 4470740509137***).*

There are reports of preparing heteroatom doped carbon materials derived from various polymer precursors through pyrolysis.[64] One such method is presented in **Figure 1.14**, which represents how a nitrogen doped carbon catalyst could be prepared by pyrolysis of the polymer derived

from o-phenylenediamine. Here, hard silica template provides the surface required to polymerize the monomer, giving a porous carbon morphology upon the etching out of the silica template. Thus formed nitrogen doped hierarchical porous carbon gave a specific surface area of 1280 m^2/g.[64]

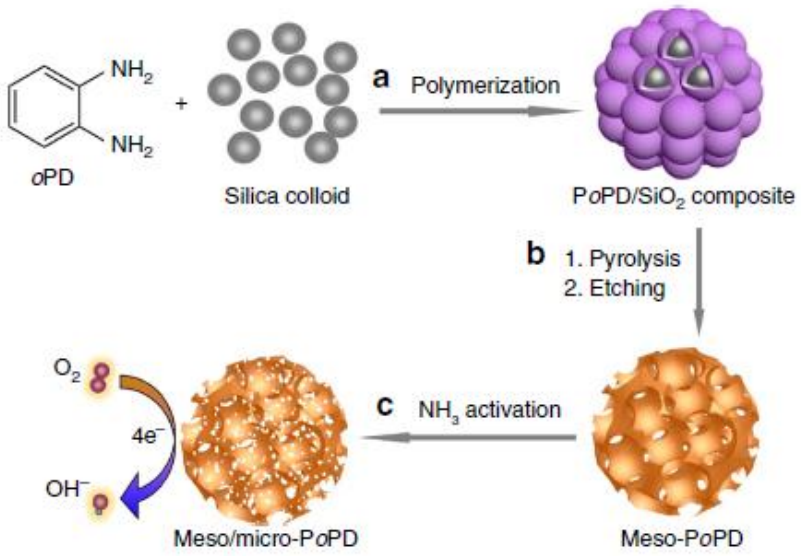

Figure 1.14.*Schematic illustration of the synthesis of the meso/micro-PoPD electrocatalyst.*[64] (*Reprinted with the permission from* **Springer Nature; License Number: 4471191160460***).*

1.4.2.Electrocatalysts based on Metal Oxides, Metal Nitrides and Metal Chalcogenides: Transition metal oxides such as ZrO_{2-x}, Co_3O_{4-x}, TiO_{2-x}, SnO_{2-x} and Nb_2O_{5-x} have been reported to show ORR activities in H_2SO_4 solution.[41]These metal oxide were synthesized using sputtering with the respective metal oxide targets in inert atmosphere. In the sputtered metal oxides, the oxygen vacancies are created and are believed to be the main reason for the enhanced catalytic activities. However, these metal oxides are not electrically conducting, which lowers the ORR activity of the catalysts by generating more ohmic overpotential in the electrodes. As a viable strategy to overcome this issue, carbon supported metal oxide nanoparticles are reported, which are giving excellent performances for many applications. Dai *et. al.* reported Co_3O_4/graphene and $MnCo_2O_4$/N-rGO as efficient electrocatalysts for oxygen reduction in alkaline medium.[13, 16]In these cases, they have used the two-step solvothermal method to synthesize the composite materials. An advantage of these class of systems is the synergistic interactions operating between the metal oxide nanoparticles and reduced graphene

oxide, thereby giving a favorable modulation towards ORR. Systems like $CoFe_2O_4$/graphene, $CoFe_2O_4$/N-rGO, and $CuCo_2O_4$/N-rGO are also reported as the ORR catalysts working very well in alkaline medium.[10, 12] **Figure 1.15** gives a comparison of the LSV profiles of few metal oxide composite materials with the conducting carbons along with Pt/C for ORR. It can be seen that, the onset potential and $E_{1/2}$ value for catalyst $MnCo_2O_4$/N-rmGO are very close to the Pt/C catalyst.[13]

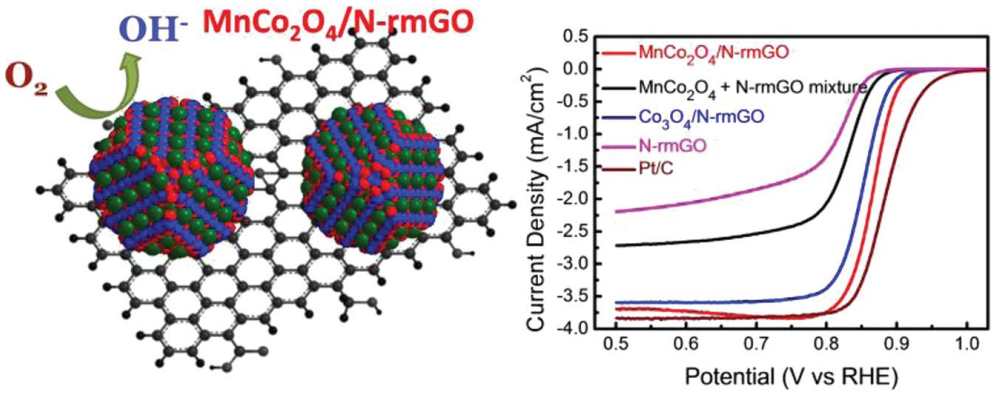

Figure 1.15 *Schematic representation of the $MnCo_2O_4$/N-rmGO catalyst and the comparative LSV profiles of the various catalysts.*[13] (*Reprinted with the permission from* **American Chemical Society**).

Other than metal oxides, metal nitride nanoparticles have also been explored for ORR in acidic medium. Of these, MoN nanoparticles having a size distribution of 4 nm are reported to be showingan onset potential of 0.58 V in 0.5 M H_2SO_4. The TiN/CNT composite gives a high ORR activity with a notable onset potential close to 0.85 V. The oxynitrides like ZrO_xN_y, TiO_xN_y, $Co_xMo_{1-x}O_yN_z$, and HfO_xN_y are also reported as potential candidates which display promising ORR activity.[69] Ba-Nb-Zr-O-N/CB is another system and a recent report claims that it displays an onset potential of 0.93 V.[70] Further, the chalcogenides of transition metals like Co, Ni and Fe have also been studied for ORR catalysis for decades. Previous studies on metal chalcogenides suggest the trend as $M_xS_y > M_xSe_y > M_xTe_y$ (where M = transition metal) for their ability to facilitate ORR.[54] The noble metal chalcogenides like Ru_xSe_y also showed good ORR activity, even though the toxicity of Se is an issue in these types of systems. A comparison of the ORR activities of a series of noble metal systems which are modified by Se and S is presented in **Figure 1.16**.

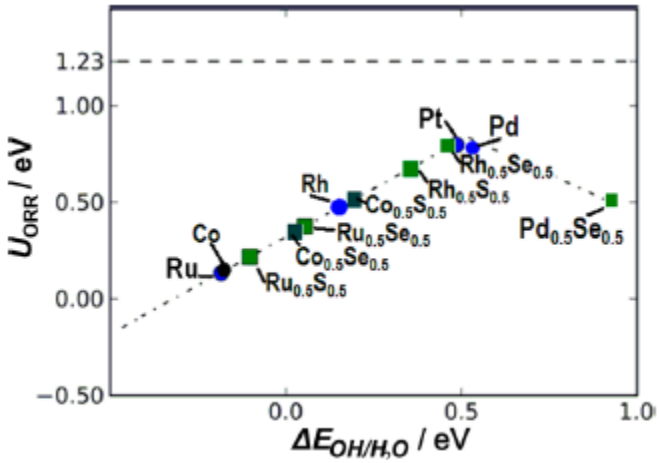

Figure 1.16. *A comparison of the ORR activities of the selenium and sulfur modified Ru, Rh, and Co metal chalcogenides (square symbols). The metallic forms of the elements are indicated as circles.*[54](*Reprinted with the permission from* **Elsevier; License Number: 4471200231756**).

1.5. ORR Catalystsfor theZn-air Battery Application:

In the case of the metal-air batteries, metals such as Ca, Al, Fe, Cd and, Zn are appropriate candidates for the aqueous type of battery applications.[32, 71] However, in case of the Li-air battery, the Li metal explosively reacts with water, and, thus, suitable non-aqueous electrolytes should be used instead of the aqueous electrolytes. In spite of several drawbacks, the metal-air batteries are having very high energy density which makes them attractive in the battery domaign.[71] Among all the air-batteries, the Zn-air battery (ZAB) appears to be the most promising and widely explored one considering the cost and user-friendly features of the system. The battery uses the Zn metal as the active anode and a suitable ORR catalyst as the cathode. These batteries can be classified as primary and secondary (rechargeable) batteries based on the type of catalysts used in the cathode. The fundamental chemical reactions occurring at the electrodes of the ZAB are summarized below[2, 21, 55]:

Anode reactions: These reactions take place over the zinc anode, where oxidation of the zinc metal occurs by the release of electrons to the external circuit.

$$Zn(s) \rightarrow Zn^{2+} + 2e^- \quad (19)$$

$$Zn^{2+} + 4OH^- \rightarrow Zn(OH)_4^{2-}(sol) \quad E^o = -1.25 \text{ V vs SHE} \quad (20)$$

$$Zn(OH)_4^{2-}(sol) \rightarrow ZnO(s) + H_2O + 2OH^- \quad (21)$$

The formation of ZnO over the Zn metal restricts the further oxidation of the metal and this plays a critical role in limiting the power density of the battery.[72]

Cathode reactions: These reactions takes place over the catalyst coated gas diffusion layer (GDL) in the cathode.[73] The oxygen stream at the cathode side through the GDL gets reduced to the hydroxyl ions by consuming the electrons reaching the cathode side as a result of the oxidation reaction happening at the anode. Depending on the nature of the catalyst which facilitates ORR, the reduction process may involve either two or four electron pathway.[74]

Four-electron transfer process:

$$O_2 + 2H_2O + 4e^- \leftrightarrow 4OH^- \text{E}^o = 0.40 \text{ V vs SHE} \quad (22)$$

Two-electron transfer process:

$$O_2 + 2H_2O + 2e^- \leftrightarrow HO_2^- + OH^- \text{E}^o = -0.07 \text{ V vs SHE} \quad (23)$$

$$HO_2^- + H_2O + 2e^- \leftrightarrow 3OH^- \text{E}^o = 0.87 \text{ V vs SHE} \quad (24)$$

Parasitic anode reaction: This reaction takes place over the Zn metal. Since the standard reduction potential of hydrogen is more positive against Zn, in aqueous electrolytes, the hydrogen evolution reaction (HER) takes place over the Zn metal, leading to a decrease in the battery performance.[75]

$$Zn + 2H_2O \rightarrow Zn(OH)_2 + H_2 \uparrow \quad (25)$$

Parasitic cathode reaction: This parasitic reaction occurs in the electrolyte. The carbonate salt is formed in the electrolyte by CO_2 intake from the air electrode.[76-77] Carbon supported catalyst also shows increased level of salt formation.

$$2KOH + CO_2 \rightarrow K_2CO_3 + H_2O \quad (26)$$

Primary Zn-air Battery: These types of systems often display attractive high energy density. The main limitations are related to the cathode electrode fabrication and overall design strategies

to ensure sustained activities. Jaephil Cho *et. al.* reported a primary ZAB by using Mn_3O_4/IL-rGO as the ORR catalyst.[72] The system delivered a power density of 120 mW/cm^2. Similarly, pyrolyzed CoTMPP (Co-N-C) and FeCo-EDA (FeCo-N-C) were reported to be used as the cathode catalysts in the primary ZAB by providing current densities of 120 and 150 mA/cm^2, respectively at 1 V.[78-79]

Secondary Zn-air Battery: Similar to the primary ZABs, the secondary ZABs also use the ORR catalysts during the discharge process and the performance of the battery in the discharge process is determined mainly by the ORR activity of the catalysts employed. However, during the charging of the battery, the oxygen evolution reaction (OER) takes place and an OER catalyst is required for the purpose. If a bifunctional catalyst which can perform as an ORR catalyst while discharging and an OER catalyst while charging of the battery, an efficient rechargeable ZAB can be realized without making many complexities in the cathode of the cell. Even though this is a relatively new concept, there are few reports in the literature dealing with the application of such electrocatalysts for serving the purpose. For example, Liu *et. al*. reported Co_3O_4 decorated on Mn_3O_4 nanotubes as a bifunctional catalyst.[80] A more refined study of the bifunctional $NiCo_2O_4$ catalyst was documented by Shanmugam *et.al.*.[81] The group reported an overall low overpotential of 0.840 V (OER-ORR) for both the processes. A report from Dai *et. al.* suggests that the separate use of ORR and OER catalysts can also improve the rechargeability of the secondary ZABs.[14] The group used CoO/N-CNT as the ORR catalyst and NiFe LDH/CNT as the OER catalyst separately in the system. The configuration effectively delivered a low charge-discharge overpotential of 0.70 V at a current density of 20 mA/cm^2.

1.6. Hurdles Related to the Commercialization Aspects of ZABs:

The major challenges in the present scenario of any alternative energy generation/storage devices are related to the cost, durability and how well they can minimize the impact to the environment. The ZAB is a much better system compared to the Li-ion and lead-acid batteries considering the efficiency of the system to simultaneously address the abovementioned issues. However, in the path of commercialization, ZABs face several other issues such as relatively high overpotential for the faradaic reactions (ORR and OER), parasitic reactions, electrolyte drying, along with the other issues related to the separator membrane and fabrication strategies etc. During the discharge of the battery, a constant flow of the oxygen flux is required. The porosity of the

catalyst layer plays a crucial role in the oxygen flux and simultaneously the hydrophobic nature of the air electrode contributes to reduce the electrolyte leakage. The parasitic reactions like the reaction of the electrolyte KOH with carbon, and hydrogen evolution reaction also decrease the performance of the battery. Herein, it should be noted that although the parasitic reactions and electrolyte drying decrease the performance of the device, many of such problems can be sorted out by preparing effective catalysts (ORR and OER) and also by adopting adequate fabrication strategies of the air electrodes.

1.7. Scope for the Present Research Work and Objectives of Thesis:

Based on the critical review presented above highlighting the scope, issues and challenges related to the future energy requirements, it is clear that a multi-directional approach is necessary to come up with commercially viable modern energy generation and storage devices for the futuristic applications. The above sections clearly highlighted the need of developing cost-effective ORR and OER catalysts, particularly considering the demand of such catalysts for the applications like PEMFCs (ORR) and metal-air batteries (ORR and OER). The commercialization potentials of these systems are largely depending on the cost of the devices. The exorbitant cost of the noble-metal catalysts will never help to reduce the cost of PEMFCs and metal-air batteries to an industrially acceptable level. Hence, one of the effective ways is to develop potential ORR and OER catalysts based on non-noble metals. In a similar way, in the case of the metal-air batteries, the feature of rechargeability should be brought in to make them commercially more effective and attractive. This can be achieved if the electrodes can tackle both ORR (during the discharging process) and OER (during the charging process) at reduced overpotential levels. Here, if a bifunctional electrocatalyst with an ability to facilitate both ORR and OER can be developed, radical changes in the performance characteristics and design aspects can be achieved in the case of the metal-air batteries.

The main objective of the present thesis is to develop active and durable electroctalysts based on oxides with spinel structures for facilitating both ORR and OER with an assumption that the ability of the spinel structure to change the metal distribution within the coordinated sites will help to tune the performance characteristics in a desirable way. The spinels are highly stable metal oxides phases and they provide a unique opportunity of changing the metal coordinated

sites by stoichiometrically replacing one metal with another suitable species. This switch over between the normal-inverse phases and its associated benefits of tuning the catalytic activities in a desirable and controllable way, offer great opportunities to systematically develop a set of high performing ORR and OER catalysts. Even though ferrites such as $CoFe_2O_4$ are electrically insulating in nature, as an electrocatalyst, the material can be made conducting by dispersing nanoparticles of these materials on a suitable carbon support. An additional benefit of synergistic interaction between the support and active component phases can be achieved if a heteroatom doped carbon support such as nitrogen-doped graphene can be used as the support for dispersing the ferrite nanoparticles. Also, the small order dislocations expected in the case of nitrogen-doped graphene can assist to improve the dispersion of the ferrite nanoparticles on the support surface. Considering all these factors and interrelating parameters, one consideration of the present work is to prepare a series of systems based on cobalt ferrite nanoparticles dispersed on nitrogen-doped graphene and explore their activities towards ORR and OER. Further, the study can gain insightful information on the mechanistic aspects of the systems independently towards ORR and OER or directly as a bifunctional system to facilitate both ORR and OER simultaneously by modulating the system features through stoichiometric replacement of one metal for another. Realistic system level validations of the primary and secondary ZABs are also considered as important steps in the realization of the working systems.

The specific objectives of the work enlisted in this thesis are set out in this perspective as follows:

1. To develop a simple and scalable synthesis methodology for the cobalt ferrite nanoparticles with a selective narrow size distribution. A strategy to accomplish *in-situ* homogeneous decoration of the ferrite nanoparticles over the nitrogen-doped reduced graphene oxide (N-rGO) also has to be demonstrated.
2. To gain a basic understanding on how the particle size distribution of the cobalt ferrite catalysts influences the electrochemical performance towards ORR and OER, and how durable the catalysts are in connection with their dispersion on the graphene substrate.
3. To develop Zn and Zr substituted cobalt ferrite nanoparticle-dispersed N-rGO through stoichiometric metal displacement and further to study how the ORR and OER performance characteristics are influenced though these compositional alternations.

Strategies to impart the bifunctional feature to enable the catalyst to display both ORR and OER also need to be worked out at this stage.

4. To perform realistic system level validation by demonstrating primary and secondary zinc-air battery systems by employing the prepared cobalt ferrite catalysts for fabricating the air electrodes.
5. Finally, to understand the mechanistic aspects on how acidic and basic pH conditions influence the intrinsic activity characteristics of the various active centers as expected in the above systems on the ORR performance. Here, the aim is to perform the study by engrafting Fe and Co active centers on the carbon substrates and by evaluating the ORR performance based on various performance indicators as obtained through a set of electrochemical studies.

1.8. References

(1) Oladokun, M. G.; Odesola, I. A., Household Energy Consumption and Carbon Emissions for Sustainable Cities – A Critical Review of Modelling Approaches. *International Journal of Sustainable Built Environment* **2015,** *4*, 231-247.

(2) Lee, J.-S.; Tai Kim, S.; Cao, R.; Choi, N.-S.; Liu, M.; Lee, K. T.; Cho, J., Metal–Air Batteries with High Energy Density: Li–Air versus Zn–Air. *Adv. Energy Mater.* **2011,** *1*, 34-50.

(3) Rosli, R. E.; Sulong, A. B.; Daud, W. R. W.; Zulkifley, M. A.; Husaini, T.; Rosli, M. I.; Majlan, E. H.; Haque, M. A., A Review of High-temperature Proton Exchange Membrane Fuel Cell (HT-PEMFC) system. *Int. J. Hydrogen Energy* **2017,** *42*, 9293-9314.

(4) Goodenough, J. B.; Park, K.-S., The Li-Ion Rechargeable Battery: A Perspective. *J. Am. Chem. Soc.* **2013,** *135*, 1167-1176.

(5) Li, Y.; Dai, H., Recent Advances in Zinc-air Batteries. *Chem. Soc. Rev.* **2014,** *43*, 5257-5275.

(6) Balaish, M.; Kraytsberg, A.; Ein-Eli, Y., A Critical Review on Lithium-air Battery Electrolytes. *Phys. Chem. Chem. Phys.* **2014,** *16*, 2801-2822.

(7) Nie, Y.; Li, L.; Wei, Z., Recent Advancements in Pt and Pt-free Catalysts for Oxygen Reduction Reaction. *Chem. Soc. Rev.* **2015,** *44*, 2168-2201.

(8) Jiao, Y.; Zheng, Y.; Jaroniec, M.; Qiao, S. Z., Origin of the Electrocatalytic Oxygen Reduction Activity of Graphene-Based Catalysts: A Roadmap to Achieve the Best Performance. *J. Am. Chem. Soc.* **2014,** *136*, 4394-4403.

(9) Li, B.; Ge, X.; Goh, F. W. T.; Hor, T. S. A.; Geng, D.; Du, G.; Liu, Z.; Zhang, J.; Liu, X.; Zong, Y., Co_3O_4 Nanoparticles Decorated Carbon Nanofiber Mat as Binder-free Air-Cathode for High Performance Rechargeable Zinc-air Batteries. *Nanoscale* **2015,** *7*, 1830-1838.

(10) Ning, R.; Tian, J.; Asiri, A. M.; Qusti, A. H.; Al-Youbi, A. O.; Sun, X., Spinel $CuCo_2O_4$ Nanoparticles Supported on N-Doped Reduced Graphene Oxide: A Highly Active and Stable Hybrid Electrocatalyst for the Oxygen Reduction Reaction. *Langmuir* **2013,** *29*, 13146-13151.

(11) Ge, X.; Liu, Y.; Goh, F. W. T.; Hor, T. S. A.; Zong, Y.; Xiao, P.; Zhang, Z.; Lim, S. H.; Li, B.; Wang, X.; Liu, Z., Dual-Phase Spinel $MnCo_2O_4$ and Spinel $MnCo_2O_4$/Nanocarbon Hybrids for Electrocatalytic Oxygen Reduction and Evolution. *ACS Appl. Mater. Interfaces* **2014,** *6*, 12684-12691.

(12) Bian, W.; Yang, Z.; Strasser, P.; Yang, R., A $CoFe_2O_4$/Graphene Nanohybrid as an Efficient Bi-functional Electrocatalyst for Oxygen Reduction and Oxygen Evolution. *J. Power Sources* **2014,** *250*, 196-203.

(13) Liang, Y.; Wang, H.; Zhou, J.; Li, Y.; Wang, J.; Regier, T.; Dai, H., Covalent Hybrid of Spinel Manganese–Cobalt Oxide and Graphene as Advanced Oxygen Reduction Electrocatalysts. *J. Am. Chem. Soc.* **2012,** *134*, 3517-3523.

(14) Li, Y.; Gong, M.; Liang, Y.; Feng, J.; Kim, J.-E.; Wang, H.; Hong, G.; Zhang, B.; Dai, H., Advanced Zinc-air Batteries Based on High-performance Hybrid Electrocatalysts. *Nat. Commun.* **2013,** *4*, 1805.

(15) Ma, T. Y.; Zheng, Y.; Dai, S.; Jaroniec, M.; Qiao, S. Z., Mesoporous $MnCo_2O_4$ with Abundant Oxygen Vacancy Defects as High-performance Oxygen Reduction Catalysts. *J. Mater. Chem. A* **2014,** *2*, 8676-8682.

(16) Liang, Y.; Li, Y.; Wang, H.; Zhou, J.; Wang, J.; Regier, T.; Dai, H., Co_3O_4 Nanocrystals on Graphene as a Synergistic Catalyst for Oxygen Reduction Reaction. *Nat. Mater.* **2011,** *10*, 780-786.

(17) Wu, Z.-S.; Yang, S.; Sun, Y.; Parvez, K.; Feng, X.; Müllen, K., 3D Nitrogen-Doped Graphene Aerogel-Supported Fe_3O_4 Nanoparticles as Efficient Electrocatalysts for the Oxygen Reduction Reaction. *J. Am. Chem. Soc.* **2012,** *134*, 9082-9085.

(18) Zhu, H.; Zhang, S.; Huang, Y.-X.; Wu, L.; Sun, S., Monodisperse $M_xFe_{3-x}O_4$ (M = Fe, Cu, Co, Mn) Nanoparticles and Their Electrocatalysis for Oxygen Reduction Reaction. *Nano Lett.* **2013,** *13*, 2947-2951.

(19) Ge, X.; Sumboja, A.; Wuu, D.; An, T.; Li, B.; Goh, F. W. T.; Hor, T. S. A.; Zong, Y.; Liu, Z., Oxygen Reduction in Alkaline Media: From Mechanisms to Recent Advances of Catalysts. *ACS Catal.* **2015,** *5*, 4643-4667.

(20) Fu, J.; Cano, Z. P.; Park, M. G.; Yu, A.; Fowler, M.; Chen, Z., Electrically Rechargeable Zinc–Air Batteries: Progress, Challenges, and Perspectives. *Adv. Mater.* **2017,** *29*, n/a-n/a.

(21) Prabu, M.; Ramakrishnan, P.; Nara, H.; Momma, T.; Osaka, T.; Shanmugam, S., Zinc–Air Battery: Understanding the Structure and Morphology Changes of Graphene-Supported $CoMn_2O_4$ Bifunctional Catalysts Under Practical Rechargeable Conditions. *ACS Appl. Mater. Interfaces* **2014,** *6*, 16545-16555.

(22) Prabu, M.; Ramakrishnan, P.; Shanmugam, S., $CoMn_2O_4$ Nanoparticles Anchored on Nitrogen-doped Graphene Nanosheets as Bifunctional Electrocatalyst for Rechargeable Zinc–air Battery. *Electrochem. Commun.* **2014,** *41*, 59-63.

(23) Prabu, M.; Ketpang, K.; Shanmugam, S., Hierarchical Nanostructured $NiCo_2O_4$ as an Efficient Bifunctional Non-precious Metal Catalyst for Rechargeable Zinc-air Batteries. *Nanoscale* **2014,** *6*, 3173-3181.

(24) Capsoni, D.; Bini, M.; Ferrari, S.; Quartarone, E.; Mustarelli, P., Recent Advances in the Development of Li–air Batteries. *J. Power Sources* **2012,** *220*, 253-263.

(25) Ogasawara, T.; Débart, A.; Holzapfel, M.; Novák, P.; Bruce, P. G., Rechargeable Li_2O_2 Electrode for Lithium Batteries. *J. Am. Chem. Soc.* **2006,** *128*, 1390-1393.

(26) Girishkumar, G.; McCloskey, B.; Luntz, A. C.; Swanson, S.; Wilcke, W., Lithium−Air Battery: Promise and Challenges. *J. Phys. Chem Lett.* **2010,** *1*, 2193-2203.

(27) Yi, J.; Liu, X.; Guo, S.; Zhu, K.; Xue, H.; Zhou, H., Novel Stable Gel Polymer Electrolyte: Toward a High Safety and Long Life Li–Air Battery. *ACS Appl. Mater. Interfaces* **2015,** *7*, 23798-23804.

(28) Zhou, H.; Wang, Y.; Li, H.; He, P., The Development of a New Type of Rechargeable Batteries Based on Hybrid Electrolytes. *ChemSusChem* **2010,** *3*, 1009-1019.

(29) Laoire, C. O.; Mukerjee, S.; Abraham, K. M.; Plichta, E. J.; Hendrickson, M. A., Elucidating the Mechanism of Oxygen Reduction for Lithium-Air Battery Applications. *J. Phys. Chem. C* **2009,** *113*, 20127-20134.

(30) Yoo, E.; Zhou, H., Li−Air Rechargeable Battery Based on Metal-free Graphene Nanosheet Catalysts. *ACS Nano* **2011,** *5*, 3020-3026.

(31) Wang, Y.; Zhou, H., A Lithium-air Battery with a Potential to Continuously Reduce O_2 from Air for Delivering Energy. *J. Power Sources* **2010,** *195*, 358-361.

(32) Li, Y.; Lu, J., Metal–Air Batteries: Will They Be the Future Electrochemical Energy Storage Device of Choice? *ACS Energy Letters* **2017,** *2*, 1370-1377.

(33) Yang, D.; Zhang, L.; Yan, X.; Yao, X., Recent Progress in Oxygen Electrocatalysts for Zinc–Air Batteries. *Small Methods* **2017,** *1*, 1700209.

(34) Wang, M.; Qian, T.; Zhou, J.; Yan, C., An Efficient Bifunctional Electrocatalyst for a Zinc–Air Battery Derived from Fe/N/C and Bimetallic Metal–Organic Framework Composites. *ACS Appl. Mater. Interfaces* **2017,** *9*, 5213-5221.

(35) Shimizu, K.; Sepunaru, L.; Compton, R. G., Innovative Catalyst Design for the Oxygen Reduction Reaction for Fuel cells. *Chem. Sci.* **2016,** *7*, 3364-3369.

(36) Kraytsberg, A.; Ein-Eli, Y., Review of Advanced Materials for Proton Exchange Membrane Fuel Cells. *Energy & Fuels* **2014,** *28*, 7303-7330.

(37) Omasta, T. J.; Park, A. M.; LaManna, J. M.; Zhang, Y.; Peng, X.; Wang, L.; Jacobson, D. L.; Varcoe, J. R.; Hussey, D. S.; Pivovar, B. S.; Mustain, W. E., Beyond Catalysis and Membranes: Visualizing and Solving the Challenge of Electrode Water Accumulation and Flooding in AEMFCs. *Energy Environ. Sci.* **2018,** *11*, 551-558.

(38) Palaniselvam, T.; Kashyap, V.; Bhange, S. N.; Baek, J.-B.; Kurungot, S., Nanoporous Graphene Enriched with Fe/Co-N Active Sites as a Promising Oxygen Reduction Electrocatalyst for Anion Exchange Membrane Fuel Cells. *Adv. Funct. Mater.* **2016,** *26*, 2150-2162.

(39) Lee, K.-S.; Spendelow, J. S.; Choe, Y.-K.; Fujimoto, C.; Kim, Y. S., An Operationally Flexible Fuel Cell based on Quaternary Ammonium-biphosphate Ion Pairs. *Nature Energy* **2016,** *1*, 16120.

(40) Ji, X.; Liu, X.; Tong, X.; Luo, T.; Wu, H.; Meng, X.; Zhan, Z., Enhanced Activities of Nano-$CeO_{2-\delta}$@430L Composites by Zirconium Doping for Hydrogen Electro-oxidation in Solid Oxide Fuel Cells. *Int. J. Hydrogen Energy* **2016,** *41*, 11331-11339.

(41) Liu, Y.; Ishihara, A.; Mitsushima, S.; Kamiya, N.; Ota, K.-i., Transition Metal Oxides as DMFC Cathodes Without Platinum. *J. Electrochem. Soc.* **2007,** *154*, B664-B669.

(42) Kirubakaran, A.; Jain, S.; Nema, R. K., A Review on Fuel Cell Technologies and Power Electronic Interface. *Renewable sustainable Energy Rev.* **2009,** *13*, 2430-2440.

(43) Chen, J.; Hu, J.; Waldecker, J. R., A Comprehensive Model for Carbon Corrosion during Fuel Cell Start-Up. *J. Electrochem. Soc.* **2015,** *162*, F878-F889.

(44) Wang, D.-W.; Su, D., Heterogeneous Nanocarbon Materials for Oxygen Reduction Reaction. *Energy Environ. Sci.* **2014,** *7*, 576-591.

(45) Stoerzinger, K. A.; Risch, M.; Han, B.; Shao-Horn, Y., Recent Insights into Manganese Oxides in Catalyzing Oxygen Reduction Kinetics. *ACS Catal.* **2015,** *5*, 6021-6031.

(46) Liu, S.; White, M. G.; Liu, P., Mechanism of Oxygen Reduction Reaction on Pt(111) in Alkaline Solution: Importance of Chemisorbed Water on Surface. *J. Phys. Chem. C* **2016,** *120*, 15288-15298.

(47) He, F.; Li, K.; Xie, G.; Wang, Y.; Jiao, M.; Tang, H.; Wu, Z., Theoretical Insights on the Catalytic Activity and Mechanism for Oxygen Reduction Reaction at Fe and P Codoped Graphene. *Phys. Chem. Chem. Phys.* **2016,** *18*, 12675-12681.

(48) Zhang, J.; Wang, Z.; Zhu, Z., The Inherent Kinetic Electrochemical Reduction of Oxygen into H_2O on FeN_4-Carbon: A Density Functional Theory Study. *J. Power Sources* **2014,** *255*, 65-69.

(49) Kattel, S.; Wang, G., A Density Functional Theory Study of Oxygen Reduction Reaction on Me-N_4 (Me = Fe, Co, or Ni) Clusters Between Graphitic Pores. *J. Mater. Chem. A* **2013,** *1*, 10790-10797.

(50) Unni, S. M.; Anilkumar, G. M.; Matsumoto, M.; Tamaki, T.; Imai, H.; Yamaguchi, T., Direct Synthesis of a Carbon Nanotube Interpenetrated Doped Porous Carbon Alloy as a Durable Pt-free Electrocatalyst for the Oxygen Reduction Reaction in an Alkaline Medium. *Sustainable Energy & Fuels* **2017,** *1*, 1524-1532.

(51) Čolić, V.; Bandarenka, A. S., Pt Alloy Electrocatalysts for the Oxygen Reduction Reaction: From Model Surfaces to Nanostructured Systems. *ACS Catal.* **2016**, 5378-5385.

(52) Holewinski, A.; Idrobo, J.-C.; Linic, S., High-performance Ag–Co Alloy Catalysts for Electrochemical Oxygen Reduction. *Nat Chem* **2014,** *6*, 828-834.

(53) Guo, S.; Li, D.; Zhu, H.; Zhang, S.; Markovic, N. M.; Stamenkovic, V. R.; Sun, S., FePt and CoPt Nanowires as Efficient Catalysts for the Oxygen Reduction Reaction. *Angew. Chem. Int. Ed.* **2013,** *52*, 3465-3468.

(54) Tritsaris, G. A.; Nørskov, J. K.; Rossmeisl, J., Trends in Oxygen Reduction and Methanol Activation on Transition Metal Chalcogenides. *Electrochim. Acta* **2011,** *56*, 9783-9788.

(55) Guo, Y.; Yuan, P.; Zhang, J.; Hu, Y.; Amiinu, I. S.; Wang, X.; Zhou, J.; Xia, H.; Song, Z.; Xu, Q.; Mu, S., Carbon Nanosheets Containing Discrete Co-N_x-B_y-C Active Sites for Efficient Oxygen Electrocatalysis and Rechargeable Zn-Air Batteries. *ACS Nano* **2018**.

(56) Stephens, I. E. L.; Bondarenko, A. S.; Gronbjerg, U.; Rossmeisl, J.; Chorkendorff, I., Understanding the Electrocatalysis of Oxygen Reduction on Platinum and Its Alloys. *Energy Environ. Sci.* **2012,** *5*, 6744-6762.

(57) Stamenkovic, V. R.; Mun, B. S.; Mayrhofer, K. J. J.; Ross, P. N.; Markovic, N. M., Effect of Surface Composition on Electronic Structure, Stability, and Electrocatalytic Properties of Pt-Transition Metal Alloys: Pt-Skin versus Pt-Skeleton Surfaces. *J. Am. Chem. Soc.* **2006,** *128*, 8813-8819.

(58) Stamenkovic, V. R.; Mun, B. S.; Arenz, M.; Mayrhofer, K. J. J.; Lucas, C. A.; Wang, G.; Ross, P. N.; Markovic, N. M., Trends in Electrocatalysis on Extended and Nanoscale Pt-Bimetallic Alloy Surfaces. *Nat. Mater.* **2007,** *6*, 241-247.

(59) Malacrida, P.; Escudero-Escribano, M.; Verdaguer-Casadevall, A.; Stephens, I. E. L.; Chorkendorff, I., Enhanced Activity and Stability of Pt–La and Pt–Ce Alloys for Oxygen Electroreduction: the Elucidation of the Active Surface Phase. *J. Mater. Chem. A* **2014,** *2*, 4234-4243.

(60) Yoo, S. J.; Hwang, S. J.; Lee, J.-G.; Lee, S.-C.; Lim, T.-H.; Sung, Y.-E.; Wieckowski, A.; Kim, S.-K., Promoting Effects of La for Improved Oxygen Reduction Activity and High Stability of Pt on Pt–La Alloy Electrodes. *Energy Environ. Sci.* **2012,** *5*, 7521-7525.

(61) Zhang, J.; Vukmirovic, M. B.; Xu, Y.; Mavrikakis, M.; Adzic, R. R., Controlling the Catalytic Activity of Platinum-Monolayer Electrocatalysts for Oxygen Reduction with Different Substrates. *Angew. Chem.* **2005,** *117*, 2170-2173.

(62) Chen, C.; Kang, Y.; Huo, Z.; Zhu, Z.; Huang, W.; Xin, H. L.; Snyder, J. D.; Li, D.; Herron, J. A.; Mavrikakis, M.; Chi, M.; More, K. L.; Li, Y.; Markovic, N. M.; Somorjai, G. A.; Yang, P.; Stamenkovic, V. R., Highly Crystalline Multimetallic Nanoframes with Three-Dimensional Electrocatalytic Surfaces. *Science* **2014,** *343*, 1339-1343.

(63) Shao, M.; Chang, Q.; Dodelet, J.-P.; Chenitz, R., Recent Advances in Electrocatalysts for Oxygen Reduction Reaction. *Chem. Rev.* **2016,** *116*, 3594-3657.

(64) Liang, H.-W.; Zhuang, X.; Brüller, S.; Feng, X.; Müllen, K., Hierarchically Porous Carbons with Optimized Nitrogen Doping as Highly Active Electrocatalysts for Oxygen Reduction. *Nat. Commun.* **2014,** *5*.

(65) Lv, Q.; Si, W.; He, J.; Sun, L.; Zhang, C.; Wang, N.; Yang, Z.; Li, X.; Wang, X.; Deng, W.; Long, Y.; Huang, C.; Li, Y., Selectively Nitrogen-doped Carbon Materials as Superior Metal-free Catalysts for Oxygen Reduction. *Nature Communications* **2018,** *9*, 3376.

(66) Xu, L.; Fan, H.; Huang, L.; Xia, J.; Li, S.; Li, M.; Ding, H.; Huang, K., Chrysanthemum-Derived N and S Co-doped Porous Carbon for Efficient Oxygen Reduction Reaction and Aluminum-air Battery. *Electrochim. Acta* **2017,** *239*, 1-9.

(67) Yan, W.; Cao, X.; Tian, J.; Jin, C.; Ke, K.; Yang, R., Nitrogen/Sulfur Dual-doped 3D Reduced Graphene Oxide Networks-supported $CoFe_2O_4$ with Enhanced Electrocatalytic Activities for Oxygen Reduction and Evolution Reactions. *Carbon* **2016,** *99*, 195-202.

(68) Zhao, H.; Sun, C.; Jin, Z.; Wang, D.; Yan, X.; Chen, Z. G.; zhu, G.; Yao, X., Carbon for Oxygen Reduction Reaction: A Defect Mechanism. *J. Mater. Chem. A* **2015**.

(69) Chisaka, M.; Ishihara, A.; Ota, K.-i.; Muramoto, H., Synthesis of Carbon-Supported Titanium Oxynitride Nanoparticles as Cathode Catalyst for Polymer Electrolyte Fuel Cells. *Electrochim. Acta* **2013,** *113*, 735-740.

(70) Yin, F.; Takanabe, K.; Kubota, J.; Domen, K., Polymerized Complex Synthesis of Niobium- and Zirconium-Based Electrocatalysts for PEFC Cathodes. *J. Electrochem. Soc.* **2010,** *157*, B240-B244.

(71) Zhang, X.; Wang, X.-G.; Xie, Z.; Zhou, Z., Recent Progress in Rechargeable Alkali Metal–air Batteries. *Green Energy & Environment* **2016,** *1*, 4-17.

(72) Lee, J.-S.; Lee, T.; Song, H.-K.; Cho, J.; Kim, B.-S., Ionic Liquid Modified Graphene Nanosheets Anchoring Manganese Oxide Nanoparticles as Efficient Electrocatalysts for Zn-air Batteries. *Energy Environ. Sci.* **2011,** *4*, 4148-4154.

(73) Zhang, J.; Xia, Z.; Dai, L., Carbon-Based Electrocatalysts for Advanced Energy Conversion and Storage. *Science Advances* **2015,** *1*.

(74) Zhou, R.; Zheng, Y.; Jaroniec, M.; Qiao, S.-Z., Determination of the Electron Transfer Number for the Oxygen Reduction Reaction: From Theory to Experiment. *ACS Catal.* **2016,** *6*, 4720-4728.

(75) Pei, P.; Wang, K.; Ma, Z., Technologies for Extending Zinc–air Battery's Cyclelife: A Review. *Applied Energy* **2014,** *128*, 315-324.

(76) Castanheira, L.; Silva, W. O.; Lima, F. H. B.; Crisci, A.; Dubau, L.; Maillard, F., Carbon Corrosion in Proton-Exchange Membrane Fuel Cells: Effect of the Carbon Structure, the Degradation Protocol, and the Gas Atmosphere. *ACS Catal.* **2015,** *5*, 2184-2194.

(77) Tan, H.; Tang, J.; Henzie, J.; Li, Y.; Xu, X.; Chen, T.; Wang, Z.; Wang, J.; Ide, Y.; Bando, Y.; Yamauchi, Y., Assembly of Hollow Carbon Nanospheres on Graphene Nanosheets and Creation of Iron-Nitrogen-Doped Porous Carbon for Oxygen Reduction. *ACS Nano* **2018**.

(78) Li Zhu, A.; Wang, H.; Qu, W.; Li, X.; Jong, Z.; Li, H., Low Temperature Pyrolyzed Cobalt Tetramethoxy Phenylporphyrin Catalyst and Its Applications as an Improved Catalyst for Metal Air Batteries. *J. Power Sources* **2010,** *195*, 5587-5595.

(79) Chen, Z.; Choi, J.-Y.; Wang, H.; Li, H.; Chen, Z., Highly Durable and Active Non-precious Air Cathode Catalyst for Zinc Air Battery. *J. Power Sources* **2011,** *196*, 3673-3677.

(80) Du, G.; Liu, X.; Zong, Y.; Hor, T. S. A.; Yu, A.; Liu, Z., Co_3O_4 Nanoparticle-modified MnO_2 Nanotube Bifunctional Oxygen Cathode Catalysts for Rechargeable Zinc–air Batteries. *Nanoscale* **2013,** *5*, 4657-4661.

(81) Prabu, M.; Ketpang, K.; Shanmugam, S., Hierarchical Nanostructured $NiCo_2O_4$ as an Efficient Bifunctional Non-precious Metal Catalyst for Rechargeable Zinc–air Batteries. *Nanoscale* **2014,** *6*, 3173-3181.

Chapter 2

Experimental Methods and Material Characterizations Techniques*

This chapter provides a glimpse of the synthetic strategies adopted for the preparation of the various carbon materials such as graphene oxide (GO), chemically reduced N-doped graphene oxides (N-rGO), metal oxide nanoparticles etc. by simple and scalable chemical methods. The chapter also deals with the working principles of the various material characterization techniques and the plethora of information disclosed for the materials by the techniques. Details of instrumentation and sampling of the structural characterization techniques are briefly summarized. Discussions on the high-resolution transmission electron microscopy (HR-TEM) for imaging, powder X-ray diffraction (PXRD) for structural analysis, energy dispersive X-ray diffraction for elemental analysis, Raman spectroscopy for defects in carbon framework, infrared spectroscopy for chemical bonds and X-ray photoelectron spectroscopy (XPS) for surface analysis are included for detailed understanding of the various catalysts. The working of the technique like thermogravimetric analysis (TGA) is also discussed in the chapter. Since, the electrochemical performances of the catalysts are measured through the I-V characteristic using different methods, a transitory depiction of the working principles of the electrochemical techniques such as cyclic voltametry (CV), linear sweep voltametery (LSV), rotating ring disk electrode (RRDE) and chronopotentiometry (CP) are also included in the chapter. Further, the fabrication techniques adopted for making the cathode is discussed in the present chapter.

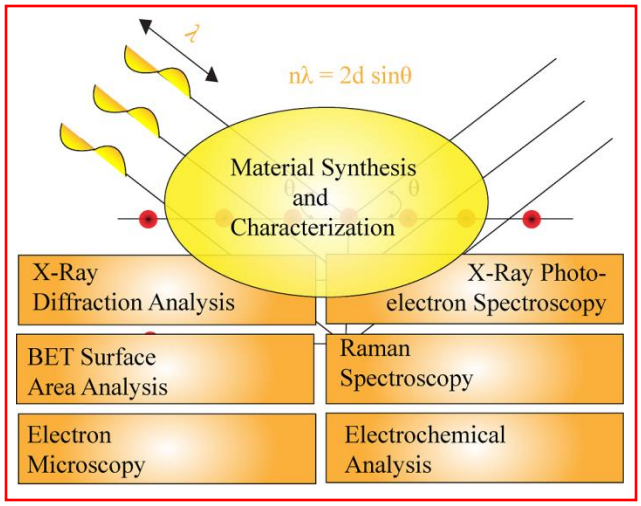

*The synthesis procedure of the nanomaterials and characterization technique used to identify the material is already published and are reproduced here with the permission from the publishers "*ACS Appl. Mater. Interfaces* **2016,** 8, 20730-20740; *ChemistrySelect* **2017,** *2*, 7845-7853 (***License No. 4436440418358)***; and *ACS Catal.* **2018**, 3715-3726".

2.1. Experimental Methods

2.1.1. Chemicals Procured: Iron acetate, cobalt acetate, potassium permanganate ($KMnO_4$), zinc acetate, zirconium acetylacetonate and potassium hydroxide (KOH) were procured from Sigma-Aldrich. Phosphoric acid (H_3PO_4), sulfuric acid (H_2SO_4), isopropyl alcohol, 30% ammonia solution and ethanol (EtOH) were procured from Thomas Baker. The procured chemicals were used for preparation of various catalysts without any further purification. Gas Diffusion Layer (GDL) were procured from SGL group Germany. Deionised water (18 mΩ) from the milli-Q set-up was used for the preparation of all the electrolytic solutions.

2.1.2. Synthesis of Graphene Oxide (GO): The graphene oxide(GO) synthesis was accomplished by following the previously reported improved Hummer's method, which overcomes the limitations of the low efficient conventional Hummer's method.[1] In a typical synthesis of GO, 12 g of $KMnO_4$ was grinded well with 2 g of graphite powder (*i.e.* 6:1 ratio of potassium permanganate to graphite) for making a uniform powder. The above powder was slowly added to the prepared solution of H_3PO_4 and H_2SO_4, in a ratio of 1:9 and kept in an ice bath with stirring. After complete addition of the powder, the colorless solution changed to greenish which is completely different from final product color (pink). As such prepared reaction mixture was refluxed at 60 °C for 12 h with constant stirring. The solution changes to pink when the reaction is complete. Finally, the reaction product was poured into a solution containing 5 mL of H_2O_2 (30%) and ice-cooled water (400 mL). As such obtained precipitate was centrifuged at 10000 rpm and washed with a considerable amount of DI water to remove the acid content and increase the pH (~6) of the solution, followed by washing with dilute HCl and ethanol. Later, the material was precipitated with diethylether and allowed to dry at room temperature

2.1.3. Synthesis of Chemically Reduced Graphene Oxide (N-rGO): The synthesis of the chemically reduced graphene oxide was conducted by using previously prepared graphene oxide as precursor and ammonium hydroxide as reducing agent. Following the procedure, in 50 mL of Mili-Q DI water 200 mg of GO was dispersed and later 50 mL of ammonium hydroxide was added to the dispersion. The obtained solution was poured into a round-bottom flask followed by refluxing at 80 °C for 12 h. After the reaction period the black-colored solution was

centrifuged and washed with DI water. As such obtained precipitate was dried under an IR lamp, and this material is named as N-rGO.[2]

2.1.4. Solvothermal Synthesis of Metal Oxide Nanoparticles: Metal oxide nanoparticles synthesis has been achieved using the metal acetate for metal precursor and water-ethanol mixture as medium. The synthesis was done in the autoclave with temperature and pressure generated inside the autoclave for controlling parameter for thermal decomposition of the metal salt. Nanoparticles with different size distributions were synthesized by varying the water to ethanol percentage which is because of variation in the pressure in the autoclave at constant temperature. In the typical synthesis of cobalt ferrite nanoparticle, water percentages of 0%, 33%, 50%, and 66% were used for the particle size variation by considering the effect of water to ethanol composition on the particle size.[3] In the hydrothermal bomb with increasing water percentage, the vapor pressure changes, and this allows the thermal decomposition of metal acetate at low temperature salts for effective formation of the spinel cobalt ferrite nanopartilces.[4-5] A ratio of 50:50 for water:ethanol was found to be the optimum composition for the formation of CF at 130 ^{o}C temperature for the desired electrochemical performance.[6]

2.1.5. Catalyst Ink Preparation and Electrode Coating: For electrochemical analysis, the catalyst slurry was prepared by dispersing 10 mg/mL of active material in IPA:water (3:2) solution. In the solution, 40 µl of 5% Nafion was added as a binder and ultrasonicated for 1 h. 10 µl of the as such prepared catalyst slurry drop coated over the glassy carbon electrode, and after drying under IR lamp, was used as the working electrode (WE) for all the electrochemical analysis.[3, 5]

2.2. Material Characterizations Techniques

2.2.1. Transmission Electron Microscopy (TEM): Transmission Electron Microscopy(TEM) is a imaging tool for nano materials in which high energy electron beams are passed through the ultrathin specimen.[7] Generally, the thickness of specimen is maintained of the order of < 100 nm over the grid. The technique is similar to optical microcopy where light waves are converged by silicates made lens through the specimen. Here, the high energy electron beam is used instead of the electromagnetic optical waves as in the optical microscopes which increase the resolution limit of the instrument. The major drawback of the TEM analysis is the

sophisticated sample preparation technique and thickness of the sample. The analysis is done under ultra-high vacuum which further restricts the analysis of the living objects.

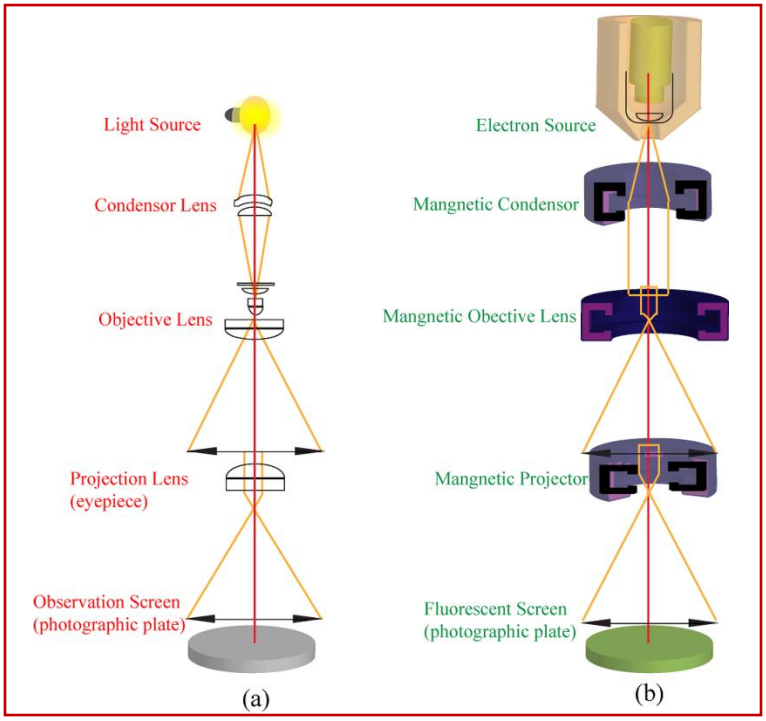

Figure 2.1. *Working principles (a) the optical microscope and (b) the electron microscope.*

Figure 2.1 shows the resemblance of the optical and the electron microscopes. As both the technologies differ in the electromagnetic wavelength used to analyze the sample, their lenses for conversing the waves are different. In light microscope, the silica made condenser lens is used while in TEM the electromagnets accomplish the job. A typical TEM instrument includes a) electron source, b) magnetic condenser, c) magnetic objective lens, d) magnetic projector and e) fluorescent screen.

a) Electron Source (Gun): The pivotal component of the instrument is V-shaped filament. Usually the filament is made of LaB_6 or W (tunguston) which is covered with Wehnelt electrode (Wehnelt Cap).[8] Because of the negative potential of the electrode, electrons are ejected from the point source and, as a result, monochromatic electron beam is obtained. **Figure 2.2** shows the typical structure of the electron source. In this, the filament is heated and a positive potential is applied to produce stream of electrons. The electrons are accelerated down the column, and because of the repulsion from the cap, they accumulate towards the optical axis. The collection

of the electrons between the cap and the tip is termed as space charge. The electrons at the bottom of the space charge region pass through the small hole in the Wehnelt cap. For simplicity, a pictorial representation of the electron gun is given in **Figure 2.2**.

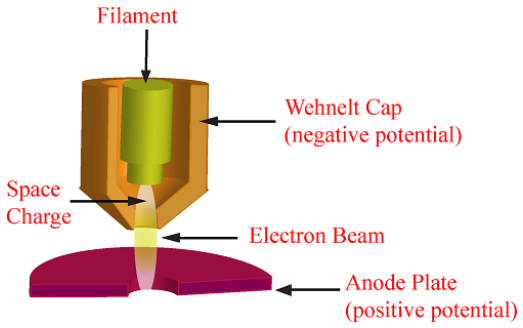

Figure 2.2. *A typical sketch of the electron gun.*

b) Magnetic Condenser: The condenser lenses focus the incoming electron beam from the gun to a small, thin and coherent beam. These lenses determine the "spot size" of the electron beam that strikes the sample. The magnetic condenser is followed by the condenser aperture. A condenser aperture is a metal strip with a small hole in it. It is used to restrict the unwanted scattered electrons and electron beam before image formation. After the condenser aperture, the electron beam strikes the sample. The interaction between the electron beam and the sample can be described as: a) unscattered electrons (transmitted beam), b) elastically scattered electrons (diffracted beam) and c) inelastically scattered electrons.

c) Magnetic Objective Lens: The purpose of the objective lens is to focus the transmitted electron beams from the sample in an image. The objective lens is followed by the objective aperture for blocking out high-angle diffracted electrons. After the objective aperture, the beam goes through the selected aperture which allows examining the periodic diffraction of the electrons from the array of atoms.

d) Magnetic projector: The magnetic projector lenses work to expand the incoming electron beam onto the fluorescent screen.

e) Fluorescent screen: The screen is made from the fine (10-100 μm) particulate zinc sulphide which generates light when electron beam strikes the screen.[9]

In the present studies, for transmission electron microscopy (TEM) analysis samples were prepared by dispersing 1 mg of the catalyst in 3:2 IPA-water mixture. As such prepared dispersion was drop-coated on a 200 mesh Cu grid and allowed to dry under an IR lamp. Finally, the dried Cu grid was used for the TEM imaging. A FEI, TECNAI G2 F20 instrument operated at 200 kV (Cs = 0.6 mm, resolution 1.7 Å) of acceleration voltage was used for TEM imaging.

2.2.2. Scanning Electron Microscopy (SEM) and Energy Dispersive X-ray Analysis (EDXA): The Scanning Electron Microscopy (SEM) is used to observe the surface morphology of the specimen.[10] In the process, fine electron probe is irradiated over the specimen and consequently secondary electrons are emitted from the surface. Topography of the specimen is obtained by two-dimensional scanning of the specimen and analyzing the secondary electron for image.

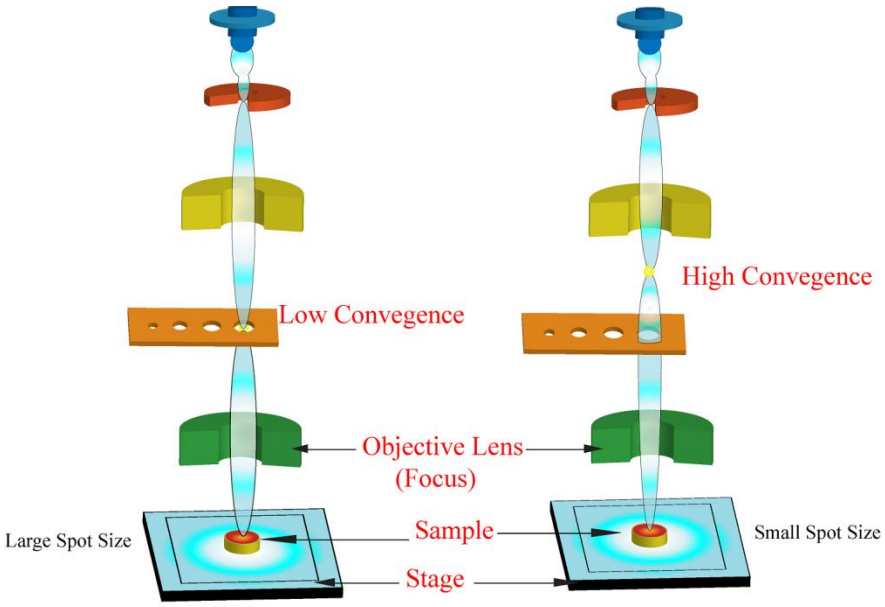

Figure 2.3. *Schematic representation of working principle of the SEM instrument.*

Figure 2.3 depicts the working of the SEM instrument. The major difference between the TEM and SEM is accelerated electron energy and mode of analysis, *i.e.*, secondary electrons are analyzed in the SEM analysis. Further, as the electrons interact with the specimen, X-rays are also generated in the process. The energy of the emitted X-ray corresponds to a difference in two energy levels of the orbitals of an atom (core energy levels) and, as a result, the analysis of the

X-ray generated gives the chemical composition of the sample. The technique of analyzing the X-ray is known as EDXA.

In present work, an FEI, Model Quanta 200 3D instrument operated at 30 kV voltage and equipped with Phoenix Energy Dispersive setup has been used for taking the SEM images of the catalysts. The instrument was also equipped with EDAX and elemental mapping facility. For the sample preparation, the catalyst was dispersed in 3:2 water-IPA mixture and drop coated over a silicon wafer. The as such prepared sample was dried under an IR lamp and projected for the SEM analysis.

2.2.3. Powder X-ray Diffraction Pattern (PXRD): In 1913, the English physicist Sir W. H. Bragg and his son W. L. Bragg developed a relation between the cleavage faces of a crystal to an incident X-ray beam. Later, the relation was known as Bragg's equation and the equation was found very useful tool for identification of the materials:

$$n\lambda = 2d \sin\theta \qquad (1)$$

where, n is the number of waves, λ is the wavelength, d is the d-spacing and θ is the angle between the incident beam and the plane of the crystal.

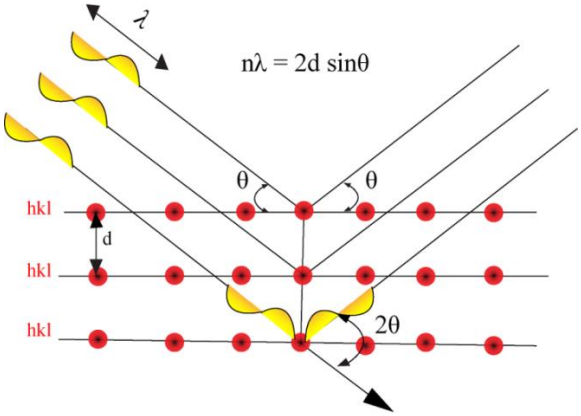

Figure 2.4. *Schematic representation of the incident X-ray beam diffraction from the surface of the crystal.*

An X-ray is an electromagnetic wave which has alternative electromagnetic field of high energy. When an X-ray of a particular energy hits the atom, the electron cloud around the atoms starts to oscillate. The electron cloud oscillates with same energy as that of the incident beam. The ejected X-ray beam in all the directions forms the destructive interference, *i.e.*, the combining waves go out of phase and as a result there is no energy leaving the crystal. However,

the regular arrangement of the atoms in the crystals allows a very few angles to have the constructive interference over the detector plate.[11] There will be well defined X-ray beams leaving the sample at particular angles. Hence, a diffracted beam comprises a large number of scattered waves mutually reinforcing one another.

In order to find out the diffraction form a material the materials are classified as:

a) Amorphous: Here, the atoms are randomly distributed similar to the disorder in the liquids. Ceramics and glasses are well known amorphous materials.[12]

b) Crystalline: In these materials, the atoms are placed in a particular pattern. The whole crystal can be constructed using a unit cell, which is a particular arrangement of the atoms. The unit cells are defined with three axes a, b and c, and the angle between them as α, β and γ.

Apart from the finger print of the materials, the grain size of the crystal can also be determined from the diffraction pattern using the Scherrer Equation:

$$B(2\theta) = \frac{K\lambda}{L\,Cos\theta} \qquad (2)$$

where, B is the peak width, K is a constant, λ is the wavelength and L is the crystallite size.

In the present research work, PAN analytical was used for the diffraction analysis. The instrument was equipped with Cu X-Ray source (Cu-Kα radiation, λ = 1.5418). The measurements were done at a scan rate of 2^{o} min^{-1} for a 2θ value of 10-80^{o}. The obtained data was analyzed withX' PertHighScore Plus software and plotted with Origin 6.

2.2.4. X-ray Photoelectron Spectroscopy (XPS): It is a non destructive surface techniquie which provides the information about the composition and oxidation state of the constituent elements in the catalyst.[13] In the measurement, X-rays are exposed to the sample and kinetic energy of the ejected electron form the sample is measured.[14] **Figure 2.6** represents the working principle of the XPS analysis. The core electrons ejectedfrom the sample gives the esteemation of the elements. A general equation given for the binding energy calculation is given as:

$$E_b = h\nu - E_k - \phi \qquad (3)$$

where, E_b is the binding energy of the element core electrons, hν is the energy of the incident X-ray source, E_k is the kinetic energy of the photoelectrons and ϕ is the work function[15] of the material.

The basic principle involved in the analysis is schematically presented in **Figure 2.6**. As the X-ray photons fall over the catalyst, the atoms from the surface eject the electrons from the core, which in turn is detected by the detector. Every atom in the periodic table have fixed core electron binding energy, which is because of the fixed electrostatic interaction between the nucleus and the core electron. Hence, it allows the analysis of chemical composition and estimation of the elements.

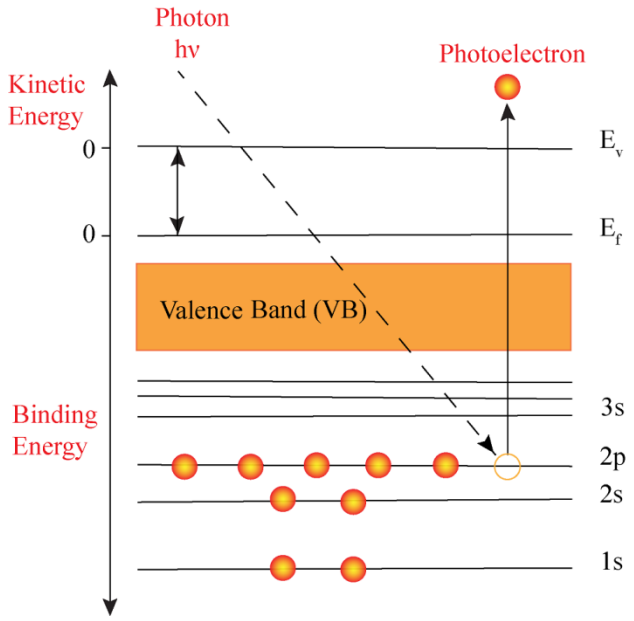

Figure 2.6. *Schematic representation of the core shell electron ejection from the catalyst surface. (**Source: Lecture note, City University of Hong Kong, Surface Science Western, UWO**)*

The instrumentation of the XPS is complex and involves several steps for complete analysis. **Figure 2.7** represents the sketch for various steps involved in the analysis. The various parts include: 1) Electron energy analyzer, 2) X-ray source, 3) Ar ion gun, 4) Neutralizer, 5) Vacuum System, 6) Electronic controls, and 7) Computer system. In general, the vacuum inside the analyzer is $< 10^{-9}$ Torr.

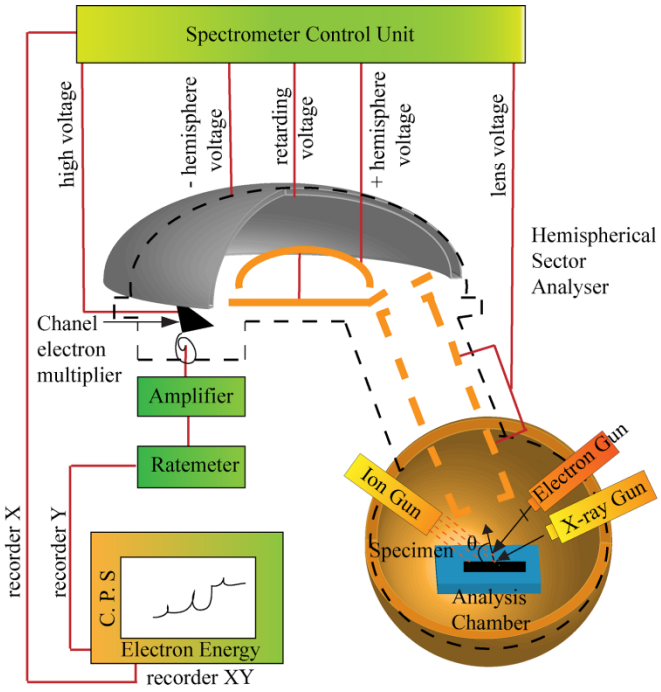

Figure 2.7. *A schematic representation of the XPS instrument.* ***(Source: Lecture note, City University of Hong Kong, Surface Science Western, UWO)***

In the present study, the X-ray photo electron spectroscopy study was carried out over a VG MicrotechMultilab ESCA 3000 spectrometer, equipped with Mg Kα X-ray source (hν = 1.2356 keV). The obtained data is decovoluted using XPSPEAK41 and plotted using Origin 6.

2.2.5. Raman Spectroscopy:

Raman spectroscopy is a non-destructive technique which is frequently used to analyse the carbon based materials in the material science.[16] The molecules having zero dipole moment, but develop dipole moment with electromagnetic irradiation, are considered as Raman active. The technique is very useful in identifying the defects in the carbon materials. The working of the Raman phenomenon involves the exposure of the laser to the sample followed by the collection of the scattered light. When the scattered and incident beam frequencies are same, the phenomenon is termed as Rayleigh scattering or elastic scattering. The frequency of the scattered light differs from the incident light when the interaction between the matter and electromagnetic radiation takes place. Depending on the energy of the scattered light, the phenomenon is termed as Stokes Raman Scattering or Anti-Stokes Raman Scattering. **Figure 2.8** shows the excitation of the molecule with the laser and simultaneously the Raman Scattering from the molecule.

In the present research work, we have used an HR 800 Raman spectrometer (Jobin Yvon, Horiba, France) equipped with a 632 nm green laser (NRS 1500 W) for analyzing the defects in the carbon materials.

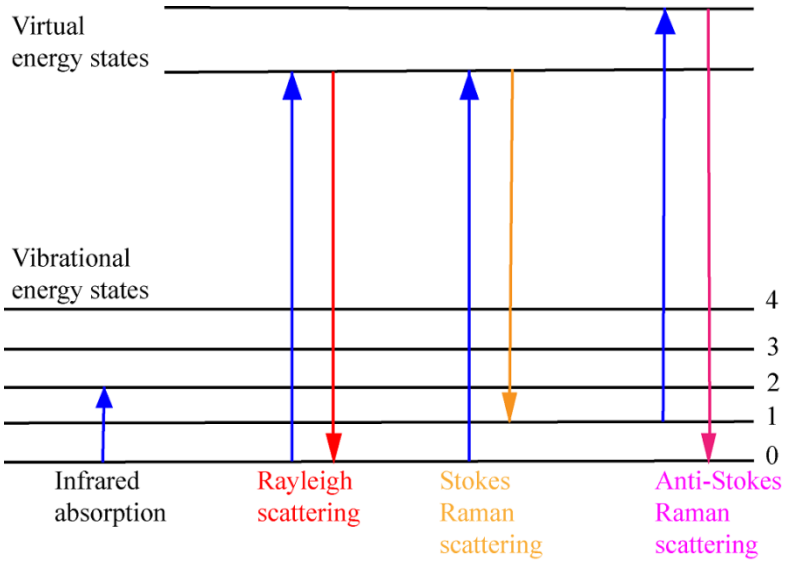

Figure 2.8. *Schematic representation of Raman scattering of the laser light.*

2.2.6. Infrared Spectroscopy (IR): Infrared Spectroscopy is a technique which deals with the vibrational mode of molecules and it helps to disclose the chemical composition of the molecules.[17] Only vibrations which produce the change in the dipole moment are observed in the IR spectra. Basic rules followed for the absorption IR radiation is depicted as Hooke's Law:

$$\bar{\nu} = \frac{1}{2\pi c}\sqrt{K\frac{m_1 m_2}{m_1 + m_2}}$$

$\bar{\nu}$ is the wavenumber, c is the velocity of light, K is the force constant of the bond and m is the mass of the atom. As from the above equation, the stronger bonds absorb at higher frequencies (higher K = higher $\bar{\nu}$), and as the mass of the atom increases, the frequency decreases. A simplified schematic of the IR instrument is presentation in **Figure 2.9.**

A typical FT-IR instrument includes IR source, beam splitter, sample holder, detector and a computer to process the data. In the FT-IR instrument, the data acquisition is faster compared to the beam splitter IR instrument.[18]

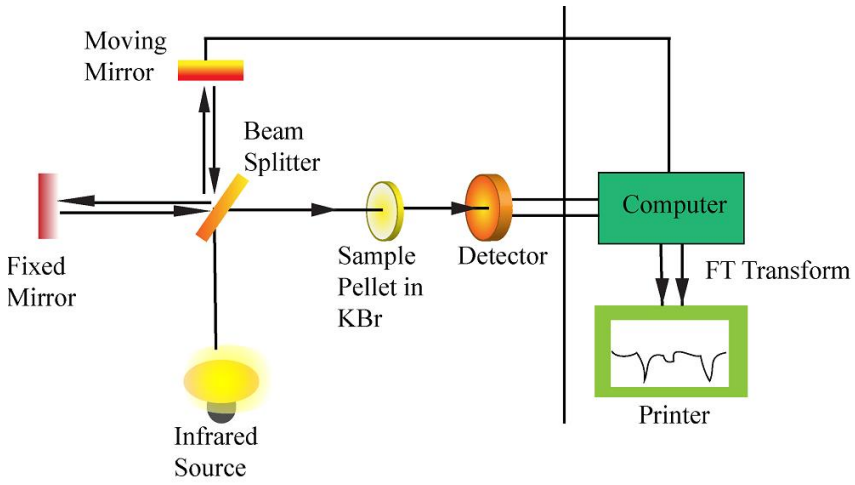

Figure 2.9. *Aschematic representation of the FT-IR instrument.*

In present study, we have employed TENSOR 27 FT-IR instrument and Opus software for IR analysis. The sample for analysis was prepared using the KBr pellet. In KBr powder, a small amount of the catalyst sample was mixed and grinded well to obtain a homogenous distribution followed by preparation of the pellet. The prepared pellet was projected to the instrument and the obtained data was analyzed using the literature values.

2.2.7. Surface Area Measurements and Pore Size Distribution Analysis: When a gas or vapor phase of a material is exposed to a solid, a part of the gas or vapor is taken up and remains attached over the surface of the solid. In the physisorption process, a weak Van der Waals interaction between the adsorbate and the solid surface takes place. The technique is useful to characterize the porous materials for determining the specific surface area, pore size distribution and pore volume. Very useful information can be obtained using the adsorption isotherms.[19]

Adsorption isotherm of various types discloses the nature of the material, *i.e.*, distribution of the pores in the material and interaction of the solid surface with the gas phase (**Figure 2.10**). Different types of solid gas adsorption isotherms are listed below[20]:

Type I: This type of curve is noted for the materials exclusively made up of micropores. The exposed surface resides inside the micropores, which after filling with adsorbate leaves no space for further adsorption.

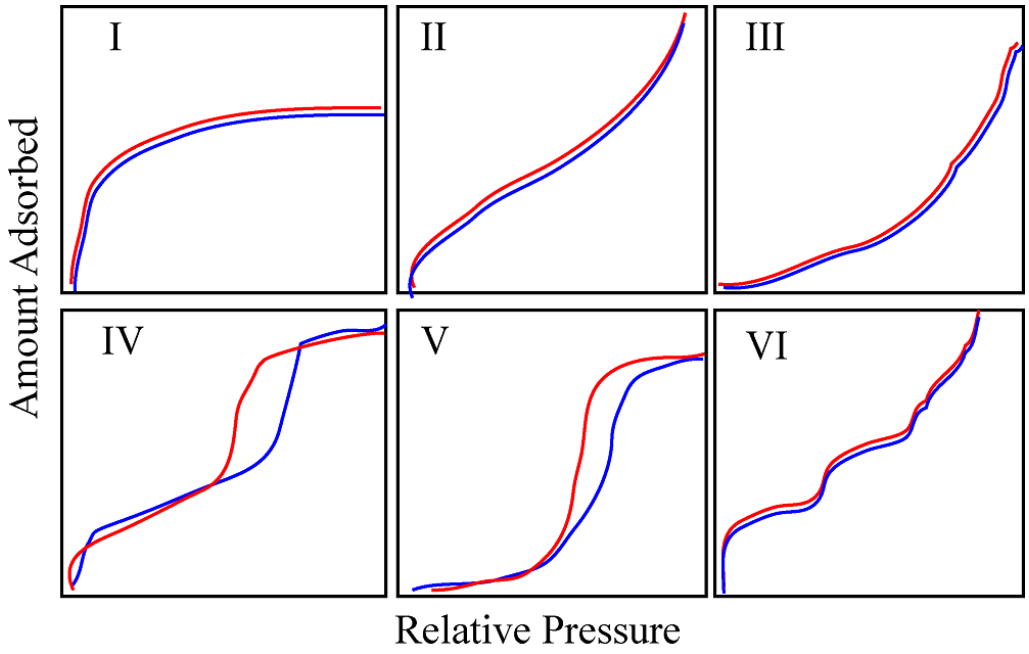

Figure 2.10. *Types of adsorption isotherms normally observed for the various solid materials.*

Type II: Most frequently found when adsorption happens over nanoporous materials (> 2 nm, pore size). In these, after adsorption of the monolayer, inflection point occurs and increase in gas pressure promotes further adsorption.

Type III: This type of curves characteristic found when heat of liquefaction of adsorbate is higher than adsorption energy. The adsorbate interacts with an adsorbed layer is greater than the interaction with the adsorbent surface and hence adsorption is facilitated after the first layer formation.

Type IV: This type of adsorption isotherm occurs with the adsorbents having pore size in the range 1.5-100 nm. Increasing the gas pressure slope shows increased uptake till first inflection point when monolayer is formed.

Type V: This type of isotherm is found when there are small adsorbate-adsorbent interaction potentials and also there is presence of pores with 1.5-100 nm range.

In the present study, a Quantachrome Quadrasorb automatic volumetric instrument has been used for the BET surface analysis. The measurements were performed at low-pressure gas adsorption method at 77 K using liquid ammonia as the cooling gas.

2.2.8. Thermogravimetric Analysis (TGA): Thermogravimetric analysis is a technique which discloses the changes taking in the sample when it is exposed to temperature. The tool gives clear idea about the structural changes in the metal oxides (*i.e.* phase change) and can reveal the transition temperature.[21] In case of the ceramics and polymeric samples, the glass transition temperature is highly desirable and TGA can provide convincing information for material synthesis. TGA can also be used to quantify the loss of water and other solvents in nanoparticles. It can quantify the metallic loading in composite materials and can give information on the ash content.

In our study, an SDTQ600 TG-DTA instrument was used for the TGA analysis. TGA analysis of the catalyst samples were performed in oxygen and nitrogen environments at a temperature ramp of 10 ^{o}C min^{-1}.

2.3. Electrochemical Measurements:

Electrochemical analysis involves several kinds of electrochemical methods. Of these, in the cyclic voltamogram (CV) and linear sweep voltamogram (LSV), the potential of the working electrode is varied and subsequently the change in the current is measured. In the case of the rotating disk electrode (RDE) and rotating ring disk electrode (RRDE) study, the working electrode is rotated and the current is measured as a function of the potential. Chronopotentiometry (CP) and chronoamperometry (CA) study provides the durability of the material in harsh condition.[22] Use of these electrochemical methods provides significant amount of knowledge about the electrode-electrolyte interface. These methods provide the information about the kinetics of the reaction, number of electron transfer involved in the electrode reaction, peroxide formation, stability of the catalyst in harsh environment, and real time characteristic of the energy devices. In our present study, all the electrochemical analysis have been done on a Bio-Logic (VMP3) using the three-electrode standard assembly. The three electrode setup consists of a working electrode (glassy carbon, 0.196 cm^2 geometrical surface area), a counter electrode (graphite rod), and a reference electrode (Hg/HgO) in alkaline medium. RDE and RRDE measurements were done over a Pine rotating electrode.

2.3.1. Cyclic Voltammetry (CV): In electrochemical analysis, cyclic voltametry is a primary experiment to be executed in order to rapidly analyzing the redox behavior of a elctro-

active species over a wide potential range. The method comprises sweeping the potential of the working electrode in a cycling manner for an unstirred electrolyte solution and subsequently measuring the change in the current. The potential of the working electrode is varied with respect to the reference electrode such as Hg/HgOor Ag/AgCl. For maintaining the current flow in the cell, a counter electrode is used. In the electrochemical study, the applied potential between the two electrodes is considered as the excitation signal. Similar to the other material characterization techniques, the excitation signal in the CV analysis is a linear potential variation against the reference electrode with a triangular waveform as in **Figure 2.12a**. Generally, the plot is represented in terms of voltage and current to analyze the redox couple present in the system (**Figure 2.12b**). As presented in **Figure 2.12b**, the reversible electrochemical process should possess the characteristics: 1) peak position unchanged with increasing the scan rate, 2) the ratio of the cathodic and anodic peak area should be one and 3) the peak current should be proportional to the square root of the scan rate (V s^{-1}). The relation between the peak current and the scan rate can be established using the Randles-Sevcik equation[23]:

$$i_p = 269n^{3/2}AD^{1/2}\nu^{1/2}C_b$$

where, i_p is the peak current, n is the number of electrons involved, A is the area, D is the diffusion coefficient, ν is the scan rate and C_b is the bulk concentration of the analyte.

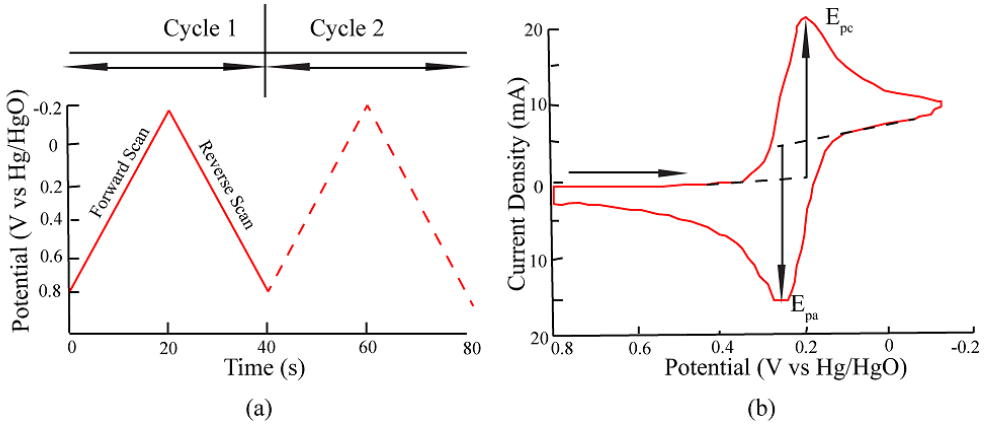

Figure 2.12. *a) Schematic representation of the cyclic voltamogram plotted between potential and time and b) schematic representation of the cyclic voltamogram plotted between current density and potential.*

2.3.2. Linear Sweep Voltammetry (LSV): In LSV, the potential is varied between the working electrode with a constant sweep rate and the current over the working electrode is measured. In typical LSV, the oxidation or reduction of a species is noted as trough in the current density at a particular potential region where the species starts to reduce or oxidize.

2.3.3. Chronopotentiometry (CP) and Chronoamperometry (CA):

Chronopotentiometry (CP) and chronoamperometry (CA) are very basic electrochemical techniques. In chronopotentiometry, a current step is applied across the electrochemical cell without stirring. On the other hand, in chronoamperometry the potential step is applied. In general, the chonopotentiometry is studied in batteries where the cell is discharged at a particular current density. The discharge of a battery at a particular current density provides a voltage at that current and increasing the current density decrease the battery voltage. The technique is also useful for the fuel cells and other faradic systems. Contrary, the chronoamperometry is useful to study the corrosion study of the electrode where electrodes are put at harsh potential and the resulting current is measured. The technique provides useful tool for the study of carbon corrosion in the OER process.

2.3.4. Rotating Disk Electrode (RDE): In electrochemistry, the reaction kinetics and mechanism is of prime importance and a rotating disk electrode (RDE) serves as a useful tool to study the Faradaic reactions. The RDE electrode consists of a glassy carbon disc encapsulated with the insulating Teflon, presented in **Figure 2.13**. The RDE is connected with the shaft of the rotator connected to the electric motor. The technique is useful in determining the reaction mechanism of the Faradaic reaction. Using the RDE technique, one can construct the Koutechy-Levich (K-L) plot. The K-L plot study discloses the diffusion and kinetic limitation of the catalyst. **Equation 1** represents the relation between the kinetic and the limiting current density.[24]

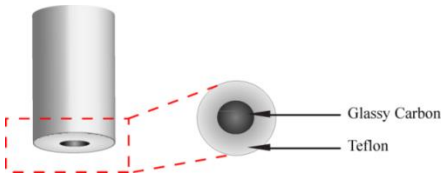

Figure 2.13. *Diagrammatic representation of the rotating disk electrode (RDE) vertically and horizontally.*

The Linear Sweep Voltamogram (LSV) of the catalyst includes contribution from diffusion-limiting (j_L) and kinetic (j_K) current density. **Equation 2** represents the more elaborated form of **Equation 1**.

$$\frac{1}{j} = \frac{1}{j_L} + \frac{1}{j_K} \quad \textbf{(1)}$$

$$\frac{1}{j} = 1/0.62nFC_o^* D_o^{2/3} v^{-1/6} \omega^{1/2} + 1/nFkC_o^* \quad \textbf{(2)}$$

where, 'j' represents the electrode current density, 'n' represents the electron transferred during ORR, 'C_o' represents the concentration of oxygen (1.22 x 10^{-6} mol/cm^3), 'D_o' denotes the diffusion coefficient of oxygen (1.93 x 10^{-5} cm^2/s), 'ν' denotes the kinematic viscosity of the electrolyte (0.01 cm^2/s), 'ω' is the angular rotation of the electrode in radians/sec ($\omega = 2\pi xrpm/60$) and 'k' is the rate constant. K-L plot gives the linear relation between 1/j and $1/\omega^{1/2}$. From the intercept of the plot, kinetic current density (j_K) can be calculated.[25]

2.3.5. Rotating Ring Disk Electrode (RRDE): The rotating ring disk electrode (RRDE) is an advanced technique and utilized to simultaneously detect the product formed in a reaction process. The structural architecture includes a glassy carbon disk in center, followed by Teflon separated ring electrode (**Figure 2.14**). In ORR analysis, the catalysts ink is coated over the RRDE electrode and the electrode is dried under an IR lamp. During the analysis, the ring potential is kept at a constant value of 0.60 V *vs* Hg/HgO and the disk electrode potential is swept at a scan rate of 10 mV/s**.** The study provides an estimation of the H_2O_2 % and the number of electron transfer for the faradaic reaction. For the calculation of H_2O_2 % and the number of electron transfer, **Equation 3** and **4** are used, respectively.[5]

$$\boldsymbol{HO_2^- = 200 \frac{I_r/N}{I_d + I_r/N}} \quad \textbf{(3)}$$

$$\boldsymbol{n = 4 \frac{I_d}{I_d + I_r/N}} \quad \textbf{(4)}$$

where,'I_d' denotes the disk current, 'I_r' denotes the ring current and 'N' denotes the collection efficiency of the ring electrode. The collection efficieny of the ring was determind to be 0.37 from $K_3Fe[CN]_6$.

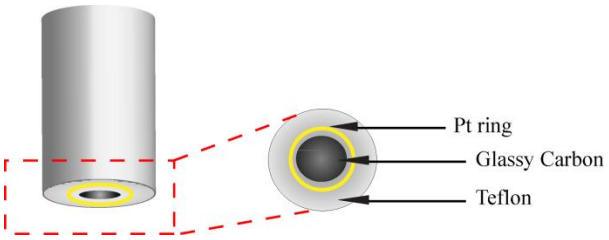

Figure 2.14. *Diagrammatic representation of the rotating ring disk electrode (RRDE) vertically and horizontally.*

2.3.6. Fabrication of Zinc-air Battery (ZAB):

A typical Zn-air battery involves two electrodes: 1) active metal zinc (anode) and 2) ORR catalyst layer (cathode). In our study, a zinc foil (0.5 mm width) has been used as the anode and a catalyst coated gas diffusion layer (GDL) has been employed as the air electrode.[26] In the study, 6 M KOH solution served as the electrolyte.[27] For the preparation of the air electrode, the catalyst was dispersed in the 3:2 water-IPA mixture followed by addition of the Fumion binder (40µl per 10 mg of the catalyst). The slurry was sonicated for 1 h and then coated over the GDL. The prepared air electrode was dried at 60 ºC for 12 h. The measurements were performed over the commercial split test cell (EQ-STC-MTI-Korea) and over the homemade battery setup. A schematic sketch of the Zn-Air battery testing setup is given in **Figure 2.15**.

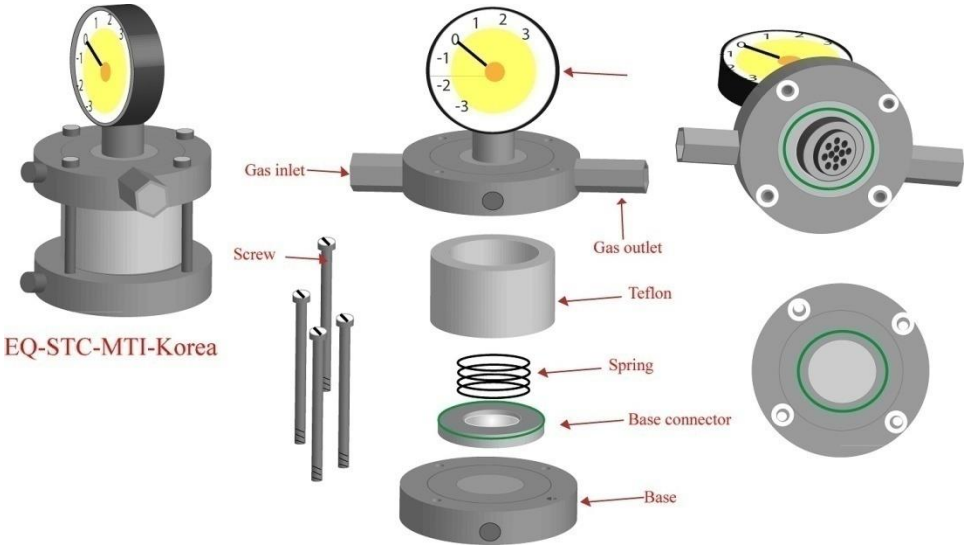

Figure 2.15. *Schematic representation of the Zn-Air battery testing setup.*

2.4. References:

(1) Marcano, D. C.; Kosynkin, D. V.; Berlin, J. M.; Sinitskii, A.; Sun, Z.; Slesarev, A.; Alemany, L. B.; Lu, W.; Tour, J. M., Improved Synthesis of Graphene Oxide. *ACS Nano* **2010,** *4*, 4806-4814.

(2) Guex, L. G.; Sacchi, B.; Peuvot, K. F.; Andersson, R. L.; Pourrahimi, A. M.; Ström, V.; Farris, S.; Olsson, R. T., Experimental Review: Chemical Reduction of Graphene Oxide (GO) to Reduced Graphene Oxide (rGO) by Aqueous Chemistry. *Nanoscale* **2017,** *9*, 9562-9571.

(3) Kashyap, V.; Singh, S. K.; Kurungot, S., Cobalt Ferrite Bearing Nitrogen-Doped Reduced Graphene Oxide Layers Spatially Separated with Microporous Carbon as Efficient Oxygen Reduction Electrocatalyst. *ACS Appl. Mater. Interfaces* **2016,** *8*, 20730-20740.

(4) Liang, Y.; Li, Y.; Wang, H.; Zhou, J.; Wang, J.; Regier, T.; Dai, H., Co_3O_4 Nanocrystals on Graphene as a Synergistic Catalyst for Oxygen Reduction Reaction. *Nat. Mater.* **2011,** *10*, 780-786.

(5) Liang, Y.; Wang, H.; Zhou, J.; Li, Y.; Wang, J.; Regier, T.; Dai, H., Covalent Hybrid of Spinel Manganese–Cobalt Oxide and Graphene as Advanced Oxygen Reduction Electrocatalysts. *J. Am. Chem. Soc.* **2012,** *134*, 3517-3523.

(6) Kashyap, V.; Kurungot, S., Zirconium-Substituted Cobalt Ferrite Nanoparticle Supported N-doped Reduced Graphene Oxide as an Efficient Bifunctional Electrocatalyst for Rechargeable Zn–Air Battery. *ACS Catal.* **2018,** *8*, 3715-3726.

(7) Ravishankar, N., Seeing is Believing: Electron Microscopy for Investigating Nanostructures. *J. Phys. Chem. Lett.* **2010,** *1*, 1212-1220.

(8) Tuggle, D. W.; Li, J. Z.; Swanson, L. W., Point Cathodes for Use in Virtual Source Electron optics. *Journal of Microscopy* **1985,** *140*, 293-301.

(9) Kanemaru, T.; Hirata, K.; Takasu, S.-i.; Isobe, S.-i.; Mizuki, K.; Mataka, S.; Nakamura, K.-i., A Fluorescence Scanning Electron Microscope. *Materials Today* **2010,** *12*, 18-23.

(10) Plemmons, D. A.; Suri, P. K.; Flannigan, D. J., Probing Structural and Electronic Dynamics with Ultrafast Electron Microscopy. *Chem. Mater.* **2015,** *27*, 3178-3192.

(11) Gregory, N. W., Standard X-Ray Diffraction Powder Patterns. *J. Am. Chem. Soc.* **1956,** *78*, 1264-1264.

(12) Elmanov, G.; Dzhumaev, P.; Ivanitskaya, E.; Skrytnyi, V.; Ruslanov, A., Influence of the chemical composition of rapidly quenched amorphous alloys (Ni, Fe, Cr)-B-Si on its

crystallization process. *IOP Conference Series: Materials Science and Engineering* **2016,** *130*, 012041.

(13) Jr., W. F. E., A New Tool for Studying Epitaxy and Interfaces: The XPS Searchlight Effect. *Journal of Vacuum Science & Technology A* **1985,** *3*, 1511-1513.

(14) Seah, M. P., Measurement: AES and XPS. *Journal of Vacuum Science & Technology A* **1985,** *3*, 1330-1337.

(15) Michaelson, H. B., The Work Function of the Elements and its Periodicity. *J. Appl. Phys.* **1977,***48*, 4729-4733.

(16) Bumbrah, G. S.; Sharma, R. M., Raman Spectroscopy – Basic Principle, Instrumentation and Selected Applications for the Characterization of Drugs of Abuse. *Egyptian Journal of Forensic Sciences* **2016,** *6*, 209-215.

(17) Pimentel, G. C., Infrared Spectroscopy: A Chemist's Tool. *Journal of Chemical Education* **1960,** *37*, 651.

(18) Ismail, A. A.; van de Voort, F. R.; Sedman, J., Chapter 4 Fourier Transform Infrared Spectroscopy: Principles and Applications. In *Techniques and Instrumentation in Analytical Chemistry*, Paré, J. R. J.; Bélanger, J. M. R., Eds. Elsevier: **1997**, pp 93-139.

(19) Foo, K. Y.; Hameed, B. H., Insights into the Modeling of Adsorption Isotherm Systems. *Chemical Engineering Journal* **2010,** *156*, 2-10.

(20) Sonwane, C. G.; Bhatia, S. K., Characterization of Pore Size Distributions of Mesoporous Materials from Adsorption Isotherms. *J. Phys. Chem. B* **2000,** *104*, 9099-9110.

(21) Pang, L. S. K.; Saxby, J. D.; Chatfield, S. P., Thermogravimetric Analysis of Carbon Nanotubes and Nanoparticles. *J. Phys. Chem.***1993,** *97*, 6941-6942.

(22) Spencer, J. F., Electrochemistry and Electrochemical Analysis. Vol. II. By H. J. S. Sand. *J. Phys. Chem.* **1940,** *44*, 1011-1012.

(23) Zahn, R.; Coullerez, G.; Vörös, J.; Zambelli, T., Effect of Polyelectrolyte Interdiffusion on Electron Transport in Redox-active Polyelectrolyte Multilayers. *J. Mater. Chem.* **2012,** *22*, 11073-11078.

(24) Balan, B. K.; Kurungot, S., Highly Exposed and Activity Modulated Sandwich Type Pt Thin Layer Catalyst with Enhanced Utilization. *J. Mater. Chem.* **2011,** *21*, 19039-19048.

(25) Balan, B. K.; Manissery, A. P.; Chaudhari, H. D.; Kharul, U. K.; Kurungot, S., Polybenzimidazole Mediated N-doping Along the Inner and Outer Surfaces of a Carbon Nanofiber and its Oxygen Reduction Properties. *J. Mater. Chem.* **2012,** *22*, 23668-23679.

(26) Prabu, M.; Ramakrishnan, P.; Nara, H.; Momma, T.; Osaka, T.; Shanmugam, S., Zinc–Air Battery: Understanding the Structure and Morphology Changes of Graphene-Supported $CoMn_2O_4$ Bifunctional Catalysts Under Practical Rechargeable Conditions. *ACS Appl. Mater. Interfaces* **2014,** *6*, 16545-16555.

(27) Lee, J.-S.; Park, G. S.; Lee, H. I.; Kim, S. T.; Cao, R.; Liu, M.; Cho, J., Ketjenblack Carbon Supported Amorphous Manganese Oxides Nanowires as Highly Efficient Electrocatalyst for Oxygen Reduction Reaction in Alkaline Solutions. *Nano Lett.* **2011,** *11*, 5362-5366.

Chapter 3

Size Optimized Cobalt Ferrite Nanoparticle Supported N-doped Reduced Graphene Oxide as an Efficient Oxygen Reduction Catalyst for Primary Zinc-air Battery

The present chapter discloses how high quality dispersion of fine particles of cobalt ferrite (CF) could be attained on nitrogen doped reduced graphene oxide (CF/N-rGO) and how this material in association with a microporous carbon phase could deliver significantly enhanced activity towards electrochemical oxygen reduction reaction (ORR). Our study indicates that the microporous carbon phase plays a critical role in spatially separating the layers of CF/N-rGO and in creating a favorable atmosphere to ensure the seamless distribution of the reactants to the active sites located on CF/N-rGO. In terms of the ORR current density, the heat-treated hybrid catalyst at 150 ºC (CF/N-rGO-150) is found to be clearly outperforming (7.4±0.5 mA/cm^2) the state-of-the-art 20 wt.% Pt supported carbon catalyst (PtC) (5.4±0.5 mA/cm^2). The mass activity and stability of CF-N-rGO-150 are distinctly superior to PtC even after 5000 electrochemical cycles. As a realistic system level exploration of the catalyst, testing of a primary zinc-air battery could be demonstrated using CF/N-rGO-150 as the cathode catalyst. The battery is giving a galvanostatic discharge time of 15 h at a discharge current density of 20 mA/cm^{2}and a specific capacity of ~630 mAh g^{-1}in 6 M KOH by using a Zn foil as the anode. Distinctly, the battery performance of this system is found to be superior to that of Pt/C in less concentrated KOH solution as the electrolyte.

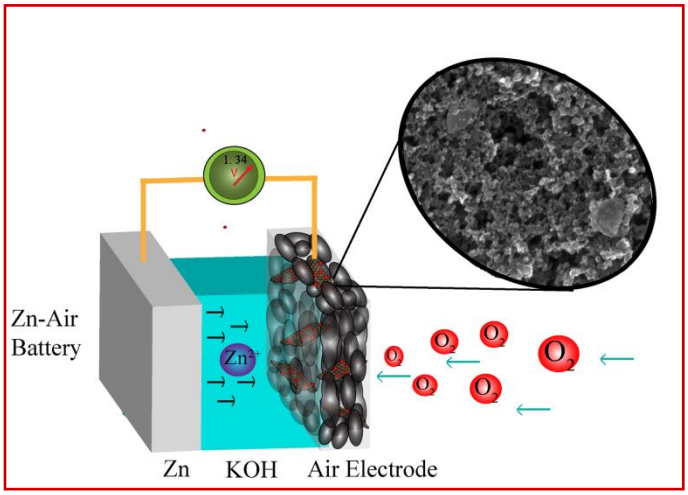

*The content of this chapter is published in "*ACS Appl. Mater. Interfaces* **2016,** 8, 20730-20740."
-Reproduced with permission from (*ACS Appl. Mater. Interfaces* **2016,** 8, 20730-20740). Copyright (2016) American Chemical Society.

3.1. Introduction

Energy generation and storage systems such as lithium ion batteries[1], supercapacitors[2], fuel cells[3] and metal-air batteries[4-5] have created diverse scientific and technological interest as clean substitutes for the traditional energy resources. In order to ensure penetrability of such systems in the energy market, which is already a highly competitive sector, it is important that these devices should be active and cost effective. Since electrodes of many of these systems are the major cost contributing components, in recent days, a significant level of attention has been given to develop economically more viable alternatives of the state-of-the-art systems. For example, the electrocatalysts for oxygen reduction reaction (ORR), which are the essential electrode components for the construction of polymer electrolyte membrane fuel cells (PEMFCs) and metal-air batteries, significantly contribute towards the system costs because of the utilization of the expensive Pt.[6-8]

Among the viable and cost-effective alternatives to Pt for ORR, the first row transition metals are being widely explored because of their intrinsically promising ORR activities and easy availability. Of these, the transition metal based spinel metal oxides exhibit interesting electrocatalytic activities, including towards ORR.[9] The spinel oxides are a class of compounds of the general formula AB_2O_4 (where, A and B are metals), belonging to *Fd3m*space group.[10] The cubic unit cell contains 56 atoms; the 8 tetrahedral sites are occupied by the "A" metal and the 16 octahedral sites by the "B" metal.[10] Even though the spinel oxides are generally insulating in nature, the presence of defects and phase separation help to increase the number of charge carriers in the conduction band with a concomitant reduction in the resistivity.[9] Furthermore, these spinel oxides are generally supported on conducting supports to improve the overall conductivity of the catalyst.[7]The ORR activities over the surface of the hybrid catalysts have been extensively explored at experimental and theoretical levels in various reports.[11-13] Electrocatalytic activities of hybrid Co_3O_4 and $MnCo_2O_4$ on nitrogen doped graphene have been reported by Dai *et al.*[14-15] The $CuCo_2O_4$nanoparticles supported on nitrogen doped reduced graphene oxide have been reported to be showing good ORR activity in alkaline media.[16] Spinel oxide-carbon nanotube hybrids are also known to exhibit remarkable ORR activities.[17-18] Again, Sun *et al.* have recently reported the electrocatalytic activity exhibited by monodispersed magnetite nanoparticles formed on a conducting support through an *ex-situ* mixing

process.[19]This report claims that a physical mixture of magnetite nanoparticles with carbon after annealing is capable of outperforming PtC for ORR. Monzonet *et al*. have reported amplification of the catalytic activity under the magnetic field, and the activity enhancement is credited to the magnetohydrodynamic (MHD) phenomena.[20]

From the above discussion on the exploration of the spinel structured oxides for ORR applications, it is clear that the oxides of cobalt and iron, which are having mixed vacancies, are capable of displaying interesting catalytic activity characteristics to position as versatile non-precious ORR catalysts. However, the intrinsic activities of these types of systems are found to be largely depending on other parameters such as particle size, morphology and how well the catalyst particles are dispersed on a conducting substrate. Considering this close relation and controlled interplay of these parameters in tuning the performance characteristics of the ferrite materials as electrocatalysts, we thought of exploring how the ORR performance of $CoFe_2O_4$ particles will be tuned if it is dispersed on a heteroatom doped graphene surface. Of the heteroatom doped graphene systems, nitrogen doped graphene (NGr) is in the limelight due to its intrinsically high ORR activity and electrical conductivity.[12, 21] Along with this, the nitrogen doping is found to be slightly buckling the graphene layers, and this morphological alteration can be utilized as an effective means to accomplish anchoring of nanoparticles on the surface.[22-23] Taking into account of all these favorable conditions, we prepared a nanohybird of $CoFe_2O_4$ nanoparticles dispersed on N-rGO (CF/N-rGO) through a solvothermal process. The approach helped to provide fine distribution of the $CoFe_2O_4$ nanoparticles homogeneously on the N-rGO surface without any indication of particle aggregation, thanks to the rich anchoring sites provided by the doped nitrogen and the carbon vacancies created by the buckling of the graphene layers. The heat treated CF/N-rGO at 150 ^oC (CF/N-rGO-150) in association with a microporous carbon phase (Vulcan XC-72)[24] is found to be bringing in a healthy synergistic interaction, leading to excellent ORR activity and high performance as an electrocatalyst in a Zn-air battery system. The work presented in this chapter is a focused effort to understand how the various factors are working in tandem in this multi component system to position this as a potential ORR catalyst with some clear edges over PtC in its performance, especially in terms of the high achievable current density, mass activity and electrochemical durability.

3.2. Experimental Section

3.2.1. Synthesis of Cobalt Ferrite Supported Nitrogen Doped Reduced Graphene Oxide (CF/N-rGO and CF/N-rGO-150): Prior to CF/N-rGO synthesis, CF nanoparticles with different size distributions were synthesized by varying the water to ethanol percentage. The water percentages of 0, 50 and 66 were used for the compositional variation by considering the effect of water to ethanol composition on the particle size based on the phase diagram of the components.[27] With increasing the water percentage, the vapor pressure in the hydrothermal bomb changes and this allows the low temperature thermal decomposition of the acetate salts for effective formation of the spinel metal oxide nanopartilces. The water to ethanol ratio of 50:50 was found to be the optimum composition leading to CF/N-rGO with the desired electrochemical activity. Considering this, in a typical synthesis of CF/N-rGO, 50 mg of N-rGO was dispersed in 25 mL of DI water. This solution was mixed with 50 mg of iron acetate ($Fe(C_2H_3O_2)_2$) and cobalt acetate ($Co(C_2H_3O_2)_2$) in the molar ratio of 2:1. Subsequently, ethanol was added to make the volume up to 50 mL. The mixture was kept on stirring at room temperature for 24 h so that the Co^{2+} and Fe^{2+} ions get coordinated with the nitrogen and the oxy functional groups on the graphene surface. Subsequently, the solution was transferred into a 100 mL Teflon coated stainless steel autoclave and this was kept in an oven at 130 ^oC for 12 h. Thus obtained solution was filtered and washed several times, followed by drying at 60 ^oC. The product is designated as CF/N-rGO. A portion of the sample was heat treated at 150 ^oC for 12 h in order to induce better crystallization of the spinel phase. This sample is designated as CF/N-rGO-150. Similarly, CF/N-rGO-600 was prepared by annealing the sample in Ar environment at 600 ^oC for 4 h. For the comparison purpose, we have also prepared two Vulcan based CF catalysts, where one is the *in-situ* grown CF nanoparticles over the Vulcan carbon (CF/Vulcan*) and the other one is a physical mixture of CF nanoparticles and the Vulcan carbon (CF-Vulcan).

3.2.2. Primary Zn-air Battery Testing: For the Zn-air battery (ZAB) testing, a polished Zn foil was used as the active anode material. Air electrode with a geometrical surface area of 1 cm^2 was made by maintaining a catalyst loading of 1.2 mg/cm^2. 1 M and 6 M KOH solutions were served as the electrolytes during the battery testing.

3.3. Result and Discussion

The methodology followed for the synthesis of CF/N-rGO-150 is illustrated in **Figure 3.1**, which shows the steps involved in the preparation of the active catalyst, followed by the realistic validation of the material by using it as the cathode catalyst in a ZAB. Homogeneous and size-controlled distribution of the CF nanoparticles on the graphene surface could be accomplished through the solvothermal synthesis process as described in the experimental section. It is important to note that the water/ethanol solvent composition plays a critical role in controlling the growth of the nanocrystalline spinel oxide particles.

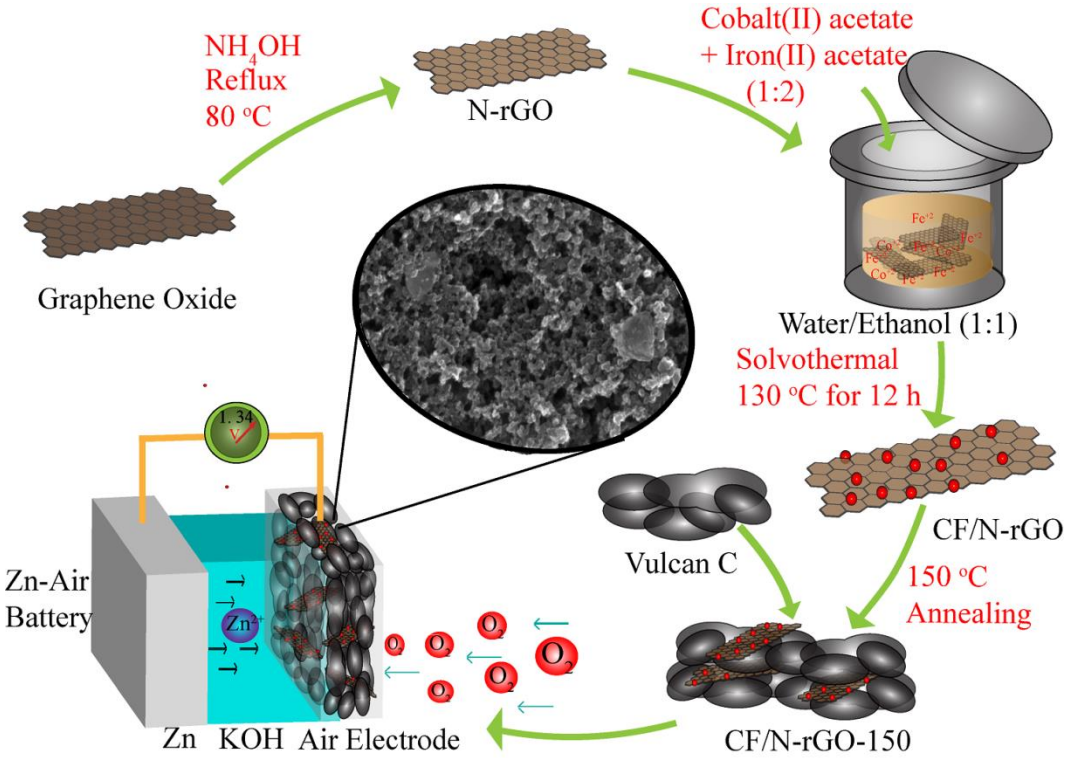

***Figure 3.1**: Schematic illustration of the strategies involved in the preparation of the active catalyst and demonstration of its application by using as an air electrode in Zn-air battery.*

3.3.1. TEM Analysis: Prior to the hydrothermal experiments focused on the dispersion of CF on N-rGO, the influence of the compositional variation of water and ethanol in the hydrothermal condition on the morphology and particle size distribution of CF has been investigated by changing the water content as 0, 50 and 66% in the system. The corresponding TEM images along with the SAED patterns (inset) are presented in **Figure 1a, 1b** and **1c** and the particle size distribution profiles in **Figure 1e, 1f and 1g**.[28-29] The SAED patterns of the CF

nanoparticles presented in **Figure 1** show the presence of diffused ring patterns in the case of the particles prepared up to a water content of 50% (*i.e.*, up to an ethanol/water ratio of 1:1).

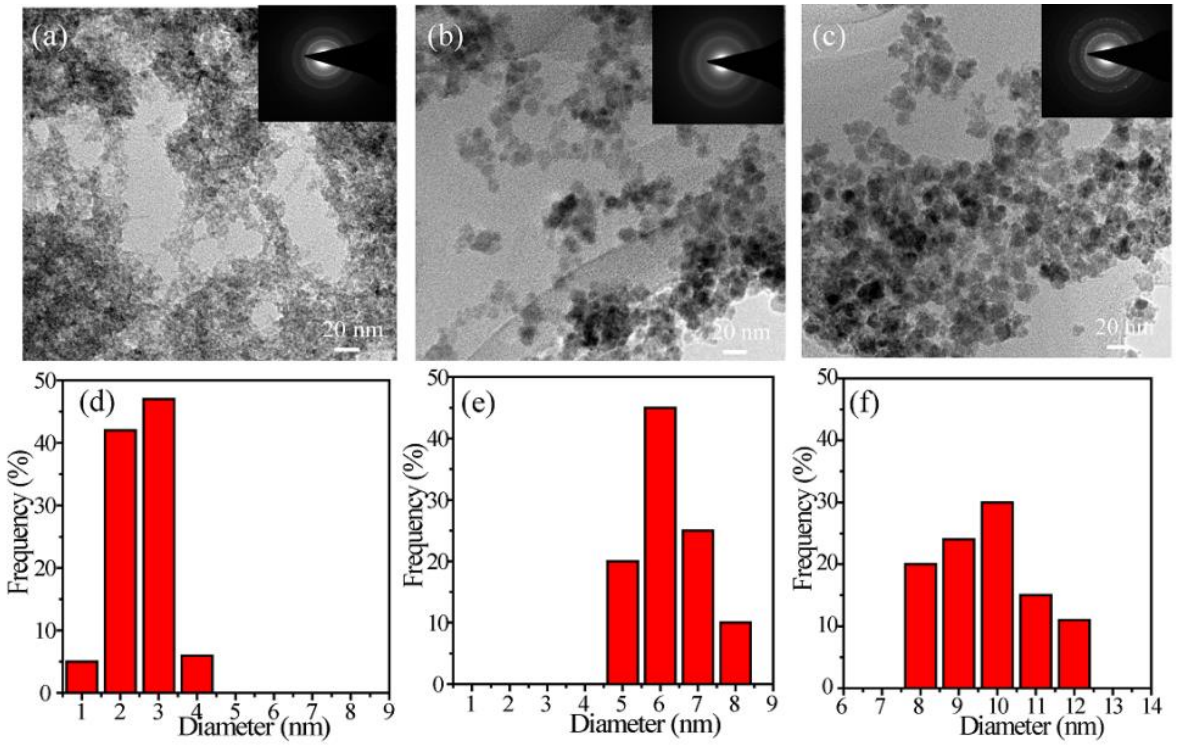

Figure 3.2. *(a), (b) and (c) are the TEM images of the unsupported cobalt ferrite (CF) nanoparticles synthesized under the water contents of 0, 50 and 66%, respectively, in ethanol. The corresponding diffraction patterns are presented in the insets of the respective images. (d), (e) and (f) represent the particle size histograms of CF nanopartilces prepared under the water contents of 0, 50 and 66%, respectively, in ethanol.*

The size of the CF nanoparticles is found to be increased as the water content in the system increases. The particle size distribution profiles presented in **Figure 1** clearly show that the average particle size distributions in the samples change as 1-4 nm, 5-8 nm and 8-12 nm when the water content in the hydrothermal bomb changes as 0, 50 and 66%, respectively. The change in the particle size with the water to ethanol composition is related to the phase diagram of the components.[27] A pre-screening of the catalysts towards ORR indicates that the 50% water to ethanol composition has shown superior ORR activity as reflected from the cyclic voltammogram and LSV presented in the section dealing with the electrochemical data **(Figure 3.11)**. Based on this pre-screening study, the 50% water composition, where particle size is ~5-6 nm has been taken as the standard condition in the experiments meant for decorating CF on N-

rGO in the hydrothermal bomb. **Figure 3.3a, 3.3b** and **3.3c** correspond to the TEM images of the CF nanoparticles decorated on N-rGO (CF/N-rGO-150, where the digit 150 indicates the heat treatment temperature), which was prepared under the same hydrothermal condition by using N-rGO as the conducting support in the system.

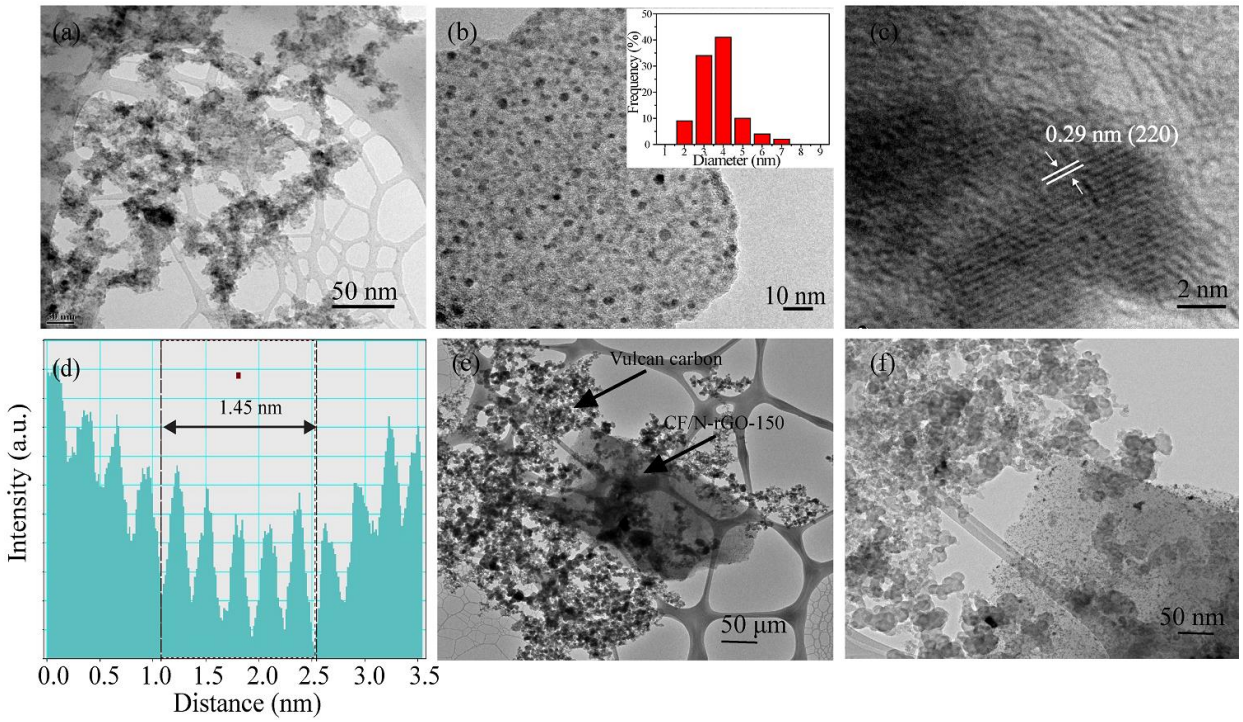

Figure 3.3. *(a)and (b) are the TEM images showing the homogenous distribution of the cobalt ferrite nanocrystals over the nitrogen-doped reduced graphene oxide (CF/N-rGO-150); the corresponding particle size distribution profile is presented in the inset of Figure b. (c) HR-TEM image at higher magnification elucidating the (220) plane of the CF nanocrystal with a d-spacing of 0.29 nm. Line profile of the CF nanocrystal indicating the 0.29 nm fringe width corresponding to the (220) plane of CF is shown in (d). TEM images of CF/N-rGO-150-Vulcan are presented in (e) and (f). CF/N-rGO-150 appears as distinct carbon phase with cobalt ferrite nanoparticles evenly distributed on the surface.*

The TEM images of CF/N-rGO-150 represent highly homogenous distribution the CF nanoparticles without any indication of particle aggregation or extended growth. The CF particles having size in the range of 2-5 nm are uniformly distributed on the N-rGO surface and the corresponding particle size histogram is presented in the inset of **Figure 3.3b**. The controlled particle size as well as the uniform distribution of the CF nanoparticles are originated from the fertile environment offered by the synthetic methodology and the effective interaction

established between the N-rGO framework and the CF nanoparticles. **Figure 3.3c** represents the high resolution TEM (HR-TEM) image of CF/N-rGO-150, from which the d-spacing of the CF nanoparticles is estimated to be 0.29 nm. This d-spacing value is corresponding to the (220) plane of the cobalt ferrite phase.[30] To validate the obtained fringe width from the HR-TEM data, line profile analysis has also been carried out as shown in **Figure 3.3d**. The fringe width value calculated here matches perfectly with the previous calculated value of 0.29 nm. Further, the TEM images corresponding to the active catalyst CF/N-rGO-150-Vulcan are presented in **Figure 3.3e** and **3.3f**. The sheet bearing the cobalt ferrite nanoparticles appears as a distinct carbon phase in comparison to the Vulcan carbon.

3.3.2. XRD Analysis: A clear understanding on the nature of the spinel phase of CF and the CF/N-rGO systems has been obtained from the XRD analysis of the samples.

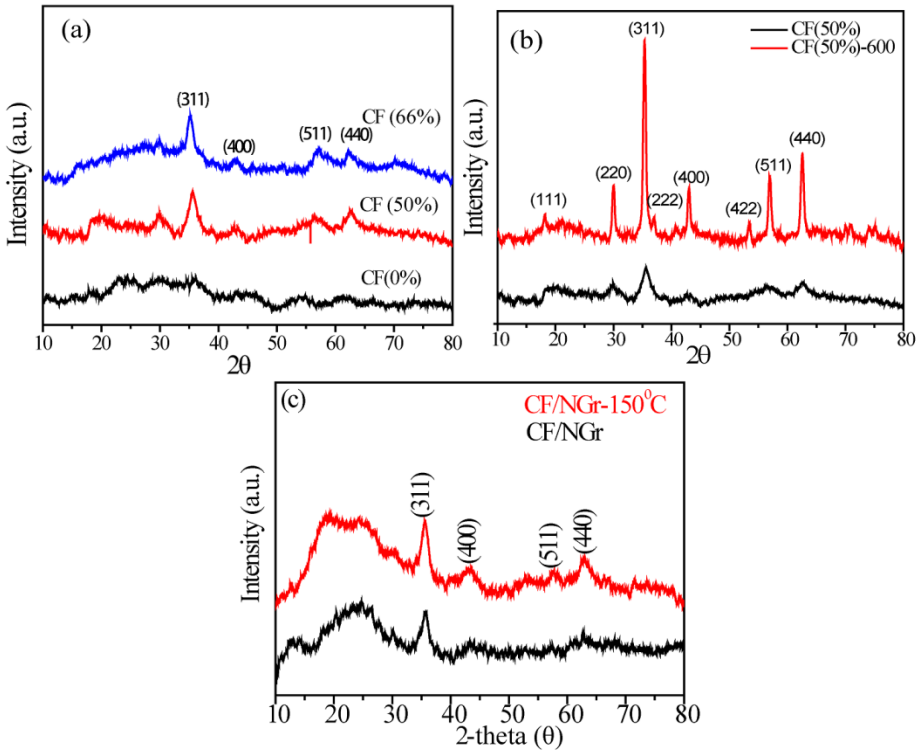

Figure 3.4.*(a) X-ray diffractograms of the unsupported CF nanoparticles synthesized under various water to ethanol ratios by the solvothermal method; (b) X-ray diffratogram of CF (50%) after 600 °C annealing for 4 hours; (c) X-ray diffraction patterns of CF/N-rGO and CF/N-rGO-150.*

The XRD profiles of the unsupported CF samples synthesized under various water to ethanol ratios are presented in **Figure 3.4a**. The intensity of the peaks corresponding to the spinel phase is found to be increased with increasing the water percentage, which clearly demonstrates the critical role played by water in controlling the growth kinetics of the CF nanoparticles. As can be seen from the **Figure 3.4a**, the 50% water composition has helped to generate the material possessing the well-developed spinel phases of the cobalt ferrite. In order to confirm the phase purity and spinel nature of the nanoparticles, CF (50%) was annealed at 600 ^{o}C for 4 h (**Figure 3.4b**). The increased intensity of spinel phase clearly justifies the phase and temperature effect over particles. Subsequently, a comparison of the XRD profiles of the graphene supported samples, *i.e*., CF/N-rGO and CF/N-rGO-150, is made and the corresponding diffractograms are presented in **Figure 3.4c**. The diffraction peaks obtained at the 2θ values of 30.1, 35.5, 43.1, 57.1 and 62.6^{o} are corresponding to the (220), (311), (400), (511) and (440) planes, respectively, of the cobalt ferrite system **(JCPDS 22-1086).** These results explicitly indicate that the spinel phase of the CF nanoparticles appeared under the unsupported condition could be successfully retained even in the supported state, all the while maintaining the dispersion substantially high and particle size well within 5 nm. Compared to the peak intensities of the as synthesized CF/N-rGO, the characteristic peaks of the spinel phase in CF/N-rGO-150 are found to be well resolved with increased intensity. This indicates that compared to the unsupported case, a favorable structural modulation of the nanoparticles in the N-rGO supported case happens at slightly elevated temperature. Most probably, the hydroxyl and other oxygen containing functional groups on the reduced graphene oxide surface might have given more hydroxide characteristics to the CF nanoparticles anchored on the N-rGO surface in the beginning and the heat treatment at 150 ^{o}C might have helped to bring in more crystallinity to the system. Hence, 150 ^{o}C has been taken as the standard drying condition for the supported system. Apart from the peaks corresponding to the cobalt ferrite phases, the XRD profiles in **Figure 3.4c** indicate abroad peak at a 2θ value of 25.4^{o} corresponding to the (002) graphitic plane of N-rGO.

3.3.3. TGA: The hydrothermal experiment was carried out with a targeted CF loading of 40% on the N-rGO surface. The TGA spectrum recorded under air atmosphere **(Figure 3.5)** shows two prominent weight loss regions. The initial distinct weight loss up to 150 ^{o}C might be caused

by the removal of the adsorbed water molecules and the surface functional groups hosted by the rGO surface. At 150 ^{o}C, the removal of these moieties appeared to be completed.

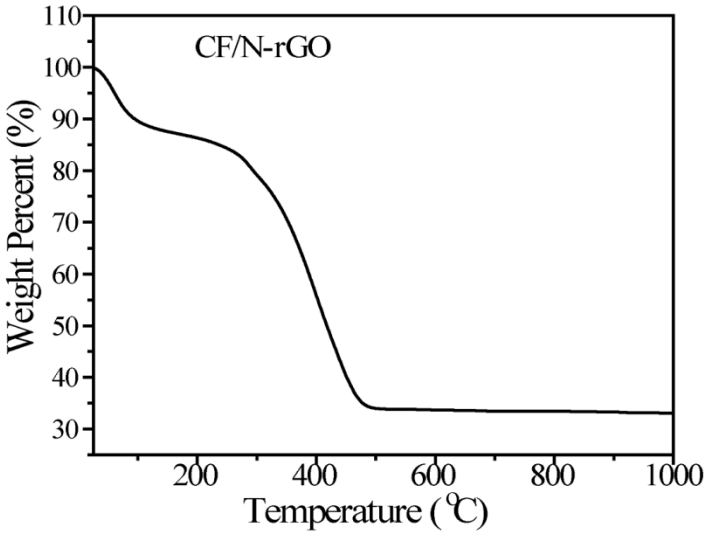

Figure 3.5. *TGA profile of CF/N-rGO recorded under air media indicating a residue content of 35%, which is corresponding to the amount of CF accommodated by N-rGO.*

A furthermore prominent weight loss region begins at 300 ^{o}C, which is ascribed to the burning of carbon in the graphite substrate. The oxidation of the carbon completes at around 500 ^{o}C, leaving a residue content of ~ 34% corresponding to the amount of CF accommodated on the N-rGO surface. Actually, the heat treatment temperature of 150 ^{o}C maintained for the preparation of CF/N-rGO-150 was fixed based on the observation in the TGA profile that the coordinated water molecules and functional groups on the rGO surface leave the system at this temperature.

3.3.4. Pore Size Distribution and BET Analysis: The pore size distribution profiles and BET isotherms are presented **Figure 3.6a** and **3.6b,** respectively. The pore size distribution profile corresponding in CF/N-rGO-150 reveals the presence of mesopores (2.5 to 6 nm) in the system, with apparently no indication of microporosity. Microporosity is an important parameter of a catalyst system in deciding the healthy utilization of the active sites by their interactions with the reactants.[31-32] Vulcan carbon contains more micropores and the microporosity is derived from the defects in the graphitic system.[33] Micropores are responsible for defect sites and these defect sites can contribute towards ORR. They also help to attain better dispersion of the

reactants within the system. Also, micropores make surface unsaturation, which in turn can help to improve the wettability of the catalyst surface.

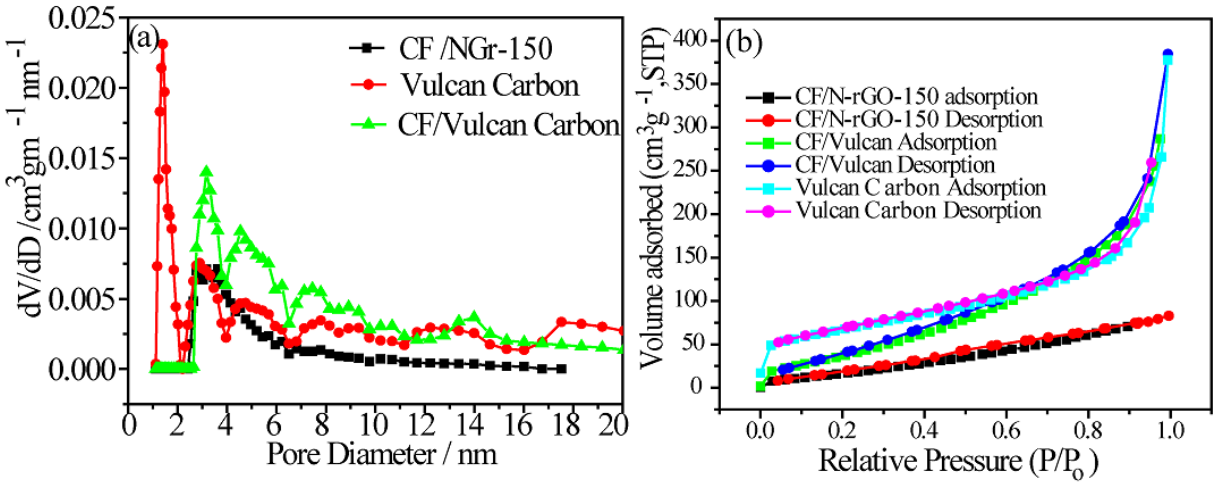

Figure 3.6. *(a) The comparative pore size distribution profiles of Vulcan carbon, CF/Vulcan*, CF/N-rGO-150 and CF/N-rGO-150-Vulcan; (b) BET isotherms of the different samples.*

All these factors work in tandem and subsequently the system attains a position to deliver improved performance characteristics.[34] As can be seen in the later sections, an important finding of this study is about the critical role played by the Vulcan carbon in spatially separating the layers of CF/N-rGO and in creating a favorable atmosphere to ensure the seamless distribution of the reactants to the active sites located on CF/N-rGO with the help of the rich micropores present on this additive. **Figure 3.6a** clearly indicates that Vulcan carbon retains good micro and mesoporous characteristics. However, the direct dispersion of the CF nanoparticles on Vulcan carbon (CF/Vulcan*) by the solvothermal process is essentially blocking the intrinsic microporosity associated with the system, which can eventually lead to the issues related to the reactant distribution towards the active sites. The data presented in **Figure 3.6a** for catalyst CF/N-rGO-150-vulcan shows the presence of micro and meso pores in the system. A high intense peak for less than 2 nm pore size corresponding to 80 wt. % Vulcan carbon and low intense peak for mesoporous CF/N-rGO-150 is present. Hence, by using Vulcan carbon as a phase to spatially separate the layer of CF/N-rGO, we have noticed a healthy synergistic interaction due to the coexistence of the phases leading to a significantly modulated performance characteristic. These aspects are highlighted in the section dealing with the activity characteristic

of the materials. The BET surface areas of CF/N-rGO-150, CF/N-rGO-150-Vulcan and CF/Vulcan* (cobalt ferrite nanoparticles *in-situ* grown over Vulcan carbon) are 77, 187 and 163 m^2/g, respectively.

3.3.5. XPS Analysis: A more insightful information on the surface chemical composition, nature of the nitrogen doping and the oxidation states of Co and Fe ions are confirmed by XPS analysis of CF/N-rGO-150. The corresponding spectral data are presented in **Figure 3.7**. The survey spectrum as given in **Figure 3.7a** displays the presence of Co 2p, Fe 2p, O 1s, N 1s and C 1s peaks at the binding energies (B.E.) of 784.16, 714.71, 533.01 , 399.13 and 284.10 eV, respectively.[35-37] In addition to this, 3s and 3p peaks for cobalt and iron also appear at lower binding energy region, which is highlighted as the inset of **Figure 3.7a**.[38] The percentage of nitrogen in the parent N-rGO was calculated prior to its employment as a substrate in the solvothermal process and the estimated value was 8.4 at.%. However, estimation from the XPS analysis of CF-N-rGO-150 indicates that the nitrogen content has been reduced to 5.0 at.% subsequent to the solvothermal process. The de-convoluted N 1s spectra presented in **Figure 3.7b** display two peaks at 398.10 and 400.20 eV, which are the signature peaks of the pyridinic and pyrrolic nitrogens, respectively.[39-40]

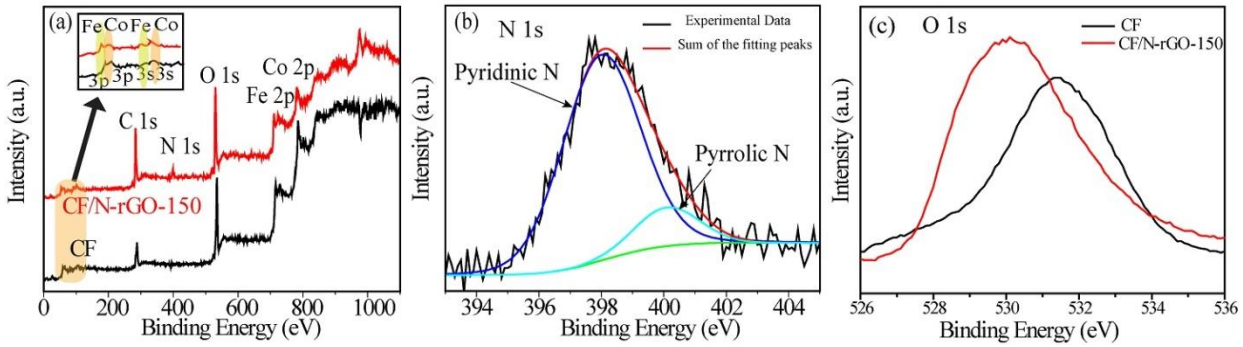

Figure 3.7. *(a) XPS survey spectra of CF/N-rGO-150and CF, where the presence of the N 1s peak can be clearly seen in CF/N-rGO-150; 3s and 3p peak for cobalt and iron is presented in inset. (b) and (d) represent the deconvoluted XPS spectra of N 1sand O 1s, respectively.*

To scrutinize the changes incurred after anchoring the CF nanoparticles on N-rGO, the O 1s spectra of CF and CF/N-rGO-150 are compared **(Figure 3.7c)**, where a negative shift in the O 1s spectra corresponding to a B.E value of 1.5 eV is detected between the two samples. This shift in B.E. substantiates the effective interaction between the supported carbon and the CF

nanoparticles. Furthermore, an analysis of the peaks corresponding to Co $2p_{3/2}$, Co $2p_{1/2}$, Fe $2p_{3/2}$ and Fe $2p_{1/2}$ in both CF and CF/N-rGO-150 confirms that cobalt as well as iron exist in +2 and +3 oxidation states. **Figure 3.8a**and **3.8b** represent the deconvoluted spectra of Co 2p and Fe 2p peaks, respectively, of CF/N-rGO-150. The corresponding deconvoluted spectra of CF are presented **Figure 3.8c** and **Figure 3.8d**, respectively.

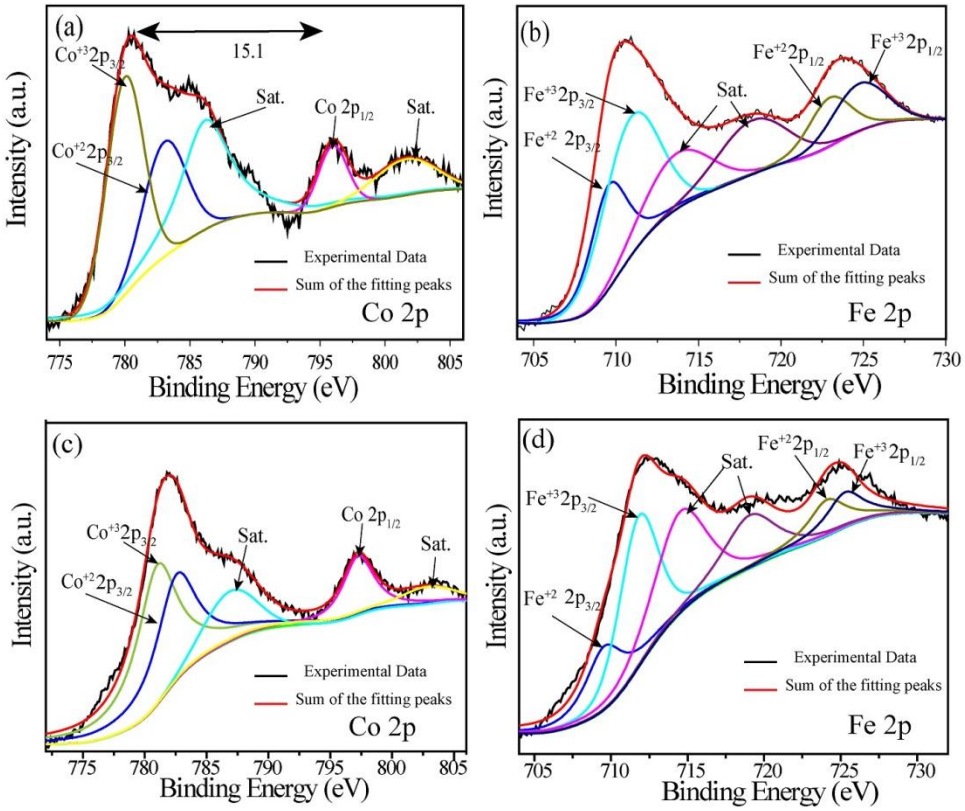

Figure 3.8. *(a) and (b) represent the deconvoluted XPS spectra of Co 2p peak, and Fe 2p, respectively in the CF/N-rGO-150 catalyst; (c) and (d) represent the deconvoluted 2p spectra of Co and Fe in CF.*

The two peaks with the B.E values of 780.09 and 783.20 eV in the case of the Co 2p spectra are equated to the +3 and +2 states of Co, respectively, in the supported systems, whereas, the corresponding peaks appear at 781.23 and 782.7 eV in the case of the unsupported system.[36-37, 41] The observed discrepancy in the Co spectra may be accounted to the small particle size (< 10 nm) of CF and its effective co-ordination with N-rGO in the case of CF/N-rGO-150. Similarly, the B.E values of 709.78 and 711.29 eV resolved in the case of the spectra corresponding to Fe 2p indicate the +2 and +3 states, respectively, of Fe in the supported system.[11, 35] The

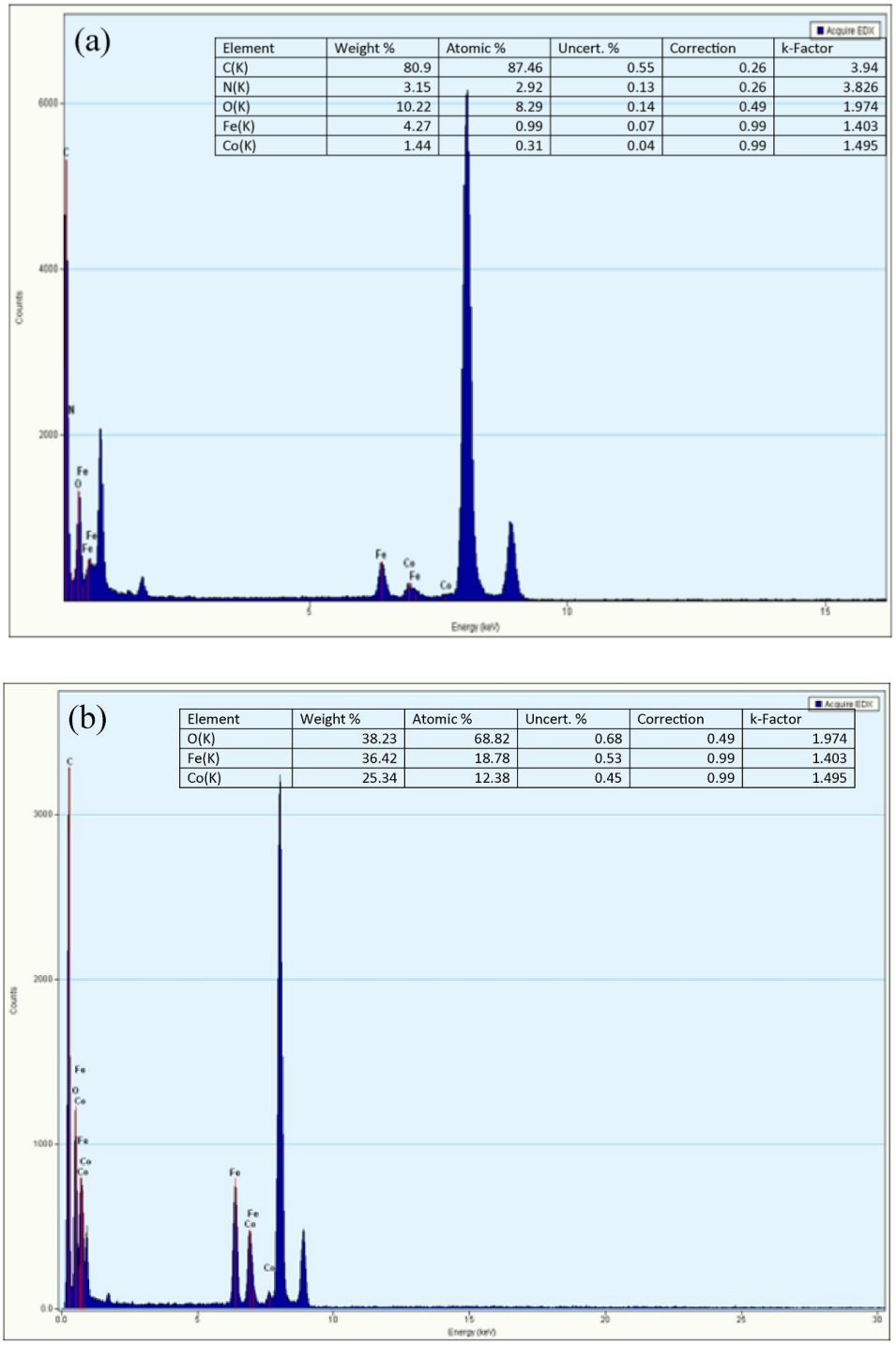

***Figure 3.9**. EDAX of CF synthesized at a water to ethanol ratio of 1:1 in the presence (a) and absence (b) of N-rGO.*

corresponding values for the unsupported system are 709.57 and 711.98 eV.[35] Along with this, the characteristic satellite peaks at 801.6 and 786.2 eV in the case of the Co 2p spectra and 718.4 eV in the case of the Fe 2p spectra are also present. The Co $2p_{1/2}$ and $2p_{3/2}$ are separated by 15.1

eV, suggesting the low spin state of the Co ion.[42] A quantitative analysis based on the spectra corresponding to Co and Fe of CF/N-rGO-150 reveals that the atomic ratio of Co to Fe is 1:2. This value has been substantiated further by the EDAX analysis and the data is presented in **Figure 3.9**. The SEM image of CF/N-rGO-150 mixed with Vulcan carbon (CF/N-rGO-150-Vulcan) in the ratio of 2:8 w/w is presented in **Figure 3.10a.** Moreover, for confirming the distribution of the CF/N-rGO-150 in the Vulcan carbon matrix, elemental analysis has been shown in **Figure 3.10**. The major phase of the catalyst is evident as carbon, whereas a uniform distribution of cobalt and iron is also present.

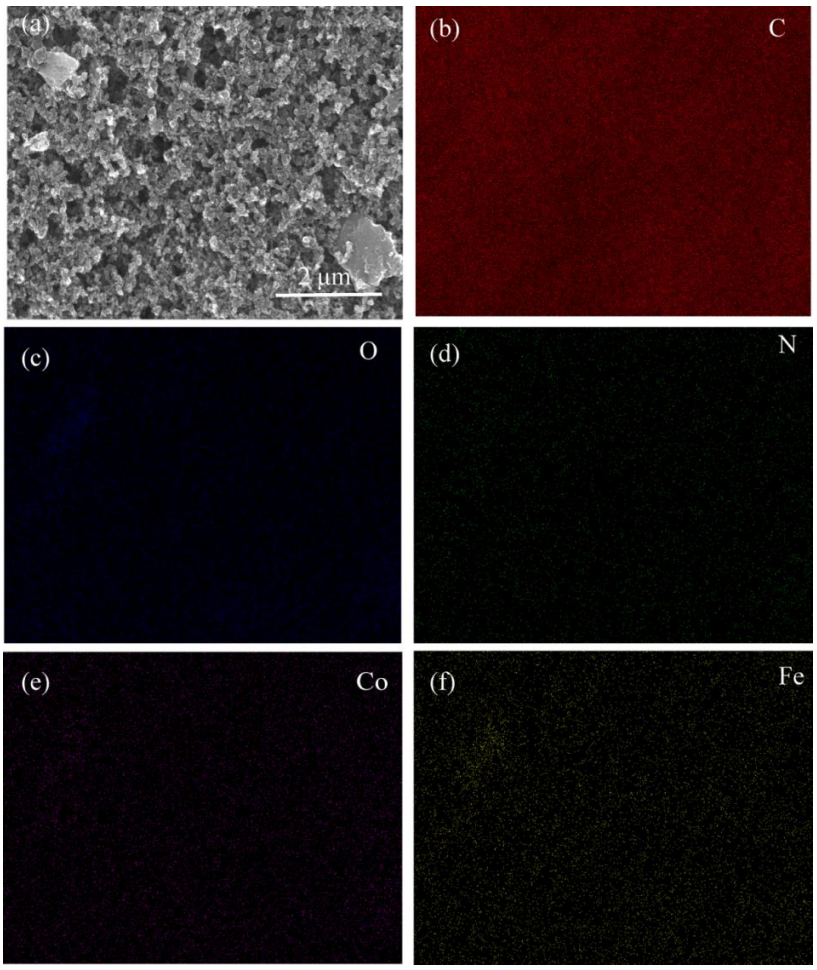

Figure 3.10*. (a) SEM image of CF/N-rGO-150-Vulcan;(b), (c), (d), (e) and (f) are the elemental mapping of CF/N-rGO-150-Vulcan.*

3.3.6. Electrochemical Studies: The electrochemical evaluations of the materials intended to unravel the intrinsic activity characteristics towards oxygen reduction reaction was performed

with the help of a set of standard analysis methodologies such as cyclic voltammetry (CV), linear sweep voltammetry (LSV) and rotating ring disc electrode (RRDE) by using N_2 and O_2 saturated 0.1 M KOH solution as the electrolyte. At this point, as also previously mentioned, it should be noted that rather than the CF/N-rGO-150 systems alone, its combination with Vulcan carbon (VulcanXC-72) as an additive to spatially separate the graphene layers has significantly helped to achieve substantial reduction in the overpotential and increased half-wave potential as well as limiting current density for ORR. From the following results, it can be seen that Vulcan carbon plays a vital role and this healthy co-existence of CF/N-rGO-150 and carbon serves as an important factor in the present set of systems in deciding the electrochemical activity characteristics in the investigations involving both single electrodes and finally in the realistic validation using a working ZAB system.

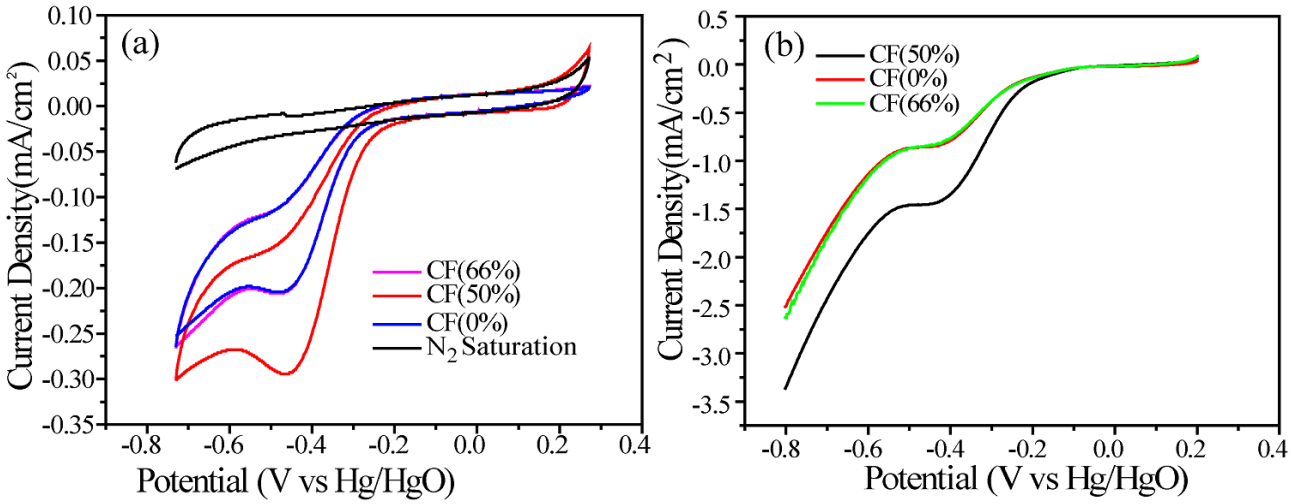

***Figure 3.11**. (a) Cyclic voltamogram recorded in oxygen saturated 0.1 M KOH at a scan rate of 50 mV/s by using the cobalt ferrite nanoparticles synthesized at different compositions of water and ethanol in the solvothermal process (the corresponding water % is indicated inside the bracket); in oxygen saturated condition faradic process overcomes capacitance whereas in N_2 saturation no contribution from the faradic reaction is evident. (b) LSVs of cobalt ferrite nanoparticles at 10 mV scan rate and 1600 rpm in oxygen saturated 0.1 M KOH solution.*

As previously mentioned, before preparing the final catalyst, a prescreening of the CF nanoparticles were done using the cyclic voltamogram and linear sweep voltamogram study (**Figure 3.11**). As from the **Figure 3.11**, the 50 % water to ethanol ratio shows the significant impact on ORR activity and hence has been used for the preparation of the final catalyst.

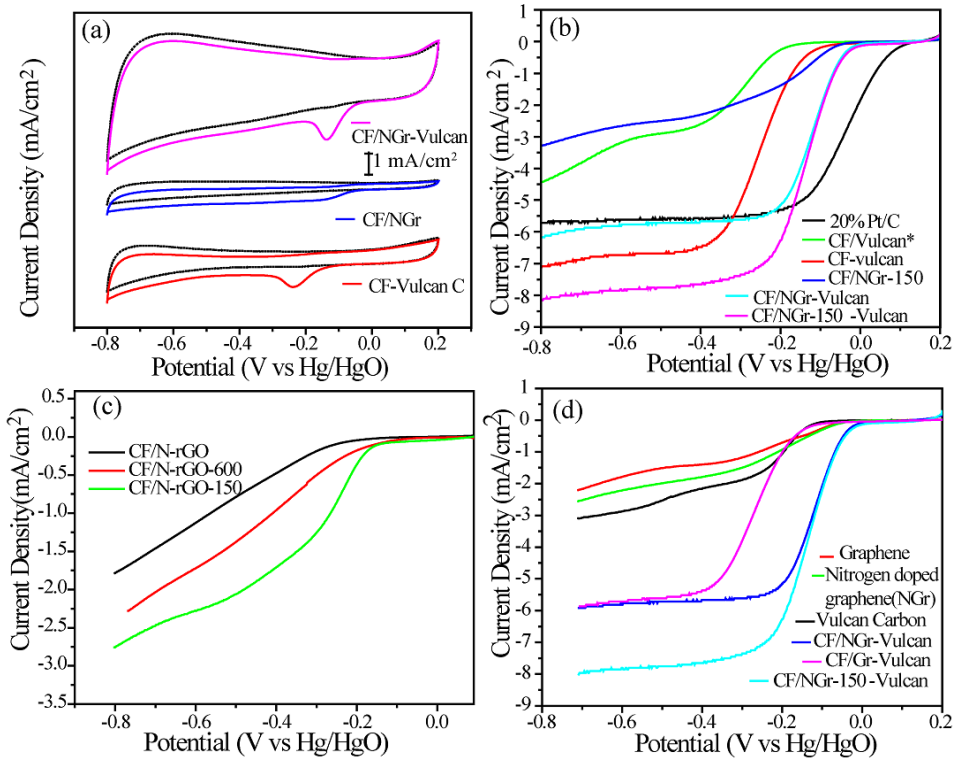

Figure 3.12. *(a) Cyclic voltamogram of CF-Vulcan, CF/N-rGO-150 and CF/N-rGO-150-Vulcan in O_2 and N_2 (black lines) saturated 0.1 M KOH solution obtained at a sweep rate of 50 mV/s; (b) LSVs of CF/Vulcan* (in-situ loading of CF on Vulcan by hydrothermal method), CF-Vulcan (physical mixture of CF and Vulcan), CF/N-rGO-150, CF/N-rGO-Vulcan, CF/N-rGO-150-Vulcan and 20wt.% PtC in O_2 saturated 0.1 M KOH solution at 1600 rpm; (c) LSVs of CF/N-rGO-150,CF/N-rGO-600and CF/N-rGO;(d)LSVs of Graphene, NGr, Vulcan carbon, CF/NGr-Vulcan, CF/Gr-Vulcan and CF/N-rGO-150-Vulcan in O_2 saturated 0.1 M KOH solution at 1600 rpm.*

Figure 3.12 shows the comparative CVs of CF-Vulcan (*i.e.*, a physical mixture of CF and Vulcan carbon in the ratio of 2:8 w/w), CF/N-rGO-150 and CF/N-rGO-150-Vulcan (*i.e.*, a physical mixture of CF/N-rGO-150 and Vulcan carbon in the ratio of 2:8 w/w) recorded at a voltage sweep rate of 50 mV/sin oxygen and nitrogen saturated 0.1 M KOH solution. The CVs of all the samples display the characteristic oxygen reduction peaks with some apparent variations on the onset and peak potentials for the samples. The oxygen reduction peaks are appeared to be more sharp and prominent in the case of the samples containing Vulcan carbon as an additive. To enable a more quantitative and comparative analysis of the ORR characteristics of the systems, linear sweep voltammograms (LSVs) were recorded by maintaining the rotation rate of the working electrode at 1600 rpm in O_2 saturated 0.1 M KOH solution (**Figure 3.12b, 3.12c** and

3.12d). The LSVs are found to be retaining the characteristic features corresponding to ORR with distinct difference in terms of the onset potential, half-wave potential and limiting current density between the samples. The onset potential of the systems towards ORR follows the order: CF/N-rGO-150-Vulcan (-0.020 V) > CF/N-rGO-Vulcan (-0.022 V) > CF/N-rGO-150 (-0.037 V) > CF-Vulcan (-0.123 V) > CF/Vulcan* (-0.187 V). Additional comparative LSV plots of graphene, N-rGO, Vulcan carbon, CF/rGO-Vulcan, CF/N-rGO-Vulcan and CF/N-rGO-150-Vulcan are presented in **Figure 3.12d**. A close look at these two sets of the LSV data clearly indicates that the physical mixing of Vulcan carbon with CF/N-rGO-150 has clearly revolutionized the ORR performance of the system in terms of the onset potential, half-wave potential and limiting current density. The onset potential and the half-wave potential in the case of CF/N-rGO-150-Vulcan are -0.110 and -0.133 V (*vs* Hg/HgO), which are respectively 17 and 27 mV higher compared to its Vulcan-free counterpart, *i.e.* CF/N-rGO-150. Along with a distinct modulation achieved with respect to these two parameters, a substantial gain in the limiting current density (5 ±0.5 mA/cm^2) has also been noticed due to the association of Vulcan carbon in the hybrid catalyst matrix. While, with respect to the onset potential, CF/N-rGO-150-Vulcan is still inferior to the state-of-the-art 20 wt.% Pt/C by 110 mV, the homemade catalyst clearly outperforms Pt/C in terms of the limiting current density. In terms of the limiting current density, CF/N-rGO-150-Vulcan is superior to Pt/C by 2±0.5 mA/cm^2. All the other catalysts are showing much inferior performance, but the favorable role played by Vulcan carbon as an additive is evident in all the catalyst compositions involving Vulcan carbon as a spacer. The increase in the limiting current is mainly caused by the better utilization of the active sites in the system as Vulcan carbon spatially separates the CF/N-rGO-150 sheets. Exposure of more active sites and seamless distribution of the reactants along with facile product dissipation result into the increased limiting current density.

The effect of Vulcan carbon is also explored from the impedance spectra of the catalyst (**Figure 3.13a**). Vulcan carbon, which is highly conducting, upon addition to the CF/N-rGO system, lowers the resistance of the system. The impedance spectra presented in **Figure 3.13a** shows two regions, semicircle and linear line, the semicircle region refers charge transfer resistance whereas slope of linear line for mass transfer. The catalyst CF/N-rGO-150-Vulcan shows smaller semicircle and high slope value for linear line owing to better charge transfer and mass transfer. The measured resistance values in the case of CF/N-rGO-150-Vulcan and CF/N-

RGO-150 are 39 and 44 Ω respectively. Moreover, the conductivity values, measured through the V-I plot (**Figure 3.13b**), are estimated to be $9x\ 10^{-2}$, $1.2\ x10^{2}$ and $1.5x10^{2}$ S m^{-1} for CF/N-rGO-150, CF/N-rGO-150-Vulcan and Vulcan carbon, respectively. Here, the low conductivity of the CF/N-rGO-150 catalyst is expected due to the presence of the metal oxide nanoparticles in the system. Vulcan carbon and its composite with CF/N-rGO-150 show high conductivity due to large proportion of the graphitic carbon in the system, enhancing the ORR activity. Thus, the role of Vulcan in tuning the conductivity is evident from this result.

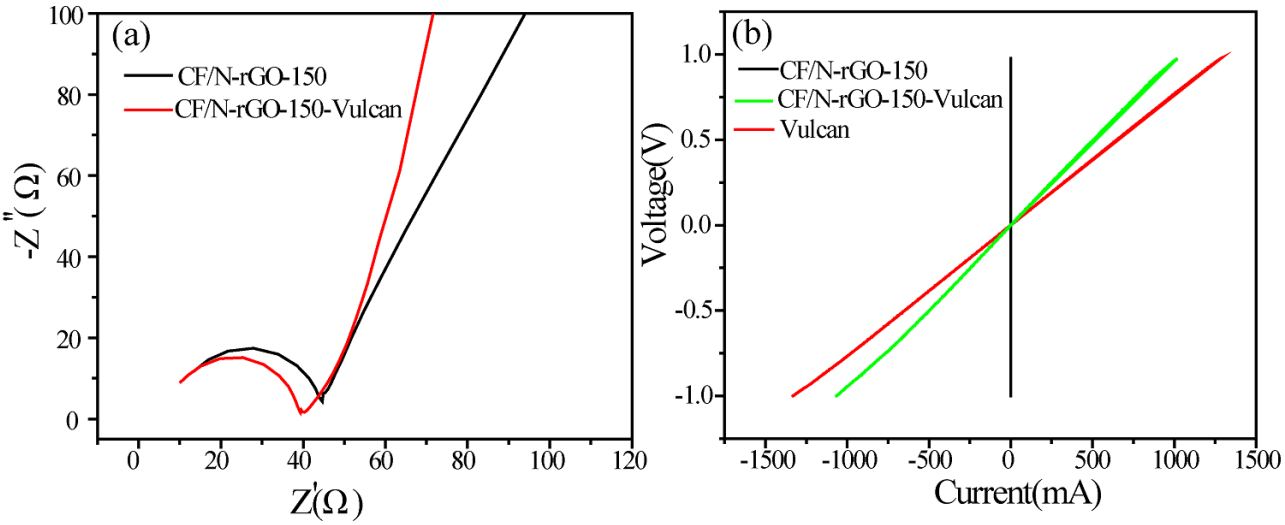

Figure 3.13. *(a) Represents the Nyquist plots of CF/N-rGO-150 and the composite with Vulcan carbon. The spectra show better conductivity, charge transfer and mass diffusion in the Vulcan mixed composite. (b) Voltage vs Current (V-I) plots showing linear relation for the different catalysts; CF/N-rGO-150 (black line) shows high resistance compared to the other catalysts.*

As previously discussed, the role of Vulcan carbon as an additive is multifold. Firstly, N-rGO with the abundantly dispersed CF nanoparticles is likely to bring in more resistive nature to the system. In addition, CF/N-rGO-150 does not possess microporosity, which is a necessary parameter in deciding the reactant distribution once the electrode is fabricated by adding an ionomer-based binder such as Nafion. Also, Nafion addition during the formulation of the catalyst ink can trigger stacking and aggregation of the layers of CF/N-rGO-150 by gravely compromising the electrochemical active area due to the burial of active sites within the stacked or aggregated layers. Vulcan carbon as an additive stands out as a complete solution to simultaneously address all the above-mentioned limitations of the present system. Being highly

conductive, Vulcan carbon helps to reduce the iR drop incurred by the CF/N-rGO-150 system whereas its microporosity acts as reservoirs and channels for enriching the active sites located on CF/N-rGO-150 with the reactants. Along with these two critical roles, the Vulcan carbon particles spatially separate out the layers of CF/N-rGO-150. Thus, a balanced controlled interplay of these features brings in a healthy synergistic interaction within the system, leading to a significant activity modulation towards ORR. Also, the large gain in the ORR activity subsequent to the Vulcan carbon addition indicates that the intrinsic activity of CF/N-rGO-150 is very high, which unfortunately could not be unraveled in the absence of Vulcan carbon due to the compounding of the multiple reasons as accounted before. The significantly fine distribution of the spinel nanoparticles is responsible for the high number density of the active sites, which is revealed from the registered high limiting current density by CF/N-rGO-150-Vulcan. Additionally, the homemade catalyst has magnetic property which is confirmed through the exposure to the magnetic field **(Figure 3.14)**.

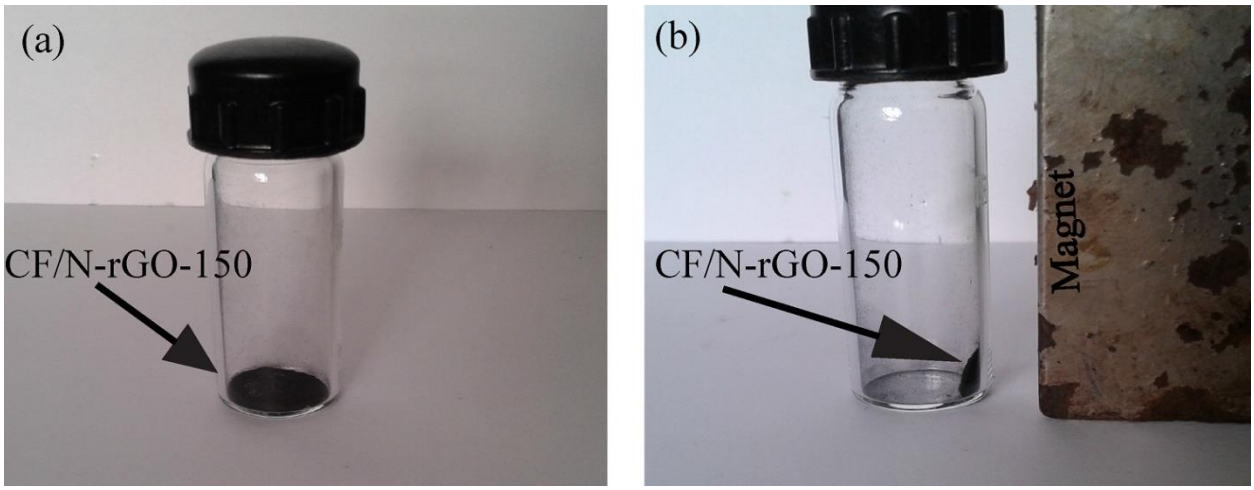

Figure 3.14*. CF/N-rGO in the absence (a) and presence (b) of an external magnetic field.*

The magnetic property of the material can also be another contributing factor, probably to a limited extent, towards ORR indirectly through the magnetohydrodynamic movement as reported in some of the previous works.[19-20] To demonstrate the actual intrinsic contribution of the catalysts, the mass activity has been calculated (**Figure 3.15**) by dividing the current density at -0.05 V *vs* Hg/HgO with the total loading of the active component (*i.e*. CF in CF-Vulcan or Pt

nanoparticles in 20 wt.% PtC; in the case of CF/N-rGO-150-Vulcan, the normalization has done with respect to the weight of CF/N-rGO as this component is the active moiety responsible for facilitating ORR**).** It is interesting to note that, among all the catalysts, CF/N-rGO-150-Vulcan is showing the highest mass activity, which is followed by 20 wt.% PtC.

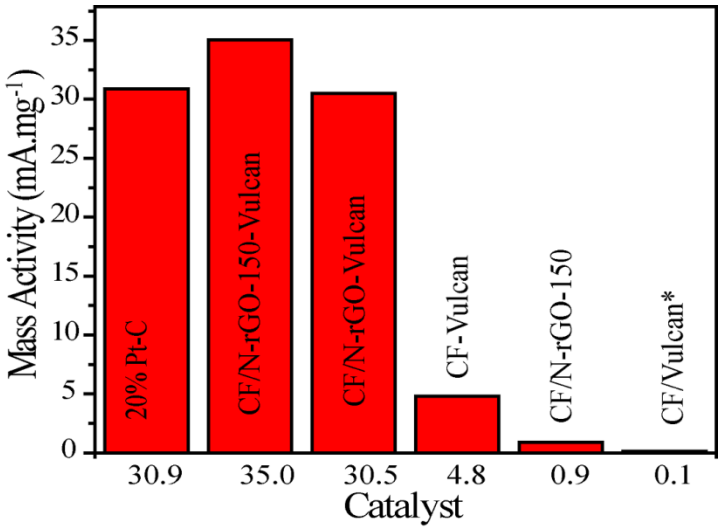

Figure 3.15. *Comparison of the mass activity of the various CF based catalysts with the commercial 20 wt.% PtC catalyst at -0.05 V (vs Hg/HgO).*

Furthermore, Koutecky-Levich (K-L) plots, which indicate the relationship between the inverse of the current density (j^{-1}) and the inverse of the square root of the rotation speed ($\omega^{-1/2}$) of the electrode at different potential values,were constructed by recording LSVs of the catalysts by maintaining the electrode at different rotation speeds.[43]**Figure 3.16a** represents the LSVs recorded at a voltage scan rate of 10 mV/s over CF/N-rGO-150-Vulcan at various electrode rotation rates in O_2 saturated 0.1 M KOH. Subsequently, the K-L plots are constructed as presented in **Figure 3.16b,** which clearly show a linear relationship between j^{-1} to $\omega^{-1/2}$. As can be seen from the figure, the K-L plots at different potentials (-0.26 to -0.42 V) display good linearity and parallelism,

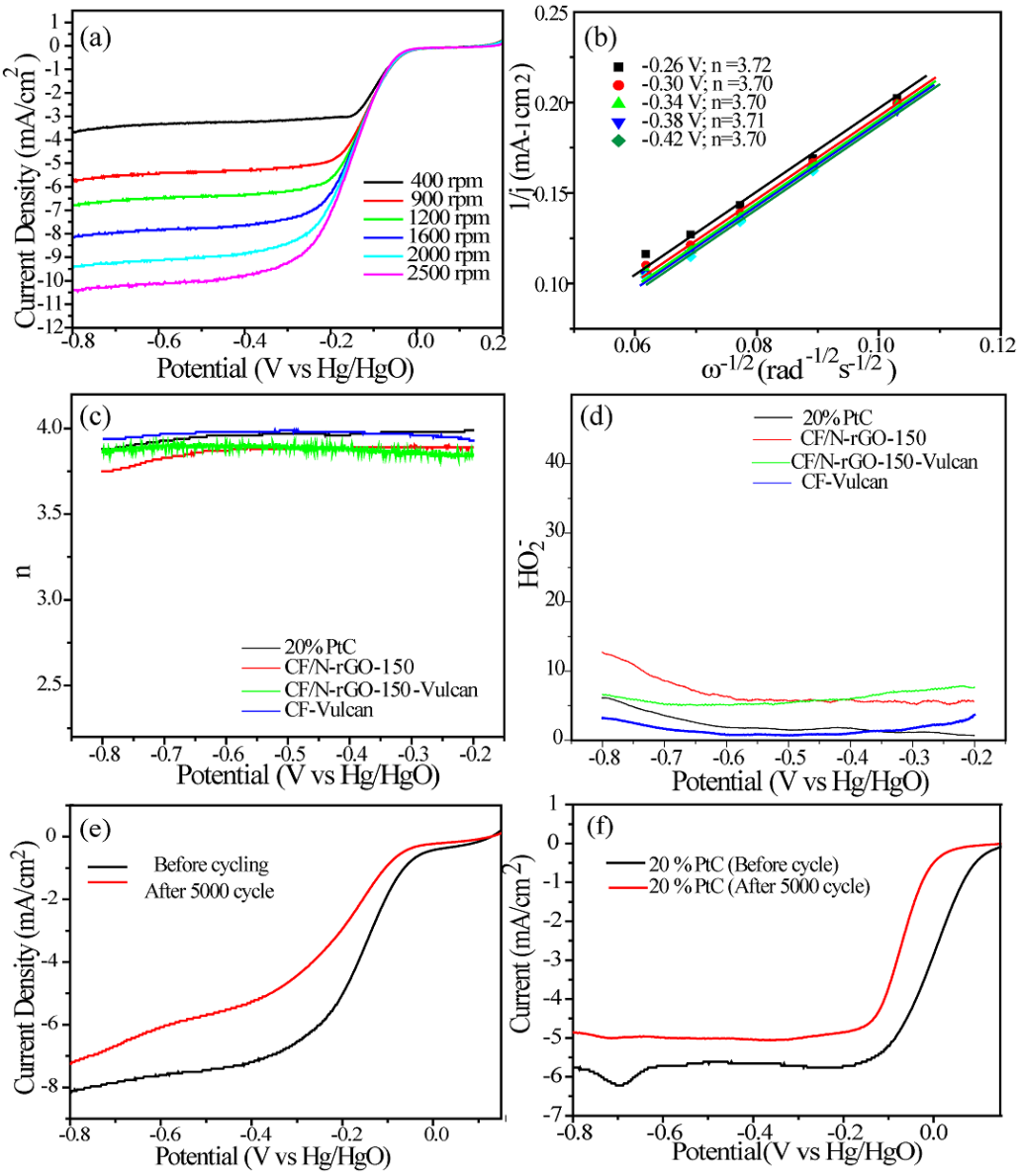

Figure 3.16.*(a) LSVs of CF/N-rGO-150-Vulcan at various electrode rotation rates in O_2 saturated 0.1 M KOH recorded at a voltage scan rate of 10 mV/s; (b) Koutecky-Levich plots for ORR in O_2 saturated 0.1 M KOH solution for CF/N-rGO-150-Vulcan in the potential range -0.26 to -0.42 V (vs Hg/HgO); (c) the number of electrons transferred during ORR as a function of the electrode potential of the various catalysts; (d) the peroxide percentage measured at different potentials of the disc electrode in RRDE; (e) and (f) LSVs of CF/N-rGO-150-Vulcan and 20 wt.% PtC catalyst in 0.1 M KOH solution recorded before and after ADT respectively.*

which is an indication of the first order kinetics of ORR with respect to the oxygen concentration.[44] The kinetic current density (j_k), which is a quantitative parameter denoting the intrinsic activity of the catalyst, has been deduced from the inverse of the intercept of the K-L

plot to the y-axis after extrapolating to the $\omega^{-1/2}$ value to 0 (which indicates an infinite rotation speed and rules out the intervention due to diffusion limitations). The measured j_k value at-0.26V(*vs* Hg/HgO) in the case of CF/N-rGO-150-Vulcan is 620 mA/mg, which is an appreciable value in the case of a Pt-free system (details on the RDE experiments and the calculation of j_k are given in the **Chapter 2**).[45] Finally, the number of electros transferred during the ORR process has been deduced from the slope of the K-L plots, which is found to be 3.7 and indicates the involvement of the preferred 4-electron (4e) reduction process.[46]

A more insightful information on the reduction pathway has been obtained with the help of Rotating Ring Disk Electrode (RRDE) studies, which help to quantify the amount of H_2O_2 formed due to the unfavorable 2-electron (2e) reduction pathway. **Figure 3.16c** indicates the number of electrons transferred as estimated from the ring current obtained from the various prepared catalysts (details on the RRDE measurements and the related calculations are given in the **Chapter 2**), where all the catalysts are found to be showing nearly 4e transfer reaction. Quantification of the peroxide percentage (**Figure 3.16d**) indicates the amount well below 10%, which is a significantly low value in the case of the Pt-free systems. The mechanical and electrochemical integrity of CF/N-rGO-150-Vulcan in comparison to 20 wt.% PtC catalysts has been monitored by performing accelerated durability test (ADT), which involves measurement of the LSVs before and after subjecting the material under potential induced conditions in oxygen enriched electrolyte. The potential cycle was performed between -0.6 and 0.4 V (*vs* Hg/HgO) for 5000 cycles where the system was essentially passing through a triggered condition which can degrade the carbon structure and thereby fouling and aggregation of the active component in the catalyst. The homemade catalyst suffered a 40 mV increase in the onset potential compared to a whopping 100 mV shift observed in the case of Pt/C **(Figure 3.16e** and **Figure 3.16f)**. However, the shift in the half-wave potential is found to be 80 mV in both the cases. The better survivability in terms of the onset potential for CF/N-rGO-150-Vulcan in comparison to PtC could be credited to the strong interaction of the CF nanoparticles to N-rGO. Compared to Vulcan carbon, N-rGO is less corrosive under electrochemical conditions. Also, the multiple anchoring sites created through N-doping, small order buckling of the graphene layers and the functional groups present on rGO are likely to be playing a crucial role in bringing in better structural integrity to the supported state in CF/N-rGO-150.[32, 47-49]

3.3.7. Primary Zn-Air Battery: CF/N-rGO-150-Vulcan catalyst was finally employed as the air breathing cathode in association with a zinc foil as an anode in a primary Zn-air Battery (ZAB) and a system level demonstration has been performed. The fabricated ZAB was tested under ambient atmospheric pressure (0.21 atm. partial pressure of O_2) as one case and in O_2saturated 6 M KOH electrolyte as the second case **(Figure 3.17a and 3.17b)**. Under the ambient atmospheric pressure condition, the battery displays a discharge plateau starting from 1.0 V and sustaining till 0.8 V at a current dragging level of 20 mA/cm^2. At atmospheric pressure of O_2, the concentration of O_2 in the electrolyte solution (6M KOH) is relatively less, whereas, in O_2 saturated solution, the high O_2 concentration allows a larger current drag condition. Consequently, in O_2 saturated 6 M KOH solution, at an elevated current dragging condition of 30 mA/cm^2, the discharge profile followed a similar plateau as in the case of the operation at lower current dragging condition and lower O_2 partial pressure.

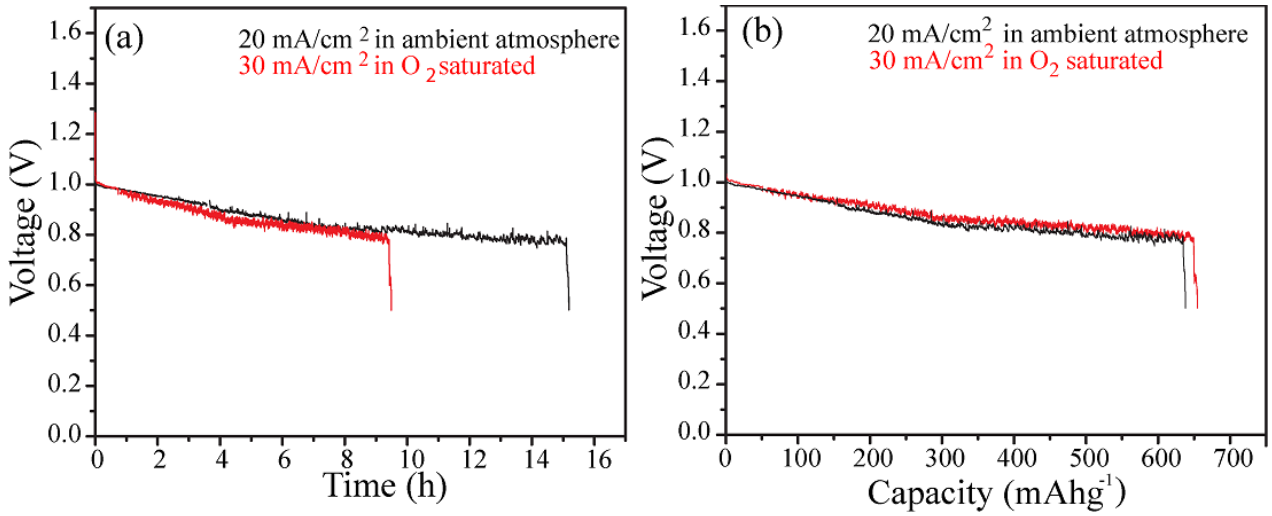

Figure 3.17. *(a) Galvanostatic discharge curves of the fabricated Zn-air battery consisting of CF/N-rGO-150-Vulcan based air electrode at 20 mA/cm^2 and 30 mA/cm^2 in 6 M KOH; (b) discharge capacity of the battery normalized with respect to the utilized amount of Zn.*

These two cases clearly indicate that the air electrode based on CF/N-rGO-150-Vulcan is performing well in a realistic system level validation even under the ambient conditions involving moderate O_2 concentration. The voltage drop in the plateau region with respect to the

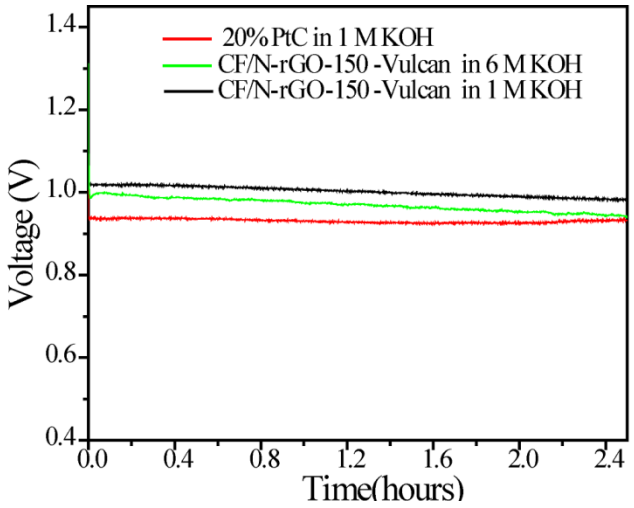

Figure 3.18.*Galvanostatic discharge of the fabricated Zn-air batteries in 1 M as well as in 6 M KOH at a discharge current density of 20 mA/cm^2.*

operation time is supposed to arise from the side reaction taking place over the Zn foil surface.[50-52] Overall, the specific capacity of the hybrid (~630 mAhg^{-1}) catalyst is in good agreement with the reported literatures.[50] Another important feature of the ZAB based on CF/N-rGO-150-Vulcan as the air electrode is better performance of the system in 1 M KOH solution compared to that in 6 M KOH. In 1 M KOH, the discharge plateau is clearly superior to the state-of-the-art PtC catalyst **(Figure 3.18)**. This gives a benefit for the present system that its performance is less vulnerable to the electrolyte dilution which can happen during the course of operation of the battery.

A comparative polarization plots of the ZABs based on the air electrodes derived from CF/N-rGO-150-Vulcan and 20 wt.% Pt/C were also recorded in 6 M KOH **(Figure 3.19a)** as well as in 1 M KOH **(Figure 3.19b)**. The power densities of 155 and 190 mW/cm^2 are obtained for the ZABs based on CF/N-rGO-150-Vulcan and Pt/C, respectively, in 6 M KOH. This trend reverses in 1 M KOH, where the ZAB based on CF/N-rGO-150-Vulcan displays a higher power density of 55.4 mW/cm^2 compared to 33.2 mW/cm^2 obtained in the case of the system based on Pt/C. To better understand the performance of the ZAB fabricated in the present case with the similar systems reported in the literature, a comparison has been made by tabulating the relevant literature data corresponding to the various air catalysts explored for the ZAB applications (**Table 3.1)**.

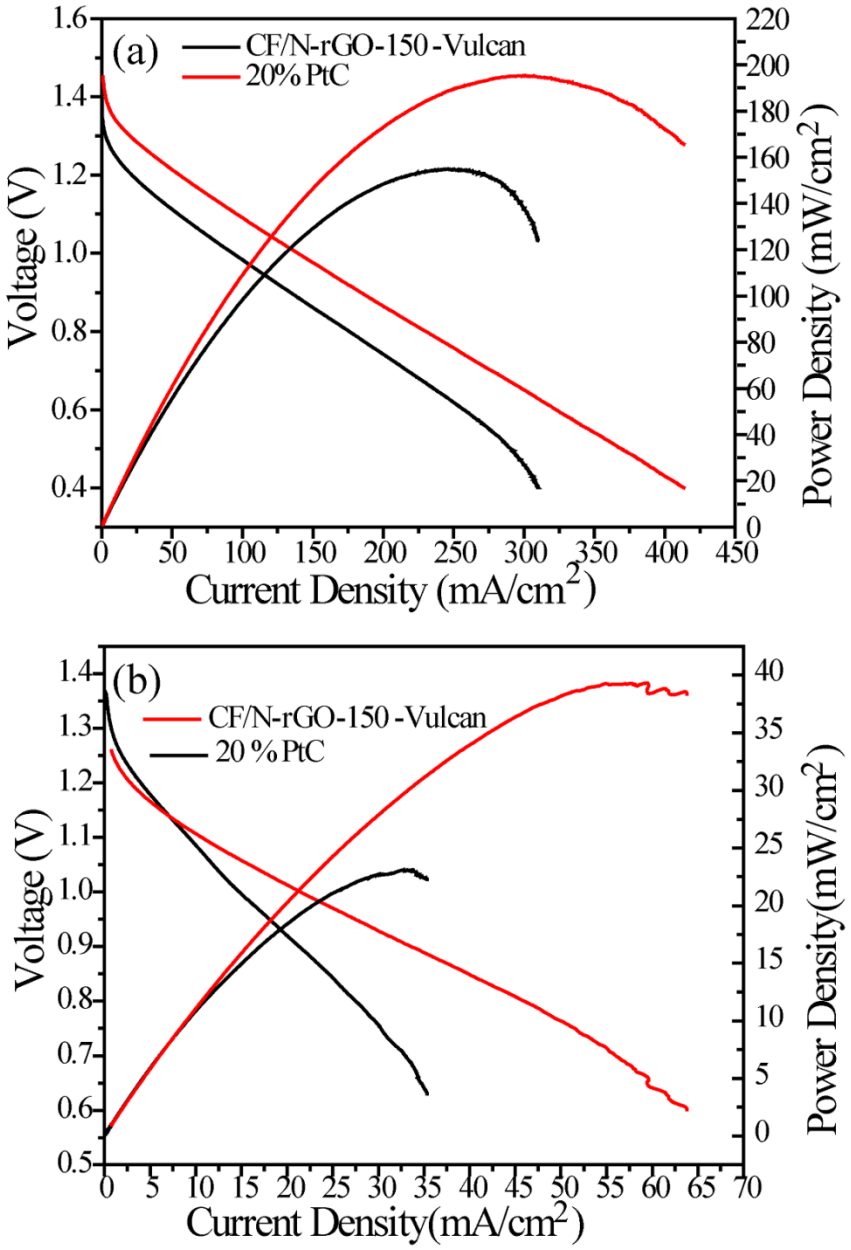

Figure 3.19. *(a) the polarization plots (V vs I) and the corresponding power density plots of the fabricated Zn-air batteries with the air electrodes made from CF/N-rGO-150-Vulcan and the commercial 20 wt.% Pt/C catalyst;(b) polarization plots obtained from the ZABs based on CF/N-rGO-150-Vulcan and 20 wt.% Pt/C as the air electrodes and 1 M KOH as the electrolyte.*

Table 3.1. *A comparison of the air catalysts explored for the cathode in zinc air batteries.*

Air Catalyst	**Battery Type**	**Performance of the Battery**	**Electrolyte**	**Battery Power Density**	**Discharge capacity**	**Reference**
Core-Shell Fe-Cu Nanoparticle	Mechanically rechargeable	1.2 V at 25 mA/cm^2 current density	6 M KOH	212 mW/cm^2	-	53
Co_3O_4 with carbon black	Flexible rechargeable	1.2 V at 20 μm	-	28.2 mW	460 mAh g^{-1}	54
CoO/N-CNT	Rechargeable	1.2 V at 50 mA/cm^2	6 M KOH	265 mW/cm^2	570 mAh g^{-1}	55
N-CNT	Primary	-	6 M KOH	69.5 mW/cm^2	-	56
Co_3O_4 decorated nanofiber	Rechargeable	1.21 v at 2 mA/cm^2	6 M KOH	125 mW/cm^2		18
CMO/N-rGO	Rechargeable	1.1 V at 20 mA/cm^2	6 M KOH	-	610 mAh g^{-1}	57
G-PMF	Primary	1.15 at 20 mA/cm^2	6 M KOH	70 mW/cm^2	400 mAh g^{-1} at cut off 0.9 V	58
Co_3O_4-SP/NGr-24	Mechanically rechargeable	1.35 at 10 mA/cm^2	6 M KOH	190 mW/cm^2	590 mAh g^{-1}	59
Cu-Pt Nanocage	Primary	~ 1.3 V at 20 mA/cm^2	6 M KOH	~250 mW/cm^2	560 mAh g^{-1}	60
CF/N-rGO-150-Vulcan	***Primary***	***1 V at 30 mA/cm^2***	***6 M KOH, 1 M KOH***	***155 mW/cm^2, 55 mW/cm^2***	***630 mAh g^{-1}***	***This work***

3.4. CONCLUSION

By carefully controlling the water to ethanol ratio under the hydrothermal synthesis conditions, fine and homogeneous distribution of the nanoparticles of cobalt ferrite (CF) on nitrogen doped reduced graphene oxide (N-rGO) could be achieved (CF/N-rGO-150). The CF nanoparticles accommodated on N-rGO displays all the characteristic crystal phases associated with the spinel structure of the particles. The synthesized catalyst in association with Vulcan carbon as an additive is found to be displaying significantly modulated performance characteristics towards electrochemical oxygen reduction reaction (ORR). The enhancement in the catalytic activity has been explained based on a healthy synergistic interaction between the active site bearing N-rGO sheets and the micropores contributing Vulcan carbon. This coexistence of the two carbon phases helps to spatially separate the nanosheets of CF/N-rGO-150 and to prevent their aggregation during the formulation of the catalyst ink by adding Nafion. The high conductivity of Vulcan carbon helps to reduce the iR drop and its microporous texture acts as a reservoir for reactant distribution at the local active site located on N-rGO. The controlled interplay between the carbon phases helps to improve the onset potential of CF/N-rGO-150-Vulcan by 17 mV compared to its Vulcan-free counterpart, CF/N-rGO-150. More interestingly, a radical enhancement in terms of the limiting current density has been obtained in the case of CF/N-rGO-150-Vulcan compared to CF/N-rGO-150 (improvement by 5±0.5 mA/cm^2), which is 2.0±0.5 mA/cm^2higher compared to the state-of-the-art 20 wt.% Pt/C. Finally, a real time demonstration of a zinc-air battery (ZAB) by employing CF/N-rGO-150-Vulcan as the air breathing electrode exhibits a power density of 155 mW/cm^2 in 6 M KOH and 55.4 mW/cm^2 in 1 M KOH solution. Compared to Pt/C as the air electrode, the performance of the system based on CF/N-rGO-150-Vulcan is less vulnerable to the electrolyte dilution which can happen during the course of operation of the battery.

3.5. REFERENCES

(1) Etacheri, V.; Marom, R.; Elazari, R.; Salitra, G.; Aurbach, D., Challenges in the Development of Advanced Li-ion Batteries: A review. *Energy Environ. Sci.* **2011,** *4*, 3243-3262.

(2) Wang, G.; Zhang, L.; Zhang, J., A Review of Electrode Materials for Electrochemical Supercapacitors. *Chem. Soc. Rev.* **2012,** *41*, 797-828.

(3) Kirubakaran, A.; Jain, S.; Nema, R. K., A Review on Fuel Cell Technologies and Power Electronic Interface. *Renewable sustainable Energy Rev.* **2009,** *13*, 2430-2440.

(4) Li, Y.; Dai, H., Recent Advances in Zinc-Air Batteries. *Chem. Soc. Rev.* **2014,** *43*, 5257-5275.

(5) Balaish, M.; Kraytsberg, A.; Ein-Eli, Y., A Critical Review on Lithium-Air Battery Electrolytes. *Phys. Chem. Chem. Phys.* **2014,** *16*, 2801-2822.

(6) Nie, Y.; Li, L.; Wei, Z., Recent Advancements in Pt and Pt-Free Catalysts for Oxygen Reduction Reaction. *Chem. Soc. Rev.* **2015,** *44*, 2168-2201.

(7) Guo, S.; Zhang, S.; Sun, S., Tuning Nanoparticle Catalysis for the Oxygen Reduction Reaction. *Angew. Chem. Int. Ed.***2013,** *52*, 8526-8544.

(8) Chung, D. Y.; Jun, S. W.; Yoon, G.; Kwon, S. G.; Shin, D. Y.; Seo, P.; Yoo, J. M.; Shin, H.; Chung, Y.-H.; Kim, H.; Mun, B. S.; Lee, K.-S.; Lee, N.-S.; Yoo, S. J.; Lim, D.-H.; Kang, K.; Sung, Y.-E.; Hyeon, T., Highly Durable and Active PtFe Nanocatalyst for Electrochemical Oxygen Reduction Reaction. *J. Am. Chem. Soc.* **2015**, *137*, 15478-15485.

(9) Toh, R. J.; Eng, A. Y. S.; Sofer, Z.; Sedmidubsky, D.; Pumera, M., Ternary Transition Metal Oxide Nanoparticles with Spinel Structure for the Oxygen Reduction Reaction. *ChemElectroChem* **2015,** *2*, 982-987.

(10) Carta, D.; Casula, M. F.; Falqui, A.; Loche, D.; Mountjoy, G.; Sangregorio, C.; Corrias, A., A Structural and Magnetic Investigation of the Inversion Degree in Ferrite Nanocrystals MFe_2O_4 (M = Mn, Co, Ni). *J. Phys. Chem. C* **2009,** *113*, 8606-8615.

(11) Wu, Z.-S.; Yang, S.; Sun, Y.; Parvez, K.; Feng, X.; Müllen, K., 3D Nitrogen-Doped Graphene Aerogel-Supported Fe_3O_4 Nanoparticles as Efficient Electrocatalysts for the Oxygen Reduction Reaction. *J. Am. Chem. Soc.* **2012,** *134*, 9082-9085.

(12) Jiao, Y.; Zheng, Y.; Jaroniec, M.; Qiao, S. Z., Origin of the Electrocatalytic Oxygen Reduction Activity of Graphene-Based Catalysts: A Roadmap to Achieve the Best Performance. *J. Am. Chem. Soc.* **2014,** *136*, 4394-4403.

(13) Li, C.; Han, X.; Cheng, F.; Hu, Y.; Chen, C.; Chen, J., Phase and Composition Controllable Synthesis of Cobalt Manganese Spinel Nanoparticles Towards Efficient Oxygen Electrocatalysis. *Nat. Commun.* **2015,** *6*.

(14) Liang, Y.; Li, Y.; Wang, H.; Zhou, J.; Wang, J.; Regier, T.; Dai, H., Co_3O_4 Nanocrystals on Graphene as a Synergistic Catalyst for Oxygen Reduction Reaction. *Nat. Mater.* **2011,** *10*, 780-786.

(15) Liang, Y.; Wang, H.; Zhou, J.; Li, Y.; Wang, J.; Regier, T.; Dai, H., Covalent Hybrid of Spinel Manganese–Cobalt Oxide and Graphene as Advanced Oxygen Reduction Electrocatalysts. *J. Am. Chem. Soc.* **2012,** *134*, 3517-3523.

(16) Ning, R.; Tian, J.; Asiri, A. M.; Qusti, A. H.; Al-Youbi, A. O.; Sun, X., Spinel $CuCo_2O_4$ Nanoparticles Supported on N-Doped Reduced Graphene Oxide: A Highly Active and Stable Hybrid Electrocatalyst for the Oxygen Reduction Reaction. *Langmuir* **2013,** *29*, 13146-13151.

(17) Ge, X.; Liu, Y.; Goh, F. W. T.; Hor, T. S. A.; Zong, Y.; Xiao, P.; Zhang, Z.; Lim, S. H.; Li, B.; Wang, X.; Liu, Z., Dual-Phase Spinel $MnCo_2O_4$ and Spinel $MnCo_2O_4$/Nanocarbon Hybrids for Electrocatalytic Oxygen Reduction and Evolution. *ACS Appl. Mater. Interfaces* **2014,** *6*, 12684-12691.

(18) Li, B.; Ge, X.; Goh, F. W. T.; Hor, T. S. A.; Geng, D.; Du, G.; Liu, Z.; Zhang, J.; Liu, X.; Zong, Y., Co_3O_4 Nanoparticles Decorated Carbon Nanofiber Mat as Binder-Free Air-Cathode for High Performance Rechargeable Zinc-Air Batteries. *Nanoscale* **2015,** *7*, 1830-1838.

(19) Zhu, H.; Zhang, S.; Huang, Y.-X.; Wu, L.; Sun, S., Monodisperse $M_xFe_{3-x}O_4$ (M = Fe, Cu, Co, Mn) Nanoparticles and Their Electrocatalysis for Oxygen Reduction Reaction. *Nano Lett.* **2013,** *13*, 2947-2951.

(20) Monzon, L. M. A.; Rode, K.; Venkatesan, M.; Coey, J. M. D., Electrosynthesis of Iron, Cobalt, and Zinc Microcrystals and Magnetic Enhancement of the Oxygen Reduction Reaction. *Chem. Mater.* **2012,** *24*, 3878-3885.

(21) Qiu, Y.; Zhang, X.; Yang, S., High Performance Supercapacitors Based on Highly Conductive Nitrogen-Doped Graphene Sheets. *Phys. Chem. Chem. Phys.* **2011,** *13*, 12554-12558.

(22) Palaniselvam, T.; Kannan, R.; Kurungot, S., Facile Construction of Non-Precious Iron Nitride-Doped Carbon Nanofibers as Cathode Electrocatalysts for Proton Exchange Membrane Fuel Cells. *Chem. Commun.* **2011,** *47*, 2910-2912.

(23) Palaniselvam, T.; Irshad, A.; Unni, B.; Kurungot, S., Activity Modulated Low Platium Content Oxygen Reduction Electrocatalysts Prepared by Inducing Nano-Order Dislocations on Carbon Nanofiber through N_2-Doping. *J. Phys. Chem. C* **2012,** *116*, 14754-14763.

(24) Ma, Y.; Wang, H.; Ji, S.; Goh, J.; Feng, H.; Wang, R., Highly Active Vulcan Carbon Composite for Oxygen Reduction Reaction in Alkaline Medium. *Electrochimica Acta* **2014,** *133*, 391-398.

(25) Marcano, D. C.; Kosynkin, D. V.; Berlin, J. M.; Sinitskii, A.; Sun, Z.; Slesarev, A.; Alemany, L. B.; Lu, W.; Tour, J. M., Improved Synthesis of Graphene Oxide. *ACS Nano* **2010,** *4*, 4806-4814.

(26) Long, D.; Li, W.; Ling, L.; Miyawaki, J.; Mochida, I.; Yoon, S.-H., Preparation of Nitrogen-Doped Graphene Sheets by a Combined Chemical and Hydrothermal Reduction of Graphene Oxide. *Langmuir* **2010,** *26*, 16096-16102.

(27) Resa, J. M.; Goenaga, J. M.; Iglesias, M.; Gonzalez-Olmos, R.; Pozuelo, D., Liquid−Liquid Equilibrium Diagrams of Ethanol + Water + (Ethyl Acetate or 1-Pentanol) at Several Temperatures. *J.Chem. Eng.Data* **2006,** *51*, 1300-1305.

(28) Tang, Z. R.; Kondrat, S. A.; Dickinson, C.; Bartley, J. K.; Carley, A. F.; Taylor, S. H.; Davies, T. E.; Allix, M.; Rosseinsky, M. J.; Claridge, J. B.; Xu, Z.; Romani, S.; Crudace, M. J.; Hutchings, G. J., Synthesis of High Surface Area $CuMn_2O_4$ by Supercritical Anti-Solvent Precipitation for the Oxidation of CO at Ambient Temperature. *Catal. Sci. Technol* **2011,** *1*, 740-746.

(29) Kim, Y. I.; Kim, D.; Lee, C. S., Synthesis and Characterization of $CoFe_2O_4$ Magnetic Nanoparticles Prepared by Temperature-Controlled Coprecipitation Method. *Physica B: Condensed Matter* **2003,** *337*, 42-51.

(30) Bian, W.; Yang, Z.; Strasser, P.; Yang, R., A $CoFe_2O_4$/Graphene Nanohybrid as an Efficient Bi-Functional Electrocatalyst for Oxygen Reduction and Oxygen Evolution. *J. Power Sources* **2014,** *250*, 196-203.

(31) Li, Y.; Li, Y.; Zhu, E.; McLouth, T.; Chiu, C.-Y.; Huang, X.; Huang, Y., Stabilization of High-Performance Oxygen Reduction Reaction Pt Electrocatalyst Supported on Reduced Graphene Oxide/Carbon Black Composite. *J. Am. Chem. Soc.* **2012,** *134*, 12326-12329.

(32) Liang, H.-W.; Zhuang, X.; Brüller, S.; Feng, X.; Müllen, K., Hierarchically Porous Carbons with Optimized Nitrogen Doping as Highly Active Electrocatalysts for Oxygen Reduction. *Nat. Commun.* **2014,** *5*.

(33) Zhao, H.; Sun, C.; Jin, Z.; Wang, D.; Yan, X.; Chen, Z. G.; zhu, G.; Yao, X., Carbon for Oxygen Reduction Reaction: A Defect Mechanism. *J.Mater.Chem. A* **2015**, *3*, 11736-11739.

(34) Largeot, C.; Portet, C.; Chmiola, J.; Taberna, P.-L.; Gogotsi, Y.; Simon, P., Relation between the Ion Size and Pore Size for an Electric Double-Layer Capacitor. *J. Am. Chem. Soc.* **2008,** *130*, 2730-2731.

(35) Liu, C.; Zhang, Y.; Jia, J.; Sui, Q.; Ma, N.; Du, P., Multi-susceptibile Single-Phased Ceramics with Both Considerable Magnetic and Dielectric Properties by Selectively Doping. *Sci. Rep.* **2015,** *5*, 9498.

(36) Tang, R.; Jiang, C.; Qian, W.; Jian, J.; Zhang, X.; Wang, H.; Yang, H., Dielectric Relaxation, Resonance and Scaling Behaviors in $Sr_3Co_2Fe_{24}O_{41}$ Hexaferrite. *Sci. Rep.* **2015,** *5*, 13645.

(37) Dominguez, M.; Taboada, E.; Idriss, H.; Molins, E.; Llorca, J., Fast and Efficient Hydrogen Generation Catalyzed by Cobalt Talc Nanolayers Dispersed in Silica Aerogel. *J. Mater. Chem.* **2010,** *20*, 4875-4883.

(38) Cao, D.; Wang, X.; Pan, L.; Li, H.; Jing, P.; Wang, J.; Liu, Q., Nonmetal Sulfur-Doped Coral-Like Cobalt Ferrite Nanoparticles with Enhanced Magnetic Properties. *J. Mater. Chem. C* **2016,** *4*, 951-957.

(39) Kumar, B.; Asadi, M.; Pisasale, D.; Sinha-Ray, S.; Rosen, B. A.; Haasch, R.; Abiade, J.; Yarin, A. L.; Salehi-Khojin, A., Renewable and Metal-Free Carbon Nanofibre Catalysts for Carbon Dioxide Reduction. *Nat. Commun.* **2013,** *4*.

(40) Kondo, T.; Guo, D.; Shikano, T.; Suzuki, T.; Sakurai, M.; Okada, S.; Nakamura, J., Observation of Landau Levels on Nitrogen-Doped Flat Graphite Surfaces Without External Magnetic Fields. *Sci. Rep.* **2015,** *5*, 16412.

(41) Li, J.; Lu, G.; Wu, G.; Mao, D.; Guo, Y.; Wang, Y.; Guo, Y., Effect of TiO_2 Crystal Structure on the Catalytic Performance of Co_3O_4/TiO_2 Catalyst for Low-Temperature CO Oxidation. *Catal. Sci. Technol* **2014,** *4*, 1268-1275.

(42) Moura, K. O.; Lima, R. J. S.; Coelho, A. A.; Souza-Junior, E. A.; Duque, J. G. S.; Meneses, C. T., Tuning the Surface Anisotropy in Fe-doped NiO Nanoparticles. *Nanoscale* **2014,** *6*, 352-357.

(43) Balan, B. K.; Manissery, A. P.; Chaudhari, H. D.; Kharul, U. K.; Kurungot, S., Polybenzimidazole Mediated N-Doping Along the Inner and Outer Surfaces of a Carbon Nanofiber and its Oxygen Reduction Properties. *J. Mater. Chem.* **2012,** *22*, 23668-23679.

(44) Jäger, R.; Härk, E.; Romann, T.; Joost, U.; Lust, E., C(Mo_2C) and Pt–C(Mo_2C) Based Mixed Catalysts for Oxygen Reduction Reaction. *J. Electroanal. Chem.* **2016,** *761*, 89-97.

(45) Balan, B. K.; Kurungot, S., Highly Exposed and Activity Modulated Sandwich Type Pt Thin Layer Catalyst with Enhanced Utilization. *J. Mater. Chem.* **2011,** *21*, 19039-19048.

(46) Lim, D.-H.; Wilcox, J., Mechanisms of the Oxygen Reduction Reaction on Defective Graphene-Supported Pt Nanoparticles from First-Principles. *J. Phys. Chem. C* **2012,** *116*, 3653-3660.

(47) Niu, W.; Li, L.; Liu, X.; Wang, N.; Liu, J.; Zhou, W.; Tang, Z.; Chen, S., Mesoporous N-Doped Carbons Prepared with Thermally Removable Nanoparticle Templates: An Efficient Electrocatalyst for Oxygen Reduction Reaction. *J. Am. Chem. Soc.* **2015**.

(48) Shao, M.; Peles, A.; Shoemaker, K., Electrocatalysis on Platinum Nanoparticles: Particle Size Effect on Oxygen Reduction Reaction Activity. *Nano Lett.* **2011,** *11*, 3714-3719.

(49) He, G.; Song, Y.; Liu, K.; Walter, A.; Chen, S.; Chen, S., Oxygen Reduction Catalyzed by Platinum Nanoparticles Supported on Graphene Quantum Dots. *ACS Catal.* **2013,** *3*, 831-838.

(50) Prabu, M.; Ramakrishnan, P.; Nara, H.; Momma, T.; Osaka, T.; Shanmugam, S., Zinc–Air Battery: Understanding the Structure and Morphology Changes of Graphene-Supported $CoMn_2O_4$ Bifunctional Catalysts Under Practical Rechargeable Conditions. *ACS Appl. Mater. Interfaces* **2014,** *6*, 16545-16555.

(51) Chakkaravarthy, C.; Waheed, A. K. A.; Udupa, H. V. K., Zinc—Air Alkaline Batteries — A Review. *J. Power Sources* **1981,** *6*, 203-228.

(52) Lee, J.-S.; Tai Kim, S.; Cao, R.; Choi, N.-S.; Liu, M.; Lee, K. T.; Cho, J., Metal–Air Batteries with High Energy Density: Li–Air versus Zn–Air. *Adv. Energy Mater.* **2011,** *1*, 34-50.

(53) Nam, G.; Park, J.; Choi, M.; Oh, P.; Park, S.; Kim, M. G.; Park, N.; Cho, J.; Lee, J.-S., Carbon-Coated Core–Shell Fe–Cu Nanoparticles as Highly Active and Durable Electrocatalysts for a Zn–Air Battery. *ACS Nano,* **2015,** *9*, 6493-6501.

(54) Fu, J.; Lee, D. U.; Hassan, F. M.; Yang, L.; Bai, Z.; Park, M. G.; Chen, Z., Flexible High-Energy Polymer-Electrolyte-Based Rechargeable Zinc–Air Batteries. *Adv. Mater.***2015,** *27*, 5617-5622.

(55) Li, Y.; Gong, M.; Liang, Y.; Feng, J.; Kim, J.-E.; Wang, H.; Hong, G.; Zhang, B.; Dai, H., Advanced Zinc-Air Batteries based on High-Performance Hybrid Electrocatalysts. *Nat. Commun.* **2013,** *4*, 1805.

(56) Zhu, S.; Chen, Z.; Li, B.; Higgins, D.; Wang, H.; Li, H.; Chen, Z., Nitrogen-Doped Carbon Nanotubes as Air Cathode Catalysts in Zinc-Air Battery. *Electrochimi. Acta.* **2011,** *56*, 5080-5084.

(57) Prabu, M.; Ramakrishnan, P.; Nara, H.; Momma, T.; Osaka, T.; Shanmugam, S., Zinc–Air Battery: Understanding the Structure and Morphology Changes of Graphene-Supported $CoMn_2O_4$Bifunctional Catalysts Under Practical Rechargeable Conditions. *ACS Appl. Mater. Interfaces*, **2014,***6*, 16545-16555.

(58) Sun, Y.; Li, C.; Shi, G., Nanoporous Nitrogen Doped Carbon Modified Graphene as Electrocatalyst for Oxygen Reduction Reaction. *J. Mater. Chem.***2012,***22*, 12810-12816.

(59) Singh, S. K.; Dhavale, V. M.; Kurungot, S., Surface-Tuned Co_3O_4 Nanoparticles Dispersed on Nitrogen-Doped Graphene as an Efficient Cathode Electrocatalyst for Mechanical Rechargeable Zinc–Air Battery Application. *ACS Appl. Mater. Interfaces*, **2015,***7*, 21138-21149.

(60) Dhavale, V. M.; Kurungot, S., Cu–Pt Nanocage with 3-D Electrocatalytic Surface as an Efficient Oxygen Reduction Electrocatalyst for a Primary Zn–Air Battery. *ACS Catal.***2015,** *5*, 1445-1452.

Chapter 4

Structural Modification in the Spinel Cobalt Ferrite Matrix with Zn Substitution for Enhanced Oxygen Reduction Reaction

Development of highly efficient and durable ORR catalysts by using non-platinum group metals (such as Co, Fe, Mn, and Zn) is a challenging task in the forward path towards the realization of low-cost energy devices in the commercial stream. The present work deals with an effective strategy wherein an efficient Pt-free electrocatalyst for oxygen reduction reaction (ORR) is prepared by stoichiometrically substituting some fraction of Fe with Zn in cobalt ferrite and anchoring these spinel nanoparticles on nitrogen doped reduced graphene oxide (N-rGO). Zn substitution is found to be significantly altering the ratio of Fe^{2+}/Fe^{3+} in the cobalt ferrite nanocrystal system with a concomitant promotional influence on its electrocatalytic activity towards ORR. The nanoparticle composition with a Co, Fe and Zn molar ratio of 1.0:1.7:0.3, represented by the formula $CoFe_{1.7}Zn_{0.3}O_4$(CFZn(0.3)), supported over N-rGO has shown 10 mV and 20 mV positive shift in the onset and half-wave potentials, respectively, for ORR in 0.1 M KOH in comparison to the nanoparticles of $CoFe_2O_4$ supported over N-rGO (CF/N-rGO). The optimum Zn substitution is found to be narrowing down the difference with the state-of-the-art Pt/C for ORR by 100 and 110 mV in terms of the onset and half-wave potentials, respectively. Most significantly, the homemade catalyst is found to be clearly outperforming the Pt catalyst in terms of the limiting current density and electrochemical durability.

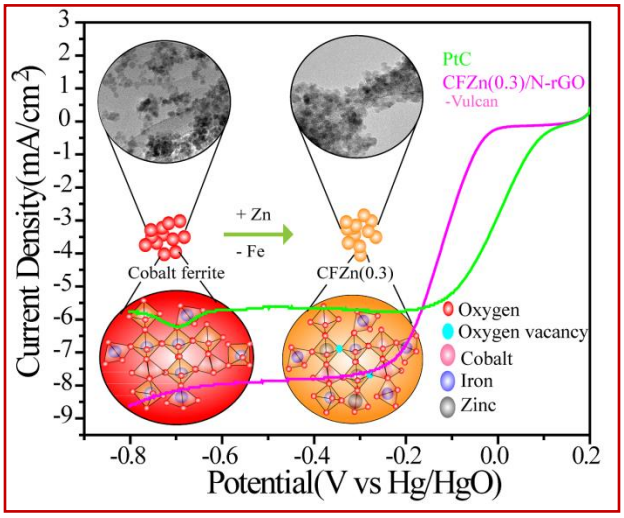

*The content of this chapter is published in "*ChemistrySelect* **2017,** *2*, 7845-7853."
-Reproduced with permission from *ChemistrySelect*, ***License No.*** *4436440418358.*

4.1. Introduction

The continuously growing gap between the energy requirement and availability along with the stringent environmental regulations in place to enforce gradual switch over to clean energy technologies have invited substantial attention on renewable energy storage and conversion devices. The next-generation energy devices like polymer electrolyte membrane fuel cells (PEMFCs)[1-3,] and metal air batteries[4-8] have great potential to overcome these issues related to the ever increasing energy demand and environmental impact. In spite of having efficient technologies in place for these systems, cost and durability of the state-of-the-art electrocatalysts make their market penetration extremely difficult.[9-10] Especially, due to the sluggish kinetics of the oxygen reduction reaction (ORR), Pt has invariably become the major ingredient in the cathode of a PEMFC and metal air batteries.[11-12] Alloys of Pt with other non-noble metals have the capability to perform better compared to pure Pt systems in terms of overpotential for ORR, but, the systems still suffer from the issues related to cost and durability.[9, 13-14] To come out of this juncture, it is important to ensure that the electrodes for the future energy systems will be free of Pt and other noble metals. Considering the fact that no other single metal component system is as active as the Pt systems for facilitating ORR, the success of realizing Pt or noble metal-free systems for ORR is entirely depending on how well one can design a multi-metallic system by effectively making use of synergistic interactions and electronic modulations to favour ORR. This requires judicious selection of the component materials, fixing the compositions to the optimum levels and development of strategies to anchor the active components on a conducting support which can further contribute towards activity modulation by facilitating faster electron transfer.

In this context, there has been a significant effort to explore various transition metal derivatives such as oxides,[15-16] oxynitrides,[17-18] chalcogenides,[19] and their hybrids with heteroatom-doped carbons for ORR as Pt-free alternatives. There is also increasing focus on developing hybrid catalysts comprising of the above-mentioned Pt-free systems with various graphitic carbon substrates by building synergistic interactions through heteroatom doping.[6, 20-22] Among such systems, the spinel oxides like $MnCo_2O_4$,[21, 23] $CoMn_2O_4$,[5] Co_3O_4,[4, 24-25] Fe_3O_4[26] and $CuCo_2O_4$[22] covalently linked with nitrogen doped graphene (NGr) have been explored as alternative catalysts with promising potentials.

Some of them, especially the spinel cobaltites, have been widely investigated as efficient bi-functional catalysts for facilitating both ORR and oxygen evolution reaction (OER). In an interesting work by Yang *et. al*., it has been reported that $CoFe_2O_4$/graphene nanohybrid works as an efficient bi-functional electrocatalyst for both ORR and OER.[27]The reported overpotentials for ORR and OER for this system compared to the PtC catalyst are 136 and 80 mV, respectively. In the previous chapter, we have highlighted a system based on $CoFe_2O_4$ nanoparticles supported over N-rGO as an efficient electrocatalyst towards ORR.[28] The catalyst displayed an ORR overpotential of 110 mV and a half-wave potential ($\delta E_{1/2}$) of 120 mV in comparison to PtC, all the while displaying excellent durability. Apart from the synergistic interactions operating between N-rGO and $CoFe_2O_4$, spatial separation of the catalyst particles by using activated carbon as a spacer also played a critical role in substantially reducing the overpotential.[29] These results clearly reveal that with a judicious strategy in place to essentially tune the intrinsic activity, electrical conductivity, and mass transfer requirements, it is practically achievable to reach a performance zone offered by the Pt catalysts.

The present chapter aims to explore how the possible electronic modulations generated by substituting some portion of Fe by Zn in the spinel lattice of cobalt ferrite nanocrystals supported over N-rGO can favourably influence to reduce the overpotential for ORR. In spinel metal oxides, oxygen ions are packed in cubic arrangement (ccp) and metal atoms share the octahedral and tetrahedral sites.[30-31] Spinel oxides have mixed valency (M^{2+} and M^{3+}) which involves the faster movement of electrons during the catalytic process by following hopping mechanism. For a normal spinel, the tetrahedral sites are occupied by divalent metal atoms and the octahedral sites by the trivalent metal atoms.[30] In a real system, partial inversion can take place by interchanging the sites of the trivalent and bivalent metal atoms to some extent, which follows the general formula:

$$(M_{\sigma}^{II}Fe_{1-\sigma}^{III})(M_{1-\sigma}^{II}Fe_{1+\sigma}^{III})O_4$$

where, (1-σ) represents the inversion parameter for the spinel structures. Even though cobalt ferrite ($CoFe_2O_4$) based systems have been studied as magnetic materials and a general heterogeneous catalysts, their electrochemical applications are not thoroughly

investigated with the consideration of the inversion parameter as a possible activity modulating factor. The present chapter, therefore, is a focused attempt to understand how the overpotential for ORR can be tuned by manipulating the extent of inversion of $CoFe_2O_4$ through Zn substitution. Here, we have synthesized Zn substituted cobalt ferrite with the compositional variation represented as $CoFe_{2-x}Zn_xO_4$ (x= 0-0.3), following a solvothermal synthesis procedure.[31-32] The composition corresponding to x = 0.3 displayed high ORR activity in terms of the onset and half-wave potentials ($E_{1/2}$). Zn substituted cobalt ferrite is supposed to be a mixed spinel due to the preference of the Zn^{2+} ions to occupy in the tetrahedral sites by replacing the stoichiometric amount of the Fe^{3+} ions present in the tetrahedral site of the inverse spinel lattice of $CoFe_2O_4$. However, the occupation of Zn^{2+} in the cobalt ferrite matrix generates oxygen vacancies which are related to catalytic enhancement.[33-34] This controlled alteration in the spinel lattice composition along with the synergistic interactive benefits achieved by anchoring the spinel nanoparticles on the nitrogen doped reduced graphene oxide (N-rGO) surface is found to be significantly helping the system to reduce the overpotential towards ORR.

4.2. Experimental Section

4.2.1. Synthesis of Zn Substituted Cobalt Ferrite/N-doped Reduced Graphene Oxide (CFZn/N-rGO): In a typical synthesis procedure, N-rGO was synthesized followed by metal oxide loading. For preparing N-rGO, 200 mg of GO was dispersed in 50 mL of DI water, followed by the addition of 50 mL ammonium hydroxide solution in a round-bottom flask. The obtained reaction mixture was kept for refluxing at 80 ^oC for 12 h. The obtained solution was filtered and kept for drying at room temperature. The resulted powder sample was identified as N-rGO. In order to decorate the metal oxide nanoparticles over the N-rGO surface, cobalt acetate, iron acetate, and zinc acetate were taken as the metal precursors. The molar ratios of cobalt, iron and zinc were varied to obtain three different catalysts, *i.e.*, $CoFe_{1.7}Zn_{0.3}$/N-rGO, $CoFe_{1.8}Zn_{0.2}$/N-rGO and $CoFe_{1.9}Zn_{0.1}$/N-rGO, which are respectively designated as CFZn(0.3)/N-rGO, CFZn(0.2)/N-rGO, and CFZn(0.1)/N-rGO. As an example, for the synthesis of CFZn(0.3)/N-rGO, 50 mg of N-rGO was dispersed in 1:1 mixture of ethanol and water

followed by the addition of 50 mg of the acetate salts in the ratio of 1:1.7:0.3 for cobalt, iron, and zinc. The above reaction mixture was stirred for 24 h and kept for hydrothermal treatment in 100 mL autoclave at 130 ^{o}C for 12 h. The finally obtained solution was filtered, and the filtrate was dried at 60 ^{o}C for 4 h to obtain CFZn(0.3)/N-rGO. A similar procedure was followed for the preparation of the other composite catalysts. N-rGO supported $CoFe_2O_4$ (*i.e.*, the parent system without any Zn substitution) was also prepared by following the same procedure without adding the Zn precursor, and this sample is designated as CF/N-rGO. All the prepared composite materials were mixed with Vulcan carbon in the ratio of 2:8 for obtaining the final catalyst material for the ORR studies.

4.2.2. ICP measurement: For ICP measurement, the samples were prepared in the following manner. The ferrite nanoparticles were digested in the aqua regia (3:1 HCL/HNO_3). As such digested sample was heated up to 95 ^{o}C for 3 h under magnetic stirring, followed by heating at 200 ^{o}C for 15 min. The sample was cooled and diluted using DI water. The diluted sample was syringe filtered and the concentration was made in the ppm level for analysis. The chemical formula was calculated from the metal presence and considering the absence of anion vacancies.

4.3. Result and Discussion

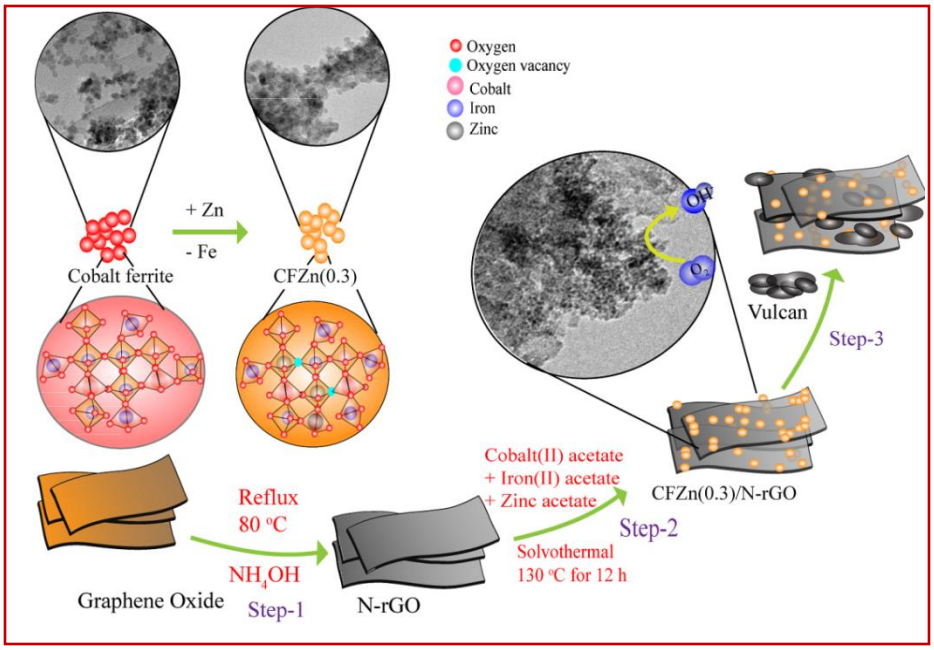

Figure 4.1. *Schematic illustration of the process involved in the controlled distribution of the Zn-substituted cobalt ferrite nanoparticles on N-rGO followed by spatially separating*

the N-rGO sheets with the help of Vulcan carbon to ensure better accessibility of the dispersed ferrite nanoparticles.

Figure 4.1 is showing a schematic presentation for the synthesis of N-rGO supported Zn-substituted cobalt ferrite nanocrystallites. As illustrated in the experimental section, the synthesis of the catalyst involves a three-step process: the first step involves the synthesis of N-rGO using ammonium hydroxide as the nitrogen precursor followed by the second step, which takes care of the *in-situ* decoration of the Zn-substituted cobalt ferrite nanoparticles on N-rGO. In the third step, Vulcan carbon was added to spatially separate the N-rGO layers bearing the cobalt ferrite nanoparticles to ensure better accessibility of the active sites in the system. The scheme clearly highlights the key steps involved in the preparation route.

4.3.1. TEM Analysis:

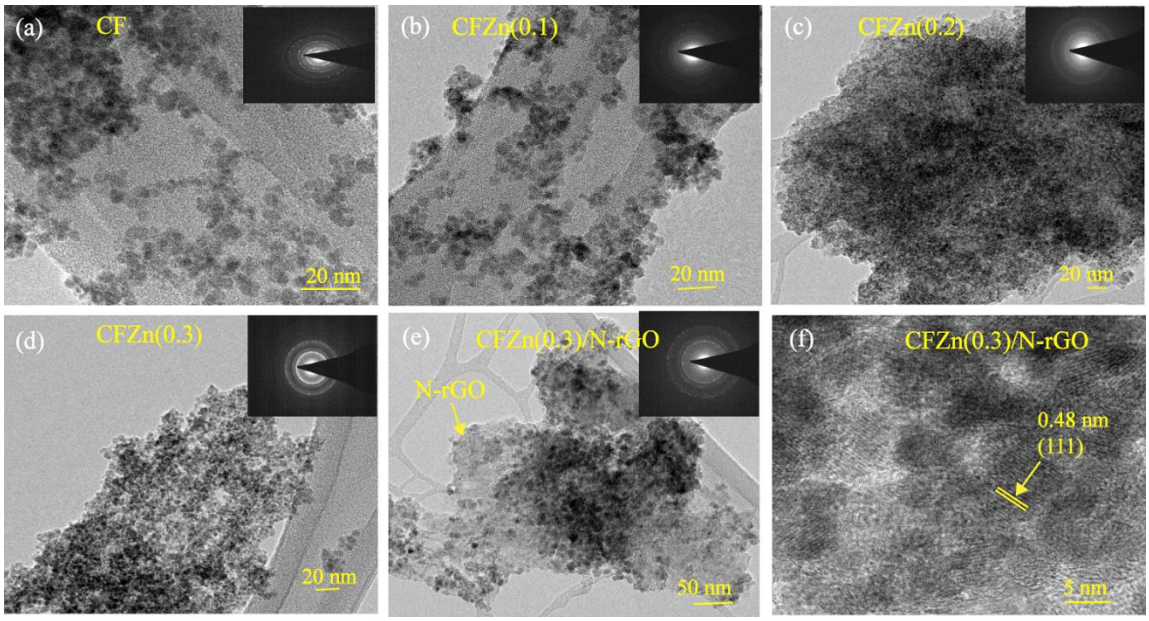

Figure 4.2. *(a), (b), (c) and (d) are the TEM images of the Zn-free (CF) and Zn-substituted (CFZn(0.1), CFZn(0.2) and CFZn(0.3)) cobalt ferrite nanoparticles. The diffused rings in the selected area electron diffraction patterns (SAED), which is a characteristic of the nanocrystalline particles, are presented in the inset of the images. Images (e) and (f) are the TEM images of CFZn(0.3)/N-rGO. Image (f) represents the nanocrystalline nature of the particles with a size of 3-6 nm and a d-spacing value of 0.48 nm corresponding to the (111) plane of CFZn(0.3).*[31]

The morphology and structure of the Zn substituted cobalt ferrite, and its Zn-free parent samples were explored by transmission electron microscopy (TEM) analysis. **Figure 4.2** shows the TEM and HRTEM images of the unsupported CF, CFZn(0.1), CFZn(0.2), CFZn(0.3) and the N-rGO supported CFZn(0.3), *i.e.*, CFZn(0.3)/N-rGO, samples. **Figure 4.2a**, **4.2b**, **4.2c**, and **4.2d** show that the Zn-free and Zn-substituted cobalt ferrite particles are nanocrystalline in nature, which is also revealed by their corresponding diffused rings of the selected area electron diffraction (SAED) patterns presented in the inset of the respective images. From the discussion, as can be seen in a later part of the chapter, it is also observed that, along with the nanocrystalline nature of the CFZn particles, the surface of the particles bears a carbon layer due to the decomposition of the acetate salts. The size of the particles is found to be in the range of 3-6 nm. The same size distribution could be maintained after their decoration on N-rGO, as evident from the TEM images of CFZn(0.3)/N-rGO presented in **Figure 4.2e** and **4.2f**. Unlike the unsupported case where the systems are supposed to be prone towards sintering and electrochemical leaching, anchoring of the particles on N-rGO has been proved as an efficient method to overcome such limitations in addition to the benefit of having a conductive backbone.[35-38]Doping of nitrogen in the graphene framework provides nucleating and anchoring sites for the growth of the nanoparticles during the solvothermal synthesis. Such sites, while playing a key role in anchoring the nanoparticles, can influence the active sites located on the substrate and induce electronic modulations due to the synergistic interactions originated due to the modified electron density and lattice overlapping. Dispersion on the graphene substrate through the intervention of the doped nitrogen atoms is also expected to improve the corrosion resistance of the material.[39-40] The size-controlled (3-6 nm) and aggregate-free dispersion of CFZn(0.3) on N-rGO validates healthy coexistence of the moieties on the fertile surface of N-rGO. **Figure 4.2f** exhibits the single crystalline nature of the nanoparticles with an estimated d-spacing value of 0.48 nm corresponding to the (111) plane of CFZn(0.3).[31] Furthermore, the substitution of Zn in the cobalt ferrite nanoparticles has been confirmed through EDAX analysis (**Figure 4.3**), which shows the distribution of Zn in the system along with the cobalt and iron atoms.

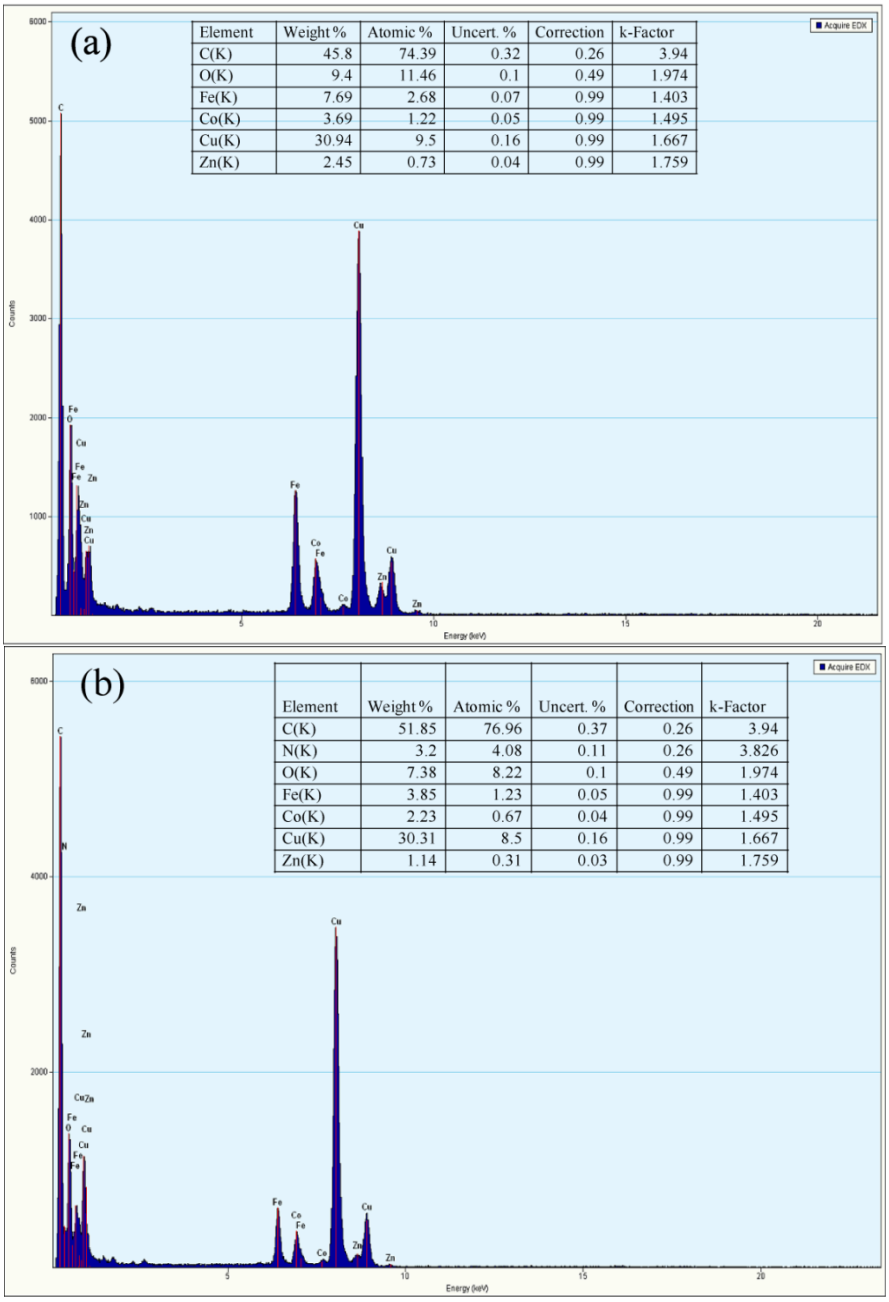

Figure 4.3. *(a) and (b)are the EDAX data of CFZn(0.3) and CFZn(0.3)/N-rGO, respectively.*

4.3.2. XRD Analysis: A more insightful information on the spinel nature of $CoFe_{2-x}Zn_xO_4$ and the corresponding metal content in the samples has been gained through powder X-ray diffraction (PXRD) analysis and inductively coupled plasma-adsorption energy spectroscopy (ICP-AES) analysis, respectively. In the ferrite structure, Zn substitution can be effected in the crystal structure of either in the place of cobalt or iron.[31-32] Here, in the adopted synthesis procedure, we have substituted Zn for iron,

whereas, the possible extent of cobalt in the octahedral sites remains the same. The PXRD pattern presented in **Figure 4.4a** matches with cobalt ferrite (**JCPDS 22-1086**).

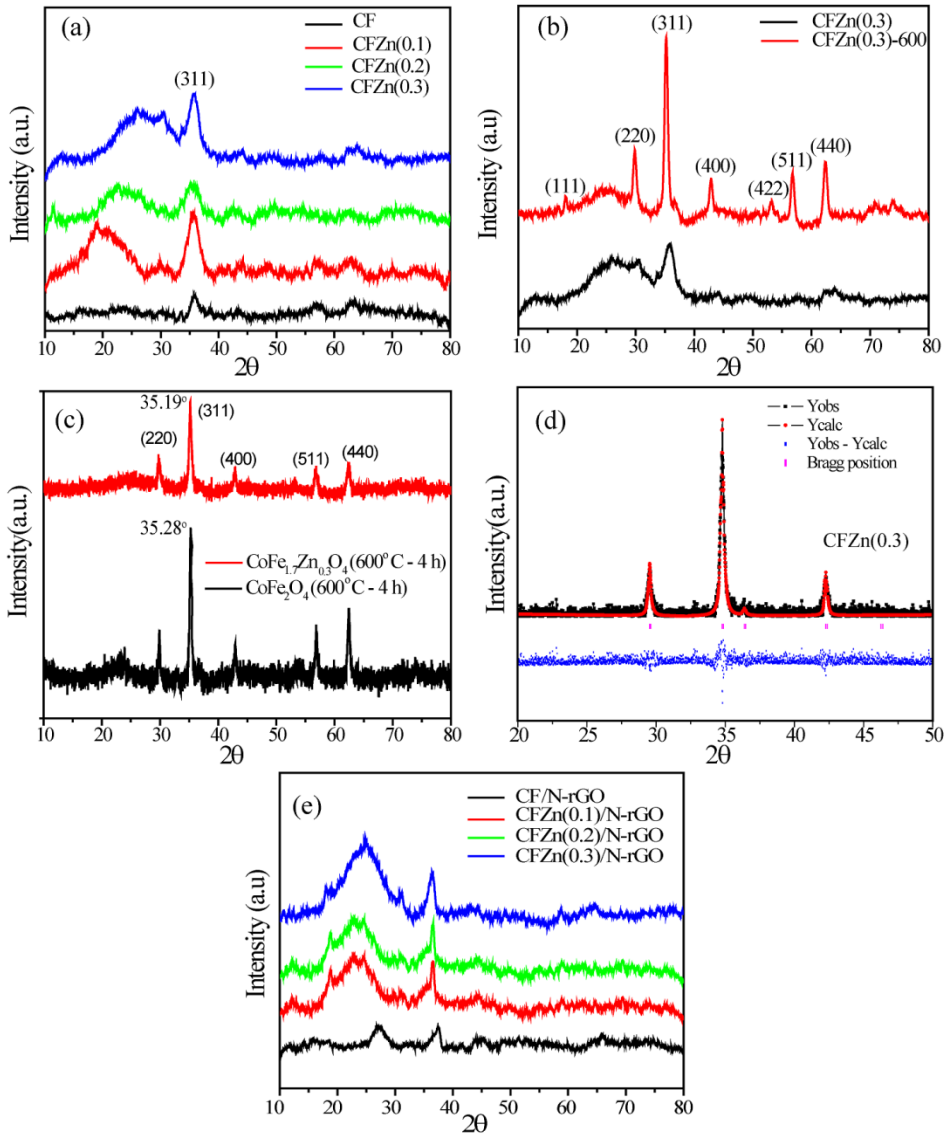

Figure 4.4.*(a) PXRD profiles of the cobalt ferrite (CF) and unsupported Zn substituted cobalt ferrite nanocrystals prepared through the solvothermal process,(b) PXRD profiles of CFZn(0.3) before (black line) and after (red line)annealing in air for 4 h at 600 °C,(c) PXRD pattern of the CFZ(0.3) and CF nanoparticle after annealing in air at 600 °C for 4 h,(d) the Retvield refinement of the PXRD pattern of the CFZn(0.3) nanoparticle after annealing at 600 °C for 4 h and (e) PXRD profiles of the Zn substituted cobalt ferrite nanocrystals supported over N-doped reduced graphene oxide.*

The occupation of the octahedral and tetrahedral sites varies with the Zn-substitution, and hence the lattice parameter also varies accordingly.[16, 41-43] The PXRD profile presented in

Figure 4.4a indicates the intense peak at the 2θ value of 35.6° corresponding to the (311) plane of the cobalt ferrite, whereas, less intense peaks appear at the 2θ values the (400), (511) and (440) for the respective planes of cobalt ferrite (**JCPDS 22-1086**).[27]Thus, from the PXRD profiles, it could be confirmed that the solvothermal synthesis conditions and thermal decomposition of the acetate salt predominantly lead to the formation of the spinel structure. The presence of less crystalline carbon on the nanocrystals hinders the diffraction intensity from the crystalline nanoparticles. In the PXRD spectra presented in **Figure 4.4a**, a broad peak was observed at a 2θ value of 26°, which changes its position with respect to the degree of Zn substitution in the system due to the variation in degree of graphitization.[44] The observed peak arises from less crystalline carbon, which is expected to be formed from the decomposition of the acetate salt during the hydrothermal treatment. Even though some specific crystal planes corresponding to the spinel phase are less intense in **Figure 4.4a**, such peaks are well resolved, once the sample was subjected to calcination at 600 °C for 4h in air (**Figure 4.4b**). Annealing of the catalyst at high temperature allows the nanoparticles to recrystallise and form bigger grain size.[45] Moreover, for the better comparison, the parent cobalt ferrite nanoparticles were also annealed at 600 °C for 4 h and a shift in the intensity of the peak was noted (**Figure 4.4c**). In order to understand the effect of Zn^{2+}substitution in the cobalt ferrite lattice, Rietveld refinement was performed for the annealed sample (**Figure 4.4d**). In the refined spectra, the lattice parameter was observed to be increasing from the parent cubic cobalt ferrite ($Fd\bar{3}m$, a = 8.391) structure to CFZn(0.3) ($Fd\bar{3}m$, a =8.542).The observed change in the lattice parameter proves the concept of Zn^{2+} substitution in the cobalt ferrite lattices. The PXRD profiles of the N-rGO supported catalysts are presented in **Figure 4.4e**. A comparison of **Figure 4.4a** and **4.4e** clearly indicates that the spinel phases present in the unsupported systems are completely retained in their N-rGO supported counterparts as well. Also, an increased intensity of the peak corresponding to the crystalline graphitic carbon (002) plane is observed for the supported catalysts in **Figure 4.4e**, justifying the higher graphitic carbon content in these systems.

4.3.3. Thermogravimetric Analysis (TGA): To estimate the percentage loading of the ferrite nanoparticles over N-rGO, thermogravimetric analysis (TGA) has been performed under an air atmosphere with a temperature ramp of 10 °C min^{-1} up to 600 °C.

The corresponding comparative TGA profiles for CFZn(0.3)/N-rGO and its unsupported counterpart, CFN(0.3), are presented in **Figure 4.5**. The weight loss in the temperature range of 250-300 ^{o}C in the case of CFZn(0.3) is attributed to the burning of the carbon deposition over the metal oxide surface. In the case of CFZn(0.3)/N-rGO, the weight loss of nearly 10% occurred up to 100 ^{o}C is expected to be originated from the moisture content in the sample. Followed by this, the weight loss observed in the range of 250-400 ^{o}C is responsible for the carbon burning, which includes both the surface carbon on the nanoparticles and the support carbon of the N-rGO. The residue content of 30% remained after 400 ^{o}C is corresponding to total metal oxide loading in the system, suggesting a 3:7 metal oxide to carbon ratio in the parent sample.[46-47]

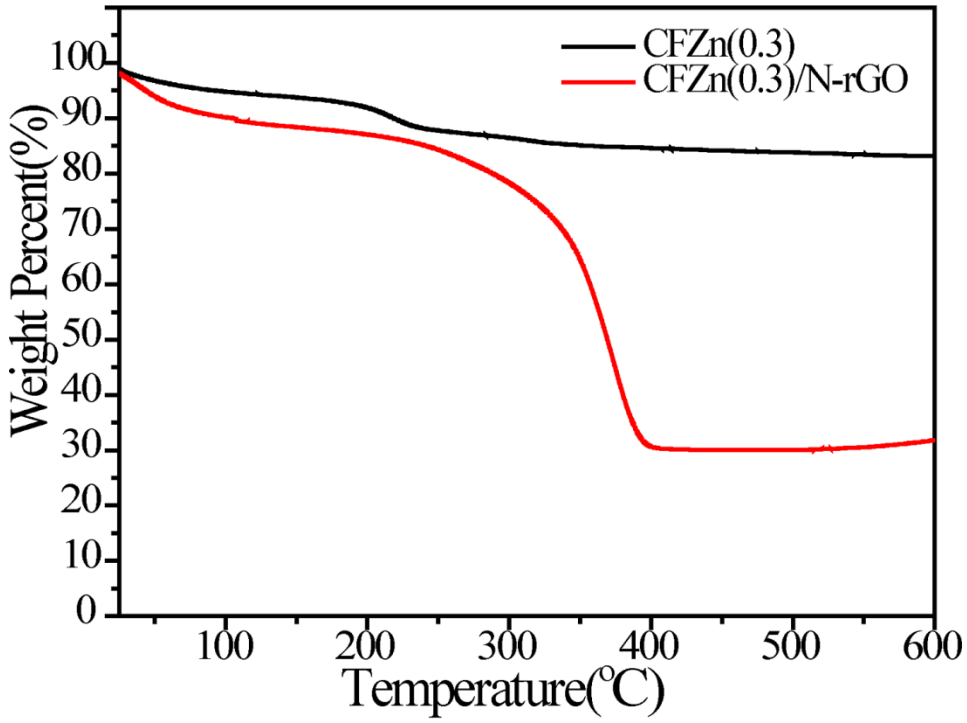

Figure 4.5. *TGA profiles for the unsupported and N-rGO supported CFZn(0.3).*

4.3.4. Infrared (IR) Spectroscopy Analysis: As a supplementary tool to probe the presence of the carbon layer on the ferrite surface, the composite materials prepared were investigated through FTIR analysis (**Figure 4.6**). Although the preparation protocol involves several washing steps in order to remove the carbon formed over the surface of CFZn particles, still the surface of the nanoparticles is found to be bound to organic molecules.[48] The peaks present at 1560 and 1401 cm^{-1} correspond to the asymmetric and

symmetric stretch of the COO^- group, respectively. A peak for the C-O bond also appears at 1075 cm^{-1}. The peaks in the three composites vary their position and features as the surface exposed metal composition changes. As explained before, with increasing the Zn concentration, concomitantly more iron is displaced. The change in the carbonyl functional group peak intensity (COO^-) with respect to the Zn substitution can be clearly identified in the FTIR spectral data presented in **Figure 4.6**.

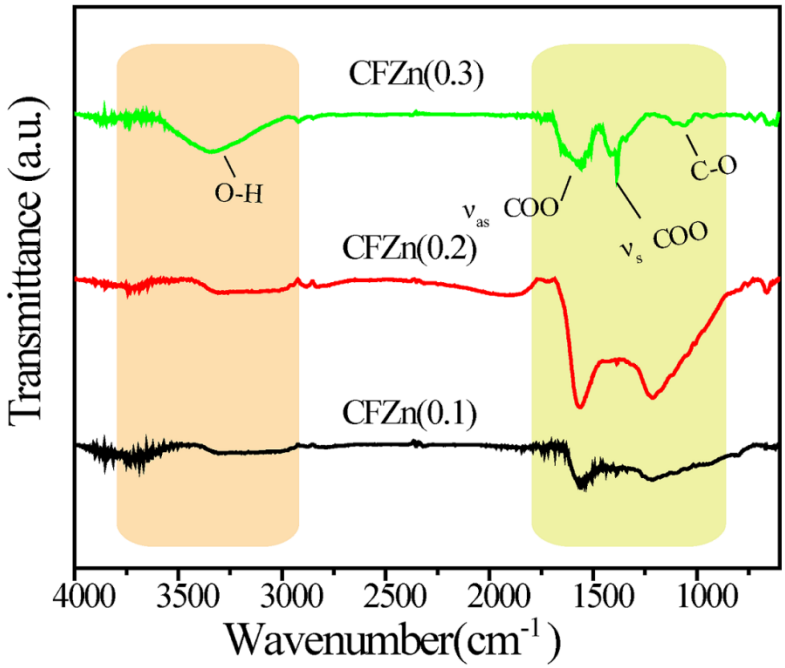

Figure 4.6. *FTIR spectra of CFZn(0.1), CFZn(0.2) and CFZn(0.3). The peak at 1075 cm^{-1} is designated as the C-O functional group. The other two peaks in the lower wavenumber region are corresponding to the symmetric and asymmetric stretching of the –COO functional group.*

A distinct difference in the intensity and feature of the peaks in the region of 1000 -1700 cm^{-1} for the three samples is clearly evident in **Figure 4.6**.[31] In the case of CFZn(0.3), the broad peak appeared in the region 3000-3500 cm^{-1} reveals the presence of the –OH functionality, and this is caused by the replacement of some amount of the Fe^{3+} ions by the Zn^{2+} ions. The EDAX data, which is a surface technique, presented in **Figure 4.3** sheds light on the exposure of more Fe moieties on the CFZn(0.3) nanocrystal surface. Here, it should be noted that for the EDAX analysis, a 20 μm *x* 20 μm length and width of sample was considered. Though the general penetration depth of the incident electron beam is ~1-2 μm, since the composite material solid ferrite, the penetration depth might get reduced. Further, the agglomeration in the particles also likely to hinder the depth

analysis of the sample. The high Fe content over the surface might be caused by the movement of the iron moieties from the tetrahedral to the octahedral sites in accordance with the Zn^{2+} substitution. Such exposed Fe moieties on the surface of the nanoparticles can form Fe-OH bonds, which is evident from the characteristic –OH group signature in the IR spectra.

4.3.5. XPS Analysis

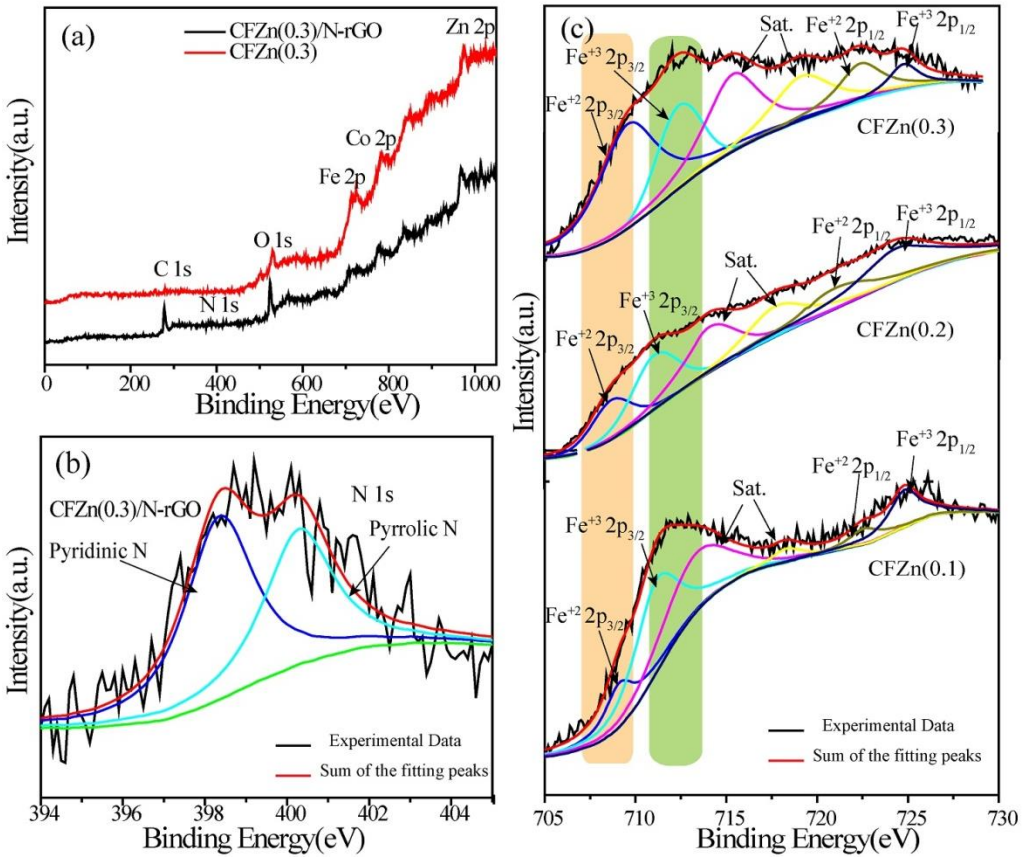

Figure 4.7. *(a) XPS survey spectra of CFZn(0.3) and CFZn(0.3)/N-rGO, (b) deconvoluted N 1s spectra showing the pyridinic and pyrrolic type of nitrogen coordinations in the system and (c) deconvoluted Fe 2p XPS spectra in the unsupported composites with different degree of Zn substitution.*

In order to understand more clearly on the state of the composition of the prepared catalysts, X-ray photoelectron spectroscopic (XPS) investigation was performed. **Figure 4.7a** shows the comparative survey scan spectrum of CFZn(0.3) and CFZn(0.3)/N-rGO. The peaks at the binding energy (BE) values of 285.29, 531.61, 714.08, 784.46 and 1020.36 eV are assigned to the C 1s, O 1s, Fe 2p, Co 2p and Zn 2p states respectively.[49-50]

An extra peak at 399.32 eV (**Figure 4.7a** and **4.7b**) seen in the XPS spectra of CFZn(0.3)/N-rGO is corresponding to the doped N 1s state of N-rGO. Deconvolution of this peak (**Figure 4.7b**) shows two peaks corresponding to the pyridinic and pyrrolic nitrogens at 398.36 and 400.40 eV respectively.[51] The active role of the pyridinic-N towards the enhancement of the ORR activity is already known in the literature.[51-54]The oxidation states of the metal entities have also been confirmed through the deconvolution of the Fe peak appeared in the survey spectrum presented in **Figure 4.7c**.[49-50] The deconvoluted Fe 2p spectra presented in **Figure 4.7c** show the presence of divalent (2+) and trivalent (3+) Fe ions in the unsupported composites with different degree of Zn substitution. The electronic exchange between Fe^{2+} and Fe^{3+} produces the p-type of the carriers.[55]The charge carriers arise from the loss of oxygen during the solvothermal synthesis. A close inspection of the deconvoluted spectra for all the three samples (*i.e.*, CFZn(0.1), CFZn(0.2) and CFZn(0.3)) shows a distinct variation in the relative concentrations of the Fe^{2+} and Fe^{3+} moieties with respect to the compositional difference.

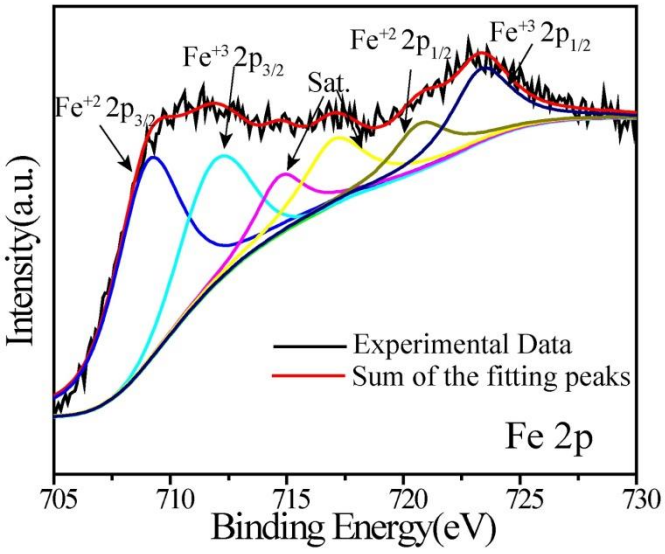

Figure 4.8. *Deconvoluted Fe 2p XPS spectra of CFZn(0.3)/N-rGO.*

It is mentioned previously that in the inverse spinel lattice, the Fe^{3+} state occupies the tetrahedral site whereas the Co^{2+}/Fe^{2+} state favours the octahedral site. From the XPS analysis, it has been observed that the ratio of Fe^{2+}/Fe^{3+} increases with the Zn^{2+} substitution. The observed Fe^{2+}/Fe^{3+} ratios are found to be 0.37, 0.60 and 1.70 for CFZn(0.1), CFZn(0.2) and CFZn(0.3) catalysts respectively. Increased Fe^{2+}/Fe^{3+} ratio in

CFZn(0.3) is in accordance with the replacement of Fe^{3+} with the Zn^{2+} ions in the tetrahedral site.[31,32] The presence of divalent Zn^{2+} ion in the trivalent Fe^{3+} site of the cobalt ferrite structure favours the formation of oxygen vacancies (Vo) to maintain the crystal neutrality.[32, 56] The observed binding energy shift in the Fe^{2+} and Fe^{3+} state of the composites hints out towards the change in the electronic environment due to the Zn^{2+} substitution in the system. The deconvoluted spectra of the Fe 2p state of CFZn(0.3)/N-rGO is shown in **Figure 4.8**.

4.3.6. Electrochemical Characterization: To evaluate how the Zn substitution and the associated changes in the cationic distribution of the spinel phase modulated the ORR characteristics of the system, the corresponding electrochemical evaluations were carried out in 0.1 M KOH solution as the electrolyte. **Figure 4.9a** shows the comparative cyclic voltammograms (CVs) of CFZn(0.1)/N-rGO-Vulcan, CFZn(0.2)/N-rGO-Vulcan and CFZn(0.3)/N-rGO-Vulcan measured at a voltage sweep rate of 50 mVs^{-1} in oxygen saturated and nitrogen saturated 0.1 M KOH solution. In all the cases, under oxygen enriched conditions, a characteristic oxygen reduction peak can be clearly seen in the CV profiles with a peak potential at -0.140 V *vs.* Hg/HgO. The Zn^{2+} substitution in the ferrite structure alters the atomic distribution over the surface of the nanoparticles. A significant change in the charging current could be attributed to the interface of the metal oxide and electrolyte. The presence of more Fe^{2+} over the metal oxide surface, as evident from the XPS analysis, can convert to Fe^{3+} oxidation state resulting in the enhanced charging current. Further, the surface charging is dependent on the metal atom and oxygen vacancies over the Zn^{2+}substituted cobalt ferrite. The change in the Fe^{2+}/Fe^{3+} ratio is small for CFZn(0.1) to CFZn(0.2), but significant change is observed for the CFZn(0.3). The claimed effects can be visualized in the CV features of the composites. Further, for more quantitative and comparative inspection on the ORR behaviour of the systems, linear sweep voltammograms (LSVs) were recorded in a rotating disc electrode (RDE) mode by maintaining the rotation rate of the working electrode at 1600 rpm (**Figure 4.9b**). Looking at the onset and half-wave potentials, the catalytic activity towards ORR for the unsupported systems follows the order as CFZn(0.3) > CFZn(0.1) > CFZn(0.2), even though the performances are considerably low.On the other hand, the LSV data shows a substantial improvement in the ORR activity after dispersion of the ferrite

particles on N-rGO and the activity of these supported catalysts follows the order as CFZn(0.3)/N-rGO-Vulcan > CFZn(0.1)/N-rGO-Vulcan > CFZn(0.2)/N-rGO-Vulcan.

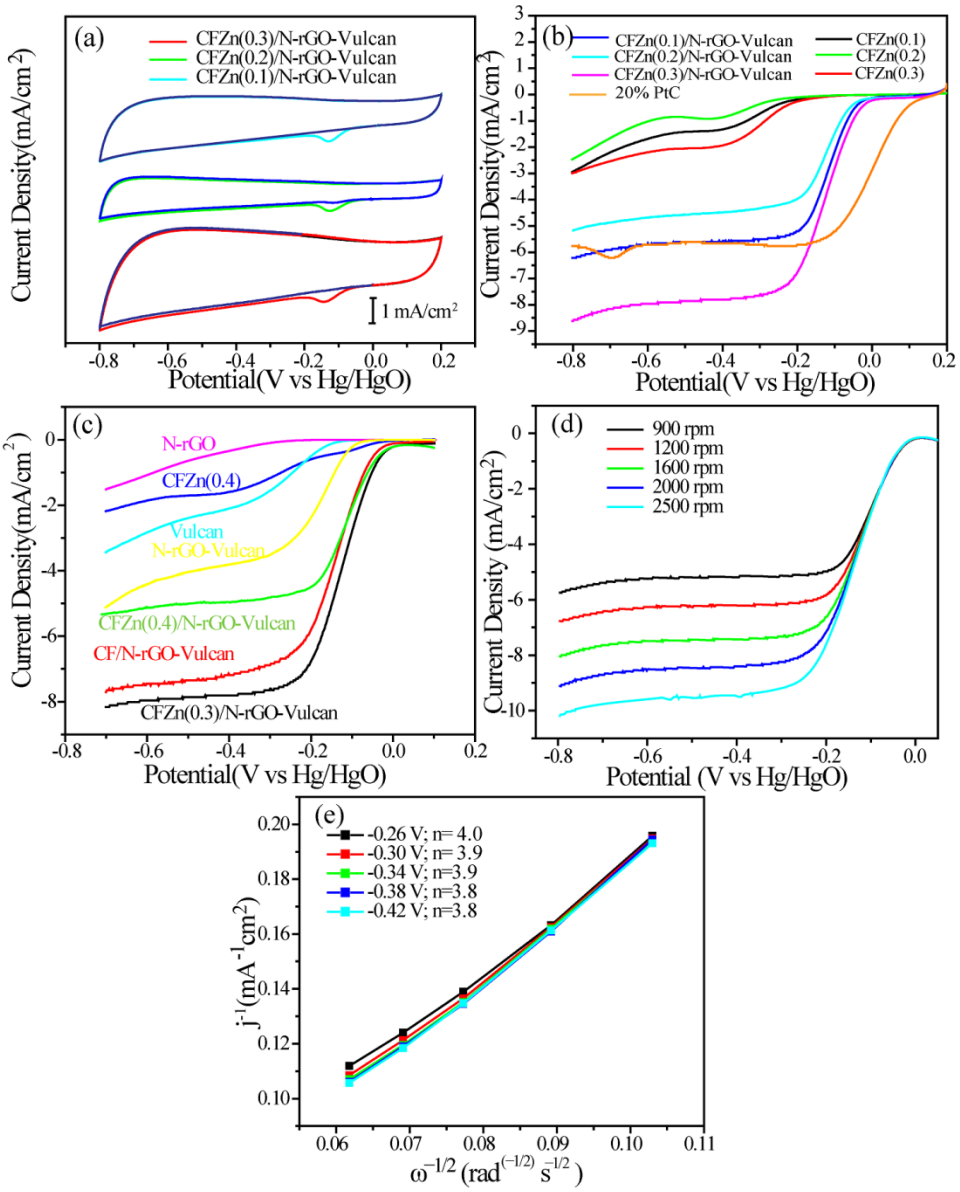

Figure 4.9.*Electrochemical data corresponding to ORR obtained on the various ferrite materials after spatially separating the catalyst particles with Vulcan carbon: (a) cyclic voltammograms of the zinc-substituted cobalt ferrite nanoparticles supported on N-rGO (electrolyte: 0.1 M KOH and scan rate: 50 mV/s) recorded under oxygen saturated and oxygen-free conditions; (b) linear sweep voltammograms of the unsupported and supported zinc-substituted cobalt ferrite nanocrystals recorded under RDE mode at a potential scan rate of 10 mV/s and an electrode rotation rate of 1600 rpm; (c) linear sweep voltamograms (LSVs) of CFZn(0.3)/N-rGO-Vulcan, CF/N-rGO-Vulcan, CFZn(0.4)/N-rGO-Vulcan, N-rGO-Vulcan, Vulcan, CFZn(0.4), and N-rGO recorded at 10 mV/s sweep rate with 1600 rpm in oxygen saturated electrolyte (0.1 M KOH). (d)*

LSVs of CFZn(0.3)/N-rGO-Vulcan recorded at various rotation speeds of the working electrode under RDE mode; (e) Koutecky-Levich plots generated for the CFZn(0.3)/N-rGO-Vulcan catalyst.

This trend in performance is clearly in accordance with the degree of Zn substitution in the ferrite structure and its associated effect on the redistribution of the iron and cobalt moieties in the octahedral and tetrahedral sites. Divalent Zn^{2+} ion when doped in the place of the trivalent Fe^{3+} ion as evident from the XPS analysis, an oxygen vacancy (Vo) can be created in the crystal structure.[32] As more Zn^{2+} goes to the Fe^{3+} site, concomitantly more the oxygen vacancies will be created to maintain the crystal neutrality.[34, 57-58] A nice correlation between the XPS and the ORR features could be arrived based on the state of the compositions as indicated in the XPS data and the performance indicators deduced from the electrochemical experiments. The change in the ORR activity from the Zn substitution value of 0.1 to 0.3 is a consequence of the interplay between the hole and ionic distribution in the B site.[3, 56] The generated oxygen vacancies subsequent to the displacement of the Fe^{3+} ions with the Zn^{2+} ions in the tetrahedral site can concomitantly affect the adsorption and desorption energy of the molecular oxygen.[58] This type of activity enhancement caused by oxygen vacancies can be explained by Marsvan Kervelen mechanism.[58] As the mechanism says, the oxygen vacancies created in the crystal structure provides the active site for adsorption of molecular oxygen. More the oxygen vacancies created in the lattice, higher the adsorption of the molecular oxygen. Here, it should be noted that the reduction of molecular oxygen takes place through the metal present at the B site.[56, 59] The increased Fe atom in the B site favours the ORR reaction as evident from our electrochemical study. The trend in the electrocatalytic activity of the unsupported and supported nanocrystals is similar. The supported catalyst with the Zn substitution value of 0.3, *i.e.*, CFZn(0.3)/N-rGO-Vulcan, has the highest performance regarding the limiting current density (8±0.5 mA/cm^2), onset (0.01 V *vs.* Hg/HgO) and half-wave (-0.120V *vs.* Hg/HgO) potential values. Compared to the supported Zn-free system, *i.e.* CF/N-rGO, substitution of Fe by a fraction of 0.3 leads to an enhancement in the half-wave potential by 20 mV. Interestingly, the limiting current density in the case of CFZn(0.3)/N-rGO-Vulcan is found to be higher than that of the state-of-the-art PtC catalyst by 2±0.5 mA/cm^2 even though the later has a lower

overpotential (90 mV) compared to the former. The relatively high current density of the homemade catalyst is attributed to the high mass diffusion and exposed catalytic sites attained in the present case in presence of Vulcan carbon as a co-component since stacking of the graphene layers can be hindered by the presence of the Vulcan carbon.[28] A recent study by Song *et al*. suggests that the curvature of the carbon structure facilitates the ORR kinetics and hinders the Oswald ripening of the catalyst.[60] The work highlights few of the structural advantages of the carbon for oxygen reduction as island-by-island configuration isolating the nanoparticles, tortuous voids restricts the Oswald ripening and curvature-induced strong interaction of nanoparticle with carbon. Similarly, a report from Liming Dai *et al*. explores the structural advantage of the graphene nanoribbons and quantum dots for ORR.[61] A combination of the layered nanoribbon and spherical quantum dots resulted into notable enhancement in ORR. In the case of our catalyst, the spherical Vulcan carbon is separating the catalyst layers by providing space for facile diffusion of the electrolyte and gases to the catalyst layer. This structure modulation is expected to be responsible for accomplishing the high current density in the in **Figure 4.9b** and **4.9c**.

The Vulcan carbon can also enhance wettability and thereby enhanced electrode-electrolyte interface. All these will help to ensure better oxygen concentration at the active sites located on the graphene surface. A controlled interplay of all these parameters is helping the system to provide a healthy environment for the reaction to happen. Further, the composition CFZn(0.4)/N-rGO-Vulcan with a Zn loading of 0.4 displays decreased ORR activity (**Figure 4.9c**). Hence, a Zn substitution value of 0.3 has been taken as the optimum value. Additionally, to ensure that the ORR response is coming from the synergistic effect of the carbon and metal oxide catalyst, the LSVs of the N-rGO, Vulcan carbon and N-rGO + Vulcan carbon are also included (**Figure 4.9c**). A comparison of the results clearly highlights the potential improvement attained in the CFZn/N-rGO-Vulcan systems through the synergistic interaction of the carbon and the metal oxide catalyst phase.

After realizing that CFZn(0.3)/N-rGO-Vulcan is the best composition among the prepared systems in terms of the ORR activity, the RDE evaluation was continued with a specific focus on this system to gain more insightful information on the kinetics of the reaction. This has been achieved by constructing the Koutecky-Levich (K-L) plots after

recording the LSVs at different electrode rotation rates and then plotting the inverse of the square root of the electrode rotation rate ($\omega^{-1/2}$) against inverse of the current density (j^{-1}) values at different potentials where the straight-line feature is maintained.[62-63] A detailed discussion on the K-L equation and the associated calculations is included in **Chapter 2**. **Figure 4.9d** shows the polarization curves obtained with the catalyst-coated electrode at different rotation rates recorded at a potential sweep rate of 10 mVs^{-1} in 0.1 M KOH solution. The significant increase in the limiting current density value with the rotation rate of the electrode is as a response to the increased hydrodynamic movement of the reactants towards the electrode surface with respect to the rotation rates. The corresponding K-L plots presented in **Figure 4.9e** give straight-line features, and the slope of the plots are used to calculate the number of electrons involved in the reduction process as a function of the potential. The estimated value of the number of the transferred electrons in the reduction process for ORR is approximately close to 4e, which validates formation of H_2O, instead of H_2O_2, as the major product of the reduction reaction. In order to get further insight on the magnitude of the ORR activity in a more quantitative term, the kinetic current is also deduced. This measurement on the kinetic current for the catalyst was carried out with the help of RDE from the y-intercept of the K-L plots made at different potentials through extrapolation. For the CFZn(0.3)/N-rGO catalyst, the kinetic current was estimated to be 714.2 mA/mg of the catalyst at -0.26 V (V vs Hg/HgO),which is an appreciable value for a noble metal free catalysts.[64]

Even though the formation of H_2O has been confirmed from the RDE studies as the major product of ORR in the present case, quantification of the amount of the possible by-product H_2O_2 using a rotating ring disc electrode (RRDE) can provide strong substantiating evidence on the proposed kinetics for the reaction. Accordingly, **Figure 4.10a** and **4.10b** respectively represent the amount of H_2O_2 formed and the number of electrons engaged in the reaction as a function of the applied potential at the disc electrode of RRDE. The current detected at the ring electrode of RRDE has been used to calculate these values. The electrochemical oxygen reduction reaction involves several transition states and the rate determining step depends on the activity of the catalyst. Frequently observed transition steps during the reduction are OOH*, O*, and OH*.[20]The products formed at the disc electrode in the reaction by following the 2e transfer get

trapped at the ring electrode andlead to the formation of H_2O_2 under the experimental conditions.[12]

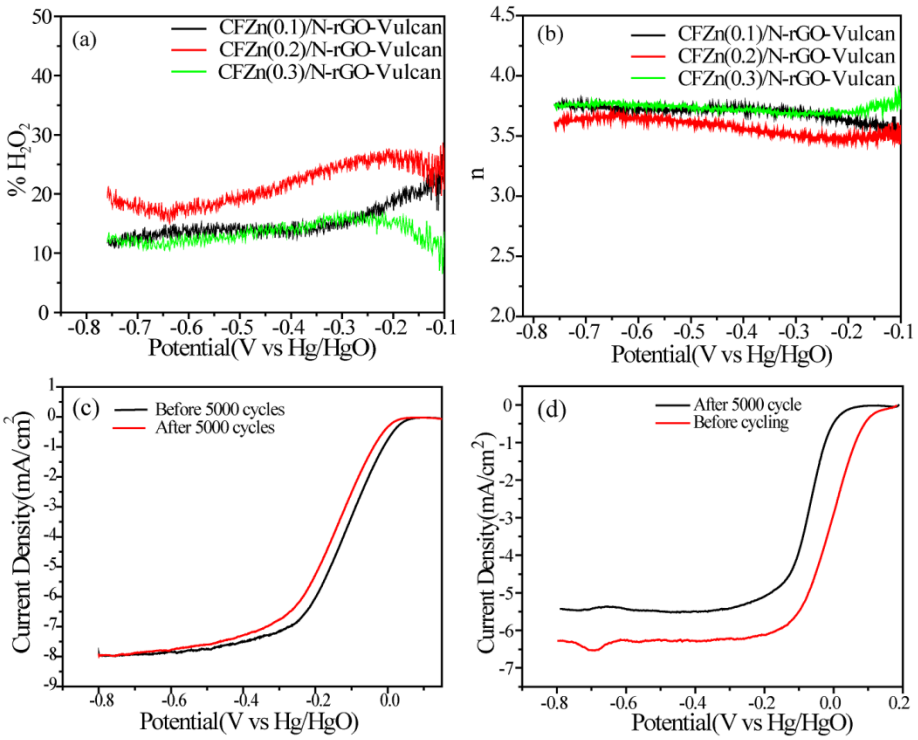

Figure 4.10. *(a) The measured number of the electrons transferred during ORR as calculated through RRDE studies;(b) the percentage of H_2O_2 detected at the ring electrode of RRDE at various potentials at an electrode rotation rate of 1600 rpm in O_2 saturated 0.1 M KOH solution; (c) and (d) are the accelerated durability test of CFZn(0.3)/N-rGO-Vulcan and 20% Pt/C catalysts.*

The formation of peroxide during the ORR process was monitored within the potential window of -0.1 to -0.75 V (*vs.* Hg/HgO) by measuring the ring current (the calculation is given in**Chapter 2**). As presented in **Figure 4.10a**, the percentage of H_2O_2 formed on the catalysts follows the order as CFZn(0.2)/N-rGO-Vulcan > CFZn(0.1)/N-rGO-Vulcan > CFZn(0.3)/N-rGO-Vulcan. As mentioned before, the H_2O_2 formation is directly related to the Faradic 2e transfer reaction, which leads to the formation of H_2O_2 as the final product compared to H_2O through the preferred 4e reduction pathway.[65-66] The calculation was extended to determine the number of electrons involved in the reduction process in the potential window of 0.10 to -0.75 V (*vs.* Hg/HgO) and **Figure 4.10b** represents the comparative plots. This number has been calculated after measuring the collection efficiency for the RRDE electrode using $K_3Fe(CN)_6$, which was found to be 0.37 (refer

Chapter 2 for details).Thus, the lowest H_2O_2 amount and an electron transfer number close to 3.8 detected in the case of CFZn(0.3)/N-rGO-Vulcan stands out as a solid evidence on the optimal activity modulation accomplished in the system after the Zn substitution to favour the ORR kinetics in the desired route. In terms of the active component, the ratio of the active catalyst to the Vulcan carbon (20:80) in the present case can be correlated to the commercial 20% PtC catalyst, where 20% active Pt metal is dispersed on 80% carbon matrix. The low peroxide yield given by the homemade catalyst indicates an optimum catalyst to carbon ratio as reported previously that the formation of peroxide with the thin catalyst coating varies with the metal amount in the catalyst layer on the working electrode.[67]

The ORR process creates a destructive environment to the catalyst by creating a favourable situation for carbon corrosion, particle ripening, and even dissolution. Particularly, in the case of the non-Pt systems, this has been pointed out as one of the major limitations for their realistic deployment for the device applications. The electrochemical stability of CFZn(0.3)/N-rGO-Vulcan in harsh oxygen reduction environment has been investigated by using the accelerated durability test (ADT) by exposing the catalyst to the oxidative environment of accelerated potential range from -0.6 to 0 V (*vs* Hg/HgO) for 5000 cycles with a sweep rate of 100 mV s^{-1} (refer **Chapter 2**for details).[68-69] A comparative LSV profiles presented in **Figure 4.10c** for the system before and after ADT indicates a reduction in the onset and half-wave potential by 30 mV with an apparently negligible change in the limiting current density value. On the other hand, the corresponding ADT profiles (**Figure 4.10d**) for 20% PtC catalyst indicates significant drops in the onset potential (100 mV), half-wave potential (70 mV) and limiting current density (14.2%). These results point towards better structural integrity and electrochemical survivability compared to the conventional PtC catalyst. This enhanced stability might have originated from the high corrosion resistive nature of the nitrogen doped graphene as a substrate along with its ability to strongly anchor the nano-ferrite particles through the sites generated by the heteroatom doping and small order structural changes.

4.4. Conclusion

This chapter discloses the tuning of oxygen reduction reaction (ORR) activity of cobalt ferrite nanoparticles by stoichiometrically substituting some fraction of Fe with Zn and anchoring these particles on nitrogen doped reduced graphene oxide (N-rGO). Zn substitution has a decisive role in controlling the ratio of Fe^{2+}/Fe^{3+} in the system, and this ratio has a direct influence on tuning the activity of the system towards ORR. The composition corresponding to CFZn(0.3)/N-rGO-Vulcan with a Co, Fe and Zn molar ratio of 1: 1.7: 0.3 is found to be the best system for ORR considering its significant positive potential shift for both onset and half-wave potential values along with the substantially improved limiting current density value. This increased ORR performance is in accordance with the increased concentration of the Fe^{2+} state in the octahedral sites of the system due to Zn substitution as revealed from the XPS studies. As the Zn^{2+} ions occupy the tetrahedral sites and displace a corresponding number of the Fe^{3+} ions from the tetrahedral sites, the Fe^{2+} to Fe^{3+} ratio increases with a concomitant enhancement in the ORR characteristics. This activity enhancement is again related to the possible oxygen vacancy created in the system as more Zn^{2+} goes to the tetrahedral site and the system tries to maintain crystal neutrality. CFZn(0.3)/N-rGO-Vulcan also displayed better structural integrity and electrochemical survivability compared to the conventional Pt/C catalyst, possibly materialized through the presence of the high corrosion resistive nature of the nitrogen doped graphene as a substrate along with its ability to strongly anchor the nano-ferrite particles.

4.5. References

(1) Kirubakaran, A.; Jain, S.; Nema, R. K., A review on fuel cell technologies and power electronic interface. *Renewable sustainable Energy Rev.* **2009,** *13,* 2430-2440.

(2) Matsumoto, K.; Fujigaya, T.; Yanagi, H.; Nakashima, N., Very High Performance Alkali Anion-Exchange Membrane Fuel Cells. *Adv. Funct. Mater.* **2011,** *21,* 1089-1094.

(3) Suntivich, J.; Gasteiger, H. A.; Yabuuchi, N.; Nakanishi, H.; Goodenough, J. B.; Shao-Horn, Y., Design principles for oxygen-reduction activity on perovskite oxide catalysts for fuel cells and metal–air batteries. *Nat Chem* **2011,** *3,* 546-550.

(4) Singh, S. K.; Dhavale, V. M.; Kurungot, S., Surface-Tuned Co_3O_4 Nanoparticles Dispersed on Nitrogen-Doped Graphene as an Efficient Cathode Electrocatalyst for Mechanical Rechargeable Zinc–Air Battery Application. *ACS Appl. Mater. Interfaces* **2015,** *7*, 21138-21149.

(5) Prabu, M.; Ramakrishnan, P.; Nara, H.; Momma, T.; Osaka, T.; Shanmugam, S., Zinc–Air Battery: Understanding the Structure and Morphology Changes of Graphene-Supported $CoMn_2O_4$ Bifunctional Catalysts Under Practical Rechargeable Conditions. *ACS Appl. Mater. Interfaces* **2014,** *6*, 16545-16555.

(6) Li, Y.; Gong, M.; Liang, Y.; Feng, J.; Kim, J.-E.; Wang, H.; Hong, G.; Zhang, B.; Dai, H., Advanced Zinc-air Batteries Based on High-performance Hybrid Electrocatalysts. *Nat. Commun.* **2013,** *4*, 1805.

(7) Lee, J.-S.; Tai Kim, S.; Cao, R.; Choi, N.-S.; Liu, M.; Lee, K. T.; Cho, J., Metal–Air Batteries with High Energy Density: Li–Air versus Zn–Air. *Adv. Energy Mater.* **2011,** *1*, 34-50.

(8) Pei, P.; Wang, K.; Ma, Z., Technologies for Extending Zinc–air Battery's Cyclelife: A Review. *Applied Energy* **2014,** *128*, 315-324.

(9) Nie, Y.; Li, L.; Wei, Z., Recent Advancements in Pt and Pt-free Catalysts for Oxygen Reduction Reaction. *Chem. Soc. Rev.* **2015,** *44*, 2168-2201.

(10) Shao, M.; Chang, Q.; Dodelet, J.-P.; Chenitz, R., Recent Advances in Electrocatalysts for Oxygen Reduction Reaction. *Chem. Rev.* **2016**.

(11) Nørskov, J. K.; Rossmeisl, J.; Logadottir, A.; Lindqvist, L.; Kitchin, J. R.; Bligaard, T.; Jónsson, H., Origin of the Overpotential for Oxygen Reduction at a Fuel-Cell Cathode. *J. Phys. Chem. B* **2004,** *108*, 17886-17892.

(12) Lim, D.-H.; Wilcox, J., Mechanisms of the Oxygen Reduction Reaction on Defective Graphene-Supported Pt Nanoparticles from First-Principles. *J. Phys. Chem. C* **2012,** *116*, 3653-3660.

(13) Guo, S.; Li, D.; Zhu, H.; Zhang, S.; Markovic, N. M.; Stamenkovic, V. R.; Sun, S., FePt and CoPt Nanowires as Efficient Catalysts for the Oxygen Reduction Reaction. *Angew. Chem. Int. Ed.* **2013,** *52*, 3465-3468.

(14) Palaniselvam, T.; Irshad, A.; Unni, B.; Kurungot, S., Activity Modulated Low Platium Content Oxygen Reduction Electrocatalysts Prepared by Inducing Nano-Order

Dislocations on Carbon Nanofiber through N_2-Doping. *J. Phys. Chem. C* **2012,** *116*, 14754-14763.

(15) Toh, R. J.; Eng, A. Y. S.; Sofer, Z.; Sedmidubsky, D.; Pumera, M., Ternary Transition Metal Oxide Nanoparticles with Spinel Structure for the Oxygen Reduction Reaction. *ChemElectroChem* **2015,** *2*, 982-987.

(16) Yao, C.; Zeng, Q.; Goya, G. F.; Torres, T.; Liu, J.; Wu, H.; Ge, M.; Zeng, Y.; Wang, Y.; Jiang, J. Z., $ZnFe_2O_4$ Nanocrystals: Synthesis and Magnetic Properties. *J. Phys. Chem. C* **2007,** *111*, 12274-12278.

(17) Chisaka, M.; Suzuki, Y.; Iijima, T.; Sakurai, Y., Effect of Synthesis Route on Oxygen Reduction Reaction Activity of Carbon-Supported Hafnium Oxynitride in Acid Media. *J. Phys. Chem. C* **2011,** *115*, 20610-20617.

(18) Chisaka, M.; Ishihara, A.; Ota, K.-i.; Muramoto, H., Synthesis of Carbon-supported Titanium Oxynitride Nanoparticles as Cathode Catalyst for Polymer Electrolyte Fuel Cells. *Electrochim. Acta* **2013,** *113*, 735-740.

(19) Tritsaris, G. A.; Nørskov, J. K.; Rossmeisl, J., Trends in Oxygen Reduction and Methanol Activation on Transition Metal Chalcogenides. *Electrochim. Acta* **2011,** *56*, 9783-9788.

(20) Jiao, Y.; Zheng, Y.; Jaroniec, M.; Qiao, S. Z., Origin of the Electrocatalytic Oxygen Reduction Activity of Graphene-Based Catalysts: A Roadmap to Achieve the Best Performance. *J. Am. Chem. Soc.* **2014,** *136*, 4394-4403.

(21) Ge, X.; Liu, Y.; Goh, F. W. T.; Hor, T. S. A.; Zong, Y.; Xiao, P.; Zhang, Z.; Lim, S. H.; Li, B.; Wang, X.; Liu, Z., Dual-Phase Spinel $MnCo_2O_4$ and Spinel $MnCo_2O_4$/Nanocarbon Hybrids for Electrocatalytic Oxygen Reduction and Evolution. *ACS Appl. Mater. Interfaces* **2014,** *6*, 12684-12691.

(22) Ning, R.; Tian, J.; Asiri, A. M.; Qusti, A. H.; Al-Youbi, A. O.; Sun, X., Spinel $CuCo_2O_4$ Nanoparticles Supported on N-Doped Reduced Graphene Oxide: A Highly Active and Stable Hybrid Electrocatalyst for the Oxygen Reduction Reaction. *Langmuir* **2013,** *29*, 13146-13151.

(23) Wang, H.; Yang, Y.; Liang, Y.; Zheng, G.; Li, Y.; Cui, Y.; Dai, H., Rechargeable Li-O_2 Batteries with a Covalently Coupled $MnCo_2O_4$-Graphene Hybrid as an Oxygen Cathode Catalyst. *Energy Environ. Sci.* **2012,** *5*, 7931-7935.

(24) Liang, Y.; Li, Y.; Wang, H.; Zhou, J.; Wang, J.; Regier, T.; Dai, H., Co_3O_4 Nanocrystals on Graphene as a Synergistic Catalyst for Oxygen Reduction Reaction. *Nat. Mater.* **2011,** *10*, 780-786.

(25) Li, B.; Ge, X.; Goh, F. W. T.; Hor, T. S. A.; Geng, D.; Du, G.; Liu, Z.; Zhang, J.; Liu, X.; Zong, Y., Co_3O_4 Nanoparticles Decorated Carbon Nanofiber Mat as Binder-free Air-cathode for High Performance Rechargeable Zinc-air Batteries. *Nanoscale* **2015,** *7*, 1830-1838.

(26) Wu, Z.-S.; Yang, S.; Sun, Y.; Parvez, K.; Feng, X.; Müllen, K., 3D Nitrogen-Doped Graphene Aerogel-Supported Fe_3O_4 Nanoparticles as Efficient Electrocatalysts for the Oxygen Reduction Reaction. *J. Am. Chem. Soc.* **2012,** *134*, 9082-9085.

(27) Bian, W.; Yang, Z.; Strasser, P.; Yang, R., A $CoFe_2O_4$/Graphene Nanohybrid as an Efficient Bi-functional Electrocatalyst for Oxygen Reduction and Oxygen Evolution. *J. Power Sources* **2014,** *250*, 196-203.

(28) Kashyap, V.; Singh, S. K.; Kurungot, S., Cobalt Ferrite Bearing Nitrogen-Doped Reduced Graphene Oxide Layers Spatially Separated with Microporous Carbon as Efficient Oxygen Reduction Electrocatalyst. *ACS Appl. Mater. Interfaces* **2016,** *8*, 20730-20740.

(29) Ma, Y.; Wang, H.; Ji, S.; Goh, J.; Feng, H.; Wang, R., Highly Active Vulcan Carbon Composite for Oxygen Reduction Reaction in Alkaline Medium. *Electrochim. Acta* **2014,** *133*, 391-398.

(30) Carta, D.; Casula, M. F.; Falqui, A.; Loche, D.; Mountjoy, G.; Sangregorio, C.; Corrias, A., A Structural and Magnetic Investigation of the Inversion Degree in Ferrite Nanocrystals MFe_2O_4 (M = Mn, Co, Ni). *J. Phys. Chem. C* **2009,** *113*, 8606-8615.

(31) Mameli, V.; Musinu, A.; Ardu, A.; Ennas, G.; Peddis, D.; Niznansky, D.; Sangregorio, C.; Innocenti, C.; Thanh, N. T. K.; Cannas, C., Studying the Effect of Zn-Substitution on the Magnetic and Hyperthermic Properties of Cobalt Ferrite Nanoparticles. *Nanoscale* **2016,** *8*, 10124-10137.

(32) Somaiah, N.; Jayaraman, T. V.; Joy, P. A.; Das, D., Magnetic and Magnetoelastic Properties of Zn-doped Cobalt-ferrites—$CoFe_{2-x}Zn_xO_4$ (x=0, 0.1, 0.2, and 0.3). *J. Magn. Magn. Mater.* **2012,** *324*, 2286-2291.

(33) Li, L.; Feng, X.; Nie, Y.; Chen, S.; Shi, F.; Xiong, K.; Ding, W.; Qi, X.; Hu, J.; Wei, Z.; Wan, L.-J.; Xia, M., Insight into the Effect of Oxygen Vacancy Concentration on the Catalytic Performance of MnO_2. *ACS Catal.* **2015,** *5*, 4825-4832.

(34) Liu, L.; Mei, Z.; Tang, A.; Azarov, A.; Kuznetsov, A.; Xue, Q.-K.; Du, X., Oxygen Vacancies: The Origin of n-type Conductivity in ZnO. *Physical Review B* **2016,** *93*, 235305.

(35) Qiu, K.; Chai, G.; Jiang, C.; Ling, M.; Tang, J.; Guo, Z., Highly Efficient Oxygen Reduction Catalysts by Rational Synthesis of Nanoconfined Maghemite in a Nitrogen-Doped Graphene Framework. *ACS Catal*. **2016,** *6*, 3558-3568.

(36) Zhu, H.; Zhang, S.; Huang, Y.-X.; Wu, L.; Sun, S., Monodisperse $MxFe_{3-x}O_4$ (M = Fe, Cu, Co, Mn) Nanoparticles and Their Electrocatalysis for Oxygen Reduction Reaction. *Nano Lett*. **2013,** *13*, 2947-2951.

(37) Yan, W.; Cao, X.; Tian, J.; Jin, C.; Ke, K.; Yang, R., Nitrogen/sulfur Dual-doped 3D Reduced Graphene Oxide Networks-supported $CoFe_2O_4$ with Enhanced Electrocatalytic Activities for Oxygen Reduction and Evolution reactions. *Carbon* **2016,** *99*, 195-202.

(38) Liang, Y.; Wang, H.; Zhou, J.; Li, Y.; Wang, J.; Regier, T.; Dai, H., Covalent Hybrid of Spinel Manganese–Cobalt Oxide and Graphene as Advanced Oxygen Reduction Electrocatalysts. *J. Am. Chem. Soc.* **2012,** *134*, 3517-3523.

(39) Prasai, D.; Tuberquia, J. C.; Harl, R. R.; Jennings, G. K.; Bolotin, K. I., Graphene: Corrosion-Inhibiting Coating. *ACS Nano* **2012,** *6*, 1102-1108.

(40) Jin, H.; Zhang, H.; Ma, Y.; Xu, T.; Zhong, H.; Wang, M., Stable Support Based on Highly Graphitic Carbon Xerogel for Proton Exchange Membrane Fuel Cells. *J. Power Sources* **2010,** *195*, 6323-6328.

(41) Kim, Y. I.; Kim, D.; Lee, C. S., Synthesis and Characterization of $CoFe_2O_4$ Magnetic Nanoparticles Prepared by Temperature-controlled Coprecipitation Method. *Physica B: Condensed Matter* **2003,** *337*, 42-51.

(42) Chae, K. P.; Lee, J.-G.; Su Kweon, H.; Bae Lee, Y., The Crystallographic, Magnetic Properties of Al, Ti Doped $CoFe_2O_4$ Powders Grown by Sol–gel Method. *J. Magn. Magn. Mater.* **2004,** *283*, 103-108.

(43) Baldi, G.; Bonacchi, D.; Franchini, M. C.; Gentili, D.; Lorenzi, G.; Ricci, A.; Ravagli, C., Synthesis and Coating of Cobalt Ferrite Nanoparticles: A First Step toward the Obtainment of New Magnetic Nanocarriers. *Langmuir* **2007,** *23*, 4026-4028.

(44) Zhang, L.; Su, Z.; Jiang, F.; Yang, L.; Qian, J.; Zhou, Y.; Li, W.; Hong, M., Highly Graphitized Nitrogen-doped Porous Carbon Nanopolyhedra Derived from ZIF-8 Nanocrystals as Efficient Electrocatalysts for Oxygen Reduction Reactions. *Nanoscale* **2014,** *6*, 6590-6602.

(45) Artus, M.; Tahar, L. B.; Herbst, F.; Smiri, L.; Villain, F.; Yaacoub, N.; Grenèche, J.-M.; Ammar, S.; Fiévet, F., Size-dependent Magnetic Properties of $CoFe_2O_4$ Nanoparticles Prepared in Polyol. *J. Phys. Condens. Matter* **2011,** *23*, 506001.

(46) Rakhi, R. B.; Chen, W.; Cha, D.; Alshareef, H. N., High Performance Supercapacitors Using Metal Oxide Anchored Graphene Nanosheet Electrodes. *J. Mater. Chem.* **2011,** *21*, 16197-16204.

(47) Kim, M.; Hwang, Y.; Min, K.; Kim, J., Concentration Dependence of Graphene Oxide-nanoneedle Manganese Oxide Composites Reduced by Hydrazine Hydrate for an Electrochemical Supercapacitor. *Phys. Chem. Chem. Phys.* **2013,** *15*, 15602-15611.

(48) Ghule, A. V.; Ghule, K.; Chen, C.-Y.; Chen, W.-Y.; Tzing, S.-H.; Chang, H.; Ling, Y.-C., In Situ Thermo-TOF-SIMS Study of Thermal Decomposition of Zinc Acetate Dihydrate. *J. Mass Spectro.* **2004,** *39*, 1202-1208.

(49) Liu, C.; Zhang, Y.; Jia, J.; Sui, Q.; Ma, N.; Du, P., Multi-susceptibile Single-Phased Ceramics with Both Considerable Magnetic and Dielectric Properties by Selectively Doping. *Sci. Rep.* **2015,** *5*, 9498.

(50) Tang, R.; Jiang, C.; Qian, W.; Jian, J.; Zhang, X.; Wang, H.; Yang, H., Dielectric relaxation, resonance and scaling behaviors in $Sr_3Co_2Fe_{24}O_{41}$ hexaferrite. *Sci. Rep.* **2015,** *5*, 13645.

(51) Unni, S. M.; Bhange, S. N.; Illathvalappil, R.; Mutneja, N.; Patil, K. R.; Kurungot, S., Nitrogen-Induced Surface Area and Conductivity Modulation of Carbon Nanohorn and Its Function as an Efficient Metal-Free Oxygen Reduction Electrocatalyst for Anion-Exchange Membrane Fuel Cells. *Small* **2015,** *11*, 352-360.

(52) Wu, J.; Ma, L.; Yadav, R. M.; Yang, Y.; Zhang, X.; Vajtai, R.; Lou, J.; Ajayan, P. M., Nitrogen-Doped Graphene with Pyridinic Dominance as a Highly Active and Stable

Electrocatalyst for Oxygen Reduction. *ACS Appl. Mater. Interfaces* **2015,** *7*, 14763-14769.

(53) Palaniselvam, T.; Kashyap, V.; Bhange, S. N.; Baek, J.-B.; Kurungot, S., Nanoporous Graphene Enriched with Fe/Co-N Active Sites as a Promising Oxygen Reduction Electrocatalyst for Anion Exchange Membrane Fuel Cells. *Adv. Funct. Mater.* **2016,** *26*, 2150-2162.

(54) Unni, S. M.; Illathvalappil, R.; Bhange, S. N.; Puthenpediakkal, H.; Kurungot, S., Carbon Nanohorn-Derived Graphene Nanotubes as a Platinum-Free Fuel Cell Cathode. *ACS Appl. Mater. Interfaces* **2015,** *7*, 24256-24264.

(55) Zhou, D.; Kittilstved, K. R., Electron Trapping on Fe^{3+} Sites in Photodoped ZnO Colloidal Nanocrystals. *Chem. Commun.* **2016,** *52*, 9101-9104.

(56) Jijil, C. P.; Bhange, S. N.; Kurungot, S.; Devi, R. N., Effect of B Site Coordination Environment in the ORR Activity in Disordered Brownmillerites $Ba_2In_{2-x}CexO_{5+\delta}$.*ACS Appl. Mater. Interfaces* **2015,** *7*, 3041-3049.

(57) Ma, T. Y.; Zheng, Y.; Dai, S.; Jaroniec, M.; Qiao, S. Z., Mesoporous $MnCo_2O_4$ with Abundant Oxygen Vacancy Defects as High-performance Oxygen Reduction Catalysts. *J. Mater. Chem. A* **2014,** *2*, 8676-8682.

(58) Agarwal, V.; Metiu, H., Energy of Oxygen-Vacancy Formation on Oxide Surfaces: Role of the Spatial Distribution. *J. Phys. Chem. C* **2016,** *120*, 2320-2323.

(59) Grimaud, A.; Diaz-Morales, O.; Han, B.; Hong, W. T.; Lee, Y.-L.; Giordano, L.; Stoerzinger, K. A.; Koper, M. T. M.; Shao-Horn, Y., Activating Lattice Oxygen Redox Reactions in Metal Oxides to Catalyse Oxygen Evolution. *Nat Chem* **2017,** *advance online publication*.

(60) Yang, J.; Kim, S. H.; Kwak, S. K.; Song, H.-K., Curvature-Induced Metal–Support Interaction of an Islands-by-Islands Composite of Platinum Catalyst and Carbon Nano-onion for Durable Oxygen Reduction. *ACS Appl. Mater. Interfaces* **2017,** *9*, 23302-23308.

(61) Jin, H.; Huang, H.; He, Y.; Feng, X.; Wang, S.; Dai, L.; Wang, J., Graphene Quantum Dots Supported by Graphene Nanoribbons with Ultrahigh Electrocatalytic Performance for Oxygen Reduction. *J. Am. Chem. Soc.* **2015,** *137*, 7588-7591.

(62) Jäger, R.; Härk, E.; Romann, T.; Joost, U.; Lust, E., C(Mo2C) and Pt–C(Mo_2C) Based Mixed Catalysts for Oxygen Reduction Reaction. *J. Electroanal. Chem.* **2016,** *761*, 89-97.

(63) Balan, B. K.; Manissery, A. P.; Chaudhari, H. D.; Kharul, U. K.; Kurungot, S., Polybenzimidazole Mediated N-doping Along the Inner and Outer Surfaces of a Carbon Nanofiber and its Oxygen Reduction Properties. *J. Mater. Chem.* **2012,** *22*, 23668-23679.

(64) Balan, B. K.; Kurungot, S., Highly Exposed and Activity Modulated Sandwich Type Pt Thin Layer Catalyst with Enhanced Utilization. *J. Mater. Chem.* **2011,** *21*, 19039-19048.

(65) Yamada, Y.; Yoneda, M.; Fukuzumi, S., High Power Density of One-Compartment H_2O_2 Fuel Cells Using Pyrazine-Bridged Fe[$MC(CN)_4$] (MC = Pt^{2+} and Pd^{2+}) Complexes as the Cathode. *Inorg Chem* **2014,** *53*, 1272-1274.

(66) Yamada, Y.; Fukunishi, Y.; Yamazaki, S.-i.; Fukuzumi, S., Hydrogen Peroxide as Sustainable Fuel: Electrocatalysts for Production with a Solar Cell and Decomposition with a Fuel Cell. *Chem. Commun.* **2010,** *46*, 7334-7336.

(67) Alonso-Vante, N., Platinum and Non-Platinum Nanomaterials for the Molecular Oxygen Reduction Reaction. *ChemPhysChem* **2010,** *11*, 2732-2744.

(68) Liang, Y.-T.; Lin, S.-P.; Liu, C.-W.; Chung, S.-R.; Chen, T.-Y.; Wang, J.-H.; Wang, K.-W., The Performance and Stability of the Oxygen Reduction Reaction on Pt-M (M = Pd, Ag and Au) Nanorods: An Experimental and Computational Study. *Chem. Commun.* **2015,** *51*, 6605-6608.

(69) Takahashi, S.; Chiba, H.; Kato, T.; Endo, S.; Hayashi, T.; Todoroki, N.; Wadayama, T., Oxygen Reduction Reaction Activity and Structural Stability of Pt-Au Nanoparticles Prepared by Arc-plasma Deposition. *Phys. Chem. Chem. Phys.* **2015,** *17*, 18638-18644.

Chapter 5

Zirconium Substitution in the Spinel Cobalt Ferrite Matrix for Bifunctional Activity: A Potential Electrode Material for Rechargeable Zinc-air Battery

This chapter deals with how solvothermal synthesis of zirconium-substituted cobalt ferrite nanoparticles has been accomplished by the introduction of zirconium (Zr) in the spinel matrix to obtain a cost-effective and robust electrocatalyst that does not use noble metals. A variation in the cobalt ferrite structure $CoFe_{2-x}Zr_xO_4$ with Zr (0.1-0.4) substitution has significantly altered the overpotential for the electrocatalytic oxygen reduction reaction (ORR) and oxygen evolution reaction (OER), leading to an optimum composition of CFZr(0.3). The incorporation of the foreign Zr^{4+} ion in the cobalt ferrite spinel lattices has effectively enhanced the oxygen evolution reaction (OER) activity from the parent cobalt ferrite (CF) nanocrystals. However, a nominal change in the ORR current density has been observed due to Zr-incorporation. For the OER, the Zr substituted catalyst has shown a 40 mV negative shift in the overpotential in comparison with the CF nanoparticles at 10mA/cm^2 current density. Interestingly, the *in-situ* grafting of Zr-substituted cobalt ferrite nanoparticles over N-doped reduced graphene oxide (CFZr(0.3)/N-rGO) has remarkably enhanced performance during the ORR and moderately favored OER with an overall potential difference(ΔE) of 0.840 V.The enhanced bifunctional electrocatalytic activity of the material is crucial for the fabrication of

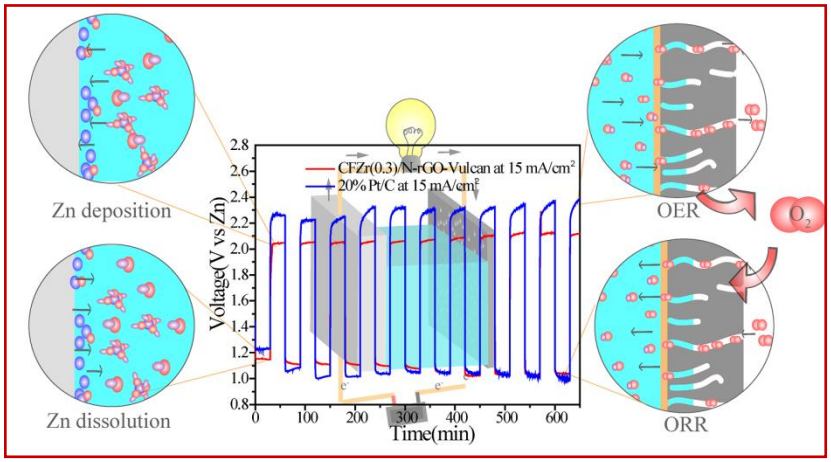

*The content of this chapter is published in "*ACS Catal.* **2018**, 3715-3726."

-Reproduced with permission from (*ACS Catal.* **2018**, 3715-3726). Copyright (2018) American Chemical Society.

high performance rechargeable Zn-air batteries. The prepared catalyst exhibited an overpotential of 80 mV for ORR in comparison with the state-of-the-art (Pt/C) catalyst and an overpotential of 340 mV at 10 mA/cm^2 current density for OER from the standard value (1.23 V *vs* RHE). This potential bifunctional electrocatalyst has been employed as an electrode material for the fabrication of a primary ZAB, where it exhibited discharge capacities of 727 mAh/g and 730 mAh/g at current densities of 20 mA/cm^2 and 30 mA/cm^2, respectively, under ambient conditions. The notable performance of the catalyst as a bifunctional material is observed during the cycling of the rechargeable ZAB. The prepared catalyst showed an increase of 200 mV in the overall operating overpotential after cycling for 10 cycles at 15 mA/cm^2 as against the 350 mV increase shown by the Pt/C catalyst.

5.1. Introduction

Owing to the ever-increasing demand for energy and the concomitant depletion of viable fossil fuel reserves, related research has veered towards renewable energy systems such as fuel cells,[1-3] metal-air batteries[4-7] and water electrolysers.[8-9] The oxygen reduction reaction (ORR) and oxygen evolution reaction (OER) are critical processes in the functioning of air-batteries and fuel cells, and enhancing their efficiency has been identified as key to the development of better materials for such applications. Until now, electrocatalysts based on noble metals (Pt and its alloys) were the most effective catalysts available for enhancing the sluggish ORR; but they are scarce, have poor durability, and have high cost.[10-13] Similarly, Ru, Ir, and their alloys exhibit outstanding OER catalysis, even though their cost hampers commercial viability to a large extent.[14-16] Considering the prohibitive cost, poor durability and scarcity of the noble metal composites, many studies that aim to develop efficient, durable, and cost-effective alternatives are being conducted. Among the noble-metal-free catalysts, transition metal oxides,[17] chalcogenides,[18] oxynitrides[19] and their complexes have shown good performance in catalyzing these crucial reactions. Attempts to develop hybrid catalysts such as the graphitic carbon framework and metal oxide composites have contributed significantly to the applications in the field. More interestingly, when hetero-atom-doped graphene or carbon nanotubes are used as support for nanoparticles of early transition metal oxides like CoO,[20] Co_3O_4,[21] $MnCo_2O_4$,[22] $ZnFe_2O_4$,[23-24] and $CuCo_2O_4$,[25] the potential synergistic effect of the hetero-atom-doped conducting carbon and the nanoparticles resulted into outstanding ORR activity. Similarly, for OER, nanometer-sized NiFe hydroxides,[26] $NiCo_2O_4$,[27] $ZnCo_2O_4$,[22] and CoO[28]exhibit reasonable

activity and stability. In addition to this, doping of an additional transition metal to the spinel transition metal oxide, such as when Ni, Zn, Fe, and Cr are doped in Co_3O_4,[29-31] modulates the surface adsorption energies of the intermediates and consequently, increases catalytic activity. Theoretical studies have suggested that the adsorption energies of the surface intermediates (*O, *OH, and *OOH) drive the OER/ORR kinetics.[32] Thus, it can be assumed that doping of the electropositive hetero-metal in the spinel matrix stabilizes the surface adsorption energies of the intermediates and, hence, increases the OER/ORR activity.

Interestingly the efficiency of the energy devices such as metal air batteries strictly depends on the kinetics of the electrode reactions. More precisely, it is the oxygen reduction reaction during the discharge and oxygen evolution reaction during the charging process. These faradaic reactions coupled with metal electrode as the active material can potentially deliver high voltage and energy density. A general electrode reaction for the Zn-air battery can be given as:

Anode:

$$Zn(OH)_4^{2-} + 2e^- \leftrightarrow Zn + 4(OH)^-$$

Cathode:

$$O_2 + 2H_2O + 4e^- \leftrightarrow 4OH^-$$

The above-mentioned electrode reactions occur in opposite directions during the charging and discharging cycling of the battery (*i.e.* Zn dissolution and oxygen reduction for the discharging; Zn deposition and oxygen evolution for the charging). Though Zn-air batteries have high theoretical energy density, low cost, safety, and environmental benignity, their commercialization is hampered by the sluggish kinetics of the electrode reactions. There have been several studies which explore individually the ORR and OER catalysis but the functioning of these catalysts in real metal-air batteries need to be explored more. Notably, Dai *et. al*. demonstrated CoO/N-CNT as the ORR catalyst in combination with NiFe LDH/CNT hybrid as the OER catalyst for rechargeable ZAB application.[33]Even though the device was reported to have adequate efficiency, the strategy simultaneously added the device components as it contains three electrodes (separate electrodes for ORR and OER). Similarly, Prabhu *et al*. have demonstrated a rechargeable Zn-air battery by employing graphene-supported $CoMn_2O_4$ material which has performed remarkably as a bifunctionalcatalyst.[34] Recently, Yan *et al*. proposed an Fe/N/C and bimetallic metal-organic-framework composite as a bifunctional catalyst for ZAB.

[35]Here, it should be noted that the high overpotential for ORR leads to low voltage and discharge capacity in the discharge process.[36] Similarly high overpotential for OER refers to increased charging voltage for the rechargeable ZAB.[37] Further, the high voltage for charging has other consequences like carbon corrosion and subsequently deterioration of the catalytic property.[38]

In the present chapter, we have prepared a catalyst by substituting Zr metal in the cobalt ferrite matrix with an optimum Zr content to achieve a balanced ORR/OER characteristics. Zr (Zr^{4+}, 72 pm) being size-compatible can be substituted in the 3d transition metal compounds for tuning the band gap and catalytic activity.[39-41] Recently, Domen *et al*. and Tian *et al*., have reported separately the effect of Zr substitution in Ta_3N_5 and In_2S_3 for photoelectrochemical water splitting.[42-43]

In the present case, Zr is introduced as the foreign ion in cobalt ferrite matrix for modifying the electrochemical behavior. Compositional variation in $CoFe_{2-x}Zr_xO_4$ (X=0.1 to 0.4) with an optimum composition of CFZr(0.3)has been identified as the system possessing the lowest overpotential in the series for OER/ORR. In addition to this, the composite of this material made with nitrogen-doped GO (CFZr(0.3)/N-rGO) exhibits considerable ORR and OER activity in a single electrode as well as in a primary ZAB system. These results indicate that the substitution of Zr in cobalt ferrite matrix and dispersion of these nanoparticles on N-doped GO lead to a significant level of improvement from the overpotentials incurred for ORR and OER and, thereby, positioning the composite as a potential bifunctional electrocatalyst in rechargeable ZABs.[44-45]

5.2. Experimental Section

5.1. Synthesis of Zirconium-Substituted Cobalt Ferrite (CFZr(x)) Nanoparticles:

Zirconium-substituted cobalt ferrite was prepared through the solvothermal synthesis method. Cobalt acetate, iron acetate, and zirconium acetylacetonate in the molar ratio 1:1.7:0.3 were dissolved in water-ethanol (1:1) mixture for preparing the CFZr(0.3) composite. The reaction mixture was kept at 130 ^oC in a 100 ml autoclave for 12 h. The precipitate so obtained was centrifuged and washed with deionized (DI) water. The sample was then dried at room temperature. Similar procedures were used for the synthesis of CFZr(0.1), CFZr(0.2), and CFZr(0.4) by keeping the metal ratios as 1:1.9:0.1, 1:1.8:0.2, and 1:1.6:0.4, respectively.

5.2. Synthesis of CFZr(0.3)/N-rGO: Solvothermal synthesis followed by physical mixing with Vulcan carbon was adopted for the preparation of the active catalyst. In the first step, 50 mg of N-rGO was dispersed in 50 ml of the water-ethanol (1:1) mixture. Then, cobalt acetate, iron acetate and zirconium acetylacetonate in the molar ratio of 1:1.7:0.3 were dissolved in it for preparing the CFZr(0.3)/N-rGO composite. The reaction mixture was heated at 130 ^{o}C for 12 h in a 100 ml autoclave. Later, the sample was collected and dried at room temperature. For the synthesis of CFZr(0.2)/N-rGO, a similar method was followed by keeping the Co, Fe and Zr metal ratio as 1:1.8:0.2 during the solvothermal process. In addition to this, cobalt ferrite nanocrystals (without Zr doping) supported over N-doped reduced graphene oxide (CF/N-rGO) were also prepared to compare and evaluate the effect of Zr substitution in a ZAB.

5.3. RESULTS AND DISCUSSION

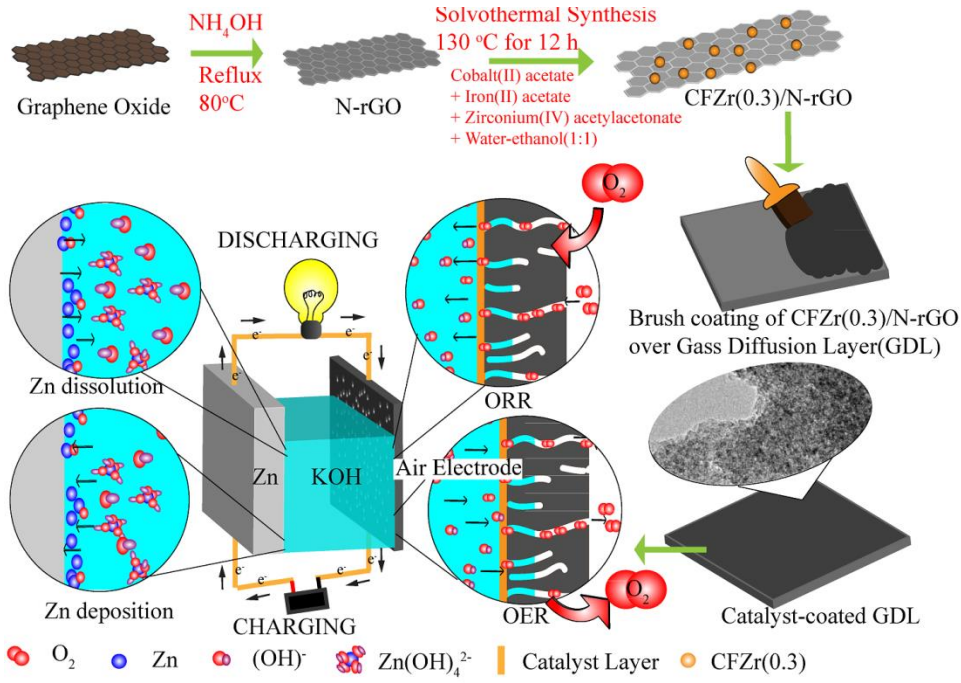

Figure 5.1.*Illustration of the processes involved in the synthesis of CFZr(0.3)/N-rGO and fabrication of the rechargeable Zn-air battery using the catalyst coated Gas Diffusion Layer (GDL) which serves both as the conducting support and passage for gas during the cycling of the battery.*

Figure 5.1 illustrates the methodology adopted to prepare the active catalyst, *i.e*. zirconium-substituted cobalt ferrite over nitrogen-doped graphene (CFZr(0.3)/N-rGO) and its functioning in a rechargeable ZAB. As shown in the scheme, the catalyst coated Gas Diffusion Layer (GDL) serves as the air electrode in the system. The pores of the GDL helps the system for passage of gas during the charge-discharge cycling whereas the coated catalyst due to its bifunctional nature helps the system to undergo the charging and discharging cycles.

5.3.1. TEM Analysis:

For examining the structural and morphological features, the composite after Zr-substitution and its supported counterpart were analyzed through TEM imaging. TEM images showing the nanocrystalline nature of the cobalt ferrite (CF) and Zr substituted CF nanoparticles (CFZr(0.3)) are presented in **Figures 5.2a** and **5.2b**, respectively. As revealed from the TEM images, the particle size of the CF nanoparticles remains in the nano regime with a homogenous distribution even after the Zr substitution in the matrix. Homogenous distribution with confined nano-size of the substituted ferrite is achieved because of the thermal decomposition of the corresponding metal salts in the solvothermal synthesis.[19,47] The selected area electron diffraction (SAED) (shown in inset) and image of CFZr(0.3) at a higher magnification are presented in **Figure 5.2c**. The diffused ring pattern in the SAED also ascertains the nanocrystalline nature of the particles. **Figure 5.2d** shows the HR-TEM image and the corresponding line profile of CFZr(0.3). The size compatibility of Zr (Zr^{4+}, 72 pm) allows the foreign ion to be perfectly incorporated in the CF matrix and hence the lattice spacing of the substituted CFZr(0.3) shows close resemblance with cobalt ferrite (0.29 nm for the (220) plane).

Considering the role of carbon as a potential component in an electrocatalyst, the nanoparticles were *in-situ* decorated over the nitrogen doped reduced graphene oxide (N-rGO). An image of N-rGO presented in **Figure 5.2e** shows a smooth surface with crumbled sheath structure.[30] After the *in-situ* decoration of CFZr(0.3) nanoparticles, the surface becomes rough with dotted sheath-like structure.Images presented in **Figure 5.2f** and **5.2g** show the presence of the nanocrystals formed over N-rGO. The dark spots over N-rGO are identified as the metal oxide nanoparticles with particle size ranging from 5-8 nm. A magnified image of CFZr(0.3)/N-rGO is shown in **Figure 5.2g** (the corresponding SAED pattern is shown in the inset).

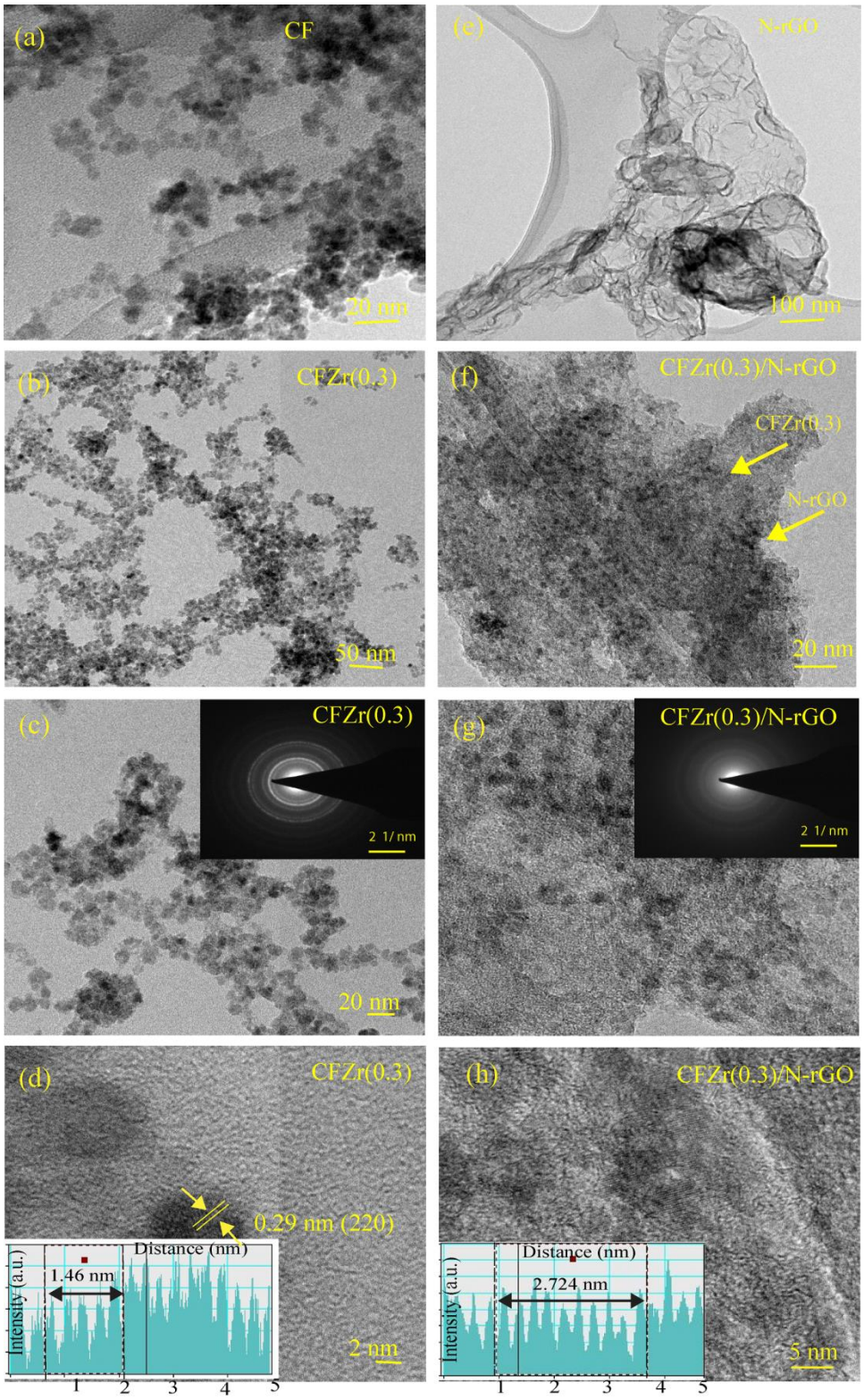

Figure 5.2. *(a)TEM image of cobalt ferrite nanoparticles (CF) prepared through the solvothermal synthesis. (b) and (c) TEM images of zirconium-substituted cobalt ferrite nanoparticles CFZr(0.3); SAED pattern of the particles is shown in the inset of (c). (d) HR-TEM*

image of CFZr(0.3) and the line profile of the particles (shown in the inset). (e) TEM image of the nitrogen doped reduced graphene oxide (N-rGO). (f) and (g) TEM images of the zirconium-substituted cobalt ferrite/nitrogen doped reduced graphene oxide(CFZr(0.3)/N-rGO) composite at different magnifications; the diffused ring pattern of CFZr(0.3)/N-rGO is presented in the SAED image (inset of (g)). (h) HR-TEM image of CFZr(0.3)/N-Rgo showing the d-spacing of 0.27 nm (line profile presented in the inset).

Homogenous distribution of the nanocrystals and highly exposed catalytic sites play crucial roles in achieving stable and efficient electrocatalysis.[47] Furthermore, as the nanocrystals are prone to leaching out from the surface in the rigorous oxidative-reductive environment of ORR/OER, here, the issue has been tackled to a large extent by decorating the particles over N-rGO.[48-49] The nitrogen doping helps to provide efficient anchoring sites for the nanocrystals during solvothermal synthesis, leading to strongly held nanoparticles.[47]

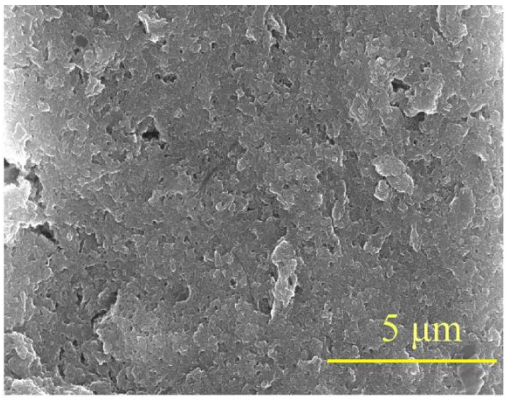

Element	Wt%	At%
CK	43.05	55.33
NK	05.53	06.10
OK	35.83	34.57
FeK	04.29	01.18
CoK	09.75	02.55
ZrK	01.55	00.26
Matrix	Correction	ZAF

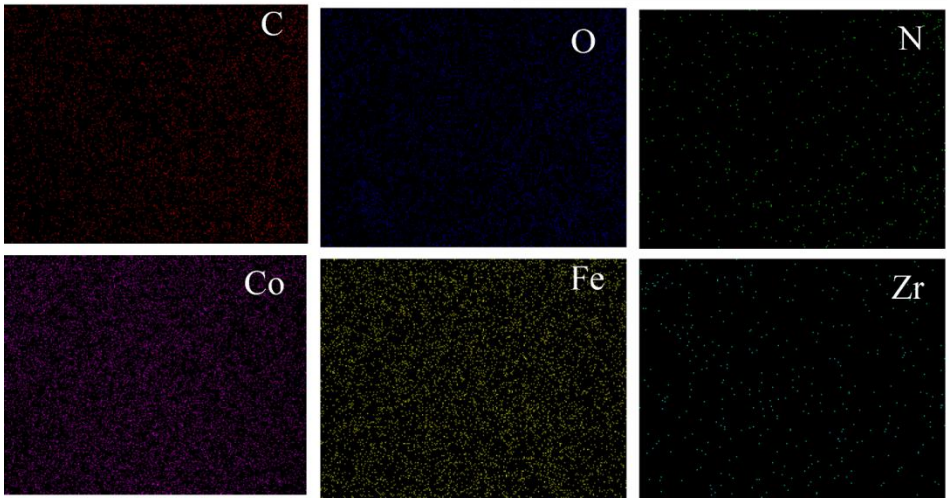

Figure 5.3.*FE-SEM images of CFZr(0.3)/N-rGO and the corresponding elemental mapping. A table is presented in order to quantitatively represent the elements present in the system.*

To confirm the formation of the nanoparticles over N-rGO, HR-TEM imaging of the catalyst was performed (**Figure 5.2h**). The d-spacing calculated from the magnified TEM image (line profile shown in **Figure 5.2h**, inset) is 0.27 nm corresponding to the (220) plane of CFZr(0.3). Data corresponding to FE-SEM imaging, energy dispersive analysis of X-rays (EDAX) and elemental mapping of CFZr(0.3)/N-rGO are presented in **Figure 5.3**. As evident from the figure, homogenous distribution of the metal oxide nanoparticles has been achieved by the solvothermal synthesis. The anomaly in the atomic percentage measured can be attributed to the surface specificity of EDAX.

5.3.2. XRD Analysis: Moreover, to explore the structural properties of the substituted catalysts, PXRD was carried out for the various substituted samples before and after supporting over N-rGO. The results of PXRD of the zirconium-substituted cobalt ferrite nanocrystals are shown in **Figure 5.4**.

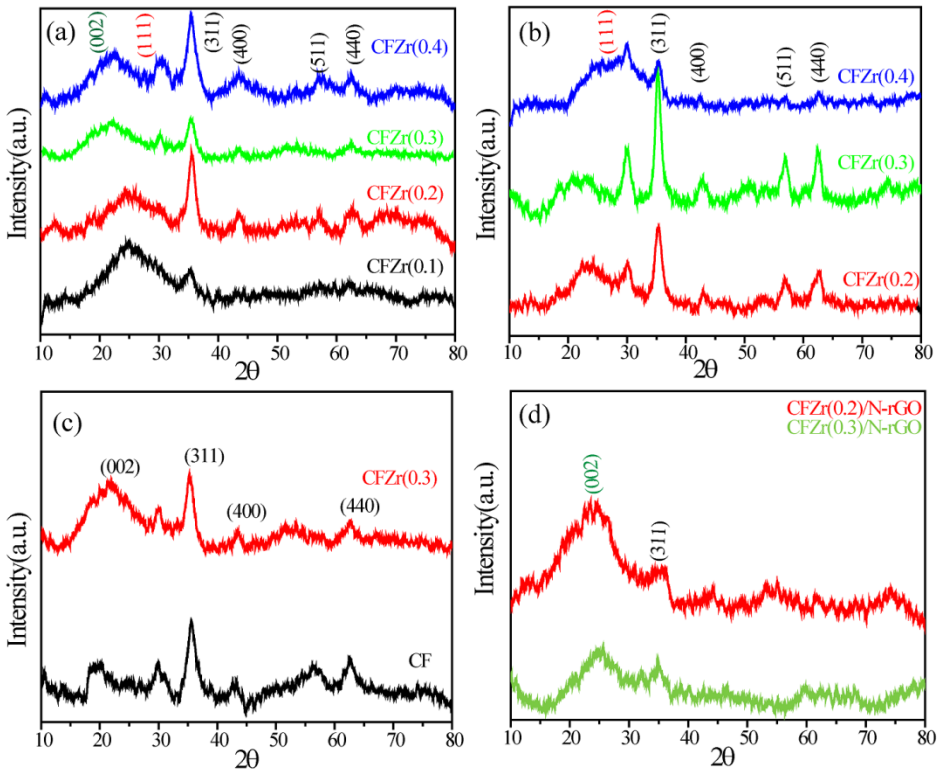

Figure 5.4. *(a) Powder X-Ray Diffraction (PXRD) patterns of the cobalt ferrite nanoparticles with varying substitution of zirconium in the spinel matrix; (b) PXRD recorded after annealing the substituted composite at 600°C for 4 h;(c) PXRD pattern of the CFZr(0.3) and CF nanocrystals. A broad peak at the 2θ value of 21.7° in CFZr(0.3) corresponds to the amorphous*

carbon, formed over the surface because of incomplete decomposition of the acetate salt. (d) PXRD recorded for the N-rGO supported zirconium-substituted cobalt ferrite nanocrystals.

In the PXRD spectra of the substituted CFs presented in **Figure 5.4a**, a characteristic intense peak at a 2θ value of 35.6°, corresponding to the (311) plane of the spinel CF **(JCPDS 22-1086)**, is visible.[50-52] Additionally, the prepared samples exhibit an intense broad peak centered at a 2θvalue of 24°, which is supposed to arise from the amorphous carbon derived from the incomplete decomposition of the acetate salt.[53-55] The peak shows a considerable shift in its position and intensity with respect to the composition, which is because of the lattice strain and surface exposed metal atoms. The Zr incorporation in the cobalt ferrite nanoparticles creates uniform lattice strain, which subsequently leads to a shift in the position of the PXRD peaks.[56-57]As seen from the TEM and SAED results, the composite nanoparticles have a size distribution in the range of 5-8 nm and they show a diffused ring pattern which is a characteristic of the amorphous materials. The amorphous materials are supposed to have short-range order, which provides them high surface area and enhanced catalytic property.[58] Here, the short-range order in the particles is likely to decide the surface metal atom distribution over the nanoparticles. The high surface content of Zr^{4+} will form more amorphous carbon because of its increased tendency to form covalent bonds, but simultaneously the phenomenon is governed by the short-range order of the metal atoms formed over the surface as a result of the decomposition of the acetate salts. Further, the substitution of the Fe^{2+} moieties with Zr^{4+} moieties displaces the Fe^{2+} species to the octahedral site.[38] In the present case, the above phenomenon continues up to a certain concentration of Zr and further increasing its concentration leads to phase separation. The phase separation with higher Zr(0.4) substitution in the CF matrix (CFZr(0.4)) is clear with a well-resolved peak at a 2θ value of 30° in the composite. We annealed the three composites CFZr(0.2), CFZr(0.3) and CFZr(0.4) at 600 °C for 4h and subjected them to PXRD analysis (**Figure 5.4b**). Annealing of the sample recrystallizes the grains to a larger size leading to well-resolved diffraction patterns. The CFZr(0.4) with Zr substitution by a fraction of 0.4 for Fe in $CoFe_{2-x}Zr_xO_4$ shows the broad peak centered at 30°, which is associated with the phase separation of the spinel ferrite and ZrO_2 structure. In case of CFZr(0.2) and CFZr(0.3), the peak intensity for (311), (400), (511) and (440) planes increased owing to the restructuring of the nanocrystals to form larger grains. The PXRD spectra of cobalt ferrite resemble that of Zr-substituted CF nanocrystals (**Figure 5.4c**).The intense peak for the (311) plane of the spinel

ferrite and the (002) plane for the amorphous carbon are observed in the case of CFZr(0.3). After confirming the well-resolved spinel crystal structure from PXRD, the experiment was extended to achieve decoration of the particles over the N-rGO support to get a homogenous distribution for enhanced catalytic activity. The spinel structures of the composites CFZr(0.2) and CFZr(0.3) are found to be retaining in the N-rGO supported system as well (**Figure 5.4d**). The two composites prepared with the N-rGO support display an intense peak at 25° for N-rGO, followed by the spinel phase peak at 35.7°.

5.3.3. Thermogravimetric Analysis (TGA): For confirmation of the loading of the metal oxide over N-rGO, thermogravimetric analysis (TGA) was carried out under oxygen atmosphere (shown in **Figure 5.5**). As evident from the graph, there is an initial weight loss of 10% up to 80 °C which corresponds to moisture and adsorbed gases over the surface. A second weight loss observed from 250-400 °C is assigned to loss of graphitic carbon in the form of CO_2. The residue content of 35% retained after completion of the oxidation of the graphitic carbon corresponds to the total metal oxide loading in the system.

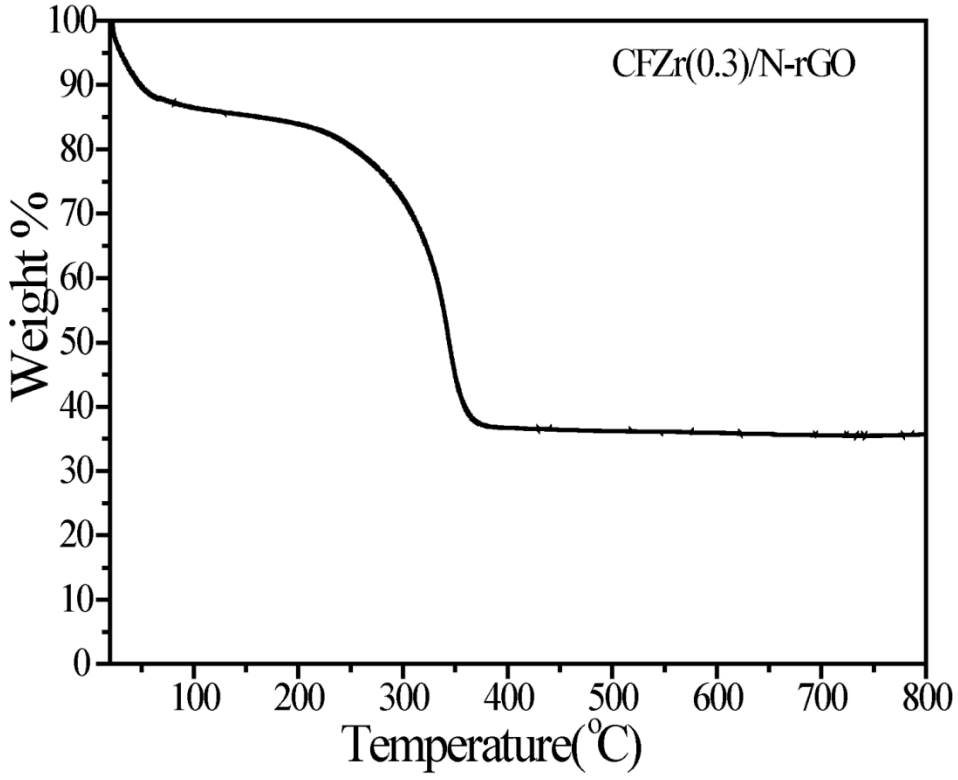

Figure 5.5. *TGA profile of the of N-rGO supported CFZr(0.3) nanocrystals.*

5.3.4. XPS Analysis: The effect of Zr substitution in the structure and the change in the electronic environment of the nanoparticles have also been confirmed through XPS analysis (**Figure 5.6**). The survey spectra of CFZr(0.2) and CFZr(0.3) are shown in **Figure 5.6a**.

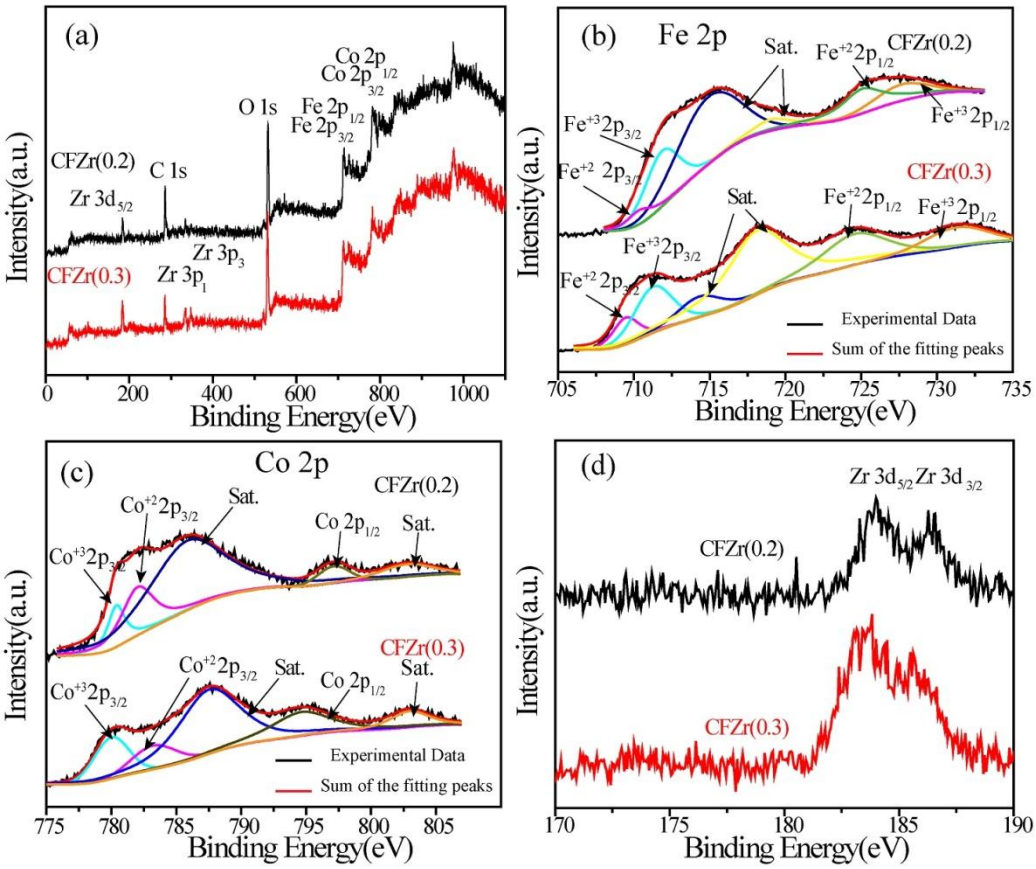

Figure 5.6.*(a) XPS survey spectra of the CFZr(0.2) and CFZr(0.3) composites. A peak of zirconium can be identified in both the composites but are more pronounced in CFZr(0.3). (b), (c), and (d) are the characteristic spectra of Fe 2p, Co 2p, and Zr 3d, respectively. As shown in (d), the zirconium intensity is the higher in CFZr(0.3) compared to CFZr(0.2).*

The binding energies recorded in the spectra are 184.46, 284.12, 529.90, 715.46, and 784.92 eV, corresponding to the Zr, C, O, Fe, and Co elements, respectively, present in the system.[50-52] A comparative spectra of iron, cobalt, and zirconium are given in **Figure 5.6b, 5.6c** and **5.6d**, respectively. A peak shift of 0.90 eV is observed in the iron spectra when the Zr substitution in the ferrite lattice varied from 0.2 to 0.3(CFZr(x), where, 'x' varies from 0.2 to 0.3), which is expected to be due to the change in the electronic environment of the nanoparticles. The deconvoluted spectra of iron of the two composites show change in the Fe^{2+}/Fe^{3+} ratio and simultaneously in the intensity of the satellite peak. Increase in the intensities of the satellite

peaks is related to the disorder in the particles.[59-60] The Zr substitution in the cobalt ferrite changes the electronic environment around the iron atom and this results in the shake-up energy loss and consequently the change in the satellite peak intensity.[59-60] In the deconvoluted spectra of CFZr(0.2) and CFZr(0.3), the Fe $2p_{3/2}$ and Fe $2p_{1/2}$ peak positions changed from 712.30 to 710.08 eV and 725.09 to 724.60 eV, respectively.[61-62] Similarly, a shift of 0.70 eV is also observed in the cobalt spectra for the substituted composites. In the deconvoluted spectra of CFZr(0.2) and CFZr(0.3), the Co $2p_{3/2}$ and Co $2p_{1/2}$ peaks are shifted from 781.40 to 780.70 and from 796.80 to 797.22 eV, respectively.[61-63]. The spectra presented in **Figure 5.6d** reveal the peak for the Zr$3d_{5/2}$ and $3d_{3/2}$ (which is overlapped with the $3d_{5/2}$ peak) states.[55] Higher concentration of Zr leads to an increase in the peak intensity as evident from the survey spectrum and the detailed spectra (**Figure 5.6a** and **5.6d**).

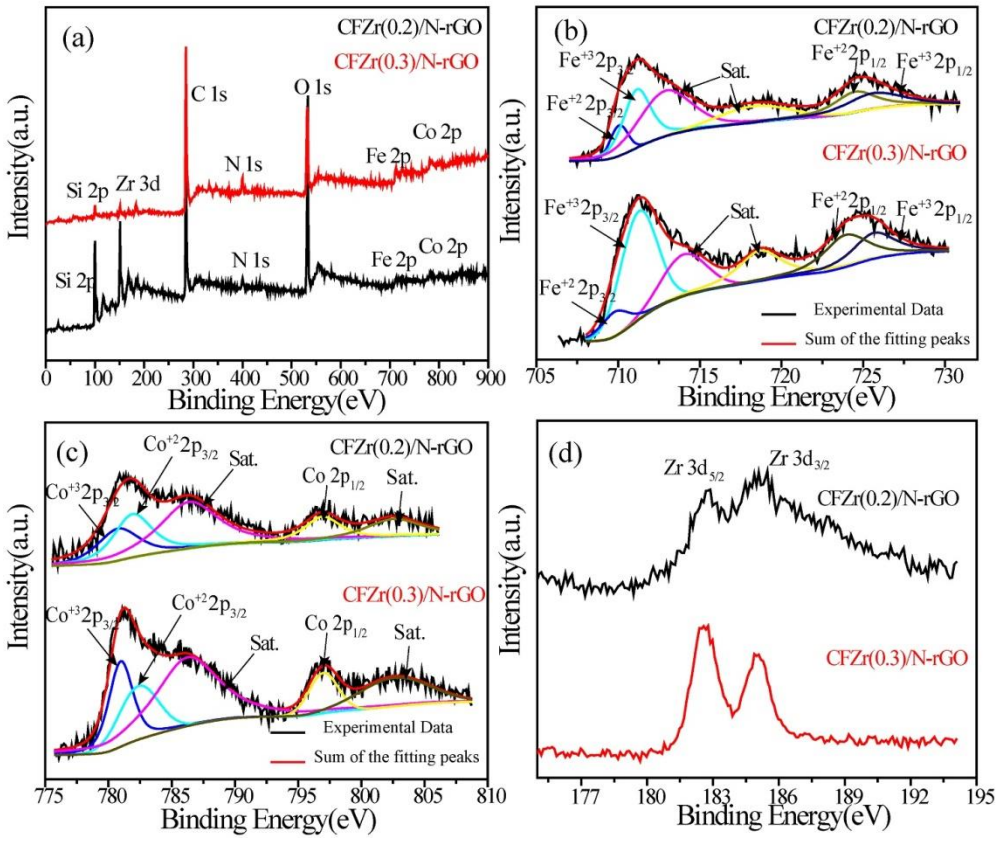

Figure 5.7. *(a) Survey spectra of the composites CFZr(0.2)/N-rGO and CFZr(0.3)/N-rGO, (b) and (c) are the deconvoluted XPS of the Fe 2p and Co 2p, respectively, of the composites CFZr(0.2)/N-rGO and CFZr(0.3)/N-rGO and (d) XPS of the Zr 3d of the CFZr(0.2)/N-rGO and CFZr(0.3)/N-rGO composites.*

Moreover, the analysis was extended for the N-rGO supported nanoparticles as the carbon supported particles are supposed to offer different electronic environment (**Figure 5.7**). In the survey spectrum, a well resolved N 1s peak appeared in both CFZr(0.2)/N-rGO and CFZr(0.3)/N-rGO composites at the binding energy value of 401.21 eV. In the deconvoluted spectra of iron and cobalt of the composites, the intensity of the peak corresponding to the 3+ state of Co and Fe is found to be increased which is because of the delocalization of the electron density by the presence of Zr^{4+} in the nanoparticles (**Figure 5.7b** and **5.7c**).[64] Here, in the case of the carbon supported nanoparticles, the electronic environment is different and hence the spectra also differ from the unsupported counterparts. In the case of the carbon supported system, the nitrogen atom provides the anchoring sites for the growth of the nanopartilcles, which reduces the disorder in the nanoparticles and thereby the intensity of the satellite peak. In addition to this, the structural formulae of the various composites were calculated from the atomic percentage obtained from the XPS data using Casa XPS version 2.3.18 (**Table 5.1**).

Table 5.1. *Atomic percentages of Co, Fe and Zr obtained in the various composites and the respective possible formula (oxygen vacancies and inversion parameters are neglected) form the XPS analysis*

Sr. No.	Composite	At.% of Co from XPS	At.% of Fe from XPS	At.% of Zr from XPS	Formula
1	CFZr(0.2)	10	12.16	2.95	$CoFe_{1.2}Zr_{0.28}O_4$
2	CFZr(0.3)	11.54	18.95	11.02	$CoFe_{1.64}Zr_{0.95}O_4$
3	CFZr(0.2)/N-rGO	0.32	2.38	0.75	$CoFe_{1.8}Zr_{0.4}O_4$
4	CFZr(0.3)/N-rGO	0.34	0.61	0.15	$CoFe_{2.04}Zr_{0.8}O_4$

Since the XPS is a surface technique, the measured atomic percentage is dependent on the surface exposed metal atoms. Further, it can be affirmed from the above XPS analysis that there is (1) presence of adequate amount of Zr in the CFZr(0.3), (2) change in the electronic properties of the CF nanoparticles and consequently the decreased binding energy of iron and cobalt, (3) effective Zr substitution in the ferrite lattice and (4) change in the electronic environment of the supported nanoparticles.

5.3.5. Electrochemical Studies: A set of standard experiments such cyclic voltammetry (CV), linear sweep voltammetry (LSV), chronopotentiometry (CP) and charge-discharge (C-D) cycling was carried out to understand how the compositional variation influences the intrinsic

electro-catalytic activity of the system. The preliminary experiments were performed with the Zr-substituted CF before supporting the optimum composition on N-rGO.

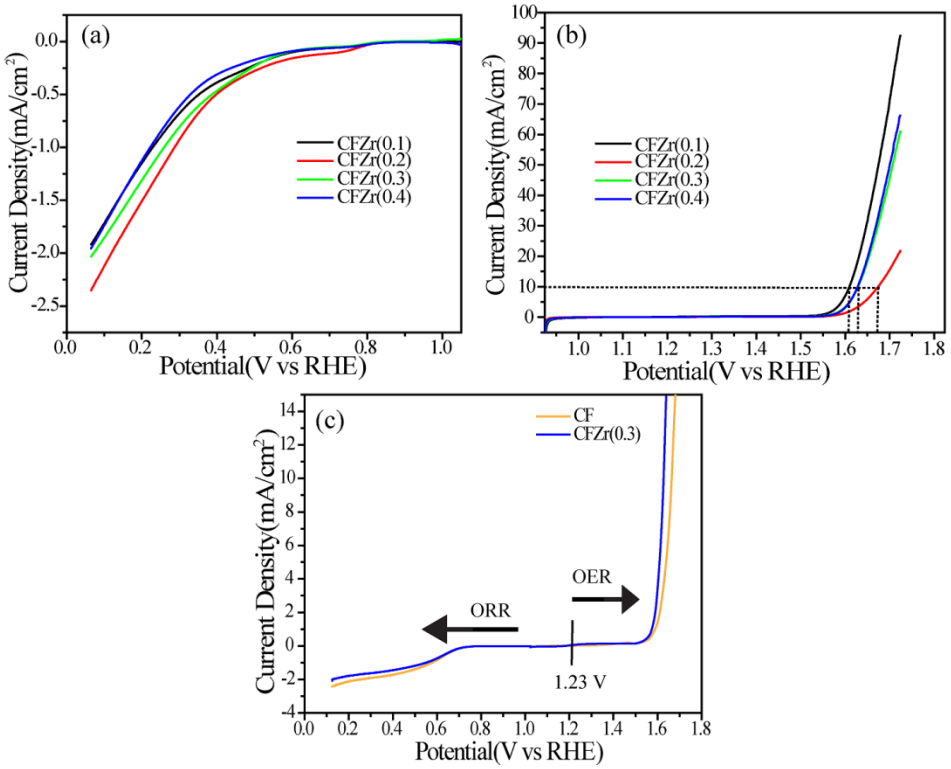

Figure 5.8. *(a) Linear Sweep Voltammograms (LSVs) recorded for the various composites in oxygen-saturated 0.1 M KOH solution at 1600 rpm with a cathodic scan rate of 10 mV/s for ORR.(b) LSVs of the composites recorded in 1 M KOH solution at 1600 rpm with an anodic scan rate of 10 mV/s for OER.(c) LSV plots of the CF and CFZr(0.3) catalysts recorded in 1 M KOH solution at a voltage sweep rate of 10 mV/s. The LSV plots for ORR were collected in oxygen saturated condition and for OER in nitrogen saturated condition.*

As presented in **Figure 5.8a**, the ORR current density in the LSVs is found to be varying with respect to the Zr substitution in the CF system. The current density at 0.06 V (*vs* RHE) follows the order as: CFZr(0.2) (-2.3 mA/cm^2) > CFZr(0.3) (-2.0 mA/cm^2) > CFZr(0.1)(-1.90 mA/cm^2) > CFZr(0.4)(-1.95 mA/cm^2). This can be attributed to the presence of exposed metal surface and change in the electronic properties of the nanoparticles due to Zr substitution in the lattice. Compared to ORR, Zr substitution has displayed a reversed trend at 10 mA/cm^2 current density in the case of oxygen evolution reaction (OER) activity in 1 M KOH solution, which follows the order as: CFZr(0.1)(1.60 V) > CFZr(0.3)(1.62 V) > CFZr(0.4)(1.63 V) > CFZr(0.2)(1.67 V) (**Figure 5.8b**). This observed reverse trend for the ORR and OER is ascribed to the change in the band gap and electronic property of the nanoparticles. In the composites, Zr

substitution causes the band structure to shift towards the standard reduction potential of molecular oxygen (1.23 V *vs* RHE) which decreases the overpotential for ORR and concomitantly increases that for OER. After a certain concentration of Zr, no further decrease in the overpotential has been observed. The shift in the binding energy observed during the XPS of the metal atoms also confirms the change in the band structure. Considering this reversed trend in ORR and OER with respect to the compositional variation, it can be identified that the system CFZr(0.3) is the right candidate as a bifunctional catalyst which possesses the optimum activity characteristics to facilitate both ORR and OER with a balanced overpotential characteristics. The overall overpotential for both the reactions is shown in **Figure 5.8c** for the parent cobalt ferrite (CF) and the composite (CFZr(0.3)). The composite shows a 40 mV lower overpotential for OER compared to CF and displays similar onset potential value as that of the parent ferritein the case of ORR. The observed remarkable changes for both ORR and OER in the ferrite matrix after the Zr ingestion can be ascribed to the changes incurred in the adsorption energy of the surface intermediates originated from the respective reactions. Zr, being an electropositive metal, increases the electron density in the nanoparticle and hence lowers the binding energy of the metal ions leading to alteration of the adsorption energy of the surface intermediates.[31,65] Generally, the adsorption energies of the intermediates (*O, *OH and *OOH) determine the kinetics of ORR and OER.[30] An optimum substitution of Zr is essential to deliver an overall low overpotential for ORR and OER.

Further, in order to ascertain the mechanistic aspects of ORR by quantitatively estimating the amount of H_2O_2 produced (as a byproduct of the parasitic 2-electron transfer reaction), rotating ring disc electrode (RRDE) analysis was performed. A detailed discussion on the RRDE analysis and the calculations involved therein are given in **Chapter 2**. Generally, the ORR reaction follows a 2- or 4-electron pathway which can be determined experimentally from RRDE by measuring the peroxide intermediate in the process.[66-67] The percentage of H_2O_2 determined in the case of CFZr(0.2) is 55%,while it was less than 40% `for the other catalysts (**Figure 5.9a**).[67] The peroxide formation can be used to identify the reaction pathway by calculating the number of electrons involved in the reaction. As presented in **Figure 5.9b**, the number of electrons for the reaction measured in the case of CFZr(0.2) is 2.9 whereas it is found to be 3.2 in the case of CFZr(0.3). For improving the catalytic activity, the nanoparticles of the composites were grafted over the N-rGO support and a comparative RRDE analysis with 20% Pt/C catalyst is presented

in **Figures 5.9c** and **5.9d**. Catalytic activity showed improvement after supporting the composite nanoparticles over N-rGO and the number of electrons transferred rose to 3.6 while the peroxide formation diminished to below 30%, thereby reducing the catalyst deterioration and increasing longevity. Thus, Zr substitution is found to be shifting the reaction pathway from the less preferred 2-electron route to the preferred 4-electron side with a favorable intervention by N-rGO as the catalyst support.

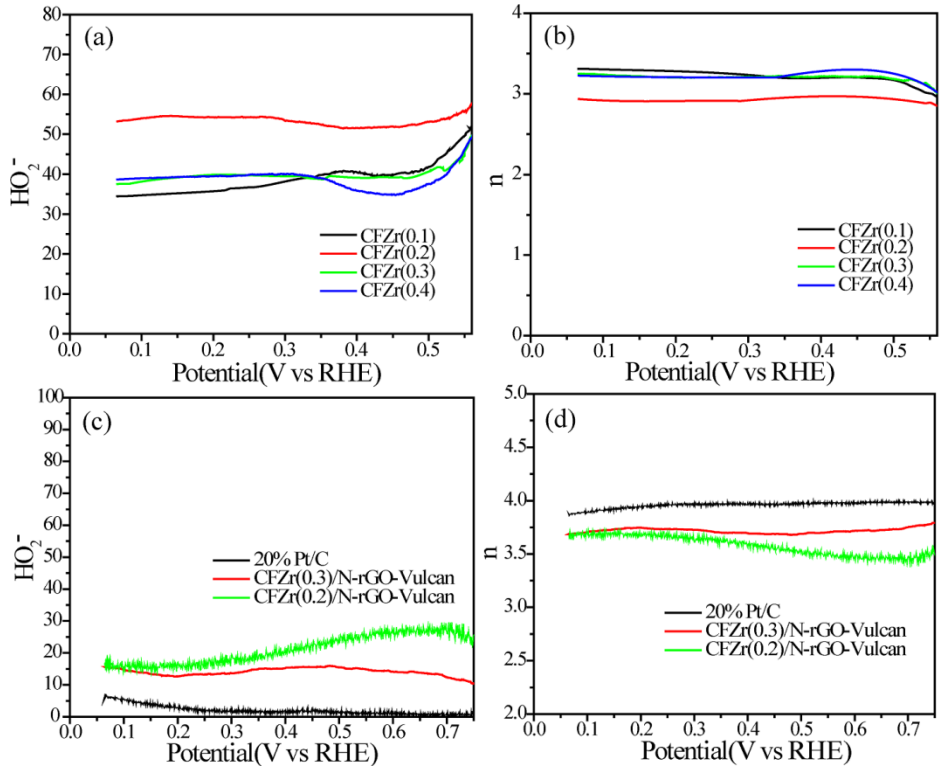

Figure 5.9. *(a) and (b) represent the % of H_2O_2 generated and the number of electrons involved in ORR as calculated from the RRDE analysis for CFZr(0.1), CFZr(0.2), CFZr(0.3), and CFZr(0.4) in oxygen saturated 0.1 M KOH solution at an electrode rotational speed of 1600 rpm. (c) and (d) represent the % of H_2O_2 generated and the number of electrons involved in ORR for the nitrogen doped graphene supported CFZr(0.2) and CFZr(0.3) composites.*

The synthesized Zr-substituted metal oxide catalysts display resistance features well within the acceptable levels. The Nyquist plots showing the equivalent series resistance(ESR) of the substituted ferrite systems are presented in **Figure 5.10**. The ESR for the prepared composites follow the order: CF(15.8Ω) < CFZr(0.1)(22.2 Ω) < CFZr(0.2)(25.0Ω) < CFZr(0.3)(32.9 Ω) < CFZr(0.4) (44.9Ω). The Zr substitution increased the ESR, presumably, as a result of the increased disorder in the CF nanocrystals.[68-69] The above results are supported by the XPS data, where, a clear increase in the intensity of the satellite peak is noted. For better catalytic activity

and stability, the composite was grafted over N-rGO and the composite CFZr(0.3)/N-RGO showed an ESR value of 38.7 **Ω**. Nitrogen doping provides the site for the growth of the nanocrystals over the graphene framework. The synergistic effect of the metal oxide and carbon support plays a major role in the enhanced intrinsic activity of the catalyst, which we have explored in the electrochemical studies as detailed in the following section.

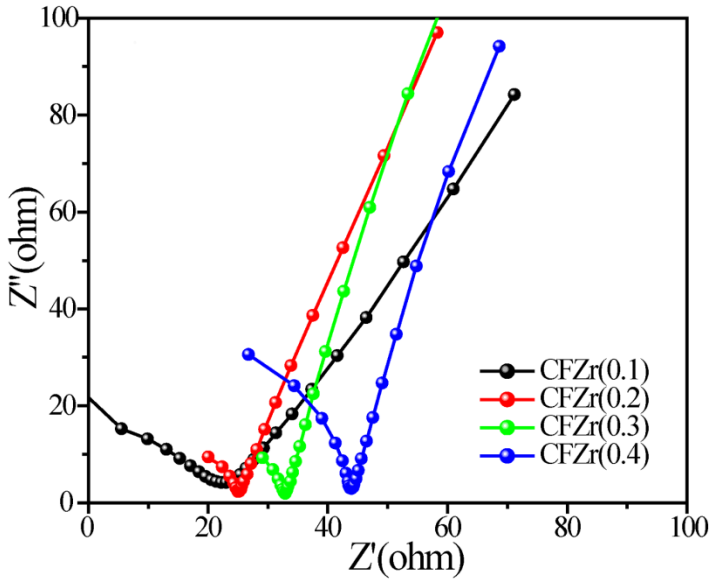

Figure 5.10.*Nyquist plots recorded for the zirconium substituted cobalt ferrite nanocrystals. The substitution in the cobalt ferrite structure increases the disorder in the matrix and finally the increased ESR.*

Prior to the actual implementation of the catalyst in the ZAB, the carbon supported nanoparticle composites were analyzed for their bifunctional activity (**Figure 5.11**). As presented in **Figure 5.11a, 5.11b** and **5.11c,** the CFZr(0.3)/N-rGO composite shows the lowest overall overpotential(ΔE) of 0.840 V which has direct influence over charge-discharge function of rechargeable Zn-Air Battery. For ORR, it is the molecular oxygen that has to be adsorbed over the catalyst surface, whereas OER requires the water molecule to be dissociated. In the electrolyte medium, surplus of water is present and accessible to the catalyst surface; hence, the OER is less influenced with the contribution from the N-rGO support. On the other hand, N-rGO support plays a vital role in favoring the oxygen binding and its subsequent advantage in modulating the activity towards ORR. Considering the observed trends related to the extent of modulations affected in the overpotentials and the overall bifunctional characteristics based on

the compositional variations, two representative systems, *viz.*, CFZr(0.2)/N-rGO and CFZr(0.3)/N-rGO, have been selected for further analysis.

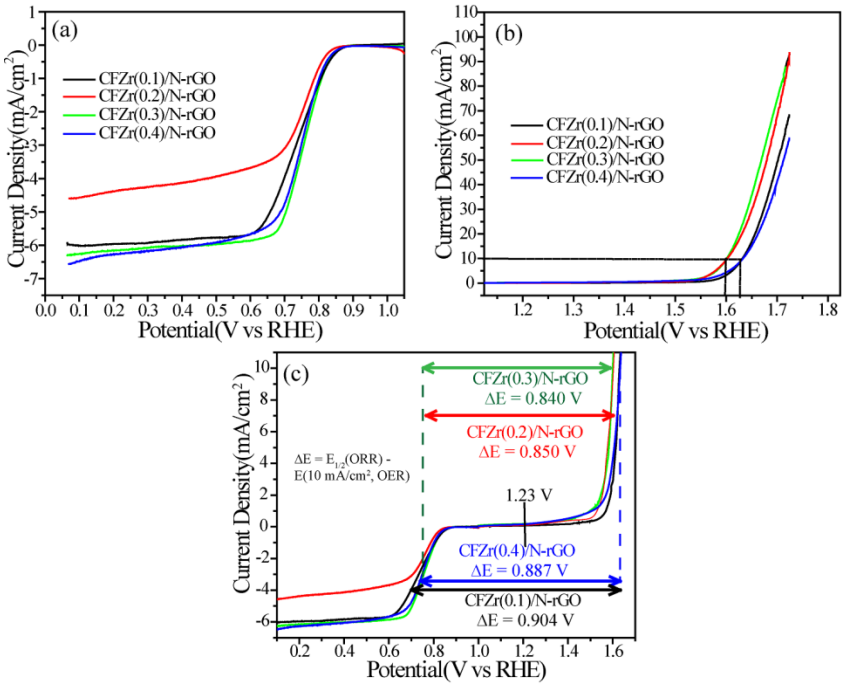

Figure 5.11. *(a)-(b) represent the LSVs recorded in the RDE mode of the composites CFZr(0.1)/N-rGO, CFZr(0.2)/N-rGO, CFZr(0.3)/N-rGO and CFZr(0.4)/N-rGO recorded in 0.1 M KOH and 1 M KOH solution for ORR and OER, respectively, by maintaining the electrode rotation speed of the working electrode as 1600 rpm and a voltage sweep rate of 10 mV/s;(c) represents the combined plot of the cathodic LSVs for ORR and anodic LSVs for OER, representing the overall overpotential* ($\Delta E = E_{\frac{1}{2}}(ORR) - E(10\ mA/cm^2)$ *for the homemade catalysts.*

The oxygen sensitivity of CFZr(0.2)/N-rGO and CFZr(0.3)/N-rGO is clearly evident from the cyclic voltammograms presented in **Figure 5.12a** and **Figure 5.12b**, respectively, because the well-defined ORR peaks are appearing in both the cases when the electrolyte is purged with oxygen. The peak potential of ORR is 0.745 V (*vs* RHE). The ORR peak of CFZr(0.3)/N-rGO is well resolved and sharp compared to CFZr(0.2)/N-rGO, which is a direct evidence on the favorable modulations in the ORR characteristics accomplished by the former system. As explained before, Zr incorporation alters the adsorption energies of the surface intermediates and subsequent reduction of oxygen. The linear sweep voltammograms (LSVs) recorded under the rotating disc electrode (RDE) mode display well featured ORR profiles as

observed in the case of the state-of-the-art catalysts. **Figure 5.12c** and **5.12d** display the LSVs forCFZr(0.2)/N-rGO and CFZr(0.3)/N-rGO, respectively.

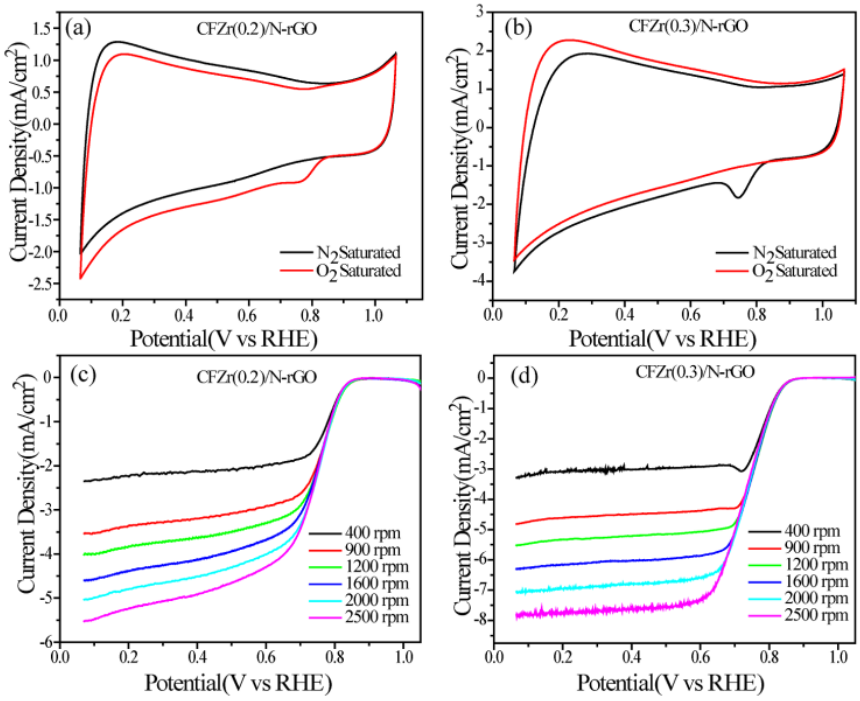

Figure 5.12. *(a) and (b) are the cyclic voltammograms (CVs) of CFZr(0.2)/N-rGO and CFZr(0.3)/N-rGO, respectively, measured at a scan rate of 50 mV in 0.1 M KOH solution (red: oxygen saturated; black: nitrogen saturated); (c) and (d) are the LSVs recorded using RDE at different rotation rates of the working electrode for CFZr(0.2)/N-rGO and CFZr(0.3)/N-rGO, respectively.*

Using the LSV profiles, the Koutecky-Levich (K-L) plots were constructed, which is a very useful way to look into an important performance indicator named the kinetic current density (j_k)(**Figure 5.13a and 5.13b).**[70] A brief detail of the K-L plot and equation involved in the calculation is given in **Chapter 2**. Additionally, a comparative K-L plots of the catalysts CFZr(0.3)/N-rGO, CFZr(0.2)/N-rGO and 20% Pt/C calculated at 0.08 V(*vs* RHE) are presented in **Figure 5.13c**. The plot represents the relation between the inverse of the current density and the inverse of the square root of the rotational speed ($\omega^{1/2}$) of the working electrode with change in the potential. The linear relationship maintained in the K-L plots between the two catalysts indicates the first order kinetics followed by the process. The plot was extrapolated to the *y*-axis and j_k value has been calculated by taking the inverse of the intercept where the *x*-axis value is 0 (this corresponds to an assumption of infinite rotation speed of the working electrode) and normalizing the obtained current with the geometrical area of the electrode. The j_k value

measured at a potential of 0.08 V(*vs* RHE) in the case of CFZr(0.2)/N-rGO and CFZr(0.3)/N-rGO are $7.6x10^{-3}$ and $14.2x10^{-3}$ A/cm^2, respectively, compared to $6.2x10^{-3}$ A/ cm^2 obtained in the case of Pt/C.[12,70]

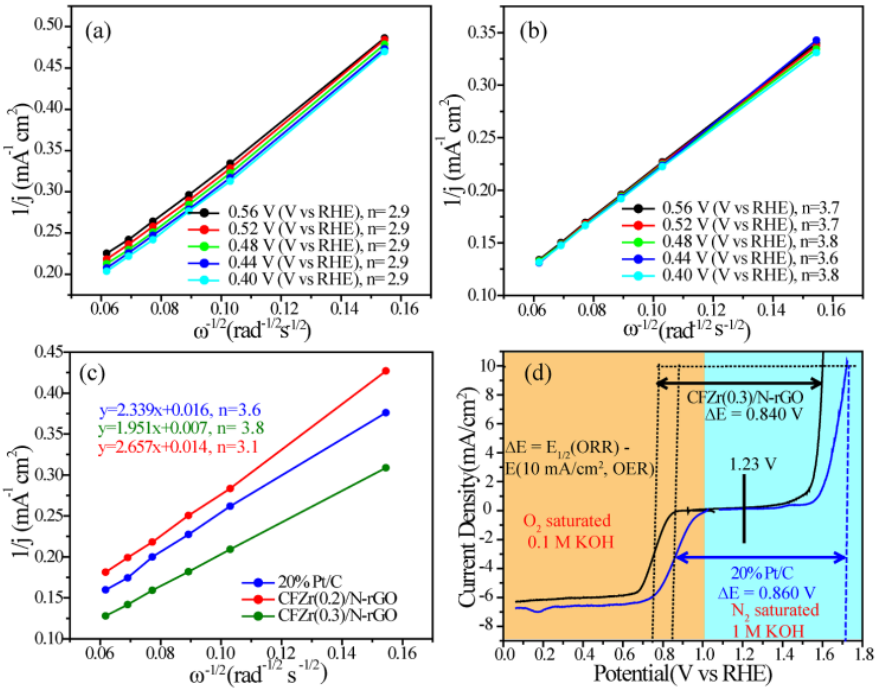

Figure 5.13. *(a) and (b) represent the K-L plots constructed from the RDE analysis of CFZr(0.2)/N-rGO and CFZr(0.3)/N-rGO, respectively;(c) comparative K-L plots of CFZr(0.3)/N-rGO, CFZr(0.2)/N-rGO and the 20% Pt/C catalyst generated at 0.08 V(vs RHE); (d) comparative LSVs of CFZr(0.3)/N-rGO and 20% Pt/C catalyst for ORR and OER in the basic electrolyte.*

Further, we have compared the activity of the homemade catalysts with that of a 20% Pt/C catalyst in terms of ORR and OER overpotential. The plots indicating the overpotential involved for ORR and OER in the case ofCFZr(0.3)/N-rGO and Pt/C catalyst are presented in **Figure 5.13d**. As per the integrated ORR/OER plots, CFZr(0.3)/N-rGO has shown an 80 mV overpotential compared to Pt/C for ORR whereas the later suffered with an overpotential of 110 mV compared to CFZr(0.3)/N-rGO for OER. The homemade catalyst shows 0.840 V overall overpotential as bifunctional catalyst against 0.860 V for 20% Pt/C. This figure thus portrays the efficient bifunctional nature of the homemade catalyst, which is a demanding characteristic needed in developing efficient rechargeable metal-air batteries. To assess the stability of the catalyst towards the electrochemical environments as set for ORR, we performed the accelerated

durability test (ADT) by subjecting the catalyst to cyclic reduction for up to 5000 cycles (**Figure 5.14**). The catalyst shows negligible change in the onset and the $E_{1/2}$ value, though some change in the current density has been observed. The high stability of the catalyst for ORR further strengthens the scope as an air electrode material for its proposed application in the rechargeable Zn-Air battery (ZAB).[36-37]

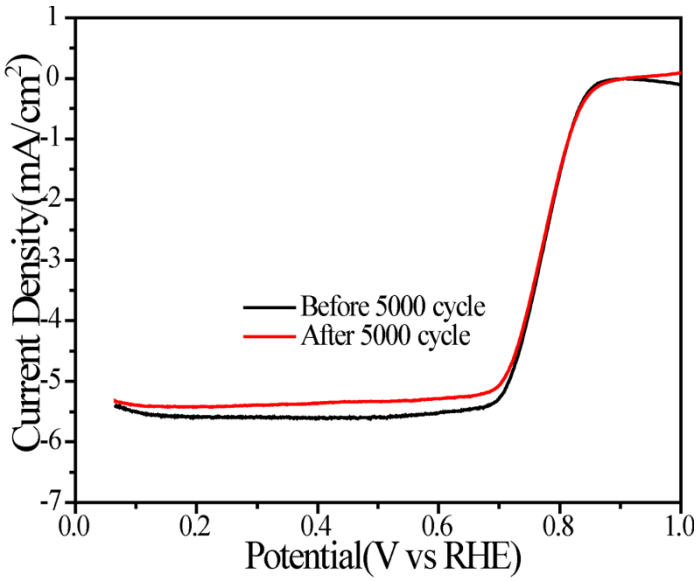

Figure 5.14. *Accelerated durability test (ADT) of CFZr(0.3)/N-rGO, which was carried out by cycling the test between the potential window of 0 to -0.60 V (vs Hg/HgO) with a voltage sweep rate of 100 mV.*

As discussed before, in a rechargeable ZAB, ORR as well as OER are required to take place over the electrodewhich necessitates the survivability of the catalyst material under drastic electrochemical environment since the system is expected to be subjected to drastic potential changes during the charge-discharge cycles.

5.3.6. Zinc-Air Battery:

A realistic system level validation of the newly-synthesized catalyst has been done by fabricating a ZAB by using this as the air electrode. The air electrode was constructed by mixing CFZr(0.3)/N-rGO along with Vulcan carbon as an additive which helps to spatially separate the graphene layers bearing the active catalytic sites The ratio of the Vulcan carbon to the catalyst was kept as 1:1 while maintaining an overall loading of 2.0 mg/cm^2 in the electrode. The prepared electrode served as the cathode in the device while a Zn foil functioned as the active anode material. A 6 M KOH solution was incorporated as electrolyte for the system.[33-34] The

constructed battery was discharged up to 0.4 V at various current densities under ambient conditions. During the discharge process, the ORR takes place over the cathode with a concomitant conversion of Zn metal to Zn^{2+} over the anode.[33-34,36-37] The complete cell reactions during the discharge process of the primary ZAB can be described as:

Anode: $$Zn \rightarrow Zn^{2+} + 2e^-$$

$$Zn^{2+} + 4OH^- \rightarrow Zn(OH)_4^{2-}$$

$$Zn(OH)_4^{2-}(sol) \rightarrow ZnO(s) + H_2O + 2OH^- \quad (E_o=-1.25\ V)$$

Cathode: $$O_2 + 2H_2O + 4e^- \rightarrow 4OH^- \quad (E_o = 0.40\ V)$$

Parasitic anode reaction: $$Zn + 2H_2O \rightarrow Zn(OH)_2 + H_2$$

The functioning of ZAB during charging and discharging process and its correlation with the overpotential for ORR and OER are presented in **Figures 5.15a** and **5.15b**, respectively. The ZAB fabricated with our catalyst has been explored for both the primary and rechargeable batteries. The open circuit potential (OCV) for ZAB fabricated with CFZr(0.3)/N-rGO is measured to be 1.39 V compared to 1.45 V for the battery fabricated with 20% Pt/C catalyst. Further, the ZAB loaded with our homemade catalyst has been discharged at 20 and 30 mA/cm^2 current densities as primary battery in ambient conditions (**Figure 5.15c**). A promising discharge feature having a flat plateau which is a desirable feature for the application of the battery has been achieved and this clearly articulates to the high ORR activity of CFZr(0.3)/N-rGO. The discharge plateaus maintained at the current densities of 20 and 30 mA/cm^2 are 1.1 and 1.0 V, respectively, which remained constant till a sudden drop to 0.40 V appears later on. The comparatively lower voltage and shorter voltage plateau while discharging at 30 mA/cm^2 can be attributed to faster consumption of the anode material and sluggishness in the faradaic reaction appeared as a result of the high current demand. The calculated discharge capacities at the discharge current densities of 20 and 30 mA/cm^2 are 732 and 727 mAh/g, respectively (**Figure 5.15d**).[71-73]It can be noted that the observed discharge capacity is comparable to our previously reported value of 630 mAh/g for the cobalt ferrite decorated system which shows a low discharge voltage of 1.0 V at a discharge current density of 20 mA/cm^2 (**Figure 5.15e**).[50] After the realistic validation of the primary ZAB by using the homemade catalyst as the cathode in the system, the validation has been extended in are chargeable ZAB mode. Here, during the charging

process, the cell reactions take place in the opposite directions as compared to the reactions occurring during the discharging process:

$$Zn(OH)_4^{2-}(sol) + 2e^- \rightarrow Zn + 4OH^-$$

$$4OH^- \rightarrow O_2 + 2H_2O + 4e^-$$

Parasitic reactions:

$$C + O_2 \rightarrow CO_2$$

$$KOH + CO_2 \rightarrow K_2CO_3 + H_2O$$

In this case, while the system undergoes the oxidation-reduction (OER/ORR) cycling in the charge-discharge process, the strong coupling of the CFZr(0.3) nanoparticle with the N-rGO support plays a vital role in retaining the active centers even under the harsh electrochemical corrosive environment excreted by the cycling process.

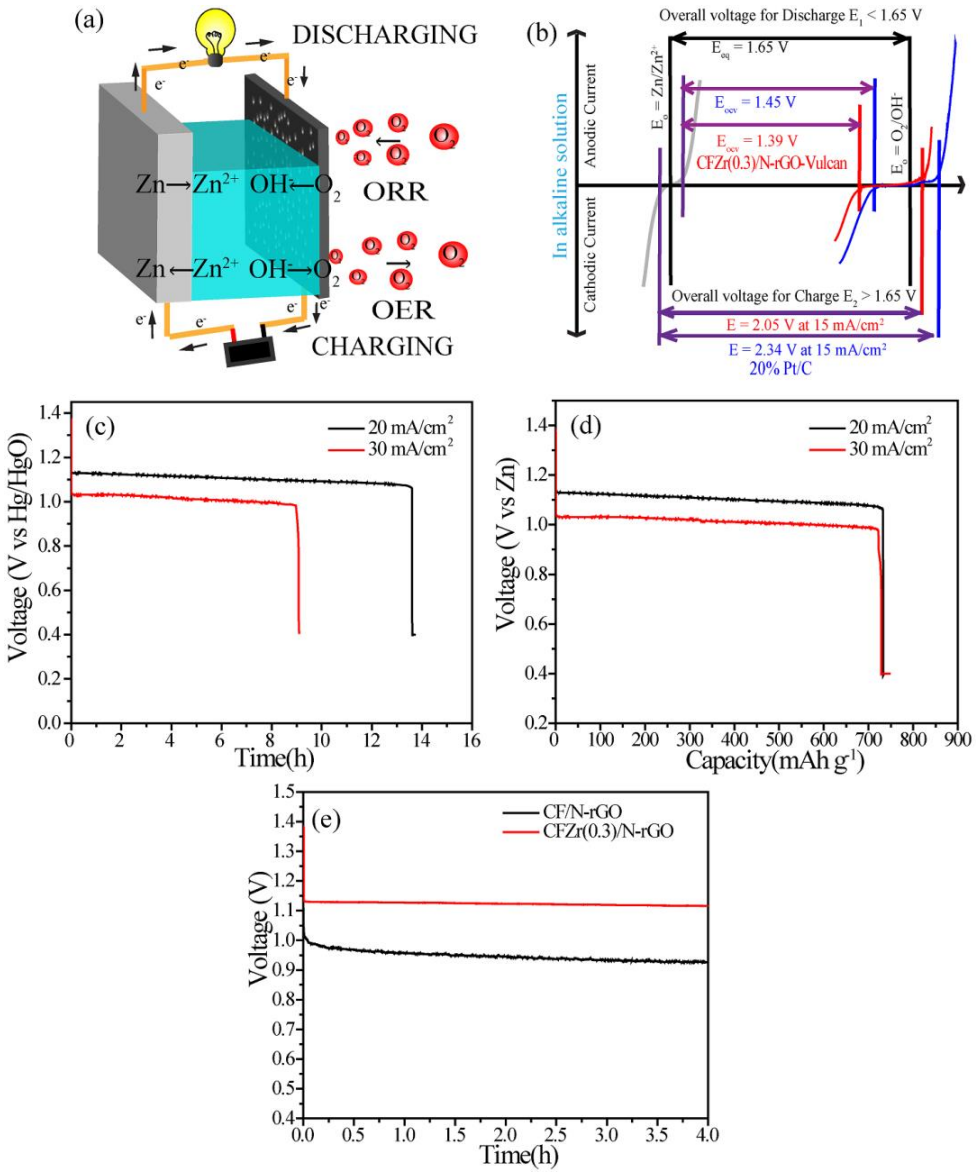

Figure 5.15. *(a) A typical ZAB operation for charging and discharging processes; (b) correlation of the overpotental of ORR and OER for a rechargeable ZAB; (c) galvanostatic discharge curve of the primary ZAB fabricated with CFZr(0.3)/N-rGO as the cathode, which operates at the discharge rates of 20 and 30 mA/cm^2 in 6 M KOH solution; (d) discharge capacity of the battery after normalization with the amount of zinc used for the discharge;(e)Galvanostatic discharge profiles of CF/N-rGO and CFZr(0.3)/N-rGO for the fabricated primary ZAB.*

It is known that since the recharging of the battery involves carbon corrosion as mentioned in the equations above, the active nanoparticles are prone to be detached from the support surface in the conventional systems.[74-75] As shown in **Figure 5.15b**, during the charging of the ZAB, the overall potential needed for charging the system varies with respect to the intrinsic activity of the catalyst employed (*i.e.*, 2.05 V for CFZr(0.3)/N-rGO and 2.34 V for 20%

Pt/C). This means that with its higher overall overpotential for the Pt/C catalyst compared to the homemade counterpart, the system is expected to be corroded or deteriorated at a faster rate.[38,76-77]

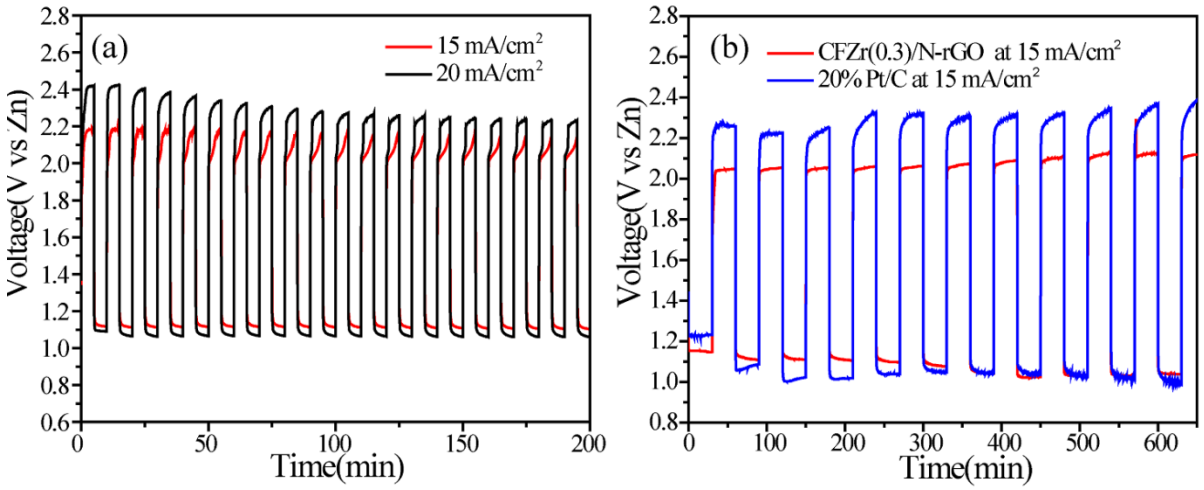

Figure 5.16. *(a) charge-discharge cycles of the rechargeable battery operated at the current densities of 15 and 20 mA/cm^2; (b) cycling data of the rechargeable ZAB fabricated with CFZr(0.3)/N-rGO and 20% Pt/C catalyst as the air electrodes and operating at a current density of 15 mA/cm^2.*

Figures 5.16a and **5.16b** display the charge-discharge profiles recorded in the case of the rechargeable ZAB.[68] Similar to the primary Zn-air battery, the discharge profile maintained the voltage region of 1.1 V at a discharge current density of 20 mA/cm^2. On the other hand, while charging, the voltage required for the charging progressively decreases in the initial few cycles as the catalyst gets activated with the cycling for OER, owing to the optimum defects created in the carbon support (**Figure 5.16a**).The charge-discharge profile of the battery at the current densities of 15 and 20 mA/cm^2 shows a constant charge-discharge plateau after initial few cycles. The high overpotential associated with high current density is accountable for the slow kinetics of OER/ORR. It is interesting to note that the ZAB fabricated with the Pt/C catalyst requires high overpotential during the charging process (**Figure 5.16b**) when compared to our homemade catalyst. Though the Pt/C catalyst has high ORR kinetics, the deterioration of the catalyst during the charging process causes decreased activity in the continuous cycles. Contrary to this, in the case of CFZr(0.3)/N-rGO, the nanoparticles are grafted over N-rGO and the strong interactions operating between the nanoparticles and the substrate help the system to survive in a better way under the harsh electrochemical environment. In the rechargeable Zn-air batteries, one

of the major issues other than the degradation of the electrode material which arises during the rechargeability is the dendrite growth of the deposited Zn metal. The dendritic growth short circuits the electrodes and makes the cell dead.[36] Continuous discharging of the battery followed by more duration for charging causes increased dendritic growth. In order to look into the durability aspects in a practical perspective, we have performed a testing by subjecting 200 charge-discharge cycles by reducing the time of charging and discharging (with 5 min duration each for the charging and discharging processes).This is expected to be a better way of judging the durability characteristics of ZAB in a realistic operating condition.

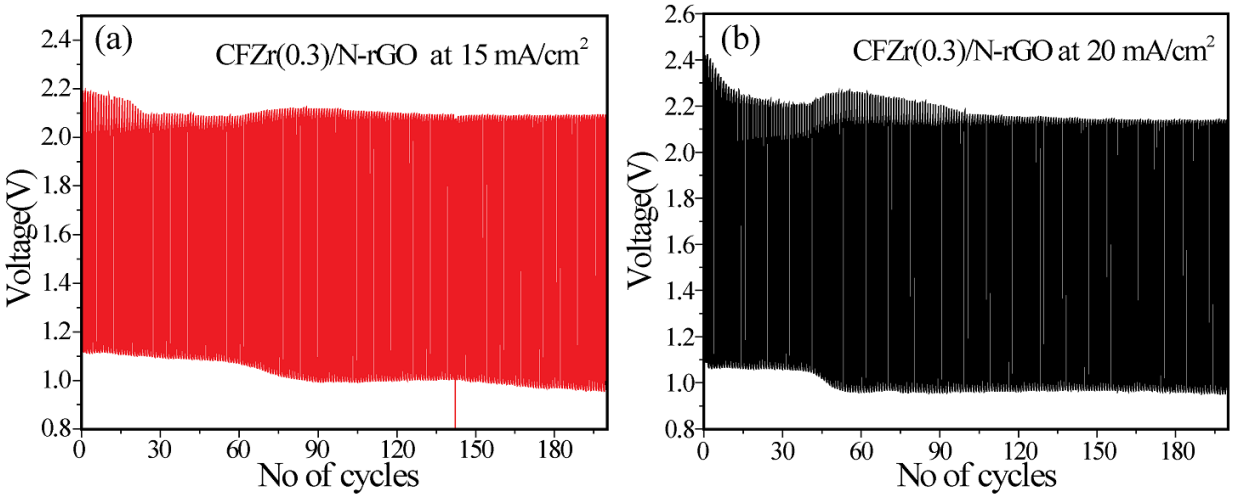

Figure 5.17. *(a) and (b) represent the charge-discharge cycles performed for the reachable ZAB at 15 mA/cm^2 and 20 mA/cm^2 current density, respectively.*

The ZAB cycling profiles recorded at the current densities of 15 mA/cm^2 and 20 mA/cm^2 are included in **Figure 5.17**.The system attained a stable charge-discharge profile with a discharge plateau of 1 V and charging plateau of2.1 V after the first 60 charge-discharge voltage cycles. This charge-discharge run for 200 cycles correspond to 33.3 h duration for each current density and this longer duration coupled with significantly more number of cycles mimic a more rigorous and adequate condition to better understand the durability characteristics of the cell. Thus, the testing results of the rechargeable ZAB justify the intrinsic activity and durability characteristics as derived from the single-electrode studies. The homemade catalyst thus positioned itself as a promising less expensive, robust, and environmentally benign alternative to the noble metal catalysts for the rechargeable metal-air battery applications.

5.4. Conclusion:

A solvothermal procedure was adopted for the synthesis of zirconium-substituted cobalt ferrite nanocrystals with an optimum composition of CFZr(0.3) having a particle size domain of 5-8 nm and promising performance characteristics towards electrochemical oxygen reduction reaction (ORR) and oxygen evolution reaction (OER). A significant change in the binding energy of the host metals (0.90 eV for iron and 0.70 eV for cobalt) could be measured with the compositional variation from CFZr(0.2) to CFZr(0.3). The compositional variation in the ferrite structure was reflected in the ESR value of the composites (25.0 Ω for the CFZr(0.2) and 32.9 Ω for CFZr(0.3)). Interestingly, the *in-situ* grafting of the nanoparticles of CFZr(0.3) over N-doped reduced graphene oxide (CFZr(0.3)/N-rGO) remarkably enhanced the performance during ORR as well as OER. A desirable low peroxide formation, ORR involving the preferred 4-electron transfer kinetics, and corrosion resistive nature of the system etc. stood out as the promising features of the homemade catalyst. During the single-electrode studies for understanding the ORR and OER characteristics, CFZr(0.3)/N-rGO showed an 80 mV overpotential compared to Pt/C for ORR whereas the later suffered with an overpotential of 110 mV compared to CFZr(0.3)/N-rGO for OER. An overall potential difference(ΔE) of 0.840 V has been achieved for the bifunctional nature of the homemade catalyst, which is a demanding characteristic required in developing efficient rechargeable metal-air batteries. During the realistic demonstration of a primary ZAB derived from the homemade catalyst as the air electrode, the system exhibited discharge capacities of 727 and 730 mAh/g at current densities of 20 and 30 mA/cm^2, respectively, under ambient conditions. In its extended validation towards the rechargeability of the system, the battery consisting of CFZr(0.3)/N-rGO as the air electrode showed lower overpotential during the charging process as compared to the system based on 20 wt.% Pt/C as the cathode. Additionally, in the durability test of the battery, the system could maintain a stable voltage profile for the charging-discharging processes after 60 initial cycles. Overall, the present system retains all the essential characteristics required to serve as a promising less expensive, robust, and environmentally benign alternative to the noble metal catalysts for its application as an air electrode in rechargeable metal-air batteries.

5.5. REFERENCES:

(1) Rosli, R. E.; Sulong, A. B.; Daud, W. R. W.; Zulkifley, M. A.; Husaini, T.; Rosli, M. I.; Majlan, E. H.; Haque, M. A., A Review of High-Temperature Proton Exchange Membrane Fuel Cell (HT-PEMFC) System. *Int. J. Hydrogen Energy* **2017,** *42*, 9293-9314.

(2) Shimizu, K.; Sepunaru, L.; Compton, R. G., Innovative Catalyst Design for the Oxygen Reduction Reaction for Fuel Cells. *Chem. Sci.* **2016,** *7*, 3364-3369.

(3) Palaniselvam, T.; Kashyap, V.; Bhange, S. N.; Baek, J.-B.; Kurungot, S., Nanoporous Graphene Enriched with Fe/Co-N Active Sites as a Promising Oxygen Reduction Electrocatalyst for Anion Exchange Membrane Fuel Cells. *Adv. Funct. Mater.* **2016,** *26*, 2150-2162.

(4) Wang, Y.; Zhou, H., A Lithium-Air Battery with a Potential to Continuously Reduce O_2 from Air for Delivering Energy. *J. Power Sources* **2010,** *195*, 358-361.

(5) Wang, Y.; Zhou, H., A Lithium-Air Fuel Cell Using Copper to Catalyze Oxygen-Reduction based on Copper-Corrosion Mechanism. *Chem. Commun.* **2010,** *46*, 6305-6307.

(6) Li, Y.; Wang, X.; Dong, S.; Chen, X.; Cui, G., Recent Advances in Non-Aqueous Electrolyte for Rechargeable Li–O_2 Batteries. *Adv. Energy Mater.* **2016,** *6*, 1600751.

(7) Chang, Y.; Dong, S.; Ju, Y.; Xiao, D.; Zhou, X.; Zhang, L.; Chen, X.; Shang, C.; Gu, L.; Peng, Z.; Cui, G., A Carbon- and Binder-Free Nanostructured Cathode for High-Performance Nonaqueous Li-O_2 Battery. *Adv. Sci.* **2015,** *2*,1500092.

(8) Grimaud, A.; Diaz-Morales, O.; Han, B.; Hong, W. T.; Lee, Y.-L.; Giordano, L.; Stoerzinger, K. A.; Koper, M. T. M.; Shao-Horn, Y., Activating Lattice Oxygen Redox Reactions in Metal Oxides to Catalyse Oxygen Evolution. *Nat Chem* **2017,** *9*, 457-465.

(9) Mohamed, R.; Cheng, X.; Fabbri, E.; Levecque, P.; Kötz, R.; Conrad, O.; Schmidt, T. J., Electrocatalysis of Perovskites: The Influence of Carbon on the Oxygen Evolution Activity. *J. Electrochem. Soc.* **2015,** *162*, F579-F586.

(10) Čolić, V.; Bandarenka, A. S., Pt Alloy Electrocatalysts for the Oxygen Reduction Reaction: From Model Surfaces to Nanostructured Systems. *ACS Catal.* **2016**, 5378-5385.

(11) Nie, Y.; Li, L.; Wei, Z., Recent Advancements in Pt and Pt-free Catalysts for Oxygen Reduction Reaction. *Chem. Soc. Rev.* **2015,** *44*, 2168-2201.

(12) Dhavale, V. M.; Kurungot, S., Cu–Pt Nanocage with 3-D Electrocatalytic Surface as an Efficient Oxygen Reduction Electrocatalyst for a Primary Zn–Air Battery. *ACS Catal.* **2015,** *5*, 1445-1452.

(13) Chung, D. Y.; Jun, S. W.; Yoon, G.; Kwon, S. G.; Shin, D. Y.; Seo, P.; Yoo, J. M.; Shin, H.; Chung, Y.-H.; Kim, H.; Mun, B. S.; Lee, K.-S.; Lee, N.-S.; Yoo, S. J.; Lim, D.-H.; Kang, K.; Sung, Y.-E.; Hyeon, T., Highly Durable and Active PtFe Nanocatalyst for Electrochemical Oxygen Reduction Reaction. *J. Am. Chem. Soc.* **2015**, 15478–15485.

(14) Kuo, D.-Y.; Kawasaki, J. K.; Nelson, J. N.; Kloppenburg, J.; Hautier, G.; Shen, K. M.; Schlom, D. G.; Suntivich, J., Influence of Surface Adsorption on the Oxygen Evolution Reaction on IrO_2(110). *J. Am. Chem. Soc.* **2017,** *139*, 3473-3479.

(15) Papaderakis, A.; Pliatsikas, N.; Prochaska, C.; Vourlias, G.; Patsalas, P.; Tsiplakides, D.; Balomenou, S.; Sotiropoulos, S., Oxygen Evolution at IrO_2 Shell–Ir–Ni Core Electrodes Prepared by Galvanic Replacement. *J. Phys. Chem. C* **2016,** *120*, 19995-20005.

(16) Stoerzinger, K. A.; Qiao, L.; Biegalski, M. D.; Shao-Horn, Y., Orientation-Dependent Oxygen Evolution Activities of Rutile IrO_2 and RuO_2. *J. Phys. Chem. Lett.***2014,** *5*, 1636-1641.

(17) Toh, R. J.; Eng, A. Y. S.; Sofer, Z.; Sedmidubsky, D.; Pumera, M., Ternary Transition Metal Oxide Nanoparticles with Spinel Structure for the Oxygen Reduction Reaction. *ChemElectroChem* **2015,** *2*, 982-987.

(18) Tritsaris, G. A.; Nørskov, J. K.; Rossmeisl, J., Trends in Oxygen Reduction and Methanol Activation on Transition Metal Chalcogenides. *Electrochim. Acta* **2011,** *56*, 9783-9788.

(19) Chisaka, M.; Ishihara, A.; Ota, K.-i.; Muramoto, H., Synthesis of Carbon-Supported Titanium Oxynitride Nanoparticles as Cathode Catalyst for Polymer Electrolyte Fuel Cells. *Electrochim. Acta* **2013,** *113*, 735-740.

(20) Huo, R.; Jiang, W.-J.; Xu, S.; Zhang, F.; Hu, J.-S., Co/CoO/$CoFe_2O_4$/G Nanocomposites Derived from Layered Double Hydroxides Towards Mass Production of Efficient Pt-free Electrocatalysts for Oxygen Reduction Reaction. *Nanoscale* **2014,** *6*, 203-206.

(21) Liang, Y.; Li, Y.; Wang, H.; Zhou, J.; Wang, J.; Regier, T.; Dai, H., Co_3O_4 Nanocrystals on Graphene as a Synergistic Catalyst for Oxygen Reduction Reaction. *Nat. Mater.* **2011,** *10*, 780-786.

(22) Liang, Y.; Wang, H.; Zhou, J.; Li, Y.; Wang, J.; Regier, T.; Dai, H., Covalent Hybrid of Spinel Manganese–Cobalt Oxide and Graphene as Advanced Oxygen Reduction Electrocatalysts. *J. Am. Chem. Soc.* **2012,** *134*, 3517-3523.

(23) Yin, W.; Shen, Y.; Zou, F.; Hu, X.; Chi, B.; Huang, Y., Metal–Organic Framework Derived ZnO/$ZnFe_2O_4$/C Nanocages as Stable Cathode Material for Reversible Lithium–Oxygen Batteries. *ACS Appl. Mater. Interfaces* **2015,** *7*, 4947-4954.

(24) Liu, Z.-Q.; Cheng, H.; Li, N.; Ma, T. Y.; Su, Y.-Z., $ZnCo_2O_4$ Quantum Dots Anchored on Nitrogen-Doped Carbon Nanotubes as Reversible Oxygen Reduction/Evolution Electrocatalysts. *Adv. Mater.* **2016,** *28*, 3777-3784.

(25) Ning, R.; Tian, J.; Asiri, A. M.; Qusti, A. H.; Al-Youbi, A. O.; Sun, X., Spinel $CuCo_2O_4$ Nanoparticles Supported on N-Doped Reduced Graphene Oxide: A Highly Active and Stable Hybrid Electrocatalyst for the Oxygen Reduction Reaction. *Langmuir* **2013,** *29*, 13146-13151.

(26) Tang, C.; Wang, H.-S.; Wang, H.-F.; Zhang, Q.; Tian, G.-L.; Nie, J.-Q.; Wei, F., Spatially Confined Hybridization of Nanometer-Sized NiFe Hydroxides into Nitrogen-Doped Graphene Frameworks Leading to Superior Oxygen Evolution Reactivity. *Adv. Mater.* **2015,** *27*, 4516-4522.

(27) Prabu, M.; Ketpang, K.; Shanmugam, S., Hierarchical Nanostructured $NiCo_2O_4$ as an Efficient Bifunctional Non-precious Metal Catalyst for Rechargeable Zinc-Air Batteries. *Nanoscale* **2014,** *6*, 3173-3181.

(28) Ling, T.; Yan, D.-Y.; Jiao, Y.; Wang, H.; Zheng, Y.; Zheng, X.; Mao, J.; Du, X.-W.; Hu, Z.; Jaroniec, M.; Qiao, S.-Z., Engineering Surface Atomic Structure of Single-Crystal Cobalt (II) Oxide Nanorods for Superior Electrocatalysis.*Nat. Commun.***2016,** *7*, 12876.

(29) Chen, S.; Qiao, S.-Z., Hierarchically Porous Nitrogen-Doped Graphene–$NiCo_2O_4$ Hybrid Paper as an Advanced Electrocatalytic Water-Splitting Material. *ACS Nano* **2013,** *7*, 10190-10196.

(30) Liu, X.; Chang, Z.; Luo, L.; Xu, T.; Lei, X.; Liu, J.; Sun, X., Hierarchical $Zn_xCo_{3-x}O_4$ Nanoarrays with High Activity for Electrocatalytic Oxygen Evolution. *Chem. Mater.* **2014,** *26*, 1889-1895.

(31) Lin, C.-C.; McCrory, C. C. L., Effect of Chromium Doping on Electrochemical Water Oxidation Activity by $Co_{3-x}Cr_xO_4$ Spinel Catalysts. *ACS Catal.* **2016**, 443-451.

(32) Jiao, Y.; Zheng, Y.; Jaroniec, M.; Qiao, S. Z., Origin of the Electrocatalytic Oxygen Reduction Activity of Graphene-Based Catalysts: A Roadmap to Achieve the Best Performance. *J. Am. Chem. Soc.* **2014,** *136*, 4394-4403.

(33) Li, Y.; Gong, M.; Liang, Y.; Feng, J.; Kim, J.-E.; Wang, H.; Hong, G.; Zhang, B.; Dai, H., Advanced Zinc-Air Batteries Based on High-Performance Hybrid Electrocatalysts. *Nat. Commun.* **2013,** *4*, 1805.

(34) Prabu, M.; Ramakrishnan, P.; Nara, H.; Momma, T.; Osaka, T.; Shanmugam, S., Zinc–Air Battery: Understanding the Structure and Morphology Changes of Graphene-Supported $CoMn_2O_4$ Bifunctional Catalysts Under Practical Rechargeable Conditions. *ACS Appl. Mater. Interfaces* **2014,** *6*, 16545-16555.

(35) Wang, M.; Qian, T.; Zhou, J.; Yan, C., An Efficient Bifunctional Electrocatalyst for a Zinc–Air Battery Derived from Fe/N/C and Bimetallic Metal–Organic Framework Composites. *ACS Appl. Mater. Interfaces* **2017,** *9*, 5213-5221.

(36) Lee, J.-S.; Tai Kim, S.; Cao, R.; Choi, N.-S.; Liu, M.; Lee, K. T.; Cho, J., Metal–Air Batteries with High Energy Density: Li–Air versus Zn–Air. *Adv. Energy Mater.* **2011,** *1*, 34-50.

(37) Li, Y.; Dai, H., Recent Advances in Zinc-Air Batteries. *Chem. Soc. Rev.* **2014,** *43*, 5257-5275.

(38) Jang, S.-E.; Kim, H., Effect of Water Electrolysis Catalysts on Carbon Corrosion in Polymer Electrolyte Membrane Fuel Cells. *J. Am. Chem. Soc.* **2010,** *132*, 14700-14701.

(39) Monaji, V. R.; Das, D., Influence of Zr Doping on the Structural, Magnetic and Magnetoelastic Properties of Cobalt-Ferrites. *J. Alloy. Comp.***2015,** *634*, 99-103.

(40) Khan, K.; Rehman, S., Microwave Absorbance Properties of Zirconium–Manganese Substituted Cobalt Nanoferrite as Electromagnetic (EM) Wave Absorbers. *Materials Research Bulletin* **2014,** *50*, 454-461.

(41) Doi, S.; Ishihara, A.; Mitsushima, S.; Kamiya, N.; Ota, K.-i., Zirconium-Based Compounds for Cathode of Polymer Electrolyte Fuel Cell. *J. Electrochem. Soc.* **2007,** *154*, B362-B369.

(42) Seo, J.; Takata, T.; Nakabayashi, M.; Hisatomi, T.; Shibata, N.; Minegishi, T.; Domen, K., Mg–Zr Cosubstituted Ta_3N_5 Photoanode for Lower-Onset-Potential Solar-Driven Photoelectrochemical Water Splitting. *J. Am. Chem. Soc.* **2015,** *137*, 12780-12783.

(43) Wang, L.; Xia, L.; Wu, Y.; Tian, Y., Zr-Doped β-In_2S_3 Ultrathin Nanoflakes as Photoanodes: Enhanced Visible-Light-Driven Photoelectrochemical Water Splitting. *ACS Sustainable Chemistry & Engineering* **2016,** *4*, 2606-2614.

(44) Nam, G.; Park, J.; Choi, M.; Oh, P.; Park, S.; Kim, M. G.; Park, N.; Cho, J.; Lee, J.-S., Carbon-Coated Core–Shell Fe–Cu Nanoparticles as Highly Active and Durable Electrocatalysts for a Zn–Air Battery. *ACS Nano* **2015,** *9*, 6493-6501.

(45) Yin, J.; Li, Y.; Lv, F.; Fan, Q.; Zhao, Y.-Q.; Zhang, Q.; Wang, W.; Cheng, F.; Xi, P.; Guo, S., NiO/CoN Porous Nanowires as Efficient Bifunctional Catalysts for Zn–Air Batteries. *ACS Nano* **2017,** *11*, 2275-2283.

(46) Marcano, D. C.; Kosynkin, D. V.; Berlin, J. M.; Sinitskii, A.; Sun, Z.; Slesarev, A.; Alemany, L. B.; Lu, W.; Tour, J. M., Improved Synthesis of Graphene Oxide. *ACS Nano* **2010,** *4*, 4806-4814.

(47) Bian, W.; Yang, Z.; Strasser, P.; Yang, R., A $CoFe_2O_4$/Graphene Nanohybrid as an Efficient Bi-functional Electrocatalyst for Oxygen Reduction and Oxygen Evolution. *J. Power Sources* **2014,** *250*, 196-203.

(48) Tong, Y.; Chen, P.; Zhou, T.; Xu, K.; Chu, W.; Wu, C.; Xie, Y., A Bifunctional Hybrid Electrocatalyst for Oxygen Reduction and Evolution: Cobalt Oxide Nanoparticles Strongly Coupled to B,N-Decorated Graphene. *Angew. Chem.* **2017,** *129*, 7227-7231.

(49) Seo, B.; Sa, Y. J.; Woo, J.; Kwon, K.; Park, J.; Shin, T. J.; Jeong, H. Y.; Joo, S. H., Size-Dependent Activity Trends Combined with in Situ X-ray Absorption Spectroscopy Reveal Insights into Cobalt Oxide/Carbon Nanotube-Catalyzed Bifunctional Oxygen Electrocatalysis. *ACS Catal.* **2016**, 4347-4355.

(50) Kashyap, V.; Singh, S. K.; Kurungot, S., Cobalt Ferrite Bearing Nitrogen-Doped Reduced Graphene Oxide Layers Spatially Separated with Microporous Carbon as Efficient Oxygen Reduction Electrocatalyst. *ACS Appl. Mater. Interfaces* **2016,** *8*, 20730-20740.

(51) Singh, S. K.; Dhavale, V. M.; Kurungot, S., Surface-Tuned Co_3O_4 Nanoparticles Dispersed on Nitrogen-Doped Graphene as an Efficient Cathode Electrocatalyst for Mechanical Rechargeable Zinc–Air Battery Application. *ACS Appl. Mater. Interfaces* **2015,** *7*, 21138-21149.

(52) López-Ortega, A.; Lottini, E.; Fernández, C. d. J.; Sangregorio, C., Exploring the Magnetic Properties of Cobalt-Ferrite Nanoparticles for the Development of a Rare-Earth-Free Permanent Magnet. *Chem. Mater.* **2015,** *27*, 4048-4056.

(53) Tang, Z. R.; Kondrat, S. A.; Dickinson, C.; Bartley, J. K.; Carley, A. F.; Taylor, S. H.; Davies, T. E.; Allix, M.; Rosseinsky, M. J.; Claridge, J. B.; Xu, Z.; Romani, S.; Crudace, M. J.; Hutchings, G. J., Synthesis of High Surface Area $CuMn_2O_4$ by Supercritical Anti-Solvent Precipitation for the Oxidation of CO at Ambient Temperature. *Catal. Sci. Technol* **2011,** *1*, 740-746.

(54) Ghule, A. V.; Ghule, K.; Chen, C.-Y.; Chen, W.-Y.; Tzing, S.-H.; Chang, H.; Ling, Y.-C., In situ Thermo-TOF-SIMS Study of Thermal Decomposition of Zinc Acetate Dihydrate. *J. Mass Spectrum.***2004,** *39*, 1202-1208.

(55) Guo, J.; Zhan, G.; Liu, J.; Yang, B.; Xu, B.; Feng, J.; Chen, X.; Yang, C., Hopping Conduction in Zirconium Oxynitrides Thin Film Deposited by Reactive Magnetron Sputtering. *Physica B: Condensed Matter* **2015,** *475*, 86-89.

(56) Wan, X.; Houwman, E. P.; Steenwelle, R.; Schaijk, R. v.; Nguyen, M. D.; Dekkers, M.; Rijnders, G., Enhanced Piezoelectric Properties of (110)-Oriented $PbZr_{1-x}Ti_xO_3$ Epitaxial Thin Films on Silicon Substrates at Shifted Morphotropic Phase Boundary. *Appl. Phys. Lett.* **2014,** *104*, 092902.

(57) Kumar, R.; Kar, M., Lattice Strain Induced Magnetism in Substituted Nanocrystalline Cobalt Ferrite. *J. Magn. Magn. Mater.* **2016,** *416*, 335-341.

(58) Wang, X.; Zheng, Y.; Xu, Z.; Wang, X.; Chen, X., Amorphous MnO_2 Supported on Carbon Nanotubes as a Superior Catalyst for Low Temperature NO Reduction with NH_3. *RSC Adv.* **2013,** *3*, 11539-11542.

(59) Yu, J.; Ran, J., Facile Preparation and Enhanced Photocatalytic H_2-Production Activity of $Cu(OH)_2$ Cluster Modified TiO_2. *Energy Environ. Sci.* **2011,** *4*, 1364-1371.

(60) Buitendach, B.; Erasmus, E.; Niemantsverdriet, J.; Swarts, J., Properties of Manganese(III) Ferrocenyl-β-Diketonato Complexes Revealed by Charge Transfer and Multiplet Splitting in the Mn 2p and Fe 2p X-Ray Photoelectron Envelopes. *Molecules* **2016,** *21*, 1427.

(61) Liu, C.; Zhang, Y.; Jia, J.; Sui, Q.; Ma, N.; Du, P., Multi-Susceptibile Single-Phased Ceramics with Both Considerable Magnetic and Dielectric Properties by Selectively Doping. *Sci. Rep.* **2015,** *5*, 9498.

(62) Tang, R.; Jiang, C.; Qian, W.; Jian, J.; Zhang, X.; Wang, H.; Yang, H., Dielectric Relaxation, Resonance and Scaling Behaviors in $Sr_3Co_2Fe_{24}O_{41}$ Hexaferrite. *Sci. Rep.* **2015,** *5*, 13645.

(63) Zhang, Z.; Li, W.; Zou, R.; Kang, W.; San Chui, Y.; Yuen, M. F.; Lee, C.-S.; Zhang, W., Layer-Stacked Cobalt Ferrite ($CoFe_2O_4$) Mesoporous Platelets for High-Performance Lithium ion Battery Anodes. *J. Mater. Chem. A* **2015,** *3*, 6990-6997.

(64) Basahel, S.; Mokhtar, M.; Alsharaeh, E.; Ali, T.; Mahmoud, H.; Narasimharao, K., Physico-Chemical and Catalytic Properties of Mesoporous CuO-ZrO_2 Catalysts. *Catalysts* **2016,** *6*, 57.

(65) Lim, D.-H.; Wilcox, J., Mechanisms of the Oxygen Reduction Reaction on Defective Graphene-Supported Pt Nanoparticles from First-Principles. *J. Phys. Chem. C* **2012,** *116*, 3653-3660.

(66) Tse, E. C. M.; Barile, C. J.; Kirchschlager, N. A.; Li, Y.; Gewargis, J. P.; Zimmerman, S. C.; Hosseini, A.; Gewirth, A. A., Proton Transfer Dynamics Control the Mechanism of O_2 Reduction by a Non-precious Metal Electrocatalyst. *Nat. Mater.* **2016,** *15*, 754-759.

(67) Siahrostami, S.; Verdaguer-Casadevall, A.; Karamad, M.; Deiana, D.; Malacrida, P.; Wickman, B.; Escudero-Escribano, M.; Paoli, E. A.; Frydendal, R.; Hansen, T. W.; Chorkendorff, I.; Stephens, I. E. L.; Rossmeisl, J., Enabling Direct H_2O_2 Production Through Rational Electrocatalyst Design. *Nat. Mater.* **2013,** *12*, 1137-1143.

(68) Irvine, J. T. S.; Sinclair, D. C.; West, A. R., Electroceramics: Characterization by Impedance Spectroscopy. *Adv. Mater.* **1990,** *2*, 132-138.

(69) Huggins, R. A., Simple Method to Determine Electronic and Ionic Components of the Conductivity in Mixed Conductors a Review. *Ionics* **2002,** *8*, 300-313.

(70) Balan, B. K.; Kurungot, S., Highly Exposed and Activity Modulated Sandwich Type Pt Thin Layer Catalyst with Enhanced Utilization. *J. Mater. Chem.* **2011,** *21*, 19039-19048.

(71) Prabu, M.; Ramakrishnan, P.; Shanmugam, S., $CoMn_2O_4$ Nanoparticles Anchored on Nitrogen-Doped Graphene Nanosheets as Bifunctional Electrocatalyst for Rechargeable Zinc–Air Battery. *Electrochem. Commun.* **2014,** *41*, 59-63.

(72) Sun, Y.; Li, C.; Shi, G., Nanoporous Nitrogen Doped Carbon Modified Graphene as Electrocatalyst for Oxygen Reduction Reaction. *J. Mater. Chem.* **2012,** *22*, 12810-12816.

(73) Liang, H.-W.; Zhuang, X.; Brüller, S.; Feng, X.; Müllen, K., Hierarchically Porous Carbons with Optimized Nitrogen Doping as Highly Active Electrocatalysts for Oxygen Reduction. *Nat. Commun.* **2014,** *5*.

(74) Li, B.; Ge, X.; Goh, F. W. T.; Hor, T. S. A.; Geng, D.; Du, G.; Liu, Z.; Zhang, J.; Liu, X.; Zong, Y., Co_3O_4 Nanoparticles Decorated Carbon Nanofiber Mat as Binder-Free Air-Cathode for High Performance Rechargeable Zinc-Air Batteries. *Nanoscale* **2015,** *7*, 1830-1838.

(75) Castanheira, L.; Silva, W. O.; Lima, F. H. B.; Crisci, A.; Dubau, L.; Maillard, F., Carbon Corrosion in Proton-Exchange Membrane Fuel Cells: Effect of the Carbon Structure, the Degradation Protocol, and the Gas Atmosphere. *ACS Catal.* **2015,** *5*, 2184-2194.

(76) Engl, T.; Gubler, L.; Schmidt, T. J., Fuel Electrode Carbon Corrosion in High Temperature Polymer Electrolyte Fuel Cells—Crucial or Irrelevant? *Energy Technology* **2016,** *4*, 65-74.

(77) Chen, J.; Hu, J.; Waldecker, J. R., A Comprehensive Model for Carbon Corrosion During Fuel Cell Start-Up. *J. Electrochem. Soc.* **2015,** *162*, F878-F889.

Chapter 6

Electrochemical Activity of Fe/CoN$_x$ Grafted Carbon in Acidic and Basic Media*

Iron and cobalt metal atoms are effective active centers for the synthesis of carbon-based noble metal-free catalysts for oxygen reduction reaction (ORR) owing to their cost-effective intrinsic activity and tunable properties. The annealing of the active center with the conducting carbon enhances the ORR activity significantly. Herein, we have engrafted Fe and Co active centers in the homemade conducting carbon and the ORR performance has been closely observed under acidic and basic pH conditions to understand the influence of the medium and participating moieties towards the performance. In the half-cell reaction, the onset potential and half-wave potential for ORR is governed by the surface intermediates and concomitantly driven by the adsorption energies of the intermediates over the active centers. The iron and cobalt active center-engrafted carbon catalyst behaves differently in acidic and basic electrolytes owing to the dissociation of the surface intermediates. The iron-based catalyst shows improved onset potential as against the cobalt-based one. Similarly, the cobalt-based catalyst shows improved half-wave potential against the iron active-center-grafted catalyst. The combined synergistic effect of the two catalysts is realized in the composition represented as Fe/2Co-N-GVC where improved onset and half-wave potentials are noted in basic medium. A significant variation in the activity of the catalyst is observed as the medium changes from acidic to basic and the effect is directly

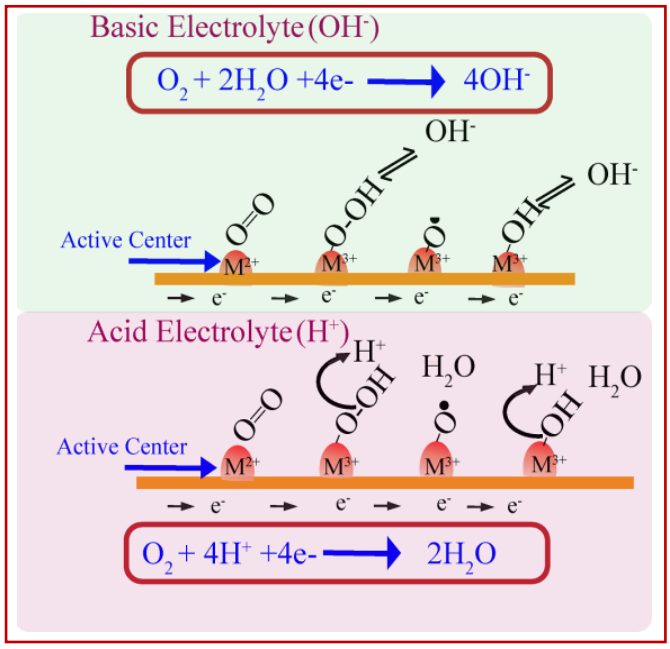

*The present work is communicated.

associated with the surface adsorption of intermediates. The Fe- and Co-based catalysts were used as the cathode materials in the zinc-air battery and for the low current density polarization and discharge, the obtained battery features were in according to the half-cell reaction characteristic of the catalyst, establishing that the inherent property of the catalysts continued to be retained in the device level as well.

6.1. Introduction

Investigation of the mechanism of the oxygen reduction reaction (ORR) on noble and non-noble metal surfaces is key to the design of highly active, inexpensive, environmentally benign and stable electrocatalysts.[1-2] In addition to their contribution to fundamental research, such studies are also important for developing technologies like fuel cells and metal-air batteries. In the past decades, Pt-based catalysts have fascinated researchers by their high performance in both acidic and basic media.[3-4] Despite their remarkable performance, these catalysts had limited technological implications as their high cost and poor stability posed considerable difficulty.[5-6] Later on, a substantial study on the active centre and the reaction mechanism over metal-electrolyte interface has led to significant improvements in the stability and performance of the catalysts. Also, several alloys of Pt with non-noble metals like Co, Ni, and Fe, with reduced Pt loading have been demonstrated to show enhanced activity.[4, 7] However, as in the case of the Pt catalysts, the high cost and poor stability of these alloy catalysts impose serious bottleneck towards their technological advancement and widespread applications in fuel cells and metal-air batteries.[8-9] As an alternative to the Pt-based catalysts, noble metal-free catalysts, such as M-N_x-C (where M= Fe, Co, etc.), graphene-supported metal oxides, chalcogenides and nitrides, have significant commercial and technological potential. Among these, Fe-N_x-C and Co-N_x-C show remarkable ORR activity in acidic and basic media which further varies with the synthesis methodology and carbon support.[10-11] Zelenay *et al*. reported a high performance electrocatalyst derived from polyaniline, iron and cobalt. The catalyst showed remarkable stability for 700 h at 0.40 V in a hydrogen fuel cell against the state-of-the-art Pt/C catalyst.[12] Similarly, several other groups have reported Fe-N_x-C as a noble metal-free electrocatalyst with high activity and durability.[13-14]

As the M-N_x-C catalysts have emerged as potential substitutes for the noble metal catalysts, it is desirable to explore the surface reactions over the active catalyst for

developing sustainable and durable devices. A noteworthy contribution to the understanding of ORR over the non-noble metal catalyst came from Mukarjee *et al*; they identified that the inner-sphere electron transfer mechanism dominated the outer-sphere electron transfer mechanism in the Fe-N_x-C catalyst.[15] Further, the variation in activity with annealing temperature of the precursor metal complexes and conducting carbon is caused by the modulation in the energy of the d_z^2 orbital of the metal atom.[16] Moreover, the activity of the catalyst relies on the number and type of the active centre, which further becomes ambiguous in the macro system.[14] The M-N_x-C catalyst is generally synthesized by high temperature annealing of the metal complex with conducting carbon, destroying the integrity of the metal complex to some extent.[13] Additionally, during the cell operation, the reaction mechanism (4e or 2e) also affects the stability of the catalyst.[17] The previously reported mechanism suggests that the 2e transfer pathway over the active centre leads to a high level of peroxide formation, resulting in catalyst degradation.[5] It must be noted that a low level of peroxide formation during device operation is desirable for device durability. In general, the oxygen reduction reaction potential is measured against the standard hydrogen electrode (SHE). The standard reduction potential and equations for the reduction of molecular oxygen in acidic and basic media is given below[18-21]:

a) In basic media:

For the direct four-electron pathway

$O_2 + 2H_2O + 4e^- \leftrightarrow 4OH^-$ E^o = 0.401 V *vs* SHE (1)

For the alternative two-electron pathway

$O_2 + 2H_2O + 2e^- \leftrightarrow HO_2^- + OH^-$ E^o = -0.076 V *vs* SHE (2)

$HO_2^- + H_2O + 2e^- \leftrightarrow 3OH^-$ E^o = 0.878 V *vs* SHE (3)

Disproportionation reaction $2HO_2^- \leftrightarrow 2OH^- + O_2$

b) In acidic media:

For the direct four-electron pathway

$O_2 + 4H^+ + 4e^- \leftrightarrow 2H_2O$ E^o= 1.229 V *vs* SHE (4)

For the alternative two-electron pathway

$O_2 + 2H^+ + 2e^- \leftrightarrow H_2O_2$ E^o = 0.695 V *vs* SHE (5)

$H_2O_2 + 2H^+ + 2e^- \leftrightarrow 2H_2O$ E^o = 1.776 V *vs* SHE (6)

Disproportionation reaction $2H_2O_2 \leftrightarrow 2H_2O + O_2$

In the light of the above studies, it is clear that, for improving the ORR activity, a deep insight into the concepts of the active centre and transition state of the non-noble metal electrocatalyst is required. Herein, we propose a different approach for enhancing the activity of the Fe-N_x-C and Co-N_x-C catalysts that involves the activity modulation in acid and basic media by varying the metal composition in the M-N_x-C system. We found that the stabilization of the transition state in the acidic and basic media governs the faradaic current density in the single electrode study as well as in the fabricated device. Generally, the highest barrier for ORR is the conversion of molecular oxygen to the –OOH species; here, it is observed that the post-transition species formation differs in acidic and basic media over the Fe and Co metals and, hence, both show significant difference in activity. From our experimental observation and previous reports, we have suggested possible route for the ORR to occur over active sites in acid and basic media.

6.2. Experimental

6.2.1. Nitrogen-doped graphene Vulcan carbon composite (N-GVC): For the synthesis of N-GVC, GO and Vulcan carbon in the ratio of 2:3 (200 mg GO, 300 mg Vulcan carbon) were taken. First, the GO and Vulcan carbon were ground in a mortar and pestle with 5 mL of DI water. This solution was then sonicated for 2 h. Afterwards, a mixture of DI water and ethanol (1:1) was added to the solution. Subsequently, 10 ml NH_4OH solution was added and then kept aside for the hydrothermal reaction at 150 °C for 6 h. The obtained solution was then centrifuged, filtered and dried under an IR lamp. A similar procedure was adopted for preparing the compositions with various ratios of GO and Vulcan carbon (VC) (*i.e.*, 1:1, 1:2 and 1:4).

6.2.2. Synthesis of Fe/2Co-N-GVC, Fe/N-GVC and Co/N-GVC: For the synthesis of Fe/2Co-N-GVC, a metal precursor was prepared using iron acetate, cobalt acetate (in the

molar ratio of Fe:Co = 1:2) and 1,10-phenanthroline-5-amine (metal:phen = 1:1), which were mixed in 25 mL iso-propyl alcohol and sonicated to obtain a homogeneous solution. Then, 50 mg of N-GVC was ground in a mortar and mixed with the metal precursor. This solution was sonicated for 1 h, subsequently dried and powdered. Further, the powder was annealed in a furnace at 900 °C for 3 h. As such obtained powder was labelled as Fe/2Co-N-GVC. Similar procedure was adopted for the synthesis of the Fe/N-GVC and Co/N-GVC.

6.3. Result and Discussion

The typical synthesis process followed for the preparation of the catalysts and their utilization in a Zn-air battery is presented in **Figure 6.1**. The possible mechanisms involved for the molecular oxygen reduction in the acidic and basic media are proposed and presented in the scheme. Here, the homemade catalysts show different ORR pathways in acid and basic environments with significant change in the reaction products, which is discussed in the later part of the thesis. For this study, we prepared three catalysts, *viz.*, Co-N-GVC, Fe-N-GVC, and Fe/2Co-NGVC, by the annealing of the corresponding metal precursors with the homemade carbon material.

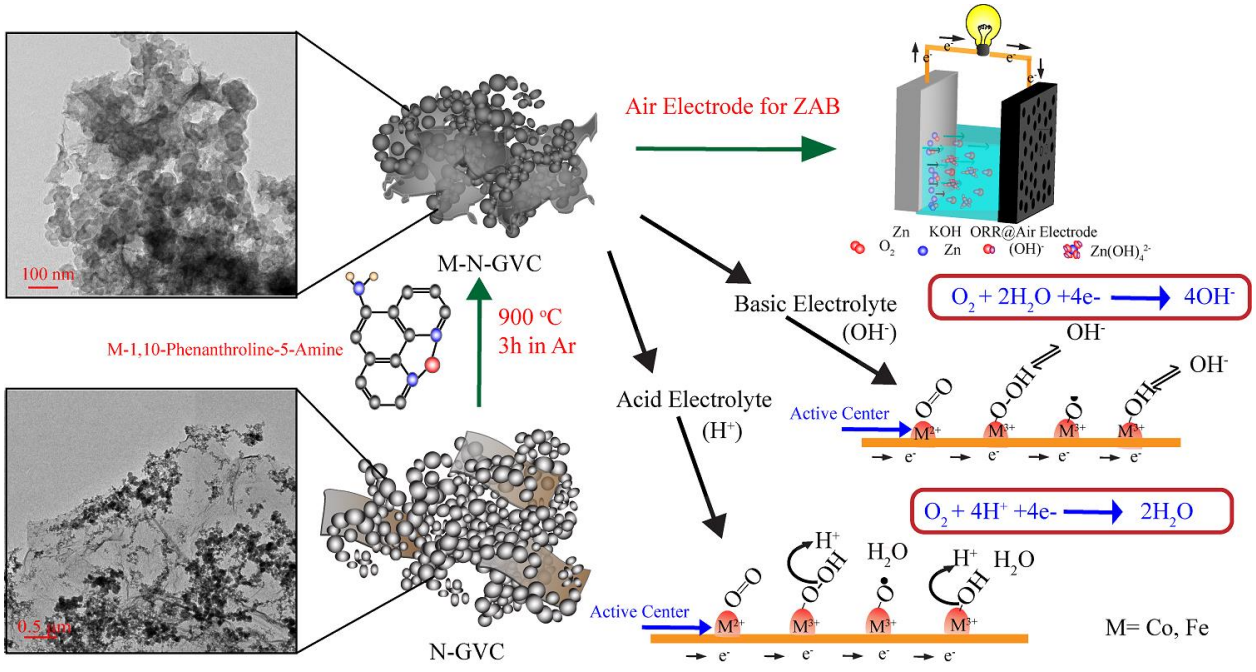

Figure 6.1. *Schematic illustration of the steps involved in the synthesis of the active catalyst, surface reactions in the acidic and basic media, and demonstration of the system as an air*

electrode for the Zn-air battery. A magnified TEM image of the precursor and product is presented in the square box.

6.3.1. TEM & SEM Analysis:

The morphological and structural features of the prepared catalysts have been analysed through transmission electron microscopy (TEM), field emission scanning electron microscopy (FE-SEM), elemental mapping **Figure 6.2a**, **6.2b** and **6.2c** represent the FE-SEM images of VC, N-GVC, and Fe/2Co-N-GVC, respectively.

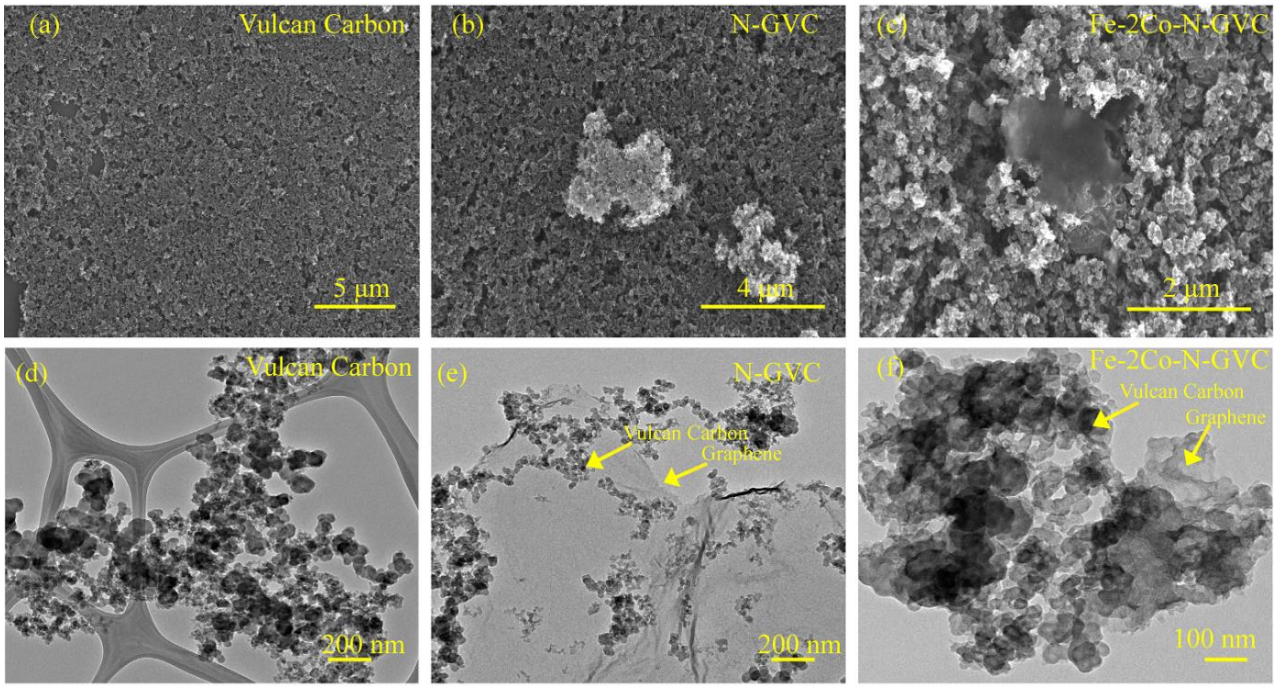

Figure 6.2. *(a), (b) and (c) show the FE-SEM images of VC, N-GVC and Fe/2Co-N-GVC, respectively. The corresponding TEM images of the three samples are shown in (d), (e) and (f).*

As evident from **Figure 6.2a**, VC has a spherical morphology with a narrow size distribution. The spherical structure is advantageous for the catalytic activity as it hinders the fusion of the catalytic sites.[22] In addition to the favourable geometry of VC, the interconnection of the carbon spheres with the two-dimensional graphene considerably enhances the faradaic process.[22-23] The composite of graphene and VC with the ratio of 2:3 as the catalyst support has notable electrocatalytic activity, discussed in a later section dealing with the electrochemical characterization. To further improve the catalytic performance of the carbon composite, active centre-containing metal ions were engrafted

in the composite. In N-GVC, the VC particles are distributed on the upper and lower surfaces of the graphene sheets which, on annealing with the metal precursor, fuse with the sheets and form an interconnected network.

The morphologies of VC, N-GVC and Fe/2Co-N-GVC were also examined through the TEM imaging. The VC shows mono-dispersed carbon spheres with sizes ranging from 50-60 nm (**Figure 6.2d**).[24] When VC forms a composite with graphene, it gets distributed on the upper as well as lower surfaces, which is conspicuous in **Figure 6.2e**. The above composite, when annealed with the metal precursors at 900 °C, gets fused into one entity. The TEM image given in **Figure 6.2f** clearly shows the fusion of VC and graphene. At high temperature, carbon-carbon bond breakage and restructuring take place, which is responsible for the formation of the fused carbon structure.[25] Additionally, different compositions of M-N-GVC (M = Fe and Co) catalysts were synthesized and analysed using SEM and elemental mapping (**Figure 6.3, 6.4** and **6.5**). After annealing the metal precursor with N-GVC, the metal gets uniformly and homogenously distributed over the entire surface as is evident from the SEM and elemental maps given in **Figure 6.3** and **6.4**, respectively. Such a homogeneous distribution of the active sites is highly desirable for high activity.

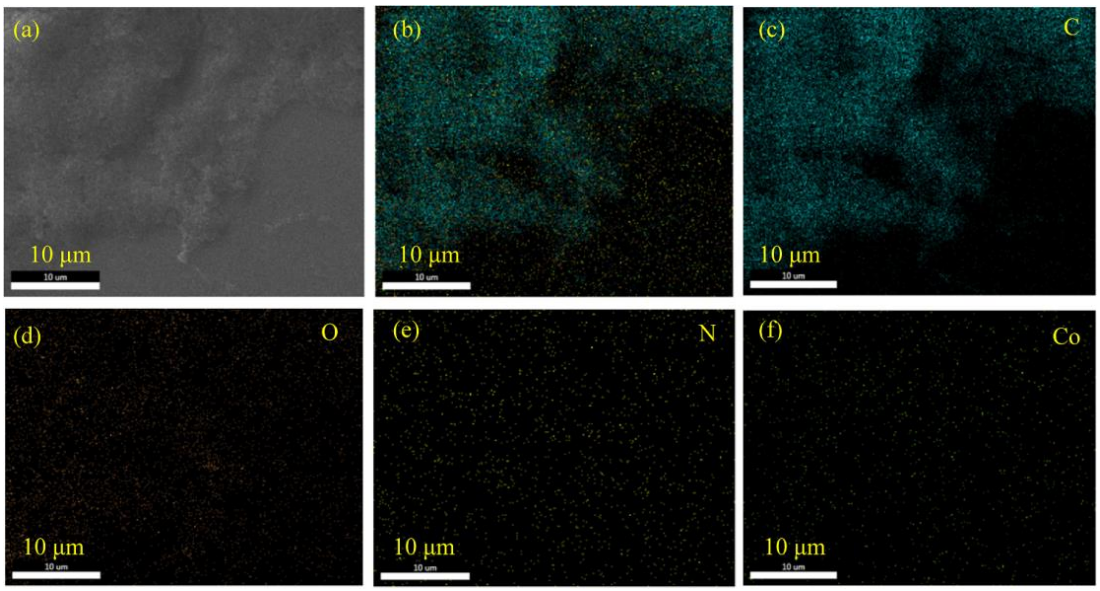

Figure 6.3. *(a) SEM image of the Co-N-GVC catalyst (scale bar 10µm); (b) overlay of the elements present in Co-N-GVC;(c), (d), (e) and (f) are the elemental mapping images for carbon, oxygen, nitrogen and cobalt, respectively.*

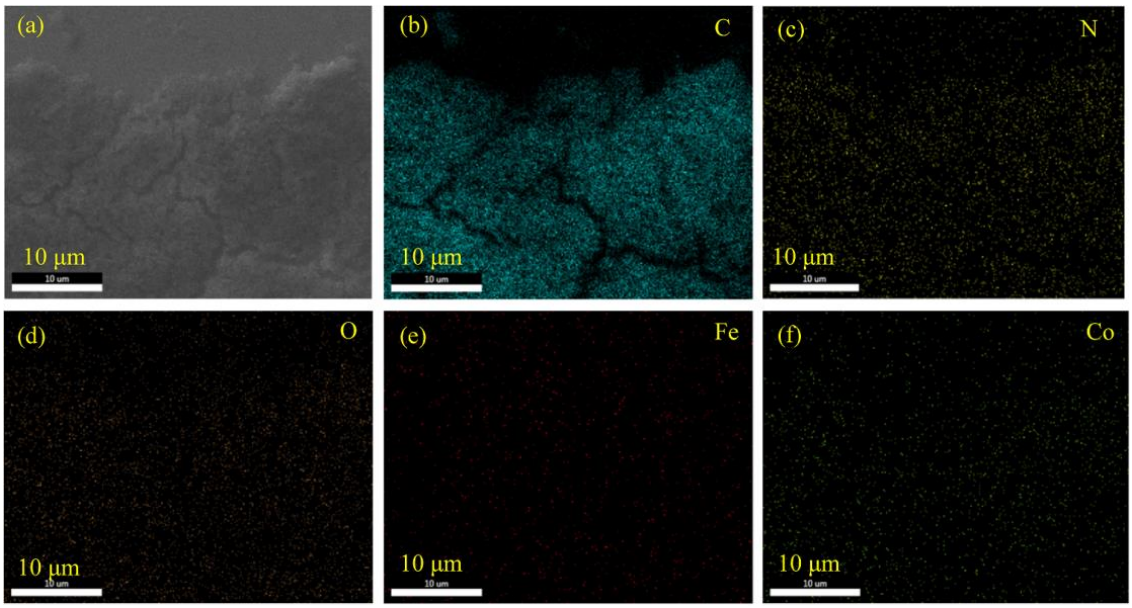

Figure 6.4. *(a) SEM image of the Fe/2Co-N-GVC catalyst (scale bar 10µm);(b), (c), (d), (e) and (f) are the elemental mapping images for carbon, nitrogen, oxygen, iron and cobalt, respectively.*

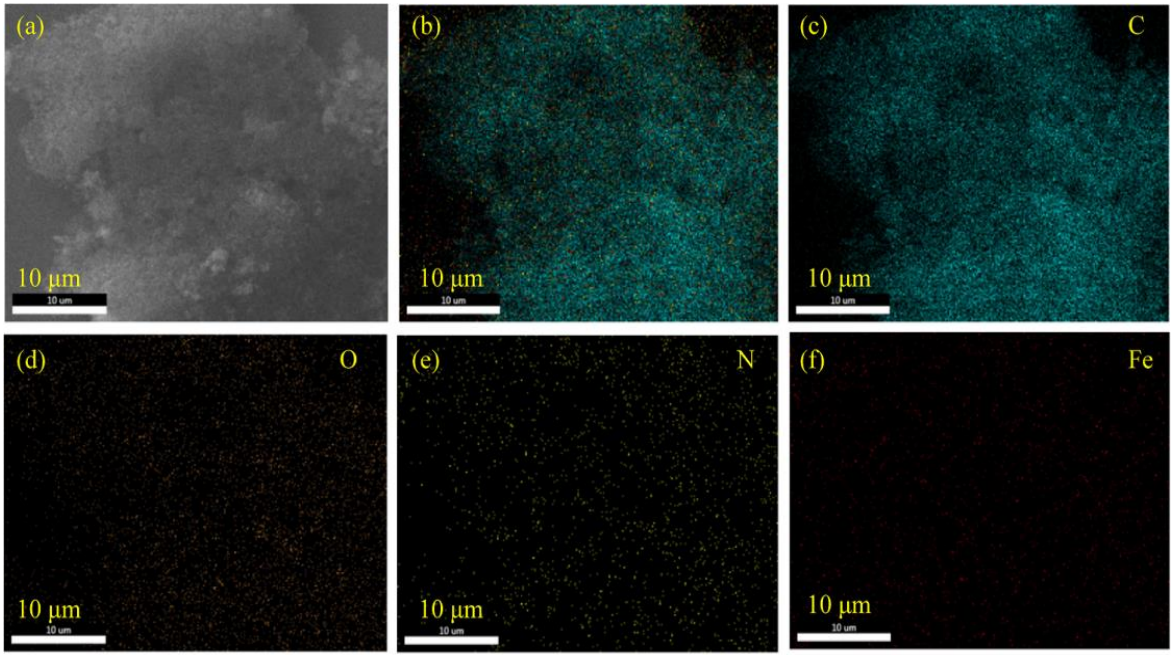

Figure 6.5. *(a) SEM image of the Fe-N-GVC catalyst (scale bar 10 µm); (b) overlay of the elements present in Fe-N-GVC;(c), (d), (e) and (f) are the elemental mapping images for carbon, oxygen, nitrogen, and iron, respectively.*

6.3.2. XRD Analysis:

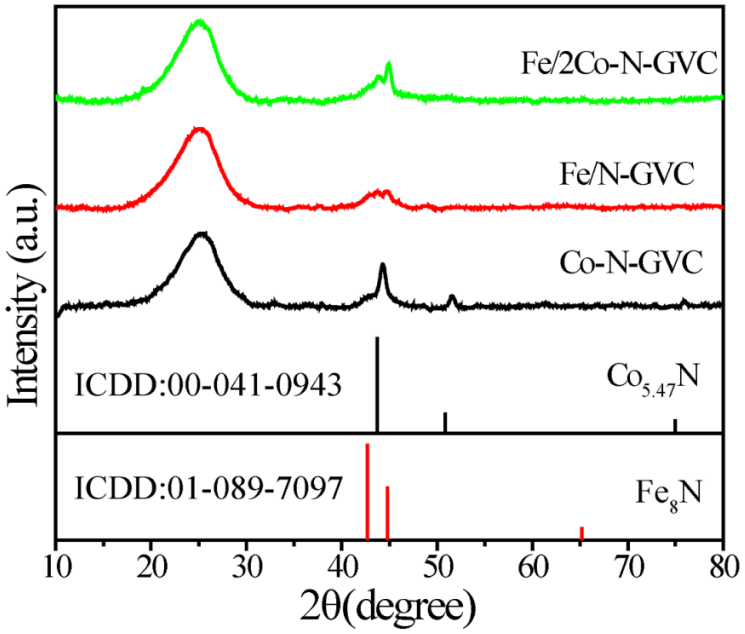

Figure 6.6. *PXRD patterns of Fe/2Co-N-GVC, Fe/N-GVC and Co/N-GVC, recorded at a scan rate of 0.2° min^{-1} with Cu Kα (λ = 1.54 Å) X-Ray source.*

The structural composition of the catalysts is compared using the PXRD analysis presented in **Figure 6.6**. An intense peak centred at a 2θ value of 25° appeared, which was attributed to the graphitic carbon present in the system.[26] The high intensity of this peak also indicates the graphitic carbon as the major phase of the system. In the case of Co-N-GVC, two less intense peaks at the 2θ values of 44.4 and 51.6° corresponding to the CoN_x phase (ICDD reference code: 00-041-0943). A fraction of CoC_x phase may also form because of the decomposition of cobalt complex, however it is not detected in the present case.[27] Similarly, in Fe-N-GVC, broad peaks at 43.8 and 44.8° that represent the FeN_x phase (ICDD reference code: 01-089-7097) are observed. The FeC_x phase which may form in the system during annealing was not detected.[28-29] In the XRD pattern of Fe/2Co-N-GVC, two peaks lying closely at the 2θ values of 43.8 and 44.8° are observed; these peaks are assigned to the FeN_x and CoN_x phases which are expected since the composite contains both Fe and Co as the metal precursors during its synthesis.[30-32] Here, it should be noted that the carbide phase is formed in the system along with the grafting of the active centre. [33] Here, the carbon framework plays a crucial role in the modulation of the

catalytic activity. The defects in the carbon network and the micro-level morphology assist in the mass diffusion of products during the process.[34]

6.3.3. Raman Analysis:

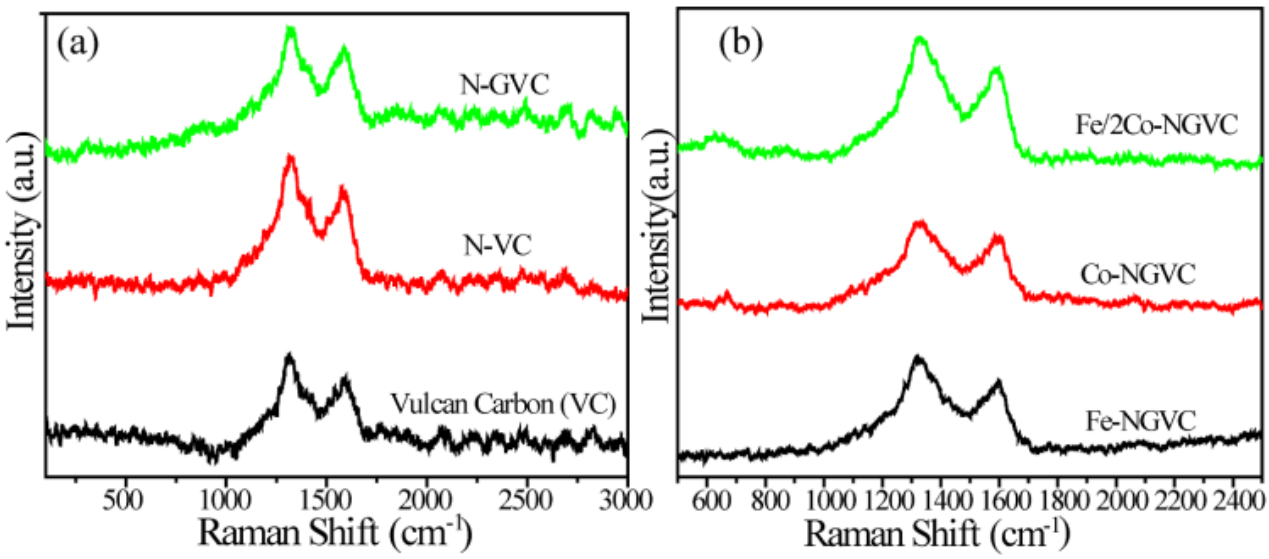

Figure 6.7. *(a) Raman spectra of Vulcan Carbon (VC), N-VC and N-GVC composite; (b) Raman spectra of Fe/2Co-N-GVC, Co-N-GVC and Fe-N-GVC.*

To ascertain the defects in the carbon framwork, Raman analysis of the catalyst and carbon framework was performed. **Figure 6.7a** and **6.7b** show the Raman spectra of the carbon and active catalysts, respectively. The defects in the carbon framework also can contribute towards the catalytic activity, which decreases after a certain optimum level.[34] In the Raman spectra, the ratio of the D and G bands gives an indirect measure of the defects.[35] The $_{D}/I_{G}$ ratio calculated for the different samples follows the order: VC (1.28) > N-VC (1.12) > N-GVC (1.04). The measurement was further extended for the active catalyst: Fe/2Co-N-GVC (1.25) > Co-N-GVC (1.22) > Fe-N-GVC (1.14). As the order indicates, a significant degree of defects is present in all the catalysts, and as previously mentioned, the defects are important to achieve good catalytic activity.

6.3.4. XPS Analysis:

The compositions of the carbon and the active catalyst were analysed with the X-ray photoelectron spectroscopy (XPS), and the corresponding XPS spectra are given in **Figure 6.8**. The survey spectra of N-GVC, Fe/2Co-N-GVC, Fe-N-GVC, and Co-N-GVC are given in **Figure 6.8a**; the peaks at 285.28, 398.99, 531.68, 712.65, and 781.97 eV

show the presence of C 1s, N 1s, O 1s, Fe 2p and Co 2p, respectively.[23, 36-37] As the nature of nitrogen present in the doped-carbon has direct influence over the activity, we deconvoluted the N 1s spectra of the composites for correlating the activity with the N dopant.

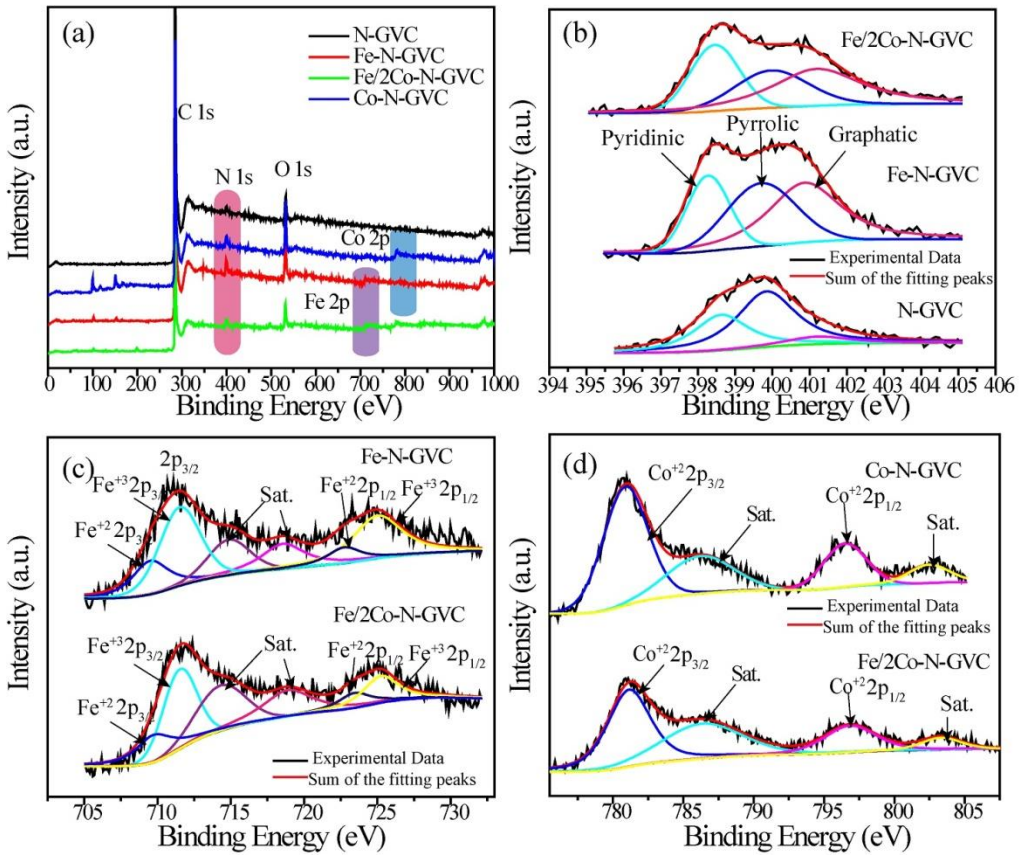

Figure 6.8. *(a) XPS survey spectra of N-GVC, Fe-N-GVC, Fe-2Co-N-GVC, and Co-N-GVC, (b) deconvoluted N 1s spectra of Fe-2Co-N-GVC, Fe-N-GVC and N-GVC, (c) deconvoluted Fe 2p spectra of Fe-N-GVC and Fe-2Co-N-GVC and (d) deconvoluted Co 2p spectra of Co-N-GVC and Fe-2Co-N-GVC.*

The deconvoluted XPS, which is given in **Figure 6.8b**, shows the presence of pyridinic, pyrrolic and graphitic nitrogens with binding energies of 398.5, 399.6 and 400.9 eV, respectively.[38] The pyrrolic nitrogen content decreases in the order of N-GVC > Fe-N-GVC > Fe/2Co-N-GVC, whereas the pyridinic and graphitic nitrogens increased from N-GVC to Fe/2Co-N-GVC.[38] The results indicate the analogy with the previous reports where the pyridinic and graphitic content increase with the annealing.[38] A better illustration of the type of iron and cobalt in the catalyst is presented in **Figure 6.8c** and **6.8d**, respectively. The formation of Fe^{2+} and Fe^{3+} is observed in Fe-N-GVC and Fe/2Co-N-GVC, whereas Co^{2+} is present in the Co-N-GVC and Fe/2Co-N-GVC composites.[39-40]

6.3.5. Electrochemical Studies:

From the XPS analysis, it is apparent that the pyrolysis of the metal precursor with N-GVC plays a key role in determining the type of nitrogen (*i.e.*, pyrrolic, pyridinic and graphitic) formed in the final product and also its relative content. It is well documented in the literature that different types of nitrogen sites contribute differently to the ORR activity. A comparatively higher content of graphitic nitrogen in Fe-N-GVC and Fe/2Co-N-GVC is caused by the annealing of the sample with the metal precursor, whereas, the pyrrolic nitrogen content remains less in these cases.

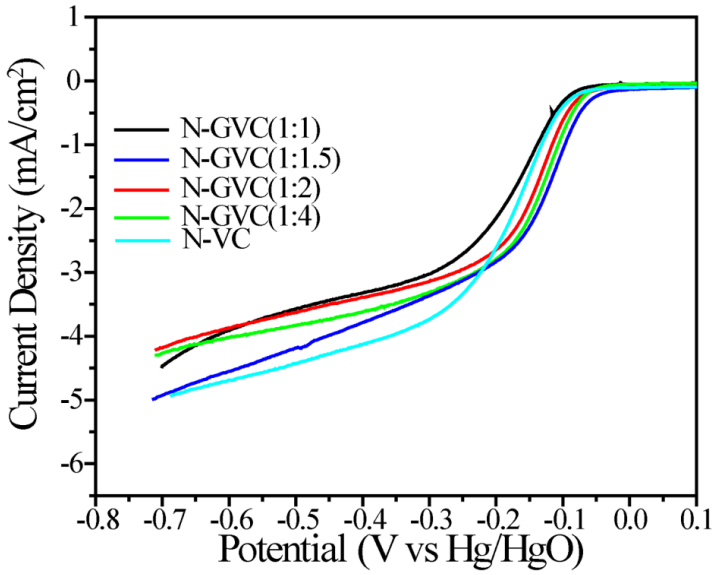

Figure 6.9. *Linear sweep voltamograms (LSVs) of the nitrogen-doped graphene-vulcan carbon composites recorded in 0.1 M KOH solution at 1600 rpm with a sweep rate of 10 mV/s in oxygen saturated environment.*

It is to be noted that the presence of different types of nitrogen is directly related to the metal atoms, and the synergistic interaction between the metal and nitrogen has a direct effect on the electrocatalytic activity. Prior to the analysis of the catalyst material for their intrinsic ORR characteristics, different ratios of N-rGO and VC, which was to be used as a support, were assessed for the ORR activity (**Figure 6.9**). In **Figure 6.9**, the linear sweep voltammogram (LSV) corresponding to the 2:3 composition shows better onset and half-wave potentials compared to the other compositions. Based on the above results, the carbon support with 2:3 composition was chosen for the catalyst preparation.

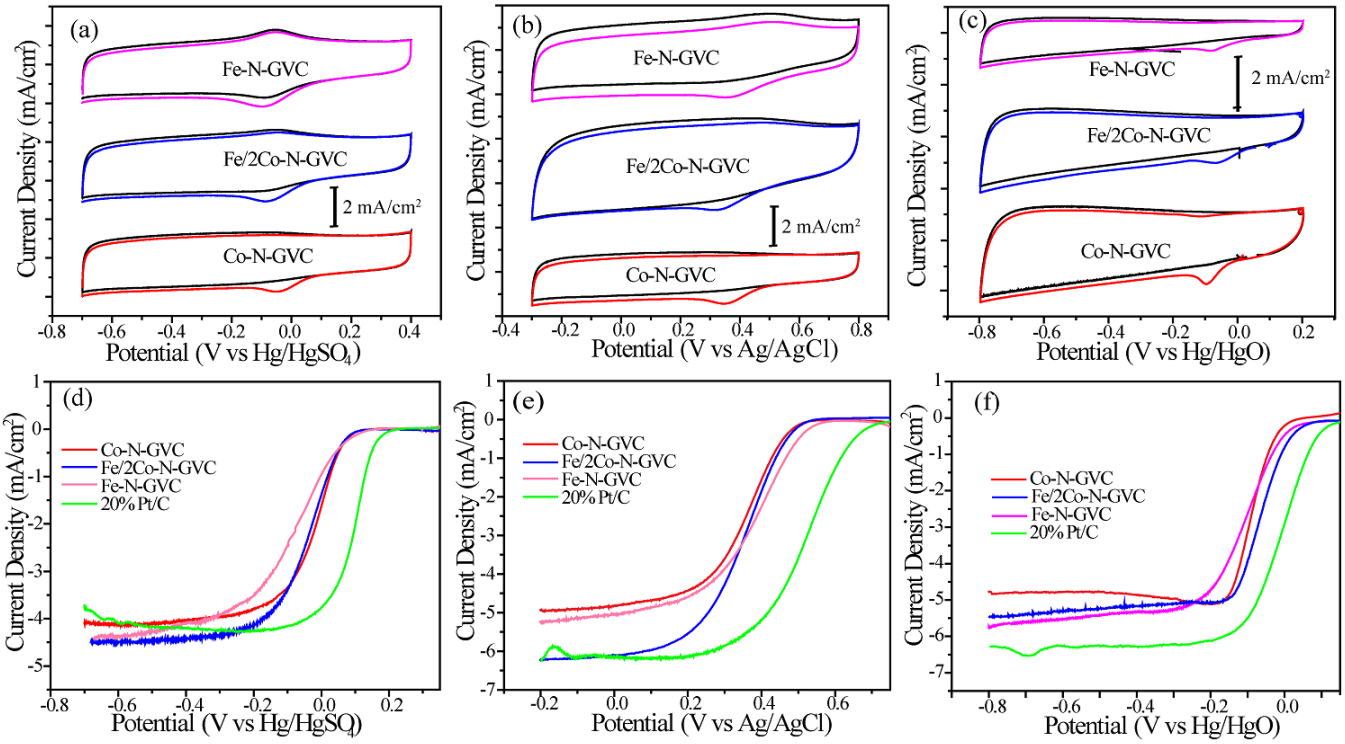

Figure 6.10. *(a), (b) and (c) Cyclic Voltammograms (CVs) of the Fe-N-GVC, Fe/2Co-N-GVC and Co-N-GVC catalysts recorded in 0.1 M $HClO_4$, 0.5 M H_2SO_4 and 0.1 M KOH solution at a sweep rate of 50 mV/s in oxygen saturated and nitrogen saturated environments. The corresponding Linear Sweep Voltammograms (LSVs) of the catalysts, measured in 0.1 M $HClO_4$, 0.5 M H_2SO_4 and 0.1 M KOH solution with 1600 rpm at the sweep rate of 10 mV/s are presented in (d), (e) and (f).*

We subsequently analysed the effect of the electrolyte medium on the ORR activity of the catalysts by using 0.5 M H_2SO_4, 0.1 M $HClO_4$ and 0.1 M KOH solution as the electrolytes. To evaluate the divergence in the electrocatalytic activity of Co-N-GVC,

Fe-N-GVC and Fe/2Co-N-GVC, cyclic voltammogram (CV) and LSV responses were investigated for acidic and basic media.[41] CVs recorded for Co-N-GVC, Fe-N-GVC and Fe/2Co-NGVC catalysts in oxygen- and nitrogen-saturated 0.5 M H_2SO_4, 0.1 M $HClO_4$ and 0.1 M KOH solutions at a sweep rate of 50 mV/s are given in **Figure 6.10a**, **6.10b** and **6.10c**, respectively. In the CVs presented, a clear ORR peak is evident in the oxygen-saturated condition which diminishes when the solution is saturated with nitrogen. The area swept in the CVs is different for the three catalysts in each electrolyte, and also for a particular catalyst in the different electrolytes. This observation can be ascribed to the different interactions of each catalyst with the electrolyte and electrical double layer capacitance. The change in the electrolyte from H_2SO_4 and $HClO_4$ to KOH actively changes the anion and cation in the system, resulting in the variation in double layer capacitance. In acidic medium, a peak for iron oxidation is visible in the Fe-N-GVC and Fe/2Co-N-GVC samples, which has also been observed by Zeleny *et al.*[12]

Table 6.1. *Onset (E_o) and half-wave($E_{1/2}$) potentials of the various catalysts calculated from the LSVs of the corresponding catalysts.*

S.No.	Potential	Active Catalyst	0.5 M H_2SO_4 (V *vs*Hg/$HgSO_4$)	0.1 M $HClO_4$ (V *vs* Ag/AgCl)	0.1 M KOH (V *vs* Hg/HgO)
1	E_o	Fe-N-GVC	0.131	0.559	0.027
2	$E_{1/2}$	-	-0.091	0.400	-0.110
3	E_o	Co-N-GVC	0.095	0.496	0.010
4	$E_{1/2}$	-	-0.014	0.369	-0.090
5	E_o	Fe/2Co-N-GVC	0.093	0.531	0.062
6	$E_{1/2}$	-	-0.038	0.364	-0.065

Further, to analyse the activity variation of the catalyst in acidic and basic media, we performed LSV of the catalysts at a rotation speed of 1600 rpm in oxygen-saturated electrolyte (**Figure 6.10d**, **6.10e** and **6.10f**). As can be seen in **Figure 6.10d**, the Fe-N-GVC catalyst shows the highest onset potential but a more negative $E_{1/2}$. The trend in the onset potential value (more positive potential indicates high intrinsic activity for ORR) for the different catalysts in 0.5 M H_2SO_4 can be represented as Fe-N GVC > Fe/2Co-N-GVC > Co-N-GVC.[42] On the other hand, for the $E_{1/2}$, the trend corresponding to the shift towards more positive potential is: Co-N-GVC > Fe/2Co-N-GVC > Fe-N-GVC.[12] The study was further extended in 0.1 M $HClO_4$ and 0.1 M KOH electrolyte. The trend

observed in the onset potential in $HClO_4$ is: Fe-N-GVC > Fe/2Co-N-GVC > Co-N-GVC whereas the $E_{1/2}$ value varies as: Fe-N-GVC > Fe/2Co-N-GVC > Co-N-GVC. In 0.1 M KOH, the order in the onset value is, Fe/2Co-N-GVC > Fe-N-GVC > Co-N-GVC; for $E_{1/2}$ value, the order becomes as Fe/2Co-N-GVC > Co-N-GVC > Fe-N-GVC. **Table 6.1** lists out the onset and half-wave potentials of all the three catalysts in acidic and basic media. To explain the above anomalous behaviour, we have suggested mechanisms for molecular oxygen reduction in acidic and basic media, which are shown in **Figure 6.1**. As shown in the **Figure 6.1**, in an acidic medium, after the formation of the peroxo group, the protons from the medium react with it and form water molecules. On the other hand, the reaction in the basic medium leads to the formation of the OH^- ions (**Equation 1**, **2** and **3**). The onset potential of ORR on the catalyst surface is directly related to the oxygen adsorption energy of the catalyst and the sharp change in the current density (half-wave potential, $E_{1/2}$) accompanies the removal of the product from the surface.[12, 42] The data obtained from the reports of various groups regarding the binding energies of the intermediates produced during ORR are given in **Table 6.2**. In a significant number of reports, the adsorption energy of oxygen has been calculated on the FeN_x and CoN_x moieties. The adsorption of oxygen is more favourable in the case of FeN_x compared to that of CoN_x. The onset value is the consequence of the molecular oxygen adsorption energy, which is well reflected in our results.[42] In the acidic medium, the Fe-N-GVC catalyst has a better onset value (low overpotential) whereas the value decreases in Fe/2Co-N-GVC and Co-N-GVC. On the other hand, in the case of the half-wave potential, the desorption of the reaction intermediate from the catalyst surface plays a crucial role. Herein, for half-wave potential, the 0.5 M H_2SO_4 and 0.1 M $HClO_4$ show deviation in trend for the catalysts; the deviation may be because of ion-pair formation as the electrolytes have different anionic part (SO_4^{2-} and ClO_4^-).[43-44] In the acidic medium, the removal of the surface intermediates is facilitated through the protonation of the surface intermediates; additionally, the desorption of the intermediates also depends on the surface binding energy and ion pair formation. In the basic medium, Fe-N-GVC has a significantly better onset value compared to Co-N-GVC; however, in the case of Fe/2Co-N-GVC, synergism between FeN_x and CoN_x leads to an even better onset value and enhanced activity. The role of the

intermediate species formation effect is clearly visible in the half-wave potentials of the catalysts. The half-wave potentials of the catalysts in the basic medium follow the order as Fe/2Co-N-GVC > Co-N-GVC > Fe-N-GVC. This order can be explained on the basis of the adsorption energies of the intermediate ions on the surface.

Table 6.2. *Adsorpotion energies of the oxygen reduction reaction intermediates, onest potential and half-wave potentialover the CoN_x and FeN_x active centers.*

S.No.	ORR species	Adsorption site CoN_x (Binding Energy in eV)	Adsorption site FeN_x (Binding Energy in eV)	References
1	O_2	-0.67	-0.98	42
	OOH	-1.23	-1.76	
	O	-3.18	-4.53	
	OH	-2.44	-2.80	
2	O_2	-0.63	-1.45	45
	OOH	-1.18	-1.88	
	O	-3.57	-4.94	
	OH	-2.48	-3.14	
3	O_2	_	-0.98	2
	OOH	_	-1.76	
	O	_	-4.53	
	OH	_	-2.80	
4	O_2	_	-0.95	46
	OOH	_	-1.87	
	O	_	-4.37	
	OH	_	-2.94	
5	O_2	-0.67	_	47
	OOH	-1.02	_	
	O	-3.18	_	
	OH	-2.44	_	
Experimental				
	Potential	**CoN_x (V *vs* RHE)**	**FeN_x (V *vs* RHE)**	**References**
6	Onset Potential	0.80-0.81	0.91-0.93	12
	$E_{1/2}$	0.75	0.81	
7	Onset Potential	0.68	0.75	10

The dissociation of –OOH requires less energy over CoN_x(binding energy -1.23 eV) when compared to the FeN_x (binding energy -1.76 eV) active centres.[42]

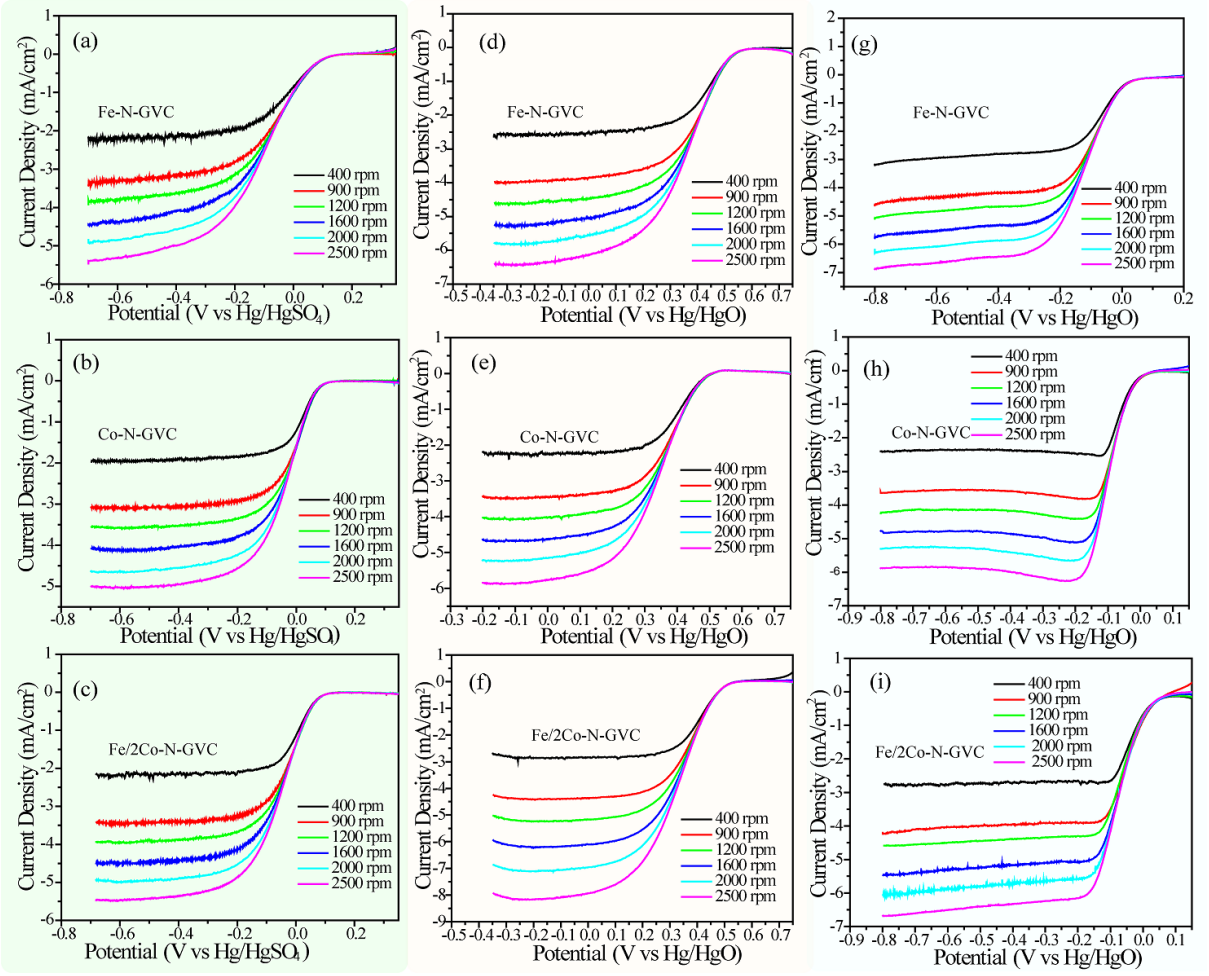

Figure 6.11. *RDE polarization curves recorded at different rotation rates of the working electrodes for Fe-N-GVC, Co-N-GVC and Fe/2Co-N-GVC: in 0.5 M H_2SO_4 (a, b and c), in 0.1 M $HClO_4$ (d, e and f) and in 0.1 M (g, h and i).*

The synergistic effect of the two centres drives the kinetics faster as can be seen in the LSVs of the Fe/2Co-N-GVC catalyst. As listed in **Table 6.2**, reports from different groups clearly state that the dissociation of the ORR transition states is more favoured over the CoN_x active centres against the FeN_x active centres. The listed theoretical reports agree with our findings in acidic and basic media.

Further, to explore the effect of oxygen concentration and removal of the products from the surface, LSVs were recorded using a rotating disc electrode (RDE) at different rotation speeds in the oxygen-saturated electrolyte (**Figure 6.10)** and the Koutecky-Levich (K-L) plots were constructed (**Figure6.11**).[48]

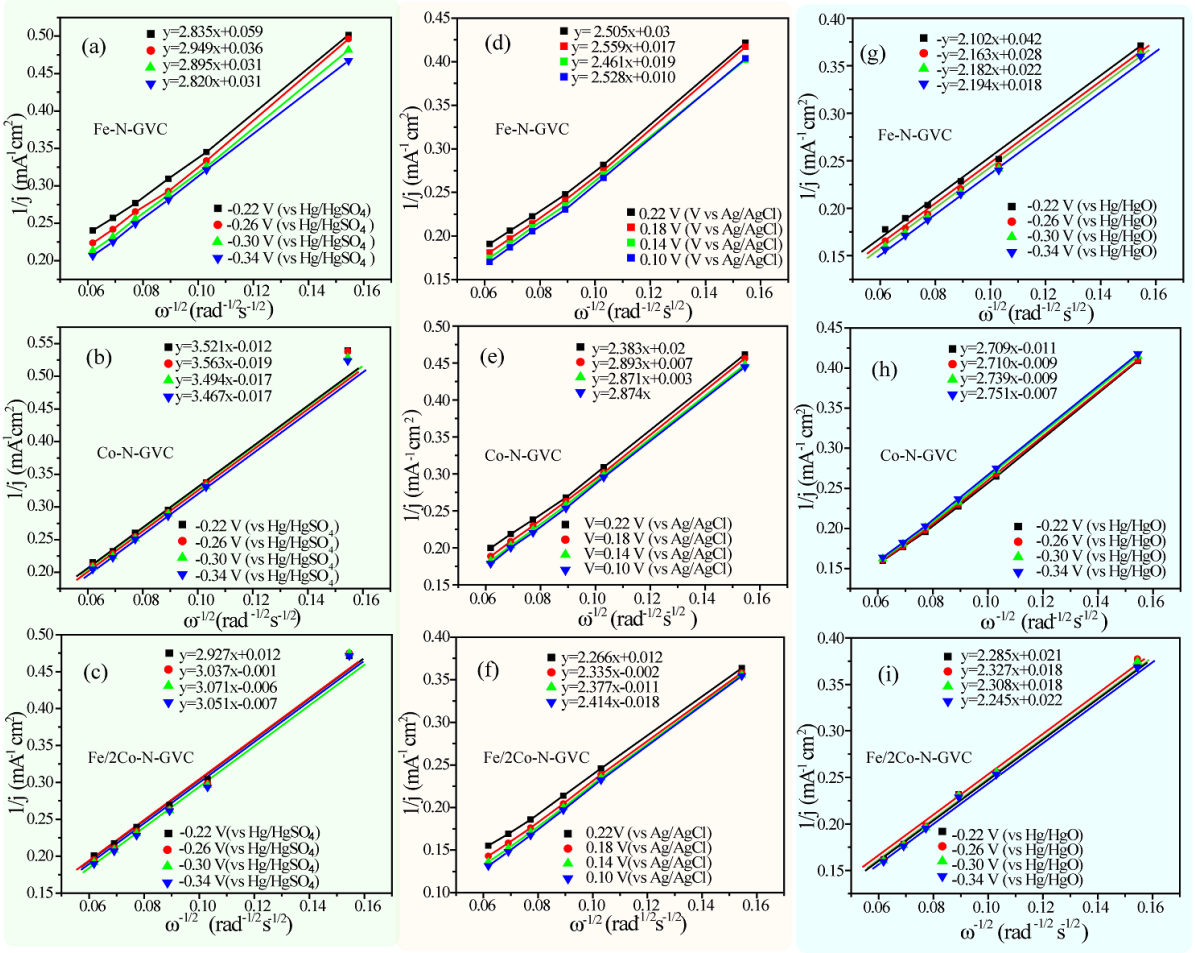

Figure 6.11. *The K-L plots generated for Fe-N-GVC, Co-N-GVC and Fe/2Co-N-GVC: in 0.5 M H_2SO_4 (a, b and c), in 0.1 M (d, e and f) and in 0.1 M KOH (g, h and i).*

As evident from **Figure 6.11**, the current density increases with the rotation rate in both basic and acidic media. Further, the mechanism was confirmed through the K-L plots of the catalysts, which are the plots representing the relation between the j^{-1} and $\omega^{-1/2}$, where, "j" stands for current density (mA/cm^2) and "ω" stands for angular rotation (radian/sec). The plot follows linearity and parallelism in both acidic and basic media, which is also a characteristic feature of the first order kinetics. A detailed description of the K-L equation is included in **Chapter 2**.[49] Moreover, to verify the difference in the reaction mechanism

of the catalysts in acidic and basic media, a rotating ring disk electrode (RRDE) analysis was performed (**Figure 6.13**). The RRDE analysis suggests that the catalyst in 0.5 M H_2SO_4 and 0.1 M $HClO_4$ have significantly low amount of peroxide formation, inferring the dominance of four-electron transfer in the reduction process.[2, 50] In acidic medium, the dissociation of the active species, *i.e.*, OOH, takes place through the protonation of the species, as proposed in **Figure 6.13**, which is subsequently removed as a water molecule (**Figure 6.13a**, **6.13b**, **6.13d** and **6.13e**).

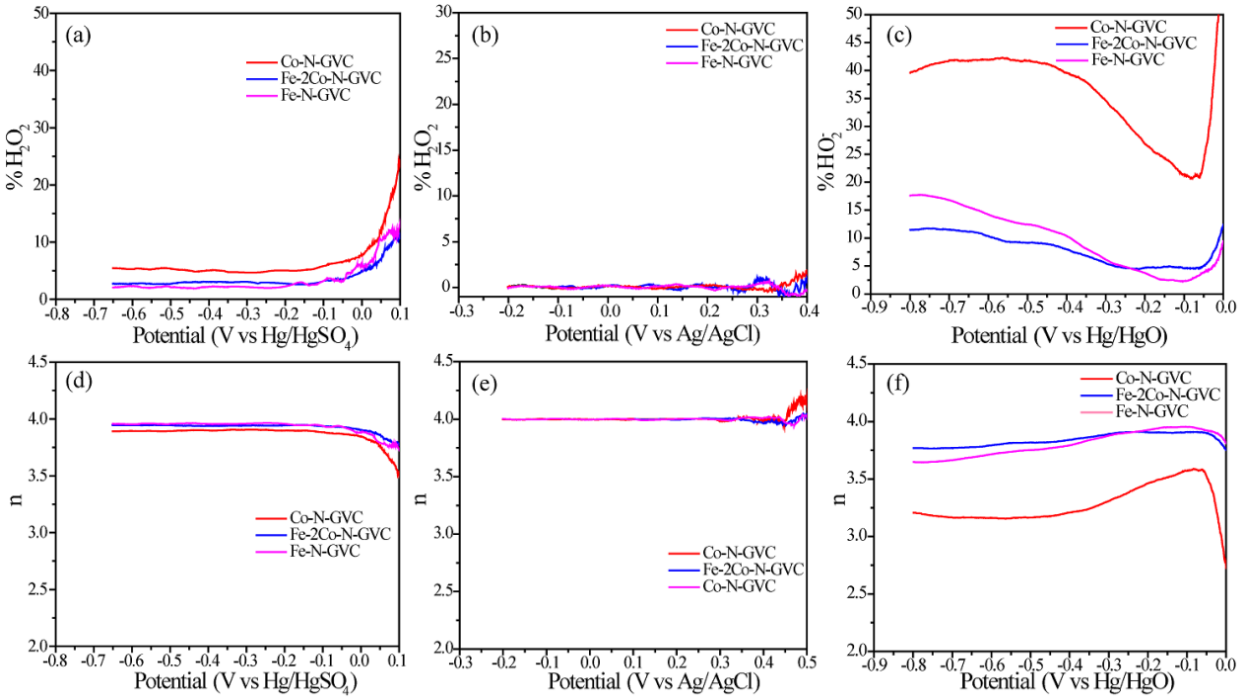

Figure 6.13. *The peroxide percentage and number of electrons involved in the faradic reaction calculated from the RRDE analysis at 1600 rpm: (a), (b) and (c) represent the peroxide percentages calculated at various potentials in 0.5 M H_2SO_4, 0.1 M $HClO_4$, and 0.1 M KOH solutions, respectively; (d), (e) and (f) represent the number of electrons involved in the electrode reaction as calculated at various potentials in 0.5 M H_2SO_4, 0.1 M HClO4, and 0.1 M KOH solutions, respectively.*

In contrary to the acidic condition, the RRDE analysis in the basic medium shows significant amount of peroxide ion formation and the electron transfer number shows a value comparatively much lower than four (**Figure 6.13c** and **6.13f**). The order for the peroxide ion formation in basic medium is Co-N-GVC > Fe-N-GVC > Fe/2Co-N-GVC and its reverse order (*i.e.*, Fe/2Co-N-GVC > Fe-N-GVC > Co-N-GVC) is followed for the

number of electrons involved in the reduction process. These trends can be directly correlated to the adsorption free energies of the ORR species **(Table 6.2)**. As can be seen from **Table 6.2**, the binding energy of the –OOH species over the CoN_x active centre is less compared to the FeN_x active centres.

In acidic medium, the dissociation of -OOH follows the protonation and, hence, less production of peroxide is noted. The experimental results in the basic medium indicate higher production of H_2O_2 on Co-N-GVC, which is a consequence of the favoured dissociation of the –OOH species from the surface.[51] The FeN_x has more favourable binding for –OOH in Fe-N-GVC, which causes less production of the peroxide ion species. In the case of Fe/2Co-N-GVC, the synergistic effect of the FeN_x and CoN_x active centres causes improved ORR performance and less peroxide ion formation. This is because, in the same catalyst, the –OOH ions generated from the CoN_x active centers can be reduced over the FeN_x centers because of the high binding energy of –OOH over the FeN_x centers.

After understanding the surface reactions, the catalysts were incorporated as the cathode catalyst for demonstrating the Zn-air battery device (detailed reaction mechanism in **Chapter 1**).[52-53] A schematic representation of the cell assembly is presented in **Figure 6.1**. The fabricated batteries with the three catalysts were discharged at 10 and 20 mA/cm^2 current densities and the corresponding discharge curves are shown in **Figure 6.14a** and **6.14b**, respectively.[52, 54] The discharge profiles of the batteries show constant discharge plateau where the output voltage follows the order Fe/2Co-N-GVC > Co-N-GVC > Fe-N-GVC. During the discharge at 10 and 20 mA/cm^2, the batteries follow the $E_{1/2}$ region of the single electrode study and hence the discharge trend is maintained similar to the $E_{1/2}$ region for ORR in 0.1 M KOH. In constant current drag, both the anode and cathode faradaic reactions get enough time span to achieve equilibrium potential and hence the constant battery voltage. In the polarisation process, the equilibrium is not established between the anode and cathode reactions, but during the constant current discharge, the time span is high to establish the equilibrium voltage. In the discharge profile of the batteries (**Figure 6.14a** and **6.14b**), Fe/2Co-N-GVC discharges at a higher voltage compared to Co-N-GVC and Fe-N-GVC, which is comparable to the results of the single cell studies in basic media.

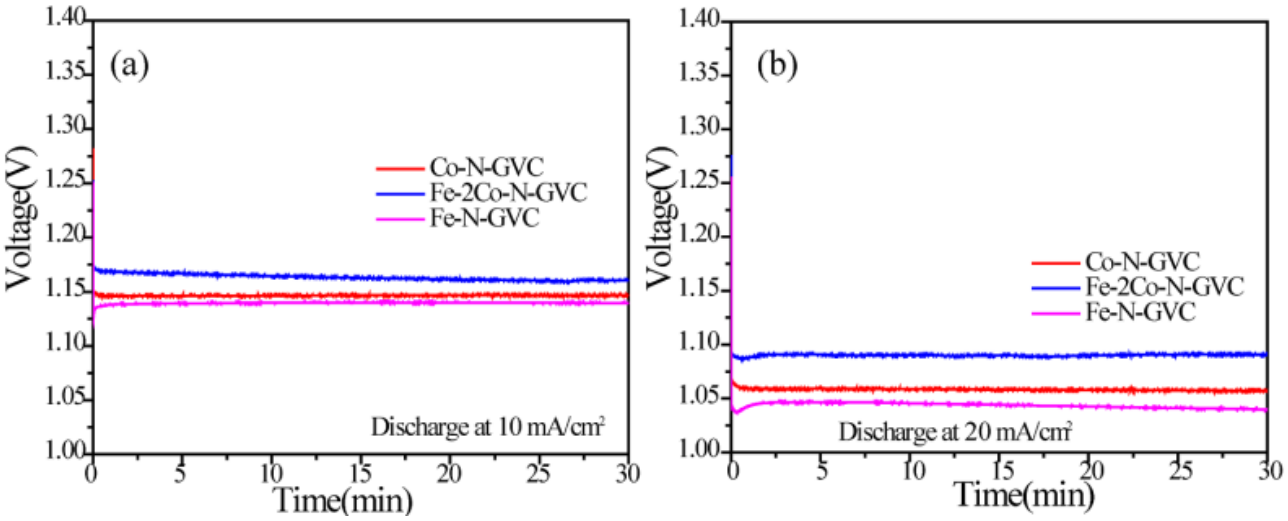

Figure 6.14. *(a) and (b) represent the observed discharge plateau of the Zn-air batteries fabricated with the homemade catalysts in 1 M KOH solution at 10 mA/cm^2 and 20 mA/cm^2, respectively.*

6.4. Conclusions

In summary, we have prepared ORR catalysts by incorporating the active metal atom centres, Fe and Co, in the composite of VC and graphene. The two active centres, CoN_x and FeN_x show different activities in acidic and alkaline media, which have been correlated to the variation in the surface binding of the transition states. Among the catalysts, Fe-N-GVC shows a low overpotential in both acidic and basic media due to the more favourable value of oxygen binding energy, whereas the overpotential is substantially higher for the Co-N-GVC due to the less favourable binding energy value for molecular oxygen. Further, the half-wave potential of the catalyst is dependent on the dissociation of the reaction intermediates from the surface, which is more favourable in the case of Co-N-GVC. In acidic medium, the dissociation of the surface species is enhanced by the protonation of the intermediates. However, in a basic medium, the dissociation of the surface species is less favoured, and the binding energies of catalyst determine the half-wave potential. Co-N-GVC shows improved half-wave potential ($E_{1/2}$) compared to Fe-N-GVC because of the favoured dissociation of the surface intermediates. Due to the presence of Fe and Co, the onset and half-wave potentials are better for Fe/2Co-N-GVC compared to the other two catalysts in basic medium. Here, the variation in the catalytic activity in acidic and basic media is correlated to the formation of surface transition species and their detachment from the surface of the catalyst. The newly

synthesized catalysts were used to fabricate a Zn-air battery to demonstrate the activity in a real system. The battery discharges at 10 mA/cm^2 and 20 mA/cm^2 current density follows the order in line with the single electrode study, which is: Fe/2Co-N-GVC > Co-N-GVC > Fe-N-GVC. These results affirm the role of the dissociation energies of the ORR intermediates in governing the catalyst activity in a single electrode study and the fabricated device which, in turn, is highly dependent on the medium.

6.5. Reference

(1) Kattel, S.; Wang, G., A Density Functional Theory Study of Oxygen Reduction Reaction on Me-N_4 (Me = Fe, Co, or Ni) Clusters Between Graphitic Pores. *J. Mater. Chem. A* **2013,** *1*, 10790-10797.

(2) Kattel, S.; Wang, G., Reaction Pathway for Oxygen Reduction on FeN_4 Embedded Graphene. *J. Phys. Chem. Lett.* **2014,** *5*, 452-456.

(3) Nie, Y.; Li, L.; Wei, Z., Recent Advancements in Pt and Pt-free Catalysts for Oxygen Reduction Reaction. *Chem. Soc. Rev.* **2015,** *44*, 2168-2201.

(4) Guo, S.; Li, D.; Zhu, H.; Zhang, S.; Markovic, N. M.; Stamenkovic, V. R.; Sun, S., FePt and CoPt Nanowires as Efficient Catalysts for the Oxygen Reduction Reaction. *Angew. Chem. Int. Ed.* **2013,** *52*, 3465-3468.

(5) Castanheira, L.; Silva, W. O.; Lima, F. H. B.; Crisci, A.; Dubau, L.; Maillard, F., Carbon Corrosion in Proton-Exchange Membrane Fuel Cells: Effect of the Carbon Structure, the Degradation Protocol, and the Gas Atmosphere. *ACS Catal.* **2015,** *5*, 2184-2194.

(6) Engl, T.; Gubler, L.; Schmidt, T. J., Fuel Electrode Carbon Corrosion in High Temperature Polymer Electrolyte Fuel Cells—Crucial or Irrelevant? *Energy Technol.***2016,** *4*, 65-74.

(7) Loukrakpam, R.; Luo, J.; He, T.; Chen, Y.; Xu, Z.; Njoki, P. N.; Wanjala, B. N.; Fang, B.; Mott, D.; Yin, J.; Klar, J.; Powell, B.; Zhong, C.-J., Nanoengineered PtCo and PtNi Catalysts for Oxygen Reduction Reaction: An Assessment of the Structural and Electrocatalytic Properties. *J. Phys. Chem. C* **2011,** *115*, 1682-1694.

(8) Lee, J.-S.; Tai Kim, S.; Cao, R.; Choi, N.-S.; Liu, M.; Lee, K. T.; Cho, J., Metal–Air Batteries with High Energy Density: Li–Air versus Zn–Air. *Adv. Energy Mater.* **2011,** *1*, 34-50.

(9) Balaish, M.; Kraytsberg, A.; Ein-Eli, Y., A Critical Review on Lithium-air Battery Electrolytes. *Phys. Chem. Chem. Phys.* **2014,** *16*, 2801-2822.

(10) Fu, X.; Choi, J.-Y.; Zamani, P.; Jiang, G.; Hoque, M. A.; Hassan, F. M.; Chen, Z., Co–N Decorated Hierarchically Porous Graphene Aerogel for Efficient Oxygen Reduction Reaction in Acid. *ACS Appl. Mater. Interfaces* **2016,** *8*, 6488-6495.

(11) Lu, L., Covalently Entrapping of Cobalt-Iron Sulfides in N-doped Mesoporous Carbon as Extraordinary Bi-functional Electrocatalysts for Oxygen Reduction and Evolution Reactions. *ACS Appl. Mater. Interfaces* **2014**.

(12) Wu, G.; More, K. L.; Johnston, C. M.; Zelenay, P., High-Performance Electrocatalysts for Oxygen Reduction Derived from Polyaniline, Iron, and Cobalt. *Science* **2011,** *332*, 443-447.

(13) Sa, Y. J.; Seo, D.-J.; Woo, J.; Lim, J. T.; Cheon, J. Y.; Yang, S. Y.; Lee, J. M.; Kang, D.; Shin, T. J.; Shin, H. S.; Jeong, H. Y.; Kim, C. S.; Kim, M. G.; Kim, T.-Y.; Joo, S. H., A General Approach to Preferential Formation of Active Fe-Nx Sites in Fe-N/C Electrocatalysts for Efficient Oxygen Reduction Reaction. *J. Am. Chem. Soc.* **2016**.

(14) Jiang, W.-J.; Gu, L.; Li, L.; Zhang, Y.; Zhang, X.; Zhang, L.-J.; Wang, J.-Q.; Hu, J.-S.; Wei, Z.; Wan, L.-J., Understanding the High Activity of Fe–N–C Electrocatalysts in Oxygen Reduction: Fe/Fe_3C Nanoparticles Boost the Activity of Fe–Nx. *J. Am. Chem. Soc.* **2016**.

(15) Ramaswamy, N.; Mukerjee, S., Influence of Inner- and Outer-Sphere Electron Transfer Mechanisms during Electrocatalysis of Oxygen Reduction in Alkaline Media. *J. Phys. Chem. C* **2011,** *115*, 18015-18026.

(16) Suntivich, J.; Gasteiger, H. A.; Yabuuchi, N.; Nakanishi, H.; Goodenough, J. B.; Shao-Horn, Y., Design Principles for Oxygen-reduction Activity on Perovskite Oxide Catalysts for Fuel Cells and Metal–air Batteries. *Nat Chem* **2011,** *3*, 546-550.

(17) Zhang, J.; Xia, Z.; Dai, L., Carbon-based Electrocatalysts for Advanced Energy Conversion and Storage. *Science Advances* **2015,** *1*.

(18) Ge, X.; Sumboja, A.; Wuu, D.; An, T.; Li, B.; Goh, F. W. T.; Hor, T. S. A.; Zong, Y.; Liu, Z., Oxygen Reduction in Alkaline Media: From Mechanisms to Recent Advances of Catalysts. *ACS Catal.* **2015,** *5*, 4643-4667.

(19) He, F.; Li, K.; Xie, G.; Wang, Y.; Jiao, M.; Tang, H.; Wu, Z., Theoretical Insights on the Catalytic Activity and Mechanism for Oxygen Reduction Reaction at Fe and P Codoped Graphene. *Phys. Chem. Chem. Phys.* **2016,** *18*, 12675-12681.

(20) Wang, D.-W.; Su, D., Heterogeneous Nanocarbon Materials for Oxygen Reduction Reaction. *Energy Environ. Sci.* **2014,** *7*, 576-591.

(21) Liu, S.; White, M. G.; Liu, P., Mechanism of Oxygen Reduction Reaction on Pt(111) in Alkaline Solution: Importance of Chemisorbed Water on Surface. *J. Phys. Chem. C* **2016,** *120*, 15288-15298.

(22) Yang, J.; Kim, S. H.; Kwak, S. K.; Song, H.-K., Curvature-Induced Metal–Support Interaction of an Islands-by-Islands Composite of Platinum Catalyst and Carbon Nano-onion for Durable Oxygen Reduction. *ACS Appl. Mater. Interfaces* **2017,** *9*, 23302-23308.

(23) Kashyap, V.; Singh, S. K.; Kurungot, S., Cobalt Ferrite Bearing Nitrogen-Doped Reduced Graphene Oxide Layers Spatially Separated with Microporous Carbon as Efficient Oxygen Reduction Electrocatalyst. *ACS Appl. Mater. Interfaces* **2016,** *8*, 20730-20740.

(24) Ma, Y.; Wang, H.; Ji, S.; Goh, J.; Feng, H.; Wang, R., Highly Active Vulcan Carbon Composite for Oxygen Reduction Reaction in Alkaline Medium. *Electrochim. Acta* **2014,** *133*, 391-398.

(25) Wang, K.; Huang, Y.; Qin, X.; Wang, M.; Sun, X.; Yu, M., Effect of Pyrolysis Temperature of 3D Graphene/carbon Nanotubes Anode Materials on Yield of Carbon Nanotubes and Their Electrochemical Properties for Na-ion Batteries. *Chemical Engineering Journal* **2017,** *317*, 793-799.

(26) Zhao, Y.; Chu, Y.; Ju, X.; Zhao, J.; Kong, L.; Zhang, Y., Carbon-Supported Copper-Based Nitrogen-Containing Supramolecule as an Efficient Oxygen Reduction Reaction Catalyst in Neutral Medium. *Catalysts* **2018,** *8*, 53.

(27) Liliang, C.; Tsutomu, M.; Chihiro, I.; Hiroki, O.; Emil, O.; Hullathy Subban, G.; Hirotaka, I.; Jidong, Z.; Zhypargul, A.; Shintaro, T.; Akira, Y., Synthesis of novel CoCx @C nanoparticles. *Nanotechnology* **2013,** *24*, 045602.

(28) Wang, H.; Côté, R.; Faubert, G.; Guay, D.; Dodelet, J. P., Effect of the Pre-Treatment of Carbon Black Supports on the Activity of Fe-Based Electrocatalysts for the Reduction of Oxygen. *J. Phys. Chem. B* **1999,** *103,* 2042-2049.

(29) Schulenburg, H.; Stankov, S.; Schünemann, V.; Radnik, J.; Dorbandt, I.; Fiechter, S.; Bogdanoff, P.; Tributsch, H., Catalysts for the Oxygen Reduction from Heat-Treated Iron(III) Tetramethoxyphenylporphyrin Chloride: Structure and Stability of Active Sites. *J. Phys. Chem. B* **2003,** *107,* 9034-9041.

(30) Chen, P.; Xu, K.; Tong, Y.; Li, X.; Tao, S.; Fang, Z.; Chu, W.; Wu, X.; Wu, C., Cobalt Nitrides as a Class of Metallic Electrocatalysts for the Oxygen Evolution Reaction. *Inorganic Chemistry Frontiers* **2016,** *3,* 236-242.

(31) Park, M.; Lee, J.; Hembram, K.; Lee, K.-R.; Han, S.; Yoon, C.; Nam, S.-W.; Kim, J., Oxygen Reduction Electrocatalysts Based on Coupled Iron Nitride Nanoparticles with Nitrogen-Doped Carbon. *Catalysts* **2016,** *6,* 86.

(32) Palaniselvam, T.; Kashyap, V.; Bhange, S. N.; Baek, J.-B.; Kurungot, S., Nanoporous Graphene Enriched with Fe/Co-N Active Sites as a Promising Oxygen Reduction Electrocatalyst for Anion Exchange Membrane Fuel Cells. *Adv. Funct. Mater.* **2016,** *26,* 2150-2162.

(33) Bezerra, C. W. B.; Zhang, L.; Lee, K.; Liu, H.; Marques, A. L. B.; Marques, E. P.; Wang, H.; Zhang, J., A review of Fe–N/C and Co–N/C Catalysts for the Oxygen Reduction Reaction. *Electrochim. Acta* **2008,** *53,* 4937-4951.

(34) Zhao, H.; Sun, C.; Jin, Z.; Wang, D.; Yan, X.; Chen, Z. G.; zhu, G.; Yao, X., Carbon for Oxygen Reduction Reaction: A Defect Mechanism. *J. Mater. Chem. A* **2015**.

(35) Wu, J.-B.; Lin, M.-L.; Cong, X.; Liu, H.-N.; Tan, P.-H., Raman Spectroscopy of Graphene-based Materials and its Applications in Related Devices. *Chem. Soc. Rev.* **2018,** *47,* 1822-1873.

(36) Bian, W.; Yang, Z.; Strasser, P.; Yang, R., A $CoFe_2O_4$/graphene Nanohybrid as an Efficient Bi-functional Electrocatalyst for Oxygen Reduction and Oxygen Evolution. *J. Power Sources* **2014,** *250,* 196-203.

(37) Kashyap, V.; Singh, S. K.; Kurungot, S., Activity Tuning of Cobalt Ferrite Nanoparticles Anchored on N-Doped Reduced Graphene Oxide as a Potential Oxygen

Reduction Electrocatalyst by Zn Substitution in the Spinel Matrix. *ChemistrySelect* **2017,** *2*, 7845-7853.

(38) Unni, S. M.; Bhange, S. N.; Illathvalappil, R.; Mutneja, N.; Patil, K. R.; Kurungot, S., Nitrogen-Induced Surface Area and Conductivity Modulation of Carbon Nanohorn and Its Function as an Efficient Metal-Free Oxygen Reduction Electrocatalyst for Anion-Exchange Membrane Fuel Cells. *Small* **2015,** *11*, 352-360.

(39) Liu, C.; Zhang, Y.; Jia, J.; Sui, Q.; Ma, N.; Du, P., Multi-susceptibile Single-Phased Ceramics with Both Considerable Magnetic and Dielectric Properties by Selectively Doping. *Sci. Rep.* **2015,** *5*, 9498.

(40) Tang, R.; Jiang, C.; Qian, W.; Jian, J.; Zhang, X.; Wang, H.; Yang, H., Dielectric Relaxation, Resonance and Scaling Behaviors in $Sr_3Co_2Fe_{24}O_{41}$ Hexaferrite. *Sci. Rep.* **2015,** *5*, 13645.

(41) Shinozaki, K.; Zack, J. W.; Richards, R. M.; Pivovar, B. S.; Kocha, S. S., Oxygen Reduction Reaction Measurements on Platinum Electrocatalysts Utilizing Rotating Disk Electrode Technique: I. Impact of Impurities, Measurement Protocols and Applied Corrections. *J. Electrochem. Soc.* **2015,** *162*, F1144-F1158.

(42) Liu, K.; Kattel, S.; Mao, V.; Wang, G., Electrochemical and Computational Study of Oxygen Reduction Reaction on Nonprecious Transition Metal/Nitrogen Doped Carbon Nanofibers in Acid Medium. *J. Phys. Chem. C* **2016,** *120*, 1586-1596.

(43) Re, S.; Osamura, Y.; Morokuma, K., Coexistence of Neutral and Ion-Pair Clusters of Hydrated Sulfuric Acid $H_2SO_4(H_2O)n$ (n = 1−5) A Molecular Orbital Study. *J. Phys. Chem. A* **1999,** *103*, 3535-3547.

(44) Seo, D. M.; Reininger, S.; Kutcher, M.; Redmond, K.; Euler, W. B.; Lucht, B. L., Role of Mixed Solvation and Ion Pairing in the Solution Structure of Lithium Ion Battery Electrolytes. *J. Phys. Chem. C* **2015,** *119*, 14038-14046.

(45) Kattel, S.; Wang, G., A Density Functional Theory Study of Oxygen Reduction Reaction on Me–N_4 (Me = Fe, Co, or Ni) Clusters Between Graphitic Pores. *J. Mater. Chem. A* **2013,** *1*, 10790-10797.

(46) Zhang, J.; Wang, Z.; Zhu, Z., The Inherent Kinetic Electrochemical Reduction of Oxygen into H_2O on FeN_4-carbon: A Density Functional Theory Study. *J. Power Sources* **2014,** *255*, 65-69.

(47) Kattel, S.; Atanassov, P.; Kiefer, B., Catalytic Activity of Co–N_x/C Electrocatalysts for Oxygen Reduction Reaction: A Density Functional Theory Study. *Phys. Chem. Chem. Phys.* **2013,** *15*, 148-153.

(48) Balan, B. K.; Manissery, A. P.; Chaudhari, H. D.; Kharul, U. K.; Kurungot, S., Polybenzimidazole Mediated N-doping Along the Inner and Outer Surfaces of a Carbon Nanofiber and its Oxygen Reduction Properties. *J. Mater. Chem.* **2012,** *22*, 23668-23679.

(49) Balan, B. K.; Kurungot, S., Highly Exposed and Activity Modulated Sandwich Type Pt Thin Layer Catalyst with Enhanced Utilization. *J. Mater. Chem.* **2011,** *21*, 19039-19048.

(50) Zhou, R.; Zheng, Y.; Jaroniec, M.; Qiao, S.-Z., Determination of the Electron Transfer Number for the Oxygen Reduction Reaction: From Theory to Experiment. *ACS Catal.* **2016,** *6*, 4720-4728.

(51) Ziegelbauer, J. M.; Olson, T. S.; Pylypenko, S.; Alamgir, F.; Jaye, C.; Atanassov, P.; Mukerjee, S., Direct Spectroscopic Observation of the Structural Origin of Peroxide Generation from Co-Based Pyrolyzed Porphyrins for ORR Applications. *J. Phys. Chem. C* **2008,** *112*, 8839-8849.

(52) Prabu, M.; Ramakrishnan, P.; Nara, H.; Momma, T.; Osaka, T.; Shanmugam, S., Zinc–Air Battery: Understanding the Structure and Morphology Changes of Graphene-Supported $CoMn_2O_4$ Bifunctional Catalysts Under Practical Rechargeable Conditions. *ACS Appl. Mater. Interfaces* **2014,** *6*, 16545-16555.

(53) Wang, M.; Qian, T.; Zhou, J.; Yan, C., An Efficient Bifunctional Electrocatalyst for a Zinc–Air Battery Derived from Fe/N/C and Bimetallic Metal–Organic Framework Composites. *ACS Appl. Mater. Interfaces* **2017,** *9*, 5213-5221.

(54) Prabu, M.; Ketpang, K.; Shanmugam, S., Hierarchical Nanostructured $NiCo_2O_4$ as an Efficient Bifunctional Non-precious Metal Catalyst for Rechargeable Zinc-air Batteries. *Nanoscale* **2014,** *6*, 3173-3181.

Chapter 7

Summary and Conclusions

The chapter presents an overview of the crucial observations and conclusions presented in each of the chapters of the thesis. The energy storage and conversion devices possessing high energy density suffer from the involvement of costly and degradable electrode materials, which restrict their commercial viability. However, these issues can be eliminated by developing adequate electrode materials for the devices. In this respect, the early transition metals offer tunable and convincing electrode activities, and, hence, appear to be affordable electrode materials for such applications. Among these transition metal compounds, the oxides of iron and cobalt are interesting owing to their tunable and high intrinsic activity towards oxygen reduction reaction (ORR) and oxygen evolution reaction (OER). The bimetallic cobalt ferrite phase of the two metal atoms shows high stability and notable performance during the harsh oxidative-reductive environments of ORR and OER. Even though notable activities are offered by these oxides, the performance is affected by their high resistive nature. This necessitates the need to support such oxide species over suitable conducting supports. Particularly, the graphitic carbon such as graphene provides a suitable solution to this problem by offering an effective way to achieve adjustable electrochemical properties. Nitrogen -doped reduced graphene oxide (N-rGO) provides a pleasant support for the cobalt ferrite nanoparticles. In the present thesis, we have adopted the solvothermal synthesis procedure for preparing the cobalt ferrite nanoparticles and their composites with N-rGO. The substitution of the Zn and Zr atoms in the cobalt ferrite matrix has substantially improved their performance towards the electrochemical faradaic reactions and finally to the efficiency of the device. The composite catalysts prepared by using these types of metal oxides and carbon supports have been evaluated for metal-air battery applications, and for the performance of the prototypes. The primary and secondary Zn-air batteries fabricated with these composites displayed notable

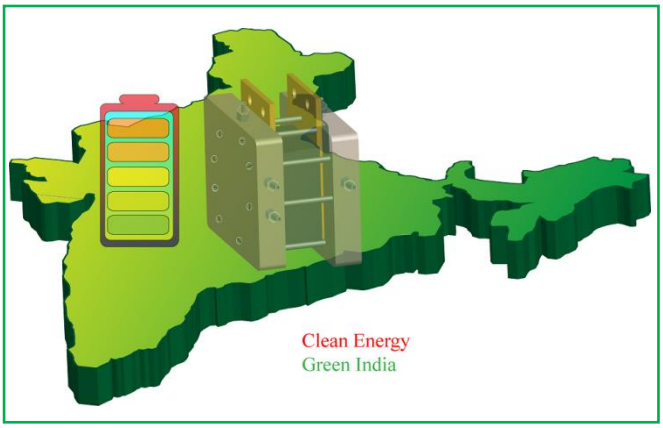

performance characteristics. Moreover, the study tried to address the relation between the nature of the ORR active centers with the transition states and finally how the performance is governed under the experimental conditions. The FeN_x and CoN_xactive centers for ORR are found to have significantly different binding energy for the transition states and this has a direct correlation with the ORR performance of the systems. The study demonstrates a viable strategy to design a suitable catalyst for facilitating ORR depending on the nature of the electrolyte conditions of the final devices.

The major accomplishments of the thesis work are summarized below:

1. Size Optimized Cobalt Ferrite Nanoparticle Supported N-doped Reduced Graphene Oxide as an Efficient Oxygen Reduction Catalyst for Primary Zinc-air Battery

Cobalt ferrite (CF) is a well-known oxide material and it shows significant activity towards ORR. For understanding the performance characteristics of these class of materials, CF nanoparticles were synthesized through a facile solvothermal route. The particles were decorated over the N-rGO support for improving the conductivity of the catalyst. The CF/N-rGO catalyst after annealing at 150 ^oC outperforms the commercial 20% Pt/C catalyst in terms of the ORR activity. The salient features of the work are:

- The CF nanoparticles with narrow size distribution has been achieved through the solvothermal decomposition of the acetate salt. The size of the particles ranging from 5-8 nm shows higher ORR activity and this size range has been chosen for their *in-situ* decoration on N-rGO.
- After annealing at 150 ^oC and mixing with Vulcan carbon, the catalyst CF/N-rGO-150 delivered a current density of 7.4± 0.5 mA/cm^2 and an overpotential of 110 mV against the state-of-the-art 20 wt.% Pt/C (5.4± 0.5 mA/cm^2).
- The CF/N-rGO-150 catalyst shows remarkable durability even after 5000 cycles of accelerated durability test (ADT),giving only a 40 mV negative shift in the half-wave potential. This value is much better compared to the degradation behavior of the Pt/C catalyst.
- A primary Zn-air battery (ZAB) was fabricated by employing CF/N-rGO-150 as the cathode catalyst and the system delivered a discharge capacity of 630 mAh/g. The

polarization of the battery showed a power density of 190 mW/cm^2. The system performed for 15 h at a discharge current density of 20 mA/cm^2. These are promising values that can be expected from a device based on the air electrode made up of a noble metal-free ORR catalyst.

2. Structural Modification in the Spinel Cobalt Ferrite Matrix with Zn Substitution for Enhanced Oxygen Reduction Reaction

The cobalt ferrite nanoparticles in association with the N-rGO have notable ORR performance. However, they still suffer from some amount ofoverpotential. Structural modification and tuning of the electronic properties of the ferrite particles are viable ways to reduce the overpotential. In the cobalt ferrite matrix, the cobalt and iron atoms are present in the tetrahedral and octahedral sites. The substitution of these metal atoms from their lattice site provides a way to improve ORR activity. In this respect, the Zn substitution in the oxide hasshownconvincing results as it substitutes the Fe^{3+} ions from the tetrahedral site and thereby helps to reduce the ORR overpotential. The salient features of the substitutional effect are listed below:

- Zn substitution hasa decisive role in determining the Fe^{2+}/Fe^{3+} ratio in the cobalt ferrite nanoparticles. The cobalt ferrite has inverse spinel structure where some of the Co^{2+} ions occupy octahedral site and similarly some of the Fe^{3+} ions also prefer to occupy the tetrahedral site. The substitution of the Fe^{3+} from the tetrahedral site with Zn^{2+} controls the Fe^{2+}/Fe^{3+} ratio.
- The composite catalyst designated as CFZn(0.3)/N-rGO-Vulcan (the Co, Fe, and Zn are present in the molar ratio of 1:1.7:0.3) has displayed improved ORR performance (an overpotential of 100 mV compared to 20 wt.% Pt/C)compared to the parent CF/N-rGO-Vulcan catalyst. This has been achieved due to the favorable property modulations accomplished through the Zn substitution.
- The catalyst (CFZn(0.3)/N-rGO-Vulcan) also displays good stability in accelerated durability test (ADT), where the system suffered only a 30 mV negative shift after the 5000 ORR cycles.

3. Zirconium Substitution in the Spinel Cobalt Ferrite Matrix for Bifunctional Activity: A Potential Electrode Material for Rechargeable Zinc-air Battery

The metal-air batteries are classified as primary and secondary (rechargeable) batteries. The rechargeable Zn-air batteries are of pivotal importance, but they often suffer from the issue of

catalyst inefficiency. The CF/N-rGO catalyst has shown notable ORR activity in primary ZAB, but, the rechargeable ZAB requires a bifunctional catalyst which can facilitate both ORR and OER. The Zr substitution in the cobalt ferrite matrix helps the system to achieve this bifunctional characteristic. Thus obtained composite catalyst, CFZr(0.3)/N-rGO, shows significantly low overall overpotential and, hence, it appears to be a promising catalyst for the rechargeable ZAB application. The key aspects of this development are:

- CFZr(0.3)/N-rGO has been synthesized through the solvothermal route by substituting the Fe^{3+} with the Zr^{4+} in the cobalt ferrite nanoparticles. The prepared catalyst functions as a bifunctional catalyst for facilitating both ORR and OER, and, thereby, making it as a suitable system for fabricating a rechargeable Zn-air battery.
- The Zr substituted catalyst has shown a 40 mV negative shift in the overpotential for OER in comparison with the CF nanoparticles at 10 mA/cm^2 current density. Further, Zr substituted cobalt ferrite nanoparticles over N-doped reduced graphene oxide (CFZr(0.3)/N-rGO) has remarkably enhanced performance during the ORR and moderately favored OER with an overall potential difference(ΔE) of 0.840 V for the bifunctional activity.
- The catalyst delivered an 80 mV overpotential for ORR against the state-of-the-art 20 wt. % Pt/C catalyst and a 340 mV overpotential at a current density of 10 $mA/cm^2$for OER from the standard value (1.23 V RHE).
- In the fabricated primary ZAB, the catalyst showed discharge capacities of 727 and 730 mAh/g at the discharge current densities of 20 and 30 mA/cm^2, respectively.
- The rechargeable ZAB fabricated with the catalyst interestingly shows only ~200 mV increase in the overall operating overpotential after cycling for 10 cycles at 15 mA/cm^2 as against the 350 mV increase shown by the 20 wt. % Pt/C catalyst. The performance of the homemade catalyst was found to be stable even after 200 cycles.

4. Electrochemical Activity of Fe/CoN_x Grafted Carbon in Acidic and Basic Media

The oxygen reduction catalyst is pivotal for making the electrodes for the energy storage and conversion devices. However, the performance of the catalyst changes as the medium changes from acidic to basic. The major cause of the variation of the performance is the stability of the transition states. The adsorption energy of the transition states varies over the FeN_x and CoN_x systems and thereby the ORR performance. The change in the performance of the catalyst is also

observed in the ZAB discharge potential. The key aspects of the work detailed in this section of the thesis are as follows:

- Engrafting of the of FeN_x and CoN_x active centers was accomplished by annealing the corresponding metal precursors with the Vulcan carbon and graphene composite (N-GVC). The catalysts thus prepared were used to understand how the ORR kinetics varies with respect to the pH conditions of the electrolyte.
- The catalysts were studied in H_2SO_4, $HClO_4$ and KOH media to closely understand how the systems facilitate ORR under different pH conditions and nature of the electrolytes. An important observation from the study is that the FeN_x sites help to achieve better onset potential value whereas the CoN_x sites contribute to attain better half-wave potential value.
- The onset and half-wave potentials of the catalysts were found to be in correlation of the adsorption energy of the transition states (-OOH, -O*, -OH).
- The CoN_x based catalyst shows high amount of peroxide ion formation compared to the FeN_x based catalyst in basic medium, and this is ascribed to the lower dissociation energy for the –OOH species from the surface. This information is crucial for the development of catalysts for specific applications because peroxide ion formation triggers catalyst degradation and thereby can influence the life-time and durability of the devices.
- Finally,the demonstration was done by fabricating and testing primary ZABs by using the catalysts containing the different types of active centers. The discharge plot of the catalyst follows the order: Co-NGVC> Fe-2Co-NGVC > Fe-NGVC. These results clearly demonstrate the dependence of the system performance on the ability of the catalyst to facilitate ORR, which in turn is depending on the nature of the active centers and transition states.

Future Prospect

The studies covered in this thesis mainly deal with the preparation of cobalt ferrite nanoparticles and their composites with nitrogen-doped graphene oxide as potential electrocatalysts for facilitating oxygen reduction reaction (ORR). The substitutional effect of the transition metal (Zn and Zr) atoms clearly demonstrates the sensitivity of this parameter in changing the electronic properties of the catalysts and thereby the ORR activity. However, these catalysts still suffer

from the issue related to overpotential for ORR and durability under the electrochemical conditions. The transition metal oxide based electrocatalysts are desirable candidates for the fabrication of the energy storage and conversion devices. The study covered in the thesis provided insightful information on the influence of the nature of the active sites and electrolytes in determining the overpotential of the ORR process. In general, the reaction products evolved in various types of the metal-air batteries vary depending on the active metals used as the catalysts for the applications. The metal-air batteries based on the first-row alkali metals require non-aqueous electrolytes to get rid of the issue of moisture sensitivity of these systems. Similarly, the transition metal-based batteries such as Zn-air battery function in aqueous electrolytes, but they suffer from the influence of the parasitic reactions (such as HER and K_2CO_3 formation).

The energy conversion devices, such as AEMFCs and PEMFCs also suffer from the slow kinetics of ORR and an adequately selected catalyst can help to achieve radical changes in the performance characteristics of these types of systems. These devices operate in different electrolyte conditions (proton exchange or anion exchange) and, hence, the selection of the ORR catalyst is critical considering the sensitivity of the different active sites to the nature of the electrolytes. An adequately designed catalyst based on transition metals can provide vast opportunities in redefining the performance durability characteristics of the systems like AEMFCs and PEMFCs. Hence, the findings of the present study can be extended to select or develop appropriate systems for these specific applications. The homemade catalysts can further be improved by changing the functionalities and through structural modifications to achieve additional reduction in the faradaic overpotentials. Strategic modifications to impart bifunctional characteristic such as ORR and OER along with structural modifications can lead to the development of better conversion devices, including rechargeable metal-air batteries.

List of Publications

1. List of Publications Included in the Thesis:

1) Cobalt Ferrite Bearing Nitrogen-Doped Reduced Graphene Oxide Layers Spatially Separated with Microporous Carbon as Efficient Oxygen Reduction Electrocatalyst. **Kashyap, V.**; Singh, S. K.; Kurungot, S., (***ACS Appl. Mater. Interfaces* 2016, *8*, 20730-20740**.)
2) Activity Tuning of Cobalt Ferrite Nanoparticles Anchored on Nitrogen Doped Reduced Graphene Oxide as a Potential Oxygen Reduction Electrocatalyst by Zn Substitution in the Spinel Matrix. **Kashyap, V.**; Singh, S. K.; Kurungot, S.,(***Chemistry Select* 2017, *2* , 7845-7853)**
3) Zirconium-Substituted Cobalt Ferrite Nanoparticle Supported N-doped Reduced Graphene Oxide as an Efficient Bifunctional Electrocatalyst for Rechargeable Zn–Air Battery. **Kashyap, V.;** Kurungot, S (***ACS Catal.* 2018, 3715-3726)**
4) Medium Modulated Oxygen Reduction Activity of Fe/Co Active Centre Grafted Electrocatalyst . **Kashyap, V.**; Kurungot, S (***Under revision: ChemElectroChem***)

2. Journal Articles:

5) Iron Catalyzed Hydroformylation of Alkenes under Mild Conditions: Evidence of an Fe(II) Catalyzed Process. Pandey, S.; Raj, K. V.; Shinde, D. R.; Vanka, K.; **Kashyap, V**.; Kurungot, S.; Vinod, C. P.; Chikkali, S. H.(***J. Am. Chem. Soc.* 2018, *140*, 4430-4439**)
6) Realizing High Capacitance and Rate Capability in Polyaniline by Enhancing the Electrochemical Surface Area through Induction of Superhydrophilicity. Soni, R.; **Kashyap, V**.; Nagaraju, D.; Kurungot, S. (***ACS Appl. Mater. Interfaces* 2018, *10*, 676-686**)
7) An Efficient and Durable Oxygen Reduction Electrocatalyst Based on CoMn Alloy Oxide Nanoparticles Supported Over N-doped Porous Graphene" Author(s): Singh, Santosh; **Kashyap, Varchaswal**; Manna, Narugopal ; Bhange, Siddheshwar; Soni, Roby; Boukherroub, Rabah; Szunerits, Sabine; Kurungot, Sreekumar (***ACS catalysis* 2017, 6700-6710)**
8) Nanoporous Graphene Enriched with Fe/Co-N Active Sites as a Promising Oxygen Reduction Electrocatalyst for Anion Exchange Membrane Fuel Cells. Palaniselvam, T.; **Kashyap, V**; Bhange, S. N.; Baek, J.-B.; Kurungot, (***Adv. Funct. Mater.* 2016, *26*, 2150-2162**.)

9) High Performing PGM-Free AEMFC Cathode from Carbon-Supported Cobalt Ferrite Nanoparticles. Xiong Peng[=a], **Varchaswal Kashyap**,[=b,c], Benjamin Ng[a], Sreekumar Kurungot[b,c], LianqinWang[d], John R. Varcoe[d], William E. Mustain[a]* (***Catalysis,* Just accepted**)
10) $[MoS_4]^{2-}$-Intercalated NiCo Layered Double Hydroxide Nanospikes: An Efficiently Synergized Material for Urine to Direct H_2 Generation. Nadeema, Ayasha; **Kashyap, Varchaswal**; Gururaj, Rakshitha ; Kurungot, Sreekumar.(***Submitted***)

Erratum